# Mission Analysis and Navigation Design

for Uranus Atmospheric Flight

Master of Science Thesis

É. Bessette

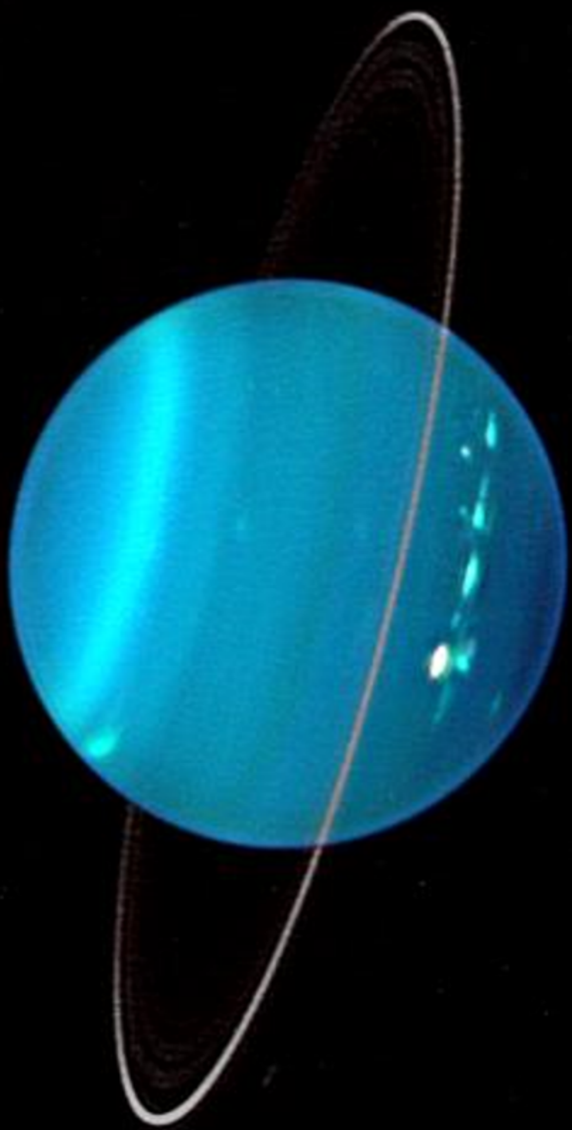

Delft University of Technology

# Mission Analysis and Navigation Design

## for Uranus Atmospheric Flight

by

É. Bessette

in fulfilment of the degree of Master of Science in Aerospace Engineering at the Delft University of Technology to be defended publicly on June 10, 2022 at 9:30.

| | | |
|---|---|---|
| Student Number: | 4534921 | |
| Thesis Duration: | March 8, 2021 - June 10, 2022 | |
| Thesis Supervisors: | Dr. ir. E. Mooij | TU Delft, Astrodynamics and Space Missions |
| | Dr. D.M. Stam | TU Delft, Astrodynamics and Space Missions |
| Thesis committee: | Dr. A. Menicucci | TU Delft, Space Systems Enginnering |
| | Dr. J.P. Lebreton | CNRS Orléans, LPC2E |

Cover Image: An infrared composite image of Uranus obtained with Keck Telescope adaptive optics, available at `https://photojournal.jpl.nasa.gov/catalog/PIA17306`, accessed on 24/11/2020.

# Preface

This report marks the last deliverable of the Space Flight MSc of Aerospace Engineering at Delft University of Technology. This work focuses on the mission analysis and navigation design of a mission to Uranus, with aim of linking new atmospheric in-situ measurements to the planet's formation and evolution, as well as those of the Solar System as a whole. The focus is on the design of the in-situ vehicles' navigation system, which is challenged by Uranus' very opaque atmosphere, thus limiting the use of any optical sensors.

This thesis, as well as my experience in Delft were marked by the contributions of numerous people I would like to express my gratitude towards. First, I would like to thank my thesis supervisors Dr. Ir. Erwin Mooij and Dr. Daphne Stam for their continuous guidance and support. Their contributions and observations were crucial in me reaching this thesis' results without losing my mind too much. I am also grateful for the continuous care and support from my cherished friends, who all play a very important role in my life. From my childhood best friend, to my high school and university friends and flatmates, without forgetting the invaluable support of my colleagues in room NB 2.44: my life would not be the same without you. Finally, I cannot thank my family enough for the constant encouragement and support they have provided me during all those years. Thank you so much to my brothers Gabriel and Antoine, and to my loving parents Dominique and Denis for believing in me. Tout ça c'est grâce à vous.

*É. Bessette*
*Delft, June 2022*

# Abstract

The planet Uranus is one of the most intriguing and unexplored bodies of the Solar System. Its mysteries include its active atmospheric dynamics, its low internal energy, its extreme obliquity, its complex magnetic field, and its ring and satellite system containing possible ocean worlds (Simon et al., 2022). As of today, none of the current formation and evolution models developed for Uranus can explain all of its chemical and dynamical aspects. A reason for this is that the only close-up knowledge available comes from the 1986 Voyager 2 mission, which performed a fly-by of the planet, probing the upper 30 km of its atmosphere with radar occultation. An in-situ mission to study Uranus' atmosphere could provide answers to this planet's mysteries, enabling the measurement of deeper layers of its atmosphere. Recent mission proposals to Uranus recommend the use of a mission architecture comprising of a parachuted descent probe and a relay spacecraft. However, this limits the in-situ measurement time to a few hours, for around twelve years of interplanetary travel to Uranus. Moreover, this leads to extremely localised measurements, limited to where the descent probe is released.

A 6 DoF flight simulator was thus designed, with a focus on identifying the specifications and limitations of its Guidance, Navigation, and Control (GNC) modules, for feasibly flying in Uranus' challenging atmosphere, and providing new science return. The chosen mission architecture consists of two gliders, supported by an orbiting spacecraft in a circular, equatorial, and synchronous orbit to allow for continuous trajectory tracking and relay of the scientific data back to Earth ground stations. The two gliders fly at constant latitudes of 17.5° N and 89° N, and are thus denoted as the *equatorial* and *polar* gliders during this work. This simulator propagates the gliders' equation of motion with aim of reaching the planet's 100 bar pressure level (at $-375$ km from the 1 bar pressure level defined at 0 km altitude), all while considering the reference vehicle's aerodynamics, the planet's atmospheric density, pressure, and temperature profiles, gravity, and the measurements of atmospheric quantities by the chosen sensors. The navigation sensors are taken from the payload suite, and modelled to feed data to the navigation state estimator.

It is crucial to identify the specifications and limitations associated with the design of the GNC modules, as well as of their integration, to ensure that such a system can perform accurately, with the chosen scientific payload suite. The tracking guidance commands generated by comparing reference and estimated trajectories should ensure no deviation from the reference heading angle and no trajectory oscillations. The control module should output control surfaces commands, which are within the vehicle's surface deflection bounds and which ensure that the vehicle follows the reference trajectory while remaining longitudinally and laterally stable. Finally, the navigation module should be able to transform the sensors' measurements into state estimates accurately. With a working system, the gliders' flight can then be simulated in Uranus' atmosphere.

It was concluded that a robust guidance module is necessary to accept the navigation system's estimates, and for a complete 6 DoF simulation to be run with the inclusion of guidance, control, and navigation blocks. When using the designed guidance and control modules, with a feedback of real data instead of estimated data, results of this study include a total glider flight time of 12.80 Earth days until the 100 bar pressure level for the equatorial glider, and 12.69 Earth days for the polar one. This allows for total travelled distances of $18,741$ km and $18,785$ km, along both gliders' constant latitudes of $\lambda_{eq} = 17.5°$ and $\lambda_{pol} = 89.0°$, respectively. The measurement phase of each glider produces a total data size of 3.29 Gbits, which results in an uplink time of 18.26 min to the relay spacecraft, and 62.88 h for the relay spacecraft to transmit it to Earth. The simulator's integration frequency is of 50 Hz, with all modules working at that same frequency, except the guidance module working at 10 Hz. The performance of the designed navigation module was assessed by running it in parallel to the main loop of the software. The designed navigation sensors' measurements were used as inputs and the EKF's performance was seen to decrease when including measurement noise and errors. Nevertheless, such a system can provide good state estimates when no noise is included, confirming that the navigation instrument suite fits the mission at hand. Recommendations for future work include further tuning of the filter when sensor noise is included, including a more robust guidance system, and filtering out the navigation filter's estimates' noise.

# Contents

# Nomenclature

## List of Abbreviations

| Abbreviation | Meaning |
|---|---|
| AC | Alternating Current |
| ACC | Accelerometer |
| ADCS | Attitude Determination and Control Subsystem |
| ARES | Aerial Regional-scale Environmental Survey |
| ASI | Italian Space Agency |
| ASRG | Advanced Stirling Radioisotope Generator |
| au | Astronomical Unit |
| AVIATR | Aerial Vehicle for In-situ and Airborne Titan Reconnaissance |
| CCD | Charge-Coupled Device |
| CFD | Computational Fluid Dynamics |
| c.o.m. | Centre of Mass |
| DC | Direct Current |
| DFMS | Double Focusing Magnetic Mass Spectrometer |
| DISR | Descent Imager and Spectral Radiometer |
| DoF | Degrees of Freedom |
| DPS | Deep-Space Positioning System |
| DSE | Design Synthesis Exercise |
| DSM | Deep Space Manoeuvre |
| EKF | Extended Kalman Filter |
| eMMRTG | Enhanced Multi-Mission Radioisotope Thermoelectric Generator |
| ESA | European Space Agency |
| FADS | Flush Air Data Sensor |
| GNSS | Global Navigation Satellite System |
| GSFC | Goddard Space Flight Center |
| HAD | Helium Abundance Detector |
| HASI | Huygens Atmospheric Structure Instrument |
| HEEET | Heatshield for Extreme Entry Environments Technology |
| IAU | International Astronomical Union |
| ICRF | International Celestial Reference Frame |
| IG-ASI | Ice Giant Atmospheric Structure Instrument |
| IMU | Inertial Measurement Unit |
| IRIS | Infrared Interferometer Spectrometer |
| JPL | Jet Propulsion Laboratory |
| LA | Launch Approval |
| LED | Light Emitting Diode |
| LKF | Linear Kalman Filter |
| LV | Launch Vehicle |
| LEAF | Lifting Entry Atmospheric Flight |
| LOAC | Light Optical Aerosol Counter |
| LQR | Linear Quadratic Regulator |
| MACE | Mars Airborn Canyon Explorer |
| MARG | Magnetic, Angular Rate, and Gravity |
| MEV | Maximum Expected Value |
| MID | Mid Infra-Red |
| MMRTG | Multi-Mission Radioisotope Thermoelectric Generator |
| MSL | Mars Science Laboratory |
| NASA | National Aeronautics and Space Administration |
| NEPA | National Environmental Policy Act |
| NFR | Net Flux Radiometer |
| NIR | Near Infra-Red |
| PPI | Pressure Profile Instrument |

| Abbreviation | Meaning |
|---|---|
| RHU | Radio Isotope Heater Unit |
| ROSINA | Rosetta Orbiter Spectrometer for Ion and Neutral Analysis |
| RPS | Radioisotope Power System |
| RTOF | Reflectron Time-Of-Flight |
| SAM | Sample Analysis at Mars |
| SDT | Science Definition Team |
| SEP | Solar-Electric Propulsion |
| SSP | Surface Science Package |
| TandEM | Titan and Enceladus Mission |
| TARA | Titan Atmospheric Research Aircraft |
| TDLAS | Tunable Diode Laser Spectrometer |
| TEC | Thermoelectric Cooler |
| TEM | Temperature sensor |
| TLS | Tunable Laser Spectrometer |
| TPS | Thermal Protective System |
| TRL | Technology Readiness Level |
| TSSM | Titan Saturn System Mission |
| TU Delft | Delft University of Technology |
| UKF | Unscented Kalman Filter |
| USO | Ultra Stable Oscillator |
| UT | Unscented Transform |
| UV | Ultra-Violet |
| WBS | Work Breakdown Structure |

# List of Symbols

| Latin Symbol | Unit | Property |
|---|---|---|
| $\mathbf{A}$ | - | State-transition Jacobian matrix |
| $\mathbf{a}$ | m/s$^2$ | Acceleration vector |
| $a$ | m | Semi-major axis of orbit |
| $a$ | m/s | Speed of sound |
| $b_{ref}$ | m | Wingspan |
| $b$ | m/s | IMU bias |
| $c_{ref}$ | m | Mean aerodynamic chord |
| $C_D$ | - | Drag coefficient |
| $C_L$ | - | Lift coefficient |
| $C_S$ | - | Side force coefficient |
| $C_l$ | - | Roll moment coefficient |
| $C_m$ | - | Pitch moment coefficient |
| $C_n$ | - | Yaw moment coefficient |
| $D$ | N | Drag force |
| $d$ | m/s$^2$ | IMU drift |
| $E$ | J | Energy |
| $E$ | rad | Eccentric anomaly |
| $e$ | - | Eccentricity of orbit |
| $e$ | - | Error |
| $\mathbf{F}$ | N | Force vector |
| $f$ | Hz | Frequency |
| $g$ | m/s$^2$ | Gravity |
| $\mathbf{H}$ | - | Observation Jacobian matrix |
| $H$ | km | Scale height |
| $h$ | m | Altitude above 1 bar pressure level |
| $h^*$ | m | Pseudo altitude |
| $\mathbf{I}$ | kg/m$^2$ | Inertia tensor |
| $i$ | rad | Orbit inclination |
| $\mathbf{J}$ | - | Jacobian |
| $\mathbf{K}$ | - | Gain matrix |
| $K$ | - | Gain |
| $\mathcal{L}$ | Nm | Aerodynamic lift moment |
| $L$ | N | Lift force |
| $\mathcal{M}$ | Nm | Aerodynamic pitch moment |
| $\mathbf{M}$ | Nm | Moment vector |
| $M$ | rad | Mean anomaly |
| $m$ | kg | Mass |
| $M$ | - | Mach number |
| $\mathcal{N}$ | Nm | Aerodynamic yaw moment |
| $n$ | rad/s | Mean motion |
| $n_g$ | W/m$^2$ | G-load |
| $\mathbf{P}$ | - | Covariance matrix |
| $p$ | Pa | Pressure |
| $p$ | rad/s | Yaw rate |
| $p_x$ | m | Position in x-direction |
| $\mathbf{Q}$ | - | Process noise matrix |
| $Q$ | - | Quaternion |
| $q$ | rad/s | Pitch rate |
| $q_c$ | W/m$^2$ | Thermal flux |
| $\bar{q}$ | N/m$^2$ | Dynamic pressure |
| $\mathbf{R}$ | - | Measurement noise matrix |
| $R$ | m | Radius |
| $R$ | J/kgK | Specific gas constant |
| $R_{s,i}$ | m | Radius of sphere of influence |

| Latin Symbol | Unit | Property |
|---|---|---|
| $r$ | m | Radial distance |
| $r$ | rad/s | Roll rate |
| $r_a$ | m | Apoapsis radius |
| $r_p$ | m | Periapsis radius |
| $S$ | N | Side force |
| $S$ | W/m$^2$ | Solar irradiance |
| $S_{ref}$ | m$^2$ | Reference area |
| $T$ | s | Period |
| $T$ | K | Temperature |
| $t$ | s | Time |
| $\Delta t$ | s | Change in time |
| $\mathbf{u}$ | - | Control vector |
| $V$ | m/s | Velocity |
| $\Delta V$ | m/s | Change in velocity |
| $\mathbf{v}$ | - | Noise vector |
| $\mathbf{W}$ | - | Observability Gramian |
| $W$ | N | Weight force |
| $\mathbf{w}$ | - | Noise vector |
| $\mathbf{x}$ | - | State vector |
| $\mathbf{z}$ | - | Measurement vector |

| Greek Symbol | Unit | Property |
|---|---|---|
| $\alpha$ | rad | Angle-of-attack |
| $\beta$ | rad | Side-slip angle |
| $\beta_U$ | - | Uranus normalised mean radius |
| $\gamma$ | - | Specific heat ratio |
| $\gamma$ | rad | Flight-path angle |
| $\delta$ | rad | Geocentric latitude |
| $\delta$ | rad | Deflection angle |
| $\epsilon$ | J/kg | Specific total energy |
| $\epsilon$ | rad | Elevation angle |
| $\theta$ | rad | True anomaly |
| $\theta$ | rad | Co-latitude |
| $\theta$ | rad | Euler pitch angle |
| $\mu$ | m$^3$/s$^2$ | Standard gravitational parameter |
| $\rho$ | km/m$^3$ | Density |
| $\rho$ | m | Pseudo range |
| $\dot{\rho}$ | m | Pseudo range rate |
| $\sigma$ | rad | Bank angle |
| $\tau$ | s | Time of periapsis passage |
| $\tau$ | rad | Longitude |
| $\boldsymbol{\phi}$ | - | State transition matrix |
| $\phi$ | rad | Azimuth angle |
| $\phi$ | rad | Euler roll angle |
| $\chi$ | rad | Heading angle |
| $\psi$ | rad | Turn angle of fly-by |
| $\psi$ | rad | Euler yaw angle |
| $\omega$ | rad | Argument of periapsis |
| $\boldsymbol{\omega}$ | rad/s | Rotational velocity |
| $\Omega$ | rad | Right ascension of the ascending node |

# 1 Introduction

Voyager 2 was the first and only spacecraft to perform a fly-by of Uranus and Neptune in 1986 and 1989, respectively. Since then, all knowledge on these planets has been obtained from ground-based and space-based telescopes, and other instruments' measurements. No vehicle, however, has ever been to these Ice Giants to perform in-situ measurements. Thanks to the alignment of our Solar System's planets, the 2030s will offer the possibility to do that, as potential gravity assists of both Venus and Jupiter, combined with the illumination of Uranus and Neptune's unobserved hemispheres should yield a smaller fuel consumption for such a mission, as well as new science return. The American National Aeronautics and Space Administration (NASA) and the European Space Agency (ESA) agencies have worked independently and collaboratively to define elements essential to such a mission: science priorities, mission concepts with different potential architectures, promising science payload suites to fulfil the science objectives, and differences in studying Uranus and Neptune (Hofstadter et al., 2017; Hofstadter et al., 2019; Fletcher et al., 2020b; Guillot, 2019; Mousis et al., 2019). The main conclusions that can be drawn from these are that Uranus and Neptune are considered equally valuable to explore, and that the presence of an atmospheric vehicle in the mission's architecture is paramount to the achievement of the highest priority science objectives: to measure abundances of noble gases and their isotopes, pressure and temperature through several layers of the atmosphere, and abundances of heavier elements and disequilibrium species, which require much deeper probing. Nearly all previous mission studies to the Ice Giants recommend the use of a mission architecture comprising of a parachuted ballistic descent probe and a relay spacecraft, to measure and transmit the scientific data back to Earth. A reason for this is that this architecture has been proven to be safe and efficient, through the heritage of the previous Galileo mission to Jupiter and Cassini-Huygens mission to Titan.

Motivation for a mission to Uranus and/or Neptune stems from the knowledge gap related to the formation of these planets, which could challenge our understanding of the formation and evolution of the Solar System as a whole. The National Academy of Sciences (2022) state that unless extreme local conditions are assumed while the nebula was still present, planetesimal accretion is predicted to be too inefficient to form Uranus and Neptune at their current locations. According to Fletcher et al. (2020b), "the atmospheres are the windows through which we interpret the bulk properties of planets". Studying Uranus' atmosphere is thus crucial to measuring the planet's physical and chemical properties. Additional knowledge on Uranus' atmosphere can then be extrapolated to the planet's formation and thus to the formation of Ice Giants and consequently of the Solar System. A mission to Uranus can hence provide insight into why several models predict the formation of the Ice Giants to be much closer to the Sun than where they presently are (Levison and Stewart, 2001; Gomes et al., 2005; Morbidelli et al., 2007; Batygin and Brown, 2010; Nesvorný, 2011; Batygin et al., 2012).

The following research question was thus defined at the beginning of this MSc thesis:

> Main Research Question
>
> **How can knowledge about Uranus' current atmosphere help us understand the formation and evolution of the Ice Giants, and in a broader sense, those of the Solar System?**

To stay within the scope of a MSc thesis, this research question was scaled down to an intermediate one, which can effectually be answered at the end of this study. More specifically, this work will aim at relating which atmospheric quantities are essential to the identification of new science return related to Uranus' formation and evolution, and on how to feasibly measure them. Amongst others, the bulk composition of an atmosphere can contribute to provide evidence for how and where a planet formed, as well as the associated protosolar nebula conditions. To retrieve information about a planet's formation, it is essential to study the variation of atmospheric composition with depth. The previously mentioned mission architecture of a single or multiple atmospheric vehicle(s) and a relay spacecraft is thus adopted, and an intermediate research question is defined to establish the approach and means necessary to the measurement of Uranus' atmospheric properties with depth:

Intermediate Research Question

**Which mission profile and GNC design can enable the measurement of essential Uranian atmospheric properties to help answer the Main Research Question?**

To answer this intermediate research question, numerical tools such as Python, XFLR5, and MATLAB/Simulink will be used. The flight simulator will be constructed in Simulink, basing the design on the work of Mooij and Ellenbroek (2011). This research question is split into sub-questions dealing with the in-situ study of the planet's atmosphere, the relay spacecraft's orbit, and the software's Guidance, Navigation, and Control (GNC) design:

1. **Which trajectory should be followed by the atmospheric vehicles to measure physical and chemical properties of Uranus' atmosphere?**
   In-situ atmospheric vehicles are paramount to the measurement of remotely inaccessible atmospheric elements such as composition, structure, and dynamics deeper than the 1 bar pressure level. It is thus important to research and determine which trajectory the chosen atmospheric platforms can feasibly fly in Uranus' atmosphere while successfully fulfilling the mission's science objectives. This sub-question requires the identification of the planet's areas that should be studied, and whether some measurements require spatial and/or temporal repeatability. The number of required atmospheric platforms can then be defined, as well as the necessary payload suite needed on-board. Finally, a communication link between the atmospheric vehicles and the carrier and relay spacecraft should be ensured.
2. **Which orbit should the relay spacecraft follow, so as to deliver the atmospheric platforms, track their trajectory, and relay scientific data to the Earth?**
   The orbital elements of the spacecraft's orbit, as well as the manoeuvres it has to perform should be determined. Elements to consider are: the continuous tracking of the atmospheric vehicles' trajectories, the communication link to the atmospheric vehicles and to Earth, and the probes' entry location.
3. **Which is the most appropriate autonomous navigation architecture for atmospheric probing of Uranus?**
   The reason for reconstructing the atmospheric vehicles' trajectory is twofold: for safely flying the vehicles, and to establish a sound basis for the scientific measurements. Indeed, it is important to be able to relate the trajectories to the scientific measurements to have a spatial and temporal reference of what was measured. To do so, the vehicle's state must be estimated, for which navigation is needed.
4. **What are the limitations and shortcomings of a standard GNC design that allows robust and autonomous mission performance?**
   The objective is to identify the specifications and limitations necessary to the modelling of each component of the flight simulator's Guidance, Navigation, and Control (GNC) blocks: reference trajectory, trim module, guidance module, control module, actuators module, navigation sensors and estimator, for them to work while integrated together.

The objectives of this thesis are the following:

**SO-01:** Define the science objectives to be fulfilled.
**SO-02:** Choose appropriate scientific payload instruments for the fulfilment of the science objectives, and design the ones to be used as navigation sensors.
**SO-03:** Choose an in-situ platform to perform the scientific measurements, ensuring feasibility of the atmospheric vehicle's flight in the planet's atmosphere, as well as ability to perform the science measurements and communicate them to Earth.
**SO-04:** Select a reference vehicle from literature, to serve as in-situ platform and retrieve or generate its aerodynamic coefficients.

**SO-05:** Determine the launch, interplanetary trajectory, Uranus approach and platform release, as well as vehicle's entry and descent options and parameters.
**SO-06:** Define mission, system, and modelling requirements.
**SO-07:** From literature, retrieve models describing Uranus' environment (gravity, temperature, pressure, density, winds), and integrate them in the simulator.
**SO-08:** Select in-situ area(s) to be probed.
**SO-09:** Design a reference trajectory for the in-situ platform(s), to include in the guidance system.
**SO-10:** Design a Linear Quadratic Regulator (LQR) controller and integrate it in the simulator.
**SO-11:** Design and include an Extended Kalman Filter (EKF) as the navigation system's state estimator.
**SO-12:** Determine orbital parameters of the spacecraft orbiting Uranus to enable continuous line-of-sight with the in-situ platform(s) and telecommunication with Earth ground stations.
**SO-13:** Verify the developed simulator.
**SO-14:** Simulate the model in 6 Degrees of Freedom (DoF) taking into account the environment, Guidance, Navigation, and Control (GNC), the chosen vehicle's aerodynamics, and the included scientific instruments.

To fulfil the objectives of this thesis, Chapter 2 will first introduce past and future missions to Uranus and Neptune, as well as past and future atmospheric entry missions using winged vehicles. A choice of target planet, scientific aims, scientific payload, and platform will also be described in this chapter. A mission definition will also be established, containing mission and system requirements. Following this, Chapter 3 will set the basis for knowledge on the target planet, and on the target area(s) to be probed. Chapter 4 will then present all necessary flight and orbital mechanics for the numerical simulations. Chapter 5 will present the chosen reference vehicle, orbiter trajectory, and communication window parameters. Chapter 6 and Chapter 7 will give theoretical explanations of Guidance, Control, and Navigation, as well as their design and development. Following this, Chapter 8 will describe the mission's software architecture. Chapter 9 will then detail the software's results, and Chapter 10 will provide the conclusions and recommendations of the work performed during this thesis research.

# 2

# Mission Heritage and Requirements

This chapter will present the knowledge that will help in the definition of the mission at hand. This includes previous and future Uranus/Neptune missions in Section 2.1, previous and future atmospheric missions using winged vehicles in Section 2.2, as well as the rationale for a choice of target planet in Section 2.3. Section 2.4 will present the scientific aims chosen for the mission, Section 2.5 the scientific payload needed to fulfil the science objectives, and the choice of science platform to explore the planet's atmosphere will be presented in Section 2.6. Then, Section 2.7 will summarise the elements that constrain the choice of reference vehicle from literature. At the end of this chapter, additional aspects such as the mission's timeline and interplanetary trajectory are looked into in Section 2.8, so as to define preliminary mission and system requirements in Section 2.9.

## 2.1. Uranus/Neptune Missions

As of today, all scientific knowledge on Uranus and Neptune has been obtained from ground-based measurements, and from science experiments performed during the fly-by of Voyager 2 in January of 1986 at Uranus, and in August 1989 at Neptune. Concerning the possibility of exploring one of the Ice Giants in the near future, both NASA and ESA have suggested potential missions, through the means of studies, surveys, as well as medium- and large-class mission proposals. It is especially interesting to visit these worlds with a launch planned in the 2030s, so as to take advantage of the Solar System's planets' alignment, which enables the possible fly-bys of Venus and Jupiter, as well as the prospect of exploring the planets' hemispheres unobserved by Voyager 2. No mission has been selected yet.

### 2.1.1. NASA: Voyager 2 (1980s)

Launched sixteen days before its twin space probe Voyager 1 in August of 1977, Voyager 2 is the only spacecraft to have visited both outer planets Uranus and Neptune. Both spacecraft' trajectories involved a fly-by of Jupiter and Saturn. Voyager 2's scientific measurements when close to Uranus enabled scientists to discover the existence of two new planetary rings, ten new satellites, and an off-axis and off-centre 55° tilt in the planet's magnetic field. Voyager 2's science data on Uranus also includes the measurement of wind speeds as high as 724 km/h in Uranus' atmosphere, and suggestion of the presence of a boiling ocean of water at around 800 km below the top cloud surface[1]. It conducted a radio occultation experiment, which provided scientists with data to construct the planet's temperature and pressure profiles. This experiment was conducted from 232.5 km alitude (0.25 mbar) to $-27.5$ km altitude (2.30881 bar) with respect to the 0 km (1 bar) altitude (Lindal et al., 1987), between 2° and 7° S latitude (Tyler et al., 1986). When passing by Neptune, it allowed the discovery of six new satellites, four new rings, and three major features in the planetary clouds: the "Lesser Dark Spot", the "Great Dark Spot", which was then shown to have disappeared when later observed from ground-based telescopes, and "Scooter", a bright feature in the planetary clouds. Winds blowing at up to $1,100$ km/h were also observed.[2]

Equipped with radioisotope thermoelectric generators (RTGs) for power generation, Voyager 2 conducted communication with the Earth through the use of the Deep Space Network (DSN). The network consists of three

[1] `https://www.jpl.nasa.gov/news/voyager-mission-celebrates-30-years-since-uranus`, accessed on 15/11/2020

[2] `https://solarsystem.nasa.gov/missions/voyager-2/in-depth/#:~:text=Voyager%202%20is%20the%20only,giant%20planets%20at%20close%20range.&text=At%20Uranus%2C%20Voyager%202%20discovered,a%20%22Great%20Dark%20Spot.%22`, accessed on 15/11/2020.

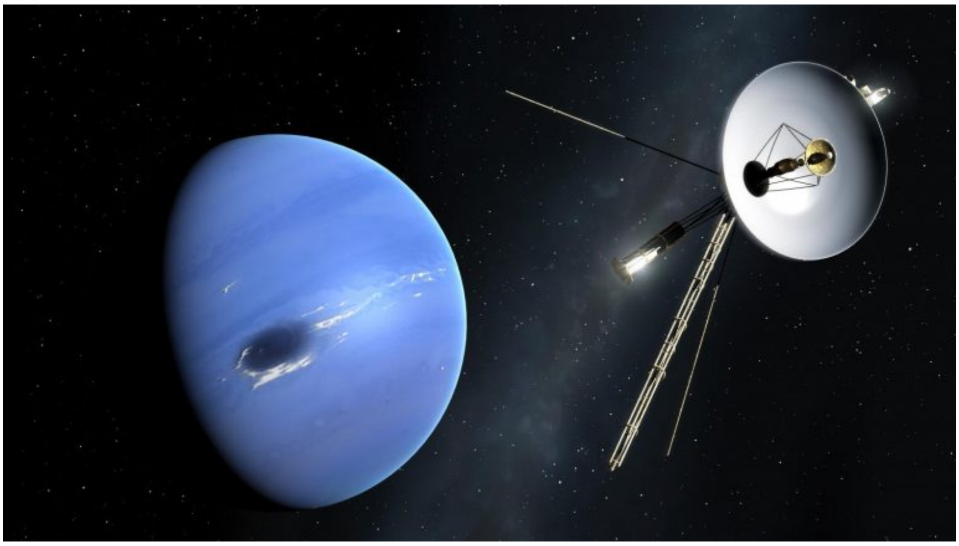

**Figure 2.1:** Artist's impression of Voyager 2 in front of Neptune and its famous "Great Dark Spot" along with bright rapidly-changing clouds.[a]
[a]`https://www.sciencephoto.com/media/734272/view`, accessed on 30/11/2020.

radio antenna facilities spaced equally around the globe, ensuring communication between at least one of the facilities and almost any spacecraft in line-of-sight of the Earth.[3]

Voyager 1 and 2 contributed to a successful mission, for it replaced the NASA cancelled "Grand Tour" program by retaining the same mission concept of visiting Jupiter, Saturn, Uranus, and Neptune. Both Voyagers are now headed into interstellar space and have left the heliosphere: the protective bubble of particles and magnetic fields created by the Sun. Their observations of the Ice Giants set a strong basis for future work, where more recent and precise instruments would be able to get additional knowledge on these planets. An artist's impression of Voyager 2 and Neptune is shown in Figure 2.1, where characteristic features of Neptune can be seen: the "Great Dark Sport", as well as a few bright clouds.

### 2.1.2. NASA: Ice Giants Pre-Decadal Survey (2017)

In preparation for the third Planetary Science Decadal Survey commissioned by NASA, the Ice Giants Pre-Decadal Study aims at re-evaluating science priorities and concepts for missions to the two outer planets. This study was led by a Science Definition Team (SDT) and Jet Propulsion Laboratory (JPL) with participation from Langley Research Centre, Ames Research Centre, The Aerospace Corporation, and Purdue University. The study team assessed and prioritised science objectives taking into account advances since the last Decadal Survey (2003-2013), current and emerging technologies, mission implementation techniques and celestial mechanics. This study examined a wide range of mission architectures, flight elements, and instruments (Hofstadter et al., 2017). The methods and results obtained are as follows:

- **Target planet:** the SDT concluded that both Uranus and Neptune are equally important to explore, each having concepts to teach us that the other cannot. An orbiter around Neptune would offer the possibility of exploring its captured satellite Triton, while a mission to Uranus would enable the study of a native ice giant satellite system, its formation, and evolution. The term 'native' refers here to the potential in-situ formation of Uranus' satellites from gaseous disks formed by the planet at the end of its formation (Szulagyi et al., 2018). It is also emphasised that, while being equally and individually compelling, the highest science return would come from an exploration of both systems.
- **Platform:** three concepts were considered, namely a single orbiter that would either perform a fly-by or orbit around one of the planets, an orbiter with a probe that would perform an atmospheric entry, and a dual orbiter. After ranking the different architectures in terms of the science objectives that could be met, the missions with by far the highest science return were the ones that included an orbiter at one ice giant, an orbiter or fly-by at the other, and at least one probe. The addition of the probe contributed to a significant increase in science return, as the concept with a probe was always ranked higher than any

[3]`https://directory.eoportal.org/web/eoportal/satellite-missions/v-w-x-y-z/voyager`, accessed on 15/11/2020.

other concept. The probe is needed to determine the planet's bulk composition, including abundances and isotopes of heavy elements, helium and heavier noble gases.

- **Entry probe analysis method:** the entry trajectories and aerothermal environments were calculated using TRAJ, a NASA Ames-developed three degrees of freedom atmospheric entry simulation. The chosen thermal protective system (TPS) was a Heatshield for Extreme Entry Environments Technology (HEEET).
- **Payload instruments on-board probe:** a mass spectrometer used to determine atmospheric composition, a helium abundance detector, an atmospheric structure instrument, ortho-para $H_2$ instrument, net-flux radiometer, and a nephelometer for the study of cloud and haze particles.

### 2.1.3. NASA and ESA: A Collaborative Study (2019)

Basing their work on the findings of NASA's 2017 Ice Giants Pre-Decadal Survey, NASA with the participation of ESA, ultimately recommends in this paper, a mission to Uranus consisting of an orbiter and an entry probe carrying a 150 kg orbiter science payload. Uranus was preferred to Neptune based on cost-conscious ground rules. Using knowledge from the Juno mission at Jupiter, it is suggested here to include an additional microwave sounder in the probe's instruments, so as to probe the deep troposphere's circulation, cloud structure, and composition (Hofstadter et al., 2019).

### 2.1.4. ESA: Voyage 2050 Call for Missions (2019)

Mission proposals were made in the form of white papers to ESA's most recent call for the planning cycle of its Science Program. They summarise the main measurements that should be performed during a future mission to Uranus or Neptune, as well as describe a potential mission's configuration and profile (Fletcher et al., 2020b; Guillot, 2019; Mousis et al., 2019).

- **Target planet:** Uranus and Neptune are considered equally valuable to explore, again emphasising the prospects of exploring Triton when passing by Neptune. An importance is put on the possibility of performing fly-bys of Solar System objects en route to Uranus and/or Neptune, such as Centaurs, which would be possible with the same payload as needed for the Ice Giants (Fletcher et al., 2020b). Uranus is mentioned to potentially offer more inactive regions to send a probe to, while showing signs of regular convective activity, as compared to Neptune (Guillot, 2019).
- **Platform:** The importance and scientific relevance of the presence of a probe is underlined in the papers mentioned above, for the combination of a probe and an orbiter is again viewed as an optimal platform for science measurements, with a focus on the investigation of the atmosphere's dynamics, chemistry, cloud formation, circulation, and energy transport (Fletcher et al., 2020b), as well as on the improvement of the current temperature profile inferred from the Voyager 2 radio-occultations (Guillot, 2019).
- **Entry probe analysis method:** as all three white papers mainly focused on the scientific potential of a probe investigating the planet's properties, they do not all give detailed indications on what type of platform could be used to perform these measurements, apart from mentioning the necessity of in situ measurements performed by a probe, and the relay of information through an orbiter. Mention is made of the atmospheric probe descent targeting the 10-bar level located about 5 scale heights beneath the tropopause, where most of the science goals can be achieved (Mousis et al., 2019). It is indicated that the orbiter that contains the probe should be placed on planetary entry trajectory, and be reoriented for probe targeting and release. After probe release, the orbiter would be placed on an overflight trajectory so as to receive the descending probe's telemetry data. The probe would then power on, warm up, and perform health checks. The end of entry would be determined from the accelerometers, after which a sequence of pilot and main parachutes would be deployed, and the heat shield released. Performing a simple parachuted descent, the probe would then perform all relevant scientific measurements and telecommunications would likely end when the link can no longer be maintained with the orbiter, or when the batteries are depleted, or when damaging thermal or pressure effects are felt (Mousis et al., 2019). This entry sequence is the same as the Galileo entry, descent and deployment sequence performed on Jupiter.
- **Payload instruments on-board probe:** Mousis et al. (2019) mention the same instruments as the ones used by Hofstadter et al. (2017), with the addition of a tunable laser spectrometer to provide for more isotopic measurements with high accuracy, and a Doppler-wind experiment to measure the altitude profile of zonal winds in Uranus' atmosphere along the probe's descent path, assuming that the probe will move with the winds beneath the parachute. This last experiment uses the radio subsystem of the orbiting spacecraft.

## 2.2. Atmospheric Missions with Winged Vehicles

After having studied past and future missions to Uranus and Neptune, let us now look at atmospheric missions. Multiple atmospheric platforms were researched, including the conventional parachuted descent probe used during the Galileo and Cassini-Huygens missions, as well as balloon-based vehicles, and winged vehicles. Section 2.6 provides a discussion leading to a trade-off between these different platforms for the mission. Following the conclusion of that trade-off, multiple un-propelled winged vehicles (gliders) were chosen as this mission's in-situ platforms, and their heritage is shown here.

Uranus and Neptune are known to be gaseous planets, which would make a potential landing and further take-off from one of these planets' surfaces unfeasible. Different types of winged vehicles will be studied here, with the aim of analysing their potential for performing a flight inside a planetary atmosphere. It is interesting to see that in most winged vehicle space missions, the science payload is placed at the extremities of the vehicle such as at the tip of the wings, nose, or tail.

Winged vehicles with fixed-wings would essentially glide through the planetary atmosphere, with changes in attitude and direction from their control surfaces, without however, being able to move up to a higher altitude unless a propulsion system is present on board. Designs for Venusian missions have shown that a solar-powered electric motor in combination with a propeller as the vehicle's propulsion is often opted for on a propelled winged craft (Landis et al., 2003; Colozza and Landis, 2005; Landis, 2006), although rocket-powered drones are also sometimes preferred (Calvin et al., 2000; Smith et al., 2004).

### 2.2.1. NASA: Aerial Regional-Scale Environmental Survey

Rocket-powered winged vehicle mission proposals include the NASA Aerial Regional-scale Environmental Survey (ARES), which led to the design of HADD2 and the high-altitude successful drop test of a 50 % scale demonstrator HADD1. The 6.2 m wing span design has a wet mass of 125 kg and dry mass of 66.5 kg. It would fly for a maximum duration of 101 min, yielding a 850 km maximum range at a groundspeed of 140 m/s and altitude of 1.5 km above Mars' ground level (Levine and ARES Science and Engineering Teams, 2005). The navigation algorithm of these vehicles was based on input data from a combination of sensors such as an air data system (airspeed, angle-of-attack, and angle of side-slip), a radar altimeter (terrain-relative altitude), a barometer (pressure altitude), and an Inertial Measurement Unit (IMU), as well as on-board topographic mapping along with initial measurements from the carrier spacecraft.[4] Vertical guidance follows a scripted barometric pressure profile, which is periodically correlated and corrected with the radar altimeter data. The vehicle possesses four control surfaces: two flaperons, which can be deflected symmetrically for pitch control as well as asymmetrically for roll control, and two ruddervators, which can be deflected symmetrically for pitch control and asymmetrically for yaw control (Braun et al., 2006). A visual of the deployment of ARES can be seen in Figure 2.2. The aircraft is transported folded in a descent probe. It is released and its wings are deployed after the heat shield release. After that, its engine turns on and it begins its cruise flight.

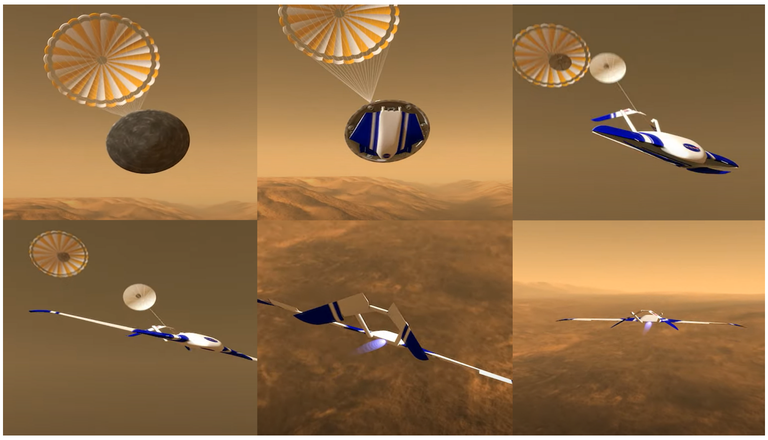

**Figure 2.2:** ARES deployment sequence of events.[a]

[a]`https://www.youtube.com/watch?v=9ykPIqgPTJE&ab_channel=bazi`, accessed on 01/03/2021.

[4]`https://www.nasa.gov/centers/dryden/news/X-Press/stories/2005/xtra_072005_PlanetaryFlightVehicle.html`, accessed on 01/12/2020.

### 2.2.2. NASA: Prandtl Wing

Armstrong Chief Scientist Al Bowers and his intern students designed the Preliminary Research Aerodynamic Design To Lower Drag (PRANDTL-D) aircraft, which is the first iteration of their work. This delta-shaped wing does not possess a vertical tail, but rather a twist in its wings, which proved to result in a reduction of drag and enhanced controllability. Flight models were successfully flown (on Earth) in 2015, which led to a concept for a Mars aircraft: the Preliminary Research Aerodynamic Design to Land on Mars, or Prandtl-M aircraft, which would be able to deploy, fly in the Martian atmosphere for about 10 minutes, glide down for the last 600 meters and land on Mars' surface. Its range would be about $30,000$ meters.[5]

### 2.2.3. TU Delft: Design Synthesis Exercises

Delft University of Technology's (TU Delft) yearly Aerospace Engineering Bachelor projects called Design Synthesis Exercises (DSE) have provided iterated designs for atmospheric probing platforms. A published executive summary of the mentioned projects is available in Melkert et al. (2003) and Melkert et al. (2008).

The 2008 Titan Atmospheric Research Aircraft (TARA) mission was designed incorporating the use of a pushing propeller aircraft for the exploration of Titan's atmosphere. The final design was one of a single bodied aircraft with a high wing configuration, an inverted V-tail and a pushing propeller mounted at the rear of the fuselage, with a total aircraft mass of 200 kg. Although the TARA team did not numerically test their navigation and guidance system, they provide a strong basis for the navigation instruments that could potentially be used for their mission: data input would be needed from different sensors (a SPEX instrument, a CCD camera, pitot-static tubes, and inertial sensors), as well as the current attitude from the Attitude Determination and Control Subsystem (ADCS), and received positioning signal from the mission's orbiter to calculate the vehicle's position (latitude and longitude) and heading. The vehicle's altitude is determined from laser altimetry and static pressure measurements. The mission's nominal cruise speed is of 10 m/s at 10 km altitude, which places this craft in a subsonic flight regime. The focus of the project was on the aircraft's design, which followed an approach similar to Earth-based aircraft designs.

The 2003 Mars Airborn Canyon Explorer (MACE) mission consisted of a single-bodied aircraft with a high wing configuration, an inverted V-tail, and a twin pushing propeller system mounted on inflatable wings. The theoretical flight time of the team's 120.7 kg design was of 6 hours, with a nominal speed of 123.6 m/s, and a range of 2680 km. Its control surfaces consist of a downward pointing all-moving V-tail for complete yaw and pitch control and partial roll control. To be able to control the roll motion completely, a set of conventional ailerons located at the rigid wing parts are also considered. Sensors used for navigation purposes include an IMU, a sun sensor, an air data sensor system, and an altimeter for the terrain mapping system. The MACE team's navigation system was simulated using MATLAB, proving that higher accuracy in state estimates can be achieved when including a Kalman filter. The lowest accuracy was yielded for the position in the y-direction because a lateral manoeuvre was performed during the simulation. The terrain mapping system seemed to induce noise and thus higher standard deviations in x-, y-, and z- direction. With a geometrical model of the aircraft as an input, software such as JKayVLM (Kay et al., 1993) and Tornado 1.0 (Melin, 2001) were used in order to yield the stability derivatives. The computation of the control derivatives was left as a further research to the report, as neither program was able to simulate the complicated deflections of the combined rudder and pitch functions of the V-tail. It was concluded that Tornado 1.0 possessed more limitations: it does not take compressibility effects into account, while JKayVLM uses a Prandtl-Glauert correction factor. Moreover, Tornado 1.0 does not take fuselage effects into account, so only the wings are present in the model. The team used the results of JKayVLM in their studies.

### 2.2.4. Northrop Grumman: Venus Atmospheric Manoeuvrable Platform

Studies on platforms for an atmospheric Venusian entry led to the design of Venus Atmospheric Manoeuvrable Platform (VAMP) by Northrop Grumman in 2013, which is an inflatable, propeller-powered, delta-shaped drone, which is theoretically able to fly for a year-long cruise in the Venusian atmosphere.[6] The advantages of this design lie in the fact that it can enter Venus' atmosphere without an aeroshell (the drone's large surface area produces benign heating loads during entry in the dense Venusian atmosphere), and the fact that it takes up less space before being deployed as it can inflate in space, thus transitioning to a semi-buoyant, manoeuvrable, solar-powered air vehicle. Altitude, latitude, and longitude can be controlled through the use of the propellers. This vehicle would be the first to perform a Lifting Entry Atmospheric Flight (LEAF).

[5] `https://www.nasa.gov/centers/armstrong/news/FactSheets/FS-106-AFRC.html`, accessed on 04/12/2020.
[6] `https://www.northropgrumman.com/vamp/`, accessed on 25/11/2020.

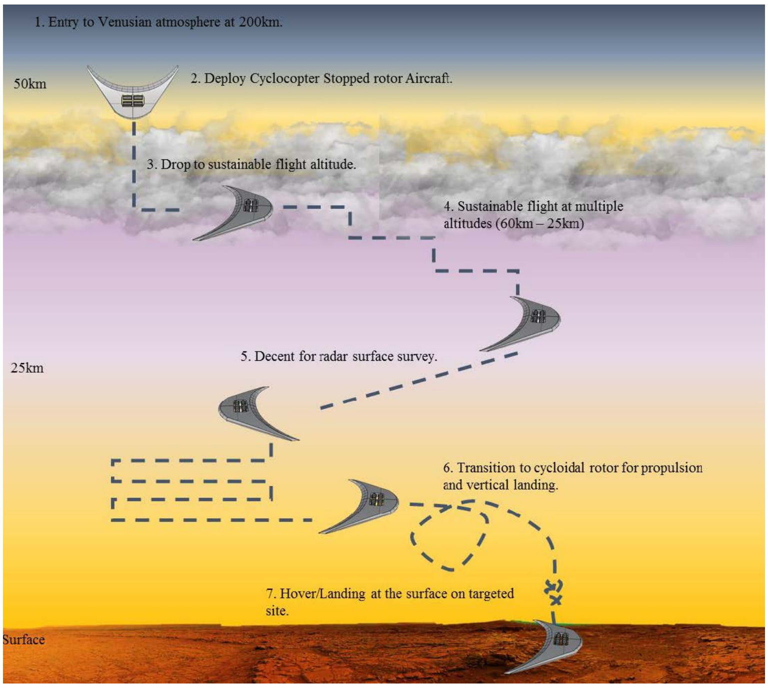


**Figure 2.3:** Flight-path possible with stopped-rotor cyclorotor technology on Venus (Hassanalian et al., 2018).

### 2.2.5. IAT21: Stopped-Rotor Cyclocopter Concept

Crafts equipped with rotary wings, whose main advantage is to vertically take-off and land, can also offer the advantage of performing vertical flights and hovering. Design considerations were performed for a stopped-rotor cyclocopter for Venus exploration (Husseyin, 2016), showing how the use of such technology could yield various flight-paths. Stopped rotors are rotors that can be stopped during forward flight, so as to act as fixed wings, providing some, if not all, of the lift generated by the vehicle. Cycloidal rotors, or cyclorotors, or cyclogyros, can use two or more rotating blades rotating about the axis parallel to the blades to create lift, propulsion, and control the vehicle. With four of these cycloidal rotors, the D-Dalus Drone from the Austrian company IAT21 can launch vertically, thrust upwards, hover, fly, and rotate in any direction. This allows for complex flight-paths, such as the one showed in Figure 2.3.

## 2.3. Choice of Target Planet

It seems clear that from previously conducted studies, Uranus and Neptune are equally interesting to study with in-situ measurements. From them both, Uranus is the planet that is the least far away from the Earth, as it stands at 19 astronomical units (au) from the Sun, so at a minimum of 18 au from the Earth. Neptune, on the other hand stands at 29 au from the Earth. Going to one of these outer planets would take a dozen years, depending on factors such as the chosen interplanetary trajectory (and thus the alignment of planets in the Solar System, and the launch date), and the type of propulsion.

Uranus, on one hand, has its equator tilted at 97.77° with respect to its orbital plane, which has the consequence of defining its rotation around itself as retrograde. This extreme tilt also leads to extreme seasons on the planet. For nearly a quarter of each Uranian year, the Sun shines directly over each pole, plunging the other half of the planet into a 21-year-long, dark Winter. Uranus' major satellites are supposed to have formed from a disk, due to them being on regular orbits and tilted with the planet. Uranus' internal heating is also much lower than Neptune's. A grazing collision could have tilted the planet without affecting its interior. In terms of its atmosphere, it is important to note that its weak internal heating renders its atmosphere inactive. The planet's troposphere is defined in the work of Lunine (1993) as going from 0.1 bar to 100 bar. Note that the nominal surface of the planet is defined as 0 km altitude, where the pressure is of 1 bar. It can be considered a reasonable region for fixed winged drones for example, although winds can go up to 250 m/s, which can be a disadvantage to this type of craft (Hassanalian et al., 2018).

Neptune on the other hand, experiences seasons lasting for over 40 years each. One of its largest satellites, Triton, has a very inclined and retrograde orbit and is therefore most likely a captured object. A head-on collision of Neptune could have strongly affected the interior without forming a disk, and is therefore consistent with the absence of large satellites on regular orbits. Such a collision, which re-mixes the deep interior, is supported by the previously mentioned larger observed heat flux of Neptune (Reinhardt et al., 2020). Concerning its atmosphere, let us note that powerful winds and rapidly-evolving storms are present, which demonstrates how internal energy can drive powerful weather, despite receiving weak sunlight at 30 AU from the Sun. It is believed that Neptune possesses the fastest winds in the Solar System, reaching speeds of 490 m/s, making this planet a challenging target for fixed wing vehicles.[7]

For the sake of simplicity, it was decided to only select one target planet during the mission analysis conducted in this report. **Uranus is the preferred candidate**, due to the fact that it is less active in regions of its atmosphere, and thus less prone to destabilise a vehicle with strong winds. Indeed, it was observed to be much quieter than Neptune, showing less cloud activity and infrequent storms (Irwin, 2003). Moreover, when looking at the mission as a whole, Uranus is closest to the Earth compared to Neptune, meaning that the mission's cost would be reduced due to a shorter travel time, and most probably lighter craft. Less time would also have to pass between the spacecraft's launch and its arrival and science return on Uranus, than on Neptune.

## 2.4. Scientific Aim

With all known properties of Uranus and Neptune having being obtained from fly-by spacecraft observations, remote sensing from orbiters, and ground- or space-based telescopes, the need for in-situ knowledge is all the more important. Remote sensing cannot provide a complete picture of a planet's atmospheric parameters, dynamics, interiors, etc, and is ultimately constrained by multiple elements such as the limited penetration depth of solar visible radiation, degeneracies between the effects of temperatures, clouds, hazes, and gas abundances on the emergent spectra, and the essential fact that key atmospheric constituents simply do not radiate at measurable wavelengths and therefore cannot be detected remotely (Atkinson et al., 2020). Indeed, remote sensing can capture sunlight scattered by the upper clouds and hazes at visible wavelengths, and thermal radiation at longer wavelengths, but some species radiate at other wavelengths, which are not measurable remotely. Several models predict the formation of the Ice Giants to be much closer to the Sun than where they presently are (Levison and Stewart, 2001; Gomes et al., 2005; Morbidelli et al., 2007; Batygin and Brown, 2010; Nesvorný, 2011; Batygin et al., 2012). Additional knowledge on Uranus' atmosphere could be extrapolated to the planet's formation and thus to the formation of Ice Giants and consequently of the Solar System as a whole.

### 2.4.1. Scientific Objectives

As a priority in this mission analysis, it was hence decided to **focus on the in-situ study of Uranus' atmosphere**. Only the penetration of the planet's layers of clouds and hazes can enable the exploration of the troposphere. Inevitably, atmospheric measurements can then provide key information about Uranus' formation and evolution. It was shown that the science objectives of a mission to one of the Ice Giants can be divided into several sections: Tier 1, Tier 2A, and Tier 2B, in order of decreasing importance (Atkinson et al., 2020). Tier 1 and Tier 2A science objectives can be performed with the same instruments and consist in measuring atmospheric constituents well beneath the tropopause, to alleviate the possibility of cold trapping of the heavy noble gases or possible adsorption onto methane ice aerosols. The precise depth required to achieve the Tier 1 and Tier 2A science objectives depends on the sensitivity of the on-board instruments, and the number of atmospheric samples required. Tier 2B science objectives require an even deeper atmospheric probing and are much more sensitive to the entry and descent location chosen. This is because the measurements are more sensitive to local weather and therefore likely not representative of the entire planet. It is interesting here, to probe layers of the atmosphere dominated by solar insolation, as well as the transition region, and the deeper, darker region of the atmosphere well beyond the reach of the sun's direct influence. The science objectives are directly taken from (Atkinson et al., 2020) and are summarised below:

### Tier 1 Science Objectives:

- Measure the atmospheric helium abundance with an accuracy comparable to measurements made by the Galileo probe helium abundance detector at Jupiter, about 2% (Von Zahn et al., 1998).
- Measure the abundance of the noble gases Ne, Xe, Kr, and Ar with an accuracy close to current uncertainties in measured solar abundances, approximately 10% (Lodders et al., 2009).
- Measure the isotopic ratio of nitrogen $^{15}N/^{14}N$ with an accuracy of $\pm 5\%$ (Mousis et al., 2018).

[7] `https://svs.gsfc.nasa.gov/11349`, accessed on 17/11/2020.

- Measure the D/H ratio of hydrogen with an accuracy of ±5% or better (Mousis et al., 2016).
- Measure the helium isotope ratio $^{3}He/^{4}He$ with an accuracy at least commensurate with measurements made by the Galileo neutral mass spectrometer, ±3% (Mahaffy et al., 1998).
- Measure key noble gas isotope ratios $^{20}Ne/^{22}Ne$, $^{36}Ar/^{38}Ar$, $^{132}Xe$/total Xe, $^{131}Xe$/total Xe, and $^{129}Xe$/total Xe with an accuracy of ±1% to enable direct comparison with other known Solar System values (Mousis et al., 2018).
- Measure atmospheric pressure and temperature during the atmospheric vehicle's descent with an accuracy comparable to the Galileo probe measurements at Jupiter, Pressure: 0.5%; Temperature: ±0.1° K in the upper troposphere, ±1° K at deeper levels (Seiff et al., 1998).
- Measure the speed of sound in the atmosphere (used to reconstruct the profile of ortho to para hydrogen along the atmospheric vehicle's descent trajectory) with an accuracy of at least 1% (Banfield et al., 2005).

### Tier 2A Science Objectives:

- Measure the isotope ratios of carbon $^{13}C/^{12}C$ and oxygen $^{18}O/^{17}O/^{16}O$ with accuracies of ±1% (Mousis et al., 2018).
- Measure the tropospheric abundances of CO and $PH_3$ with an accuracy equivalent to Jupiter and Saturn, ±5% (Fletcher et al., 2009; Mousis et al., 2014).
- Detect and measure the abundances of other disequilibrium species in the troposphere such as $AsH_3$ and $GeH_4$ with an accuracy of ±10% (Mousis et al., 2018).

### Tier 2B Science Objectives:

- Measure the vertical (altitude) profiles of elemental abundances (relative to hydrogen) of the cosmogenically abundant species carbon, nitrogen, sulfur, and oxygen from their primary host molecules $CH_4$, $NH_3$, $H_2S$, and $H_2O$, respectively with an accuracy of ±10%, approximately equal to solar abundances measured from photospheric and meteoritic data (Lodders et al., 2009; Mousis et al., 2018).
- Measure the altitude structure and properties of clouds and haze layers, including determination of the aerosol optical properties, size distributions, number/mass densities, and possibly composition.
- Measure the altitude profile of atmospheric dynamics along the atmospheric vehicle's descent path, including horizontal winds, waves, and convection.
- Measure altitude profile of the net radiative balance between solar visible insolation and upwelling thermal infrared radiation.

To answer this thesis' research question (see Chapter 1), there are science objectives that are particularly important to meet. Knowledge on the ratios of elemental abundances and isotopic ratios, for instance, can provide valuable clues concerning the types and source regions of the accreted gas, the timing of planet formation and disk evolution, as well as orbital interactions among giant protoplanets, linking to the formation and evolution of the Solar System. Moreover, the measurement of CO and noble gases can help determine if Uranus is a volatile-rich Ice Giant or a rock-dominated planet. Finally, isotope ratios of He and Xe measurements can provide clues concerning the early evolution of the protosolar disk (Simon et al., 2022). These are all part of the Tier 1 and Tier 2A science objectives.

## 2.5. Scientific Payload

Considering Tier 1, Tier 2A, and Tier 2B science objectives described above, with Tier 1 objectives being the highest priority science objectives, a list of potential scientific instruments can be set to fulfil these objectives.

Tier 1 and Tier 2A instruments include: a Mass Spectrometer, a Tunable Laser Spectrometer to increase the measurements' accuracy, a Helium Abundance Detector, and an Atmospheric Structure Instrument, which contains an accelerometer for entry deceleration measurements, sensors for atmospheric pressure and temperature profile measurements, and an acoustic velocimeter to measure the speed of sound in the atmosphere. This speed of sound data can be used to determine the ortho- to para-hydrogen ratio, which can help the interpretation of the atmosphere's properties such as its thermal profile, density structure, etc. An instrument is added to this Tier 1A instrument suite: the NanoChem. Introduced by Sayanagi et al. (2020), it is made of a set of carbon nanotube-based sensing elements, a pressure sensor, and a temperature sensor (J. Li et al., 2003; J. Li and Lu, 2009). It weighs around 1 kg, which is much less than a mass spectrometer (17.3 kg for

**Table 2.1:** Scientific instrument payload to fulfil Tier 1, Tier 2A, and Tier 2B science objectives.

| **Instrument** | **Measurements/sensors** | **Notes** |
|---|---|---|
| | **Tier 1 and Tier 2A** | |
| Mass Spectrometer[a] | Composition | Tier 1: Noble gases, D/H, $^3He/^4He$<br>Tier 2A: C, N, S, P<br>Disequilibrium species<br>Other isotopes |
| Helium Abundance Detector[a] | Abundance of helium | |
| Atmospheric Structure Instrument[a] | Scientific accelerometer<br>Pressure and temperature<br>Acoustic properties<br>Atmospheric electricity | Thermal structure<br>Atmospheric stability<br>Stratosphere thermal structure<br>Ortho/Para $H_2$ ratio |
| | **Tier 2B** | |
| Nephelometer[a] | Cloud location and properties | Cloud structure, number densities, characterise aerosol properties |
| Net Flux Radiometer[a] | Radiative flux profile | Upwelling thermal infrared<br>Deposition solar visible |
| Ultra Stable Oscillator[a] | Dynamics<br>Absorption | Winds, waves, turbulence<br>Key molecular abundances |
| Tunable Laser Spectrometer[a] | Abundances of key targeted species | CO, $PH_3$, $AsH_3$, $SiH_4$, $GeH_4$, $NH_3$, $CH_4$, $H_2S$ |
| NanoChem[b] | Composition | $CH_4$, $NH_3$, $H_2S$ |

[a](Atkinson et al., 2020) [b](Sayanagi et al., 2020)

Huygens' Gas Chromatograph Mass Spectrometer (Niemann et al., 2002)), and has demonstrated sensitivities to molecules such as $CH_4$, $NH_3$, $H_2S$. A complete list of detectable species is made available by Sayanagi et al. (2020). This instrument can thus be used to measure the spatially variable volatile molecule concentrations present in Uranus' atmosphere, in the 100 mbar to 5 bar pressure level altitudes. Tier 2B instruments are to be operated at lower altitudes than Tier 1 and 2A ones. They include the following instruments: a Nephelometer, a Net Flux Radiometer, and an Ultra Stable Oscillator, which will be part of the Doppler wind experiment using the relay spacecraft's radio subsystem. All of these instruments are meant to be present on the atmospheric vehicle itself, with the addition of radio transmitters and receivers on a potential relay spacecraft for a Doppler wind experiment. Details on each of these instruments are available in the work of Atkinson et al. (2020). Table 2.1 summarises the instruments' uses.

An imager on board the relay spacecraft can also yield valuable science return on the Uranian atmosphere's global characterisation, as well as on contextual imaging of the probe's entry site. It can also provide information on the structure of the planet's winds and clouds (Mousis et al., 2016).

It must be noted that to fulfil the Tier 1 science objectives as well as the isotope ratio measurements, an atmospheric vehicle would have to descend to one or several bars into the Uranian atmosphere. To fulfil the objectives dealing with the observation of heavier elements and disequilibrium species, pressure levels beneath the clouds would have to be reached, at 10 bar or more. Bringing an atmospheric vehicle to 10 bar would also enable to measure the thermal profile and radiative energy structure of the atmosphere, detect atmospheric chemistries, as well as measure cloud properties and dynamics of the atmosphere. Concerning hydrogen sulfide $H_2S$ and ammonia $NH_3$, they are thought to form a cloud of ammonium hydrosulfide $NH_4SH$ at around $30-50$ bar (Cavalié et al., 2020). For in-situ measurements of $H_2O$, an atmospheric vehicle would have to measure its surroundings where the water clouds are present, which are expected at several hundreds bar of depth (Atkinson et al., 2020). Voyager 2 radio occultation observations suggest that the base of a water ice cloud (assuming solar abundance of O/H) would be located in the range of $200-300$ bar, although it is also likely that this happens much deeper (Atkinson et al., 2020).

### 2.5.1. Detailed Navigation Instruments Descriptions

A description of each chosen instrument will be provided in this report, from which a science traceability matrix was drafted, as shown in Table A.1. The properties (accuracy, resolution, data rate, mass, power, volume, operational pressure range, operational temperature range, heritage, and measurement requirements) are displayed in Table 2.2 and Table 2.3. All described instruments will be present on board each glider. This chapter includes a description of the instruments modelled as navigation sensors, namely the Atmospheric Structure Instrument and the Ultra High Frequency transceiver, while Appendix B contains the description of the other scientific instruments.

### Atmospheric Structure Instrument

This instrument helps investigate the atmosphere's structure and dynamics. It measures acceleration with an accelerometer, from which density can be determined, knowing the vehicle's mass and the atmosphere's mean molecular weight from the mass spectrometer's measurements. The temperature and pressure are then determined from the density values, with the assumption of hydrostatic equilibrium. Temperature and pressure results are then compared with direct temperature and pressure samplings, using dedicated temperature and pressure sensors present in the instrument (Ferri et al., 2020).

The reason for using a dedicated accelerometer here, instead of the ones included in the IMU of the Navigation system, is that the raw data from the IMU's accelerometers are generally not transmitted and kept as processed attitude measurements (through quaternions for example). Tri-axial acceleration information can either be obtained through the positioning of one accelerometer on each of the vehicle's main axes, as close as possible to the vehicle's centre of mass, or through the inclusion of a single servo accelerometer oriented along the vehicle's vertical axis and the exploitation of the IMU's data (Ferri et al., 2020).

Temperature sensors commonly make use of wire resistance thermometers of pure platinum wire, as in the Huygens Atmospheric Instrument (HASI) and Galileo probe's instruments (Seiff and Knight, 1992). Sayanagi et al. (2020) suggest to have two temperature sensors and one pressure inlet located on a mast that places them outside of the vehicle's boundary layer, with one of the temperature sensors being coated in glass to provide an additional chemical barrier against Uranus' harsh environment. Based on the heritage of the Huygens probe, Sayanagi et al. (2020) also indicate that the expected resolution of the temperature sensors should be at least 0.02 K, with an absolute accuracy of 0.5 K. For the pressure measurement, a Kiel probe can be used at the end of the mast to measure the atmosphere's total pressure. The static pressure can then be determined by subtracting the dynamic pressure from the total pressure (Ferri et al., 2020). Dynamic corrections will be required for the temperature and pressure data, in order to derive the static temperature and pressure values. This post-processing will depend on the atmospheric physical properties and descent velocity. Finally, the speed of sound is measured by relating mean molecular weight and temperature. This measurement is used to quantify the ortho to para hydrogen ratio profile of Uranus' atmosphere. This ratio profile needs to be measured to interpret other quantities such as the planet's temperature profile, dynamics, cloud structure, and radiative structure accurately. The speed of sound can be measured with an ultrasonic velocimeter with a relatively low sampling rate (one measurement every 5-10 seconds is enough), providing a vertical resolution of a fraction of the atmospheric scale height (Banfield et al., 2005; Lorenz, 1998). An ortho-para instrument was considered in Table 2.2 and Table 2.3 to take into account the presence of a velocimeter in the atmospheric structure instrument. Figure 7.1 shows a block diagram illustrating the working principle of this instrument. Part of it was implemented in this thesis' software, as navigation sensor input.

Reference atmospheric structure instruments include the HASI, the Galileo probe atmospheric structure instrument, but also the newly-developed Ice Giant atmospheric structure instrument (IG-ASI) (Ferri et al., 2020). In addition to the previously listed atmospheric properties measured with an atmospheric structure instrument, the IG-ASI also helps investigate the tropospheric electric conductivity, ionisation, and charge carrier profiles, along with any alternating current (AC) and direct current (DC) electric fields, and search for lightning phenomena. However, as these last properties are not a science priority to this mission, the Atmospheric Electrical Package of IG-ASI will be omitted. Thus, only the scientific accelerometer (ACC), the temperature sensors (TEM), and the Pressure Profile Instrument (PPI) will be considered. The instrument's mass and power requirements are taken from the work of Hofstadter et al. (2017). Its size is assumed to be similar to Galileo's atmospheric structure instrument.

### Ultra High Frequency Transceiver

The ultra High Frequency (UHF) transceiver will be part of the Doppler wind experiment. The objective of this experiment is to use the atmospheric vehicle and the relay spacecraft's radio subsystems to measure the altitude profile of zonal winds along the vehicle's descent. To do so, a stable relay signal must be generated with an ultra-stable oscillator (USO) transmitter aboard the atmospheric vehicles and received by an USO aboard the relay spacecraft. This way, integrated atmospheric microwave absorption measurements can also

**Table 2.2:** Parameters of mission's instruments: accuracy, resolution, data rate, mass, power, and volume.

| Instrument | Accuracy | Resolution | Data Rate [bps] | Mass [kg] | Power [W] | Volume [$cm^3$] |
|---|---|---|---|---|---|---|
| Mass spectrometer[a][b] | 1 % level accuracy | - | 70 | 6.7 | 36 | 8112 |
| Tunable laser spectrometer[c][d] | Detect methane above 0.3 ppbv and measure the $^{13}C/^{12}C$ isotope with a precision of ±2 % | 0.0005 $cm^{-1}$ (ultra-high res.) | 70 | 3.7 | 10 (single channel) 24 (higher power draw methane laser channel) | 1000 |
| Helium abundance detector[e] | 0.1 % level accuracy Overall error on helium mole fraction smaller than ±0.0015 | - | 40 | 1.4 | 0.9 | 948 |
| Atmospheric structure instrument[f][g][h] | ACC: 1 % TEM: 0.5 K PPI: 1 % | ACC: 1/10 µga (high res.) 0.9/9 mg (low res.) TEM: 0.02 K PPI: 0.1 Pa | 352 | 2.5 | 3.5 | 3100 |
| Ortho-para instrument[i] | 5 cm/s | - | 640 | 1.5 | 5 | 1500 (total) 1000 (electronics) |
| NanoChem[f] | Concentration measurement accuracy of $CH_4$, $H_2S$, and $NH_3$ to within ±20 % uncertainty | - | 256 | 1 | 1 | 12 |
| Ultra-stable oscillator[f][j] | 1800-second Allan Deviation $< 4 \cdot 10^{-10}$ | - | 10 MHz ±−0.1 Hz | 1.75 | 3.2 | 866.3 |
| Nephelometer[k] | Estimates of the overall accuracy range from less than ±5 % for the 5°, 15°, and 180° channels to less than ±10 % for the 40° and 70° channels | Angular resolution for different scatter channels: 5°: 0.64° 16°: 1.08° 40°: 1.72° 70°: 1.76° 180°: 4.0° | 10 | 2.2 | 5.6 | 12,105 |
| Net flux radiometer[l][m] | - | - | 55 | 2.4 | 5 | 4539.9 |
| **Total** | - | - | 1493 | 23.15 | Max: 84.2 | 32,283.2 |

[a](Perez-Ayucar et al., 2016) [b](Hassig et al., 2015) [c](Webster and Mahaffy, 2011) [d](Mahaffy et al., 2012) [e](Von Zahn and Hunten, 1992) [f](Sayanagi et al., 2020) [g](Hofstadter et al., 2019) [h](Givens et al., 1983) [i](Banfield and Dissly, 2012) [j](Bird et al., 2003) [k](Ragent et al., 1992) [l](Atkinson et al., 2020) [m](Aslam et al., 2017)

be conducted along the vehicle's descent (Mousis et al., 2018). This can indirectly help provide measurements of ammonia, hydrogen sulfide, and water abundance (Atkinson et al., 2020). Figure 7.2 shows a block diagram of how this instruments works. Part of it was implemented as navigation sensor input.

It can be seen in Table 2.3 that instruments of the same missions were designed to sustain different pressure and temperature ranges. The Galileo probe was designed to reach depths showing 10 bar of pressure, but survived to pressures exceeding 22 bar.[8] On-board instruments such as its mass spectrometer, nephelometer, and radio science experiment were functional until the probe's loss of contact around 22 bar, while others such as the helium abundance detector and net flux radiometer stopped measuring before that (12 and 14 bar respectively), and the atmospheric structure instrument after that around 38 bar. Research into the operational ranges of these instruments showed that they are often sealed into an environment with a chosen pressure and temperature. The seal of that environment is then designed to hold until a certain pressure or temperature is reached. Considering the small total mass of the chosen scientific instruments (23.15 kg as seen in Table 2.2), it can be assumed that the same instrument suite will be present on-board all in-situ vehicles.

[8] `https://hal-insu.archives-ouvertes.fr/insu-01351010/document`, accessed on 03/01/2021.

**Table 2.3:** Parameters of mission's instruments: pressure range, temperature range, heritage, and measurement requirements.

| Instrument | Pressure range [bar] | Temperature range [$^{\circ}$ C] | Heritage/Possible Model | Measurement Requirements |
|---|---|---|---|---|
| Mass spectrometer[egi] | 1 - 15 (Huygens)<br>0.15 - 21.1 (Galileo measured)<br>$10^{-18} - 10^{-8}$ (DFMS of ROSINA) | -20 to +50 operating,<br>-20 to +60 storage (Huygens)<br>-2- to +30 (ROSINA) | ROSINA experiment on Rosetta mission (high res.)<br>GCMS on Huygens probe (low res.) | - |
| Tunable laser spectrometer[h] | Martian atmospheric pressures: 6 to 10 mbar | 26 (TDLAS for ExoMars mission) | Part of SAM instrument on Curiosity rover | - |
| Helium abundance detector[f] | 2 - 12 (Galileo measured) | -15 to +25 (Galileo) | HAD from Galileo probe | - |
| Atmospheric structure instrument[bc] | 0 - 2 (PPI of Huygens ASI)<br>$10^{-10}$ - 38 bar (Galileo) | -273.15 - 226.85 (Galileo) | IG-ASI<br>HASI from Huygens probe<br>Galileo probe | ACC: close to c.o.m on each axes (X,Y,Z) or on vertical axis (X).<br>TEM: 1 should be covered by glass to protect from the environment.<br>PPI: 8 cm pitot tube |
| Ortho-para instrument[l] | - | - | Ultrasonic anemometer originally developed for Mars | Placed on nephelometer boom outside of boundary layer |
| NanoChem[k] | - | - | International Space Station Air Quality Monitor | Sample integration period: 10 seconds |
| Ultra-stable oscillator[d] | - | - | GRAIL/APL Quartz USO<br>RUSO on Huygens probe | - |
| Nephelometer[a] | 1 bar seal environment designed to hold until at least 20 bar (Galileo) | - | Galileo probe | Placed outside of boundary layer: boom |
| Net flux radiometer[j] | - | - | 2 channel NFR: Goddard Space Flight Center Net Flux Radiometer | - |

[a](Ragent et al., 1992) [b](Seiff and Knight, 1992) [c](Fulchignoni et al., 1997) [d](Atkinson et al., 1998) [e](Niemann et al., 1998) [f](Von Zahn et al., 1998) [g](Niemann et al., 2002) [h](Le Barbu et al., 2006) [i](Balsiger et al., 2007) [j](Mousis et al., 2016) [k](Sayanagi et al., 2020) [l](Banfield et al., 2016)

### 2.5.2. Calibration, Testing, and Operational Modes

It is important for all scientific instruments to be statically and dynamically calibrated, verified, and qualified before the mission's launch. It should be checked whether the instruments can fulfil the science requirements in terms of accuracy, but also function as intended during the mission's different phases. During the interplanetary flight from Earth to Uranus, checkout of all instruments should regularly be performed, to check for any drift or degradation that could have an impact on the scientific measurements performed in Uranus' atmosphere, once the atmospheric vehicles are deployed. The scientific instruments will thus be considered to be calibrated and tested at the beginning of the winged vehicles' flights. The same is assumed concerning the instruments aboard the relay spacecraft, especially concerning the UHF transceiver, which is needed for the Doppler wind experiment. The following operation modes are defined for the mission:

- **Pre-Operational Mode:** This mode describes the state of the descent probes containing the atmospheric vehicles, the orbiting spacecraft, and the ground systems before the delivery of the atmospheric vehicles in Uranus' atmosphere has been achieved. A series of vehicle and instrument test plans are run, to verify compliance with all space and ground segment requirements. Here, the functionality of all other operating modes is verified.
- **In-Orbit Mode:** This mode describes the state of the atmospheric vehicles, the orbiting spacecraft, and the ground systems just after the delivery of at least one of the atmospheric vehicles in Uranus' atmosphere has been achieved, and the mission operations have not yet started. The atmospheric vehicles will be commanded to a certain initial position (longitude and latitude on Uranus), and attitude, which provides optimal conditions for the scientific measurements, the communications with the orbiter, and the vehicles' trajectory tracking to occur.
- **Nominal Mode:** This mode includes science operations and communications between the atmospheric vehicles and the relay spacecraft, as well between the relay spacecraft and Earth.
- **Safe Mode:** This mode reflects the situation where one of the navigation sensors would not be working anymore. Here, the IMU or FADS sensor will probably be set as faulty, as the radio range measurements are assumed to be working at all necessary times, as communication and the Doppler wind experiment

depend on the receiver and transmitter that will be needed aboard the atmospheric vehicles. Using the limited position knowledge, the safe mode should be able to make use of other knowledge to infer the vehicles' positions. During this mode, the scientific instruments are shut down and the atmospheric vehicles are waiting for commands from the mission control centre (through the relay orbiter) to recover from safe mode.

- **Post-Operational Mode:** This mode is described here, in the case where the orbiter would be used to provide data or communication services after the end of the mission, for a supplementary mission. The atmospheric vehicles are considered defective after the mission's end, as they will most probably break down after reaching Uranus' deep atmospheric layers, where the pressure keeps increasing. The orbiter, however, could still be used in an auxiliary mission, after having deployed both atmospheric vehicles, received, and transmitted all their scientific data to Earth.

## 2.6. Choice of Platform

As mentioned in Section 2.2, the use of different in-situ platforms was investigated for this mission. These include conventional descent probes, balloon-based vehicles, and winged vehicles. These platforms were studied to establish if they could both feasibly fly in Uranus' atmosphere, and provide competence for performing the mission's scientific measurements. A review of the research conducted on these different crafts, as well as a discussion leading to the final choice of platform will be given below.

### 2.6.1. Review of Platform Research

The knowledge acquired on Uranus and Neptune missions, balloon-based missions, but also winged vehicle missions will be summarised here, with aim to eliminate unfeasible options for the mission.

#### Uranus/Neptune Missions Study

Future missions planned to Uranus/Neptune suggest to use a parachuted ballistic descent probe to perform the scientific measurements. The probe should be coupled with an orbiter or a spacecraft operating a fly-by of Uranus for trajectory tracking of the probe, as well as best scientific return, as the data relay and scientific experiments such as the Doppler wind experiment require both probe and orbiter. The feasibility of this concept has been proven through the previous Galileo and Cassini-Huygens missions. However, it was mentioned that a descent probe would provide a single atmospheric measurement profile for a few hours only.

#### Balloon-Based Vehicles Study

Starting with zero-pressure balloons, their altitude change depends on atmospheric properties, especially night/-day pressure levels. Their use thus requires detailed knowledge of the chosen planet, to be able to target specific altitudes where scientific measurements have to be done. Such knowledge is not available for Uranus' atmosphere if high accuracy is desired from the mission's results. Besides, their manoeuvrability only lies in the balloon's altitude.

Super-pressure balloons that do not possess any propulsion system do not demonstrate much manoeuvrability. They lack positional control, leaving them at the hands of the planet's winds. They are not able to actively pursue a chosen trajectory. Moreover, as super-pressure balloons have to maintain a positive internal pressure with respect to the environment, this type of balloon would not be the best candidate to go to very high pressure levels inside Uranus' atmosphere.

Hot-air balloons' buoyancy depends on raising the balloon's gas temperature to a temperature higher than the ambient environment temperature, so that the hot air inside the balloon is less dense than the surrounding cooler air. Uranus' low temperatures (around 70 K to 200 K from 1 bar to 100 bar of pressure) would make hot-air balloons an option for this mission, but the planet's increasingly high pressures and densities would not. Furthermore, as seen with the 2020 Venus Flagship Mission Study (Gilmore et al., 2020) and the Titan Saturn System Mission (Reh et al., 2009), balloons are commonly left to be passively drifting with the planet's winds. A propulsion system would have to be added so as to provide lateral control, as well as the vertical one provided by venting through a valve at the top or at the bottom of the balloon. Balloons equipped with propulsion systems were optimised into so-called blimps, whose stream-lined shapes are designed to reduce drag in the forward direction, maximise buoyancy, and enhance controllability (Y. Li, 2009). Blimps are the only balloons that can be steered and change altitude, due to the presence of a propulsion system. No previous or future planetary missions have proven the feasibility of propelled-balloon manoeuvrability. It must be noted here that lateral movement can also be produced by exploiting winds on Uranus. This is however, dependent on detailed knowledge of Uranus' winds, which is not available. A heater would have to be used to heat the balloon's gas, as solar flux/infrared flux is too small at Uranus.

### Winged Vehicles Study

Simple winged vehicles such as flying wings can provide interesting measurements by performing cylindrical or straight flight-paths. Winged vehicles that possess a propeller or rocket propulsion system such as NASA's Aerial Regional-scale Environmental Survey (ARES) HADD2 concept were seen to be all the more interesting, because the vehicle can perform more complex flight-paths. Delft University of Technology's (TU Delft) yearly Aerospace Engineering Bachelor projects called Design Synthesis Exercises (DSE) have provided iterated designs for atmospheric winged vehicles. The 2008 Titan Atmospheric Research aircraft (TARA) mission and the 2003 Mars Airborn Canyon Explorer (MACE) mission were studied for this mission. Both of them suggested the use of pushing propellers for the study of Venus and Titan's atmospheres, as they were more adequate than rocket propulsion systems for the missions' low speed regimes (subsonic).

Northrop Grumman's concept (the Venus Atmospheric Manoeuvrable Platform, or VAMP)[9] showed stowing advantages of having an inflatable delta-shaped wing vehicle. The possibility of performing a lifting entry at Uranus is however very poor because of the very low average density of 0.42 kg/m$^3$ at Uranus compared to around 65 kg/m$^3$ at Venus (Lebonnois and Schubert, 2017).

IAT21's stopped-rotor cyclocopter concept offers the possibility to hover, perform vertical flights, and glide with a stopped-rotor configuration. It can yield complex flight-paths. Cyclocopter concepts have been proposed in the past, but never selected, built, or proven to perform a successful flight, except on Earth. Their performance has been numerically tested by Husseyin (2016) yielding results that showed that they should be capable of flying in all atmospheric layers of Venus, taking measurements and scouting for beneficial landing locations. Rotorcrafts have an enormous power consumption (Y. Li, 2009).

### 2.6.2. Fulfilment of Science Goals

With the aim of having an atmospheric platform whose trajectory can be known (from on-board instruments, from observation from the relay spacecraft, or from both), a few options can be dropped from the above summary. These options are zero-pressure balloons, super-pressure balloons, and hot-air balloons because they require detailed knowledge of Uranus' atmospheric profiles and would not survive the extreme environmental conditions. Northrop Grumman's lifting entry concept is also discarded because lifting entry is unfeasible considering Uranus' low atmospheric density. The concepts that are left for this type of mission are listed in Table 2.4, along with some of their advantages and disadvantages. To determine which platform is the most suited for the mission, one should check if it can fulfil the mission's science objectives: Tier 1, Tier 2A, and Tier 2B science objectives. These science objectives are fulfilled by probing the atmosphere until around 50 bar of pressure and exploring the unobserved northern hemisphere of Uranus. This is, with the exception of the detection of oxygen, which would have to be done at $200 - 300$ bar of pressure, according to Atkinson et al. (1998). Moreover, comparing Uranus' atmospheric properties in its day/Summer and night/Winter hemispheres would not only strengthen the scientific data, but also provide a comparison point with the Voyager 2 observations of the planet's night/Winter southern hemisphere of 1986.

First of all, previous descent probe missions such as Huygens or Galileo proved that such a platform can provide adequate science return, and can sustain harsh environmental conditions thanks to its shape, structure, and heatshield. Moreover, mission proposals from NASA and ESA have theoretically demonstrated that having a single (Hofstadter et al., 2017; Hofstadter et al., 2019; Fletcher et al., 2020b; Guillot, 2019; Mousis et al., 2019) or multiple (Sayanagi et al., 2020) atmospheric descent probe(s) being dropped in Uranus' atmosphere would result in the fulfilment of the scientific objectives of such a mission.

Un-propelled winged vehicles were considered enabling the possibility of performing measurement profiles over larger areas than a descent probe, as well as for a longer time. Indeed, since the mission aims at probing deep layers of the atmosphere, there would be no scientific advantages in being able to increase the vehicle's altitude during its flight. A propelled winged vehicle, similarly to a cyclocopter, would offer the possibility of performing more complex flight-paths, and follow a chosen up-going trajectory, without necessarily following the planet's winds. A possibility would be to have winged vehicles glide and be directed by Uranus' winds, with an on-board propulsion system being used only to gain altitude when needed.

[9]`https://www.northropgrumman.com/vamp/`, accessed on 10/04/2021.

**Table 2.4:** Summary of potential platforms for Uranian atmospheric probing mission.

| Platform | Advantages | Disadvantages | Comm. |
|---|---|---|---|
| Parachuted ballistic descent probe | Simple, subject of most Uranus mission studies, has been done before (Galileo, Huygens) | Yields single straight atmospheric measurement profile | A few hours |
| Un-propelled winged vehicle | Simple, can perform gliding cylindrical flight-path to yield complex measurement profiles | Need an overhead relay spacecraft for a long time, depends on wind and updraft patterns, no heritage | A few days |
| Propelled winged vehicle | Lateral and vertical control, can glide | No heritage | A few days |
| Stopped-rotor cyclocopter concept | Lateral and vertical control, can glide, can hover | Big power consumption leading to short flight endurance and coverage, no heritage | A few days |

This however, poses the problem of power source: a propelled vehicle would require a power system that would be able to provide energy for up to several days. Having solar powered energy is not feasible considering the faint solar energy received at Uranus: the solar irradiance at Uranus is of 3.69 $W/m^2$ against $1,361$ $W/m^2$ at the Earth.[10] It is not known whether having charged batteries on-board would suffice for such a mission. If the batteries' mass gets too large, another power source would have to be considered. The use of air-breathing propulsion systems was considered but set aside, mainly due to Uranus' high atmospheric density in the regions that need to be probed, which would render the particle ionisation process inefficient and too power-hungry. Radioactive power sources were then explored. Although the use of MMRTGs or eMMRTGs is considered in NASA atmospheric mission proposals, nuclear power sources are aimed at being avoided for European missions. A passive system would thus be preferred for a European mission.

It is important to note that after the Galileo probe mission to Jupiter inadvertently entered a region showing unusual "hot spot" meteorology, the need for multi-vehicles missions was highlighted, to avoid having a single vehicle perform scientific measurements that are not representative of the planet's general environment. The perceived high costs of multi-vehicle missions to giant planets have prevented them to be implemented as of today. However, this can be refuted as it is crucial to point out that not all science objectives detailed in Section 2.4 require in-situ measurements at multiple locations of Uranus. This is because some quantities, such as noble gas abundances and isotopic ratios of elements in volatile molecules (part of Tier 1 science objectives) are expected to be spatially homogeneous (Sayanagi et al., 2020). Having multiple atmospheric vehicles deployed at different locations in Uranus' atmosphere is thus an option, with knowledge that not all vehicles need to contain the same scientific payload. For their descent multi-probe-based proposal, Sayanagi et al. (2020) suggest to have one large probe carry the mission's mass spectrometer to conduct the detection of noble gases and their isotopes, while another would carry other instruments, such as a NanoChem instrument (J. Li et al., 2003; J. Li and Lu, 2009), to measure spatial variabilities. Having multiple vehicles can also help investigate Uranus' atmospheric composition and profiles globally, as some regions might be dominated by certain species, while others by other species.

Concerning communication, the use of multiple atmospheric vehicles would enable communication between themselves, as well as with an orbiter or a spacecraft performing a fly-by of Uranus, to relay the scientific data back to Earth. It is important to stay at least 2 h between the planet's 0 bar and 20 bar pressure levels, to conduct the majority of science measurements[11].

Both a descent probe and a winged vehicle concept can thus fulfil the mission's science requirements. However, descent probes have already been proven to work for such a mission, and it would be interesting to see if it could also be conducted with another type of craft. **A multiple un-propelled winged vehicles concept will thus be studied in this thesis.** The delivery of these multiple gliders will be done with descent probes contained in a carrier and relay spacecraft.

[10] `https://nssdc.gsfc.nasa.gov/planetary/factsheet/uranusfact.html`, accessed on 04/12/2020.
[11] Personal communication with Olivier Mousis, 18/01/2021.

## 2.7. Reference Vehicle Constraints

A reference glider will be chosen and scaled up or down if needed to fit the needs of the mission at hand. A preliminary research was conducted on different aspects of this vehicle, to determine the constraints that will drive the vehicle selection. They are as follows:

- **Folding properties:** Since the atmospheric vehicles will be delivered through descent probes, their size is constrained by the available volume in the mission's descent probe. In general, this requires a design with deployable wings and a deployable tail structure, or a design which fits in the descent probe in its flight configuration, which is the lowest risk packaging approach (Hassanalian et al., 2018).
- **Power:** Depending on which type of power subsystem is chosen, a reference vehicle's shape will change to accommodate it. For example the Aerial Vehicle for In-situ and Airborne Titan Reconnaissance (AVIATR) air vehicle design is based on the implementation of an advanced Stirling radioisotope generator (ASRG) which is voluminous (76 cm $\times$ 46 cm $\times$ 39 cm) and heavy (32 kg) (Barnes et al., 2012). Other options for power are the use of fuel cells, and other types of RTGs. The use of solar-powered cells is not an option because of the weak solar energy received at Uranus. The length of the mission has not been defined yet, but were it long, then the use of charged batteries would not be an option either, due to the high mass of the batteries that would be required. This especially relates to the probes' coasting period, whose longer duration implies a larger battery mass.
- **Aerodynamic configuration:** The atmospheric vehicle needs control surfaces that can achieve pitch, roll, and yaw control. It is important to be able to retrieve elements such as the vehicle's aerodynamic coefficients for the EOMs, which can be separated into stability and control derivatives. Knowing the vehicle's dimensions, the stability and control derivatives can be generated with the software XFLR5[12] (Deperrois, 2003).
- **Flight range and operational altitude:** For this mission, the aim is to go as deep as possible into Uranus' troposphere. The deepest level that must be reached to fulfil all science objectives corresponds to $200 - 300$ bar pressure level, where the detection of oxygen becomes possible (Atkinson et al., 1998). However, for now, it will be assumed that the atmospheric vehicle will go to at least 100 bar of pressure, as knowledge on Uranus' pressure-altitude profile below that level is non-existent. If no oxygen molecules are present down to 100 bar of pressure, then all scientific objectives will be fulfilled, except for the detection of oxygen, which is part of the Tier 2B Science Objectives defined in Section 2.4. To go from 1 bar of pressure at 0 km altitude until 100 bar of pressure at around $-375$ km, the altitude spanned would be 375 km. To accomplish this, and assuming that the atmospheric vehicles are delivered at their desired latitude by a descent probe, the vehicles can simply perform gliding flights. Since the zonal winds are dominating meridional winds in Uranus' atmosphere (see Figure 3.7), and with aim to have the vehicle stay close to its intended latitude for the scientific measurements, a perfectly cylindrical descending flight would not be optimal. A possibility is to make the vehicle follow a straight and symmetric flight with tailwind, such that it does not experience side force and explores several longitudinal locations. The tailwind would increase the vehicle's groundspeed. The vehicle should stay for 2 h between the 0 bar and 20 bar level[13].
- **Flight regime:** Considering Uranus's very low atmospheric temperatures, and its hydrogen dominated environment, several models suggest that the minimum speed of sound would range between 637 m/s and 650 m/s (Lorenz, 1998). So unless the vehicles would be flying at more than 500 m/s, the flight regime can be assumed to be subsonic. The expected speed of the atmospheric vehicle ranges between 9.93 m/s and 52.8 m/s as later shown in the vehicles' reference trajectory tabulated in Table 6.1.
- **Time of flight:** Considering the study done by LeBeau et al. (2015) on the design of autonomous gliders for Uranus' atmosphere, the maximum endurance was 50 h, to glide between the 0.2 bar and 20 bar pressure levels, which are at 222 km difference. So in order to reach the 100 bar pressure level, which is 375 km below the 1 bar pressure level, the time of flight of 50 h can be doubled to 100 h. However, as the vehicle would go deeper and deeper into the atmosphere, the density, pressure and temperature would increase. This would decrease the vehicle's Mach number, as the speed of sound would increase, and the vehicle's true airspeed would decrease. It would thus take the vehicle even longer to reach the desired depth, if it is still gliding. A 50% margin is taken and the total time of flight can thus be approximated at 150 h, which corresponds to 6.25 days. This is an estimate, which will change once the reference vehicle has been selected and its flight has been simulated.

[12]`http://www.xflr5.tech/xflr5.htm`, accessed on 11/07/2021.

[13]Personal communication with Olivier Mousis, 18/01/2021

A reference vehicle fitting all previously mentioned criteria was found: the GL-1 glider from Amalia et al. (2018) and Pratama (2015). The following important information was retrieved: the vehicle's dimensions, its mass and inertia properties, and the nature of its control surfaces. From this information, the stability and control derivatives were generated using the software XFLR5 (Deperrois, 2003). The standard surfaces of the vehicle (without the fuselage) were defined and used as input to the software. In terms of control surfaces, a simple configuration was chosen, where the vehicle possesses the following: elevators, ailerons, and a rudder, to control pitch, roll, and yaw movements independently. More information about the chosen reference vehicle is given in Section 5.1.

## 2.8. Mission Design and Definition

Here, some essential aspects of the mission will be explored such as its launch possibilities, interplanetary trajectory, relay spacecraft trajectory, atmospheric vehicles' entry and descent, and requirements. Most of the parameters decided upon in this section are taken from literature. It is recommended to run acceptance tests on the launch and interplanetary timeline, as well as to further investigate the Uranus approach and probe release, entry, and descent, which is out of the scope of this MSc thesis. This section will, however, provide the necessary mission parameters to the completion of this thesis.

### 2.8.1. Launch Timeline Possibilities

It took less than 9 years for Voyager 2 to reach Uranus, through performing a fly-by of Jupiter and Saturn.[14] The 2030s upcoming planetary alignment will enable a spacecraft to perform gravity assists around both Venus and Jupiter, and potentially Saturn if done before the year 2029. It would reach its Uranian destination in around 12 years, thus allowing the spacecraft to arrive at Uranus well within the lifetimes of its instruments and other subsystems.[15] In the 2019 NASA and ESA collaborative study in advance of the next Planetary Science Decadal Survey (Hofstadter et al., 2019), 10,000 trajectories were explored to bring a spacecraft from the Earth to either Uranus or Neptune in the 2024 to 2037 time frame, taking advantage of the Solar System's planetary alignment. Concerning a trajectory to Uranus, the main conclusions of this study include the following points:

- Most favourable trajectories include a launch between 2029 and 2032, through a Jupiter gravity assist.
- The mass delivered to Uranus is maximised for launches between 2029 and 2030.
- Chemical propulsion trajectories are preferred to solar-electric propulsion (SEP) trajectories considering flight time, mass delivered, and cost.
- An encounter with Uranus at of before the next equinox in 2049 would enable the observation of the planet's unseen northern hemisphere, close-up.

NASA's 2017 Ice Giant Pre-Decadal Survey (Hofstadter et al., 2017) presented similar conclusions as previously listed concerning the timing of this kind of mission.

### 2.8.2. Interplanetary Trajectory Options

Hofstadter et al. (2017) considered six mission options for Uranus and Neptune. Two of these six options are kept here, namely Mission Option 4 and 5, as they are recognised as the two most optimal trajectories to reach Uranus and perform in-situ measurements with an atmospheric probe. The two missions' characteristics are listed in Table 2.5. They differ in several aspects: the missions' scientific aims, the fact that one contains a fly-by (similarly to the Galileo spacecraft) while the other an orbiter (similarly to the Cassini spacecraft), the launch year, propellant, and geometry of interplanetary cruise.

The choice of a carrier and relay spacecraft's trajectory is dependent on several aspects such as the atmospheric vehicle's flight-path, time of flight, need to repeat measurements in time or space, communication window duration, but also on the mission's science priorities, and number of in-situ vehicles to deliver and communicate with. As can be seen in Table 2.5, an orbiter (Mission Option 5) would be ideal for a science return on the planet's atmosphere, but also on additional systems such as its rings, satellites, and magnetosphere. Moreover, as the atmospheric vehicles from the mission at hand would have to reach altitudes where the pressure level is of 100 bar, its descent time would be increased compared to the mission presented by Hofstadter et al. (2017), where the probe's objective pressure was of 10 bar.

[14]`https://voyager.jpl.nasa.gov/mission/timeline/#event-a-once-in-a-lifetime-alignment`, accessed on 02/12/2020.
[15]`https://doi.org/10.1038/d41586-020-00619-y`, accessed on 02/12/2020.

**Table 2.5:** Characteristics of the two mission architectures relevant to this project (Hofstadter et al., 2017).

| **Mission Option** | **4** | **5** |
|---|---|---|
| Case Description | Uranus Fly-by spacecraft with probe and <50 kg science payload. | Uranus Orbiter with probe and <50 kg science payload. |
| Science | Highest priority science (interior structure and composition) | Highest priority plus additional system science (rings, satellites, magnetosphere) |
| Cost Estimate [$k, FY15][a] | 1493 | 1700 |
| Aerospace ICE [$k, FY15] | 1643 | 1993 |
| Payload | 3 instruments (Narrow Angle Camera, Doppler Imager, Magnetometer) + atmospheric probe | 3 instruments (Narrow Angle Camera, Doppler Imager, Magnetometer) + atmospheric probe |
| Payload Mass MEV [kg] | 45 | 45 |
| Launch Mass [kg] | 1524 | 4345 |
| Launch Year | 2030 | 2031 |
| Flight Time [yr] | 10 | 12 |
| Time in Orbit [yr] | Fly-by | 3 |
| Total Mission Length [yr] | 10 | 15 |
| RPS use/EOM Power [W] | 4 eMMRTGs/425 | 4 eMMRTGs/376 |
| Launch Vehicle | Atlas V 541 | Atlas V 541 |
| Propulsion System | Monopropellant | Dual Mode |
| Interplanetary Cruise | Earth-Jupiter fly-by | Venus-Earth-Earth-Jupiter fly-by |

[a]Includes cost of eMMRTGs, NEPA/LA, and standard minimal operations, LV cost not included.

A fly-by spacecraft would thus have to be flying at a low enough velocity, such that it stays above the atmospheric vehicle for telecommunications during the vehicle's descent. An orbiter on the other hand, would have to increase its altitude in order to spend more time continuously above a specific location of Uranus, or be quasi-synchronous with the atmospheric vehicle. It must also be noted that having a spacecraft operating a fly-by could lead to aerocapture to then achieve orbit insertion around Uranus. However, since the aim of that manoeuvre is to pass through a planet's atmosphere, the relay spacecraft would be orbiting at a very low altitude with respect to the gliders, which would considerably decrease their communication windows. Aerocapture is thus not implemented in this thesis work. **Mission Option 5 is thus the preferred interplanetary trajectory option for this mission.**

### 2.8.3. Uranus Approach and Descent Probe Release

This phase of the mission concerns the trajectory needed to be followed by the carrier and relay spacecraft to approach Uranus, in order to deliver the descent probe(s) containing the atmospheric vehicle(s), at their desired location.

Different orbit types can thus be considered for the carrier and relay spacecraft. If it were to orbit Uranus such as in Mission Option 5, a circular or elliptic orbit would be used. A hyperbolic orbit would be used to perform a fly-by of the planet, similarly to Mission Option 4. Since the mission at hand is dealing with the delivery of multiple atmospheric vehicles to Uranus, two situations can be considered to achieve this:

1. The carrier and relay spacecraft performs a gravity-assisted capture of Uranus, releasing its first probe at periapsis of that manoeuvre. It then inserts itself into an elliptical or circular orbit and releases its potential other probes each time it reaches periapsis of that orbit, making use of the planet's short rotational period of 17.24 h to deliver the probes at different latitudes.[16]
2. The carrier and relay spacecraft performs a fly-by of Uranus through a hyperbolic orbit, releasing its potential multiple probes one after another during the fly-by, receiving the communicated scientific data and sending it to Earth before it is too far away.

Looking at these two options, it seems like the second one is the least likely to happen, as only a short period of time would be available to conduct all described actions, unless the distance between the spacecraft and Uranus is increased, to the detriment of the communication possibilities. The release of multiple descent probes containing the gliders, their trajectory tracking, and communication relay could simply not happen during a

[16]`https://nssdc.gsfc.nasa.gov/planetary/factsheet/uranusfact.html`, accessed on 20/02/2021.

fly-by. Using a perifocal distance of approximately 85,000 km, the communication window of such an orbit was estimated to be a bit less than 3 h, which is not enough. It was established that the orbiting spacecraft will have to be in continuous line-of-sight of the atmospheric vehicles during their respective measurement phases, for trajectory tracking and retrieval of scientific data. To achieve this, a circular orbit is the logical option, as the communication windows are not constrained by the periapsis passage of an elliptical orbit. The first scenario mentioned at the beginning of this section will thus be investigated in this thesis, namely, **the relay spacecraft will perform a gravity-assisted capture of Uranus and insert itself into a circular orbit**. This means that Mission Option 5 is selected from Table 2.5. The Atlas V541 launcher is the same vehicle that launched the Mars Science Laboratory mission in 2011, and more recently the Mars 2020 mission in 2020.

The descent probe(s)' entry location will be described in Section 3.7, for the relay spacecraft to perform the adequate manoeuvres to bring them at destination, as well as to fulfil the mission's scientific goals. One option to reach different latitudes and longitudes on Uranus is to take advantage of Uranus' rotation. The steps are as follows: first, the relay spacecraft brings and releases a first atmospheric vehicle to a desired location from a pre-orbit insertion hyperbolic trajectory. It then performs a circular orbit insertion at Uranus, and follows this orbit until it reaches its next periapsis. There, a second atmospheric vehicle is released, given that Uranus would have rotated around its rotational axis and offered a different entry location. The atmospheric vehicles are contained in descent probes which are released from the orbiting spacecraft.

Moreover, the coasting period of the descent probes have to be defined. This corresponds to the duration of time in between the release of a probe, and the moment it starts atmospheric entry. As references, the Galileo probe was released 120 days before its atmospheric entry, while Sayanagi et al. (2020) suggest a $30 - 40$ day coast duration for Uranus, and Hofstadter et al. (2017) a 60 day duration. A significant constraint on the coast duration is the heat source. For example, if the heating of the spacecraft's subsystems is provided by battery-powered electric heaters, then a significant battery mass must be considered. The longer the coast duration, the heavier the battery. Demonstrating the feasibility of a potential probe that does not rely on Radio Isotope Heater Units (RHUs), Sayanagi et al. (2020) calculated that a 4.8 kg battery mass would be necessary for a 30 day coast period towards Uranus. An average of 50 days is thus chosen for the coasting period of this mission's descent probe(s).

### 2.8.4. Vehicles' Entry and Descent

This phase concerns the phase during which the descent probe(s) release the atmospheric vehicle(s). After that, the scientific measurements will be conducted by the instruments on-board the atmospheric vehicle(s) and relay spacecraft. It is also the phase during which the scientific data will be communicated between the potential different atmospheric vehicles and the relay spacecraft, and between the relay spacecraft and the Earth. The science operations during glide of the atmospheric vehicles should thus be determined, in order to know the conditions in which the different instruments should be activated.

Sayanagi et al. (2020) provide a notional event sequence of this phase of the mission, taking reference points in time as when the probe is released from the orbiter, as well as when the entry deceleration pulse drops below 100 G, as they assume that after that point the deceleration pulse is only decaying. This notional event sequence is, however, dependent on the fact that the atmospheric vehicles are parachuted descent probes. Concerning the instruments, they start generating data 10 minutes prior to the expected atmospheric interface.

## 2.9. Mission and System Requirements

A few assumptions have been made in the previous sections, so as to be able to define the mission's target planet, scientific aim and payload, as well as the scientific platform possibilities. These assumptions led to mission and system requirements, which are defined below. The gliders performing atmospheric measurements will be referred to as "the atmospheric vehicle", and the orbiter will be referred to as "the relay spacecraft". The relay spacecraft contains the descent probes, themselves containing the atmospheric vehicles. The mission and system requirements are followed by their respective rationales in italics. Please note that any requirements related to launch, interplanetary trajectory, Uranus approach, as well as vehicle release and entry are defined to provide more structure to the mission, but will not be verified in the scope of this thesis.

**MIS-1:** The relay spacecraft shall encounter Uranus at or before the planet's 2049 Spring equinox.
**MIS-1.1:** The relay spacecraft shall be launched from the Earth in year 2031.
**MIS-1.1.1:** The relay spacecraft shall be launched with an Atlas V 551 launch vehicle.

**MIS-1.2:** The interplanetary trajectory shall contain a Venus-Earth-Earth-Jupiter fly-by.

**MIS-2:** The descent probes shall be brought at Uranus by the relay spacecraft.
**MIS-2.1:** The descent probes shall separate from the relay spacecraft 50 days before the probe's interface altitude is reached. *Hofstadter et al. (2017) suggest a 60 days long coasting period. Sayanagi et al. (2020) suggest 30-40 days.*
**MIS-2.1.1:** The descent probes' interface altitude shall be 1,000 km above Uranus' 1 bar pressure level altitude. *As suggested by Hofstadter et al. (2017).*
**MIS-2.1.2:** The descent probes' entry flight-path angle shall be -30 degrees. *As suggested by Hofstadter et al. (2017).*
**MIS-2.1.3:** The descent probes' entry velocity shall be $22 - 23$ km/s. *As suggested by Hofstadter et al. (2017).*

**MIS-3:** Communication shall be possible between the atmospheric vehicles and the relay spacecraft during the atmospheric vehicles' measurement phase.
**MIS-3.1:** The relay spacecraft's orbit around Uranus shall be a circular orbit.

**MIS-4:** The atmospheric vehicles shall consist of un-propelled winged vehicles.
**SYS-4.1:** The atmospheric vehicle shall be foldable inside an entry capsule such as the Mars Science Laboratory entry vehicle, which has an interior space of 3.7 m in diameter, and 1.2 m in height.

**MOD-1.1:** The chosen reference atmospheric vehicle shall have a defined vehicle geometry.
**MOD-1.2:** The chosen reference atmospheric vehicle's mass and inertia properties shall be available from literature or generated.
**MOD-1.3:** The chosen reference atmospheric vehicle shall have defined control surfaces to control pitch, roll, and yaw movements.
**MOD-1.4:** The chosen reference atmospheric vehicle's stability and control derivatives shall be retrieved from literature or generated with software such as XFLR5 (Deperrois, 2003).
**MOD-1.5:** The chosen reference atmospheric vehicle's reference trajectory shall be a downwards gliding path, with the atmospheric vehicles experiencing tailwind.
**MOD-1.6:** The chosen reference atmospheric vehicle shall be operational in subsonic flight regimes.
**MOD-1.7:** The chosen reference atmospheric vehicle shall be operational from altitudes of 0 km (1 bar) until $-375$ km (100 bar).
**MOD-1.8:** The chosen reference atmospheric vehicle shall stay at least 2 h between the 0 bar and 20 bar pressure levels[17].

[17] Personal communication with Olivier Mousis, 18/01/2021

# 3 Uranian Environment and Target Areas Choice

To perform an atmospheric entry analysis into Uranus' atmosphere, a model of that planet and atmosphere have to be defined. This chapter will present the research that was done to establish the current knowledge on the planet's properties from previous space missions such as Voyager 2, but also from ground-based measurements such as thermochemical modelling. Section 3.1 will give details on the planetary constants, shape, and structure, Section 3.2 will detail the gravity modelling of Uranus, Section 3.3 will provide information on the planet's atmospheric composition and opacity, Section 3.4 about the atmospheric temperature, pressure, and density profiles, and Section 3.5 about the atmospheric dynamics. Section 3.6 will provide insight as to how the software's environment module was verified. Section 3.7 will present the mission's target regions on Uranus. Finally, Section 3.8 will provide additional mission, system, and modelling requirements.

## 3.1. Planetary Constants, Shape, and Internal Structure

Physical and orbital properties of the planet are listed below[1] (Helled et al., 2011):

- Mass: $M_u = 86.813 \cdot 10^{24}$ kg
- Equatorial radius (1 bar level): $R_{u,e} = 25,559$ km
- Mean radius: $R_{u,m} = 25,388.2$ km
- Mean density: $\rho_u = 1,271$ kg/m$^3$
- Gravity (equatorial, 1 bar): $g_u = 8.87$ m/s$^2$
- Solar irradiance: $S_u = 3.69$ W/m$^2$
- Sidereal orbit period: $T_u = 30,685.4$ days
- Sidereal rotation period: $T_{u,rot} = -17.24$ h

Uranus is amongt the celestial bodies that can be considered to have regular bodies. The ellipticity $e_u$ of the planet can be computed as follows:

$$e_u = \frac{R_{u,e} - R_{u,p}}{R_{u,e}} = 1 - \frac{R_{u,p}}{R_{u,e}} = 1 - \frac{24973 \cdot 10^3}{25559 \cdot 10^3} = 0.022927 \approx 0.023 \tag{3.1}$$

This result means that equatorial and polar radii differ by around 2.3 %, which does not represent much flattening, as compared for example to Gas Giant Saturn, which shows a flattening of around 10 % due to its faster rotational rate (around 9.87 km/s for Saturn, against 2.59 km/s for Uranus at the equator) and internal composition. The planet's flattening can thus be ignored for the purpose of this thesis' study.

As for the planet's internal structure, it must be noted that it is, as of today, poorly understood. It is unclear whether the transition between the different layers of the planet is distinct or gradual. Figure 3.1 shows two possible models for Uranus: the left diagram denotes standard 3-layer models, while the right one shows a gradual change between the different planetary layers. It is believed that Uranus possesses a rocky core, a

[1] `https://nssdc.gsfc.nasa.gov/planetary/factsheet/uranusfact.html`, accessed on 21/12/2020.

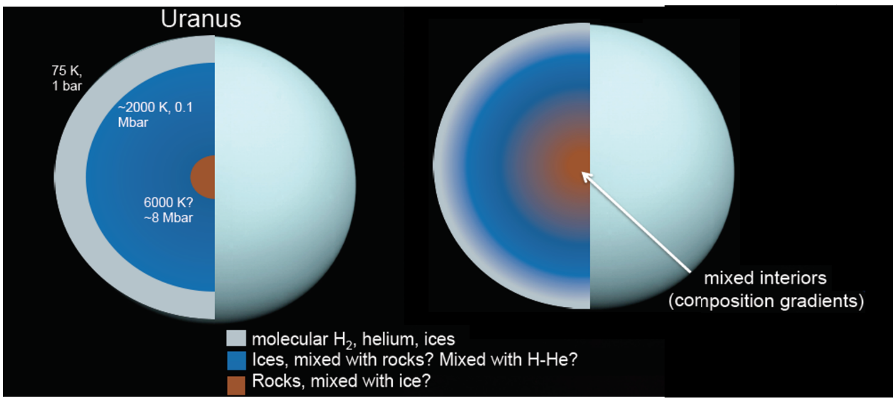


**Figure 3.1:** Two possible internal structures of Uranus.[a]

[a]`https://www.universetoday.com/18855/uranus/`, accessed on 02/03/2021.

mantle mostly made of water, ammonia, and methane ices, and an atmosphere mostly composed of hydrogen, helium, and methane gases. The planet's troposphere is defined from −300 km to 50 km altitude with respect to the 1 bar pressure level, which is defined as 0 km altitude (Hassanalian et al., 2018). Helled et al. (2020) concluded that the inferred compositions of both Uranus and Neptune are sensitive to the assumed thermal profile of the atmosphere's outer layers. Studying Uranus' troposphere will thus help provide answers to the planet's internal structure.

## 3.2. Gravity Modelling

To model the accelerations to which a body is subjected, two categories can be considered: central gravity, and perturbations. Central gravity represents the point mass acceleration due to a single body. It is often the most dominant acceleration. Perturbations are all other accelerations that might induce small variations to an orbit's Keplerian elements. Several perturbations must be evaluated to see if they have an impact on the trajectories of both the atmospheric vehicle and the relay spacecraft.

### 3.2.1. Gravitational Field

We simulated the influence of Uranus' biggest harmonic coefficients, namely the $J_2$-effect, to know if harmonic coefficients should be taken into account in the simulations, or if they can be neglected when modelling the planet's gravitational acceleration. This was done for both the relay spacecraft, and the atmospheric vehicle. The simulation was first conducted for the atmospheric vehicle's potential trajectory. The trajectory was modelled as a circular orbit, with radius equal to $(R_U - 375)$ km, which is assumed as being the deepest level attainable with an atmospheric vehicle for the mission, and thus the worst case scenario, as it is the one with the lowest altitude. This number was chosen knowing that the 100 bar pressure level is defined at −375 km. The initial inclination angle, right ascension of the ascending node, the argument of periapsis, and the mean anomaly were chosen arbitrarily and are listed in Table 3.1. The simulated trajectory and position error between perturbed and un-perturbed trajectories increases with time until around 20 minutes, when it starts decreasing again. At its maximum, the position error is of 102.04 km.

For the relay spacecraft's orbit, an elliptic orbit with a periapsis of $r_p = 1.05$ Uranus radius and a period of $T = 142$ days were chosen, as suggested by Sayanagi et al. (2020). The semi-major axis $a$ and ellipticity $e$ of the orbit were determined as follows. The other initial conditions were chosen arbitrarily and are listed in Table 3.2.

$$T = 2\pi\sqrt{\frac{a^3}{\mu}} \tag{3.2}$$

$$r_p = a(1-e) \tag{3.3}$$

The elliptic orbit was then propagated for 142 days with a Runge-Kutta 45 integrator for solving this non-stiff problem with higher precision than with an Euler integrator for example, to see how the orbital parameters would behave. The Runge-Kutta integrator is further explained in Section C.2.1. Without including the $J_2$-effect, the orbital elements stayed constant, which is to be expected for a spacecraft experiencing only point mass gravity. When the $J_2$-effect was added to the point mass gravity in the acceleration terms of the

**Table 3.1:** Initial conditions of effect of $J_2$ simulation in orbital elements and Cartesian components of atmospheric vehicle.

| **Orbital Elements** | | **Cartesian Components** | |
|---|---|---|---|
| Semi-major axis $a$ [km] | 25,088.2 | $x$ [km] | -13,545.6 |
| Eccentricity $e$ [-] | 0.0 | $y$ [km] | -9,365.5 |
| Inclination $i$ [°] | 50.0 | $z$ [km] | 18,926.7 |
| Right ascension of the ascending node $\Omega$ [°] | 320.0 | $\dot{x}$ [km/s] | 32.8062 |
| Argument of periapsis $\omega$ [°] | 150.0 | $\dot{y}$ [km/s] | -34.5299 |
| Mean anomaly $M$ [°] | 110.0 | $\dot{z}$ [km/s] | -6.3925 |

**Table 3.2:** Initial conditions of effect of $J_2$ simulation in orbital elements and Cartesian components of relay spacecraft.

| **Orbital Elements** | | **Cartesian Components** | |
|---|---|---|---|
| Semi-major axis $a$ [km] | 2,805,907.9 | $x$ [km] | 4,727,654.3 |
| Eccentricity $e$ [-] | 0.99043 | $y$ [km] | -8,780,807.9 |
| Inclination $i$ [°] | 50.0 | $z$ [km] | -4,394,724.3 |
| Right ascension of the ascending node $\Omega$ [°] | 320.0 | $\dot{x}$ [km/s] | 0.5602 |
| Argument of periapsis $\omega$ [°] | 150.0 | $\dot{y}$ [km/s] | -0.8018 |
| Mean anomaly $M$ [°] | 110.0 | $\dot{z}$ [km/s] | -0.3028 |

simulation, the propagation of the initial conditions resulted in an orbit where the orbital elements remain quasi-constant. Elements such as inclination angle, right ascension of the ascending node, as well as argument of periapsis remained constant. The position error between the perturbed and non-perturbed orbit, which can be seen as the trajectory error, rises to around 21.04 km during the 142 days simulation.

The simulation was done for the mission's lowest altitude, but the chosen orbital elements only offer a representation of a specific case, where certain latitudes and longitudes are explored, while others are not. It does not explore all trajectory possibilities but offers a fair depiction of the position error's order of magnitude. Having the atmospheric vehicle's trajectory differ by around 100 km is thus negligible in the case of this mission, as the vehicle's descent is not meant to reach specific locations in Uranus' atmosphere, but rather to explore different layers. The planet's gravity would ultimately bring an atmospheric vehicle downward.

In conclusion, since the effect of including the $J_2$ spherical harmonic to the acceleration model is minimal, **the gravity potential will be simulated as a central field in this work**.

### 3.2.2. Other Perturbations

Other perturbations were studied, with aim to see if they have a significant effect on the atmospheric vehicle and relay spacecraft's trajectories, which would have consequences on the scientific measurements. The perturbations include: radiation forces (solar radiation pressure, planetary albedo, thermal radiation, antenna thrust) and gravitational attraction of the Sun/other planets. This study mostly concerns the relay spacecraft, as the motion of the atmospheric vehicle will always be dominated by the aerodynamic forces acting on it.

Starting with solar radiation pressure, it is dependent on the solar irradiance at Uranus. As a maximum, Uranus is at 19 au from the Sun, where the solar irradiance is 3.69 W/m$^2$, against $1,361$ W/m$^2$ at the Earth.[2] The acceleration felt at Uranus due to solar radiation pressure can be calculated by multiplying this solar irradiance by the absorbing area and dividing it by the speed of light and the object's mass. For a theoretical absorbing area of 1 m$^2$ and mass of 1 kg, this yields an acceleration of the order of magnitude of $10^{-8}$ m$^2$ at Uranus, which can be neglected for both the atmospheric vehicle and the relay spacecraft.

Uranus' geometric and Bond albedo are very similar to Earth: 0.49 (Mallama et al., 2017) and 0.30 (Pearl et al., 1990) against 0.43 (Mallama et al., 2017) and 0.31 for the Earth[3]. These values might differ in terms of latitude. Uranus' albedo thus represents 30 % of the previously mentioned solar irradiance of 3.69 W/m$^2$, which was chosen to be neglected. It is thus also the case for Uranus' albedo.

The thermal radiation corresponds to the radiation from the spacecraft emitted to space. The emission of

[2]`https://nssdc.gsfc.nasa.gov/planetary/factsheet/uranusfact.html`, accessed on 04/12/2020.
[3]`https://nssdc.gsfc.nasa.gov/planetary/factsheet/earthfact.html`, accessed on 28/01/2021.

thermal photons that carry momentum generates thrust and this force acting on a rotating body in space is often termed as the "Yarkovsky effect". It is only important when considering long-term evolution of small bodies, and can thus be neglected in the analysis of this mission.

Next, antenna thrust is generated by radio signals. Radio signals emitted by a spacecraft consist of a large number of photons, which when typically transmitted in a specific direction, can create a thrust force. For Global Navigation Satellite System (GNSS) satellites, with an approximated 100 W of transmitted signal, the antenna effect is of order $\approx 3 - 5 \cdot 10^{-10}$ m/s$^2$. Sayanagi et al. (2020) suggest the atmospheric vehicle to have 10 W of transmitter output. This small acceleration is thus considered negligible for both the atmospheric vehicle and the relay spacecraft, for both emitted and received radio signals.

One last acceleration to consider is third-body acceleration. Third body perturbations will be neglected for the atmospheric vehicles, considering the proximity they will keep with Uranus. An example will be taken for the spacecraft's orbit, with a semi-major axis of $a = 2,805,907.9$ km for a 142 days elliptical orbit, as suggested by Sayanagi et al. (2020) and mentioned in Table 3.2. The perturbing acceleration of the Sun, Jupiter, Saturn, and Neptune were computed. It was found that the biggest one of them was the Sun's, being of magnitude $10^{-8}$ m/s$^2$, while Jupiter and Saturn's were of magnitude $10^{-11}$ m/s$^2$, and Neptune's of $10^{-12}$ m/s$^2$. It can be assumed that these values are negligible compared to the central acceleration experienced by the spacecraft at Uranus of $\mathbf{a_{12}} = 7.36 \cdot 10^{-4}$ m/s$^2$ for this example. **No perturbation will thus be taken into account in the simulation of both the atmospheric vehicles' flights and the relay spacecraft's orbit.**

## 3.3. Atmospheric Composition and Opacity

From current knowledge, the bulk composition of Uranus and Neptune is approximately $10 - 20$ % hydrogen and helium and $80 - 90$ % heavier elements by mass (Podolak et al., 2019). Their atmospheres become progressively enriched with $H_2$ and He with increasing altitude. More information on Uranus' and Neptune tropospheric composition is made available by Moses et al. (2020).

Only in-situ probing can provide detailed measurements of the bulk composition of a planet's atmosphere. As seen before, remote sensing techniques have been used to provide hints on the deep composition of Uranus, however they generally provide lower limits for condensible species and too large uncertainties for formation models. Here it is interesting to see at which pressure levels each element/molecule is expected to be found in the Uranian atmosphere, for an atmospheric vehicle to provide more accurate data on the atmosphere's composition. Following, is a summary of the studied literature on this matter.

- In both Ice Giants, methane ($CH_4$) condenses at approximately 1 bar and must be measured below this level (Cavalié et al., 2020).
- Hydrogen sulfide ($H_2S$) and ammonia ($NH_3$) are thought to form a cloud of ammonium hydrosulfide ($NH_4SH$) at around $30 - 50$ bar, only leaving traces of the most abundant of these molecules up to their own condensation levels. The most abundant molecule would then condense in another cloud, at pressures between 5 and 10 bar (Deboer and Steffes, 1994). Gulkis and Depater (1984) state that ammonia would have its condensation level at around 8 bar.
- Oxygen ($O_2$) is mainly carried by water ($H_2O$). However, as water condenses in the troposphere of the giant planets, it would occur at pressures ranging from 200 to 1,000 bar in Uranus, according to Leconte et al. (2017). As previously mentioned, Voyager 2 radio occultation observations suggest that the base of a water ice cloud (assuming solar O/H) would be located in the range of $200 - 300$ bar, although it is also likely that this happens much deeper since the O/H is expected to be greatly enhanced above solar (Atkinson et al., 2020). However, Baines (1997) states that considering a solar oxygen abundance, water clouds would form near the 120 bar pressure level. Considering a water mole fraction similar to the mole fraction of methane (3 %), the water cloud base would be at about a 550 bar depth. Different studies thus yield different results, even for the same conditions.
- In terms of latitude, the equatorial domain (from 0° to $15 - 30°$ N/S) shows a local minima in volatile species in the upper troposphere and a maxima of $CH_4$ and $H_2S$ abundance at deeper levels. The mid-latitude domain (from $15 - 30°$ N/S to $60 - 75°$ N/S) shows anticyclonic jovian zones, where a probe might encounter localised storm activities in the upper-tropospheric upwelling, enhanced optical depths of clouds and hazes, as well as negligible vertical shear on the zonal winds. Finally, the polar domain (poleward of $60 - 75°$ N/S) shows depletion in volatiles $CH_4$, $H_2S$, $NH_3$, and perhaps $H_2O$. A probe entering this region might be able to perform noble gas measurements, but would only return upper

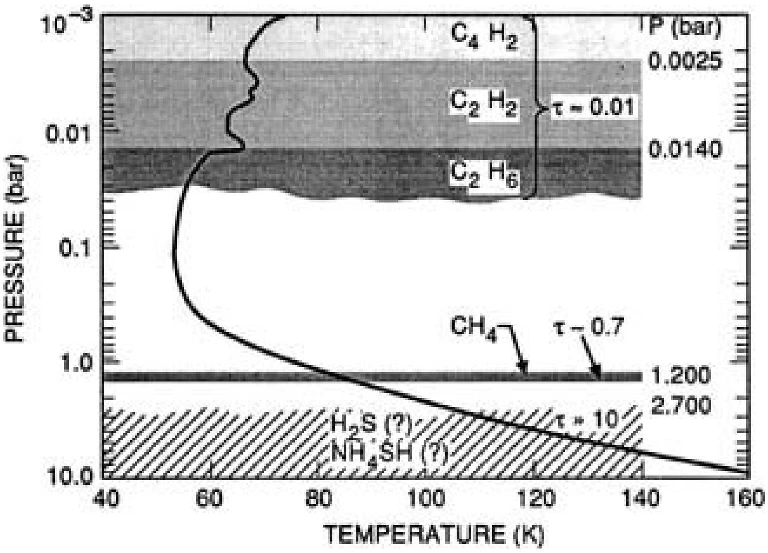


**Figure 3.2:** Uranus' thermal and aerosol structure in the stratosphere and upper troposphere (Baines, 1997).

limits on key elemental abundances and isotopic ratios. The poles are unique regions, where despite the net subsidence of species, a small-scale convective activity persists, potentially leading to enhanced humidity of $H_2S$ immediately above the clouds (Fletcher et al., 2020a).

Hazes and clouds' vertical location are shown in Figure 3.2 for a pressure range of 0.001 bar to 10 bar pressure. The hydrocarbon aerosols seen at the top of Figure 3.2 are believed to precipitate downward throughout the stratosphere and upper troposphere in 10-100 years, evaporating near the 1 bar pressure level. At 1.2 bar, a cloud of methane can be seen, which is physically and optically thin. Near the 2.7 bar level, an optically thick cloud, most probably comprised of condensed hydrogen sulfide ($H_2S$), is present. The volatile species ($CH_4$, $NH_4SH$, $H_2S$, and $H_2O$) that are expected to be present in the troposphere are predicted to form discrete condensation cloud layers as they are transported upward nearly adiabatically, and cooled (Baines, 1997).

Concerning the atmosphere's opacity, it is the collisions between different hydrogen molecules, as well as helium and methane molecules, that causes it to increase the most in the planet's troposphere (Lunine, 1993). Near the peak of the Planck function seen at around 0.1 bar, unit optical depth is reached (Marley and McKay, 1999). Below that region, the opacity increases. However, as seen in Figure 3.3, Irwin et al. (2010) argue that the opacity first decreases below 0.1 bar pressure level, and then increases after 1 bar, to then decrease again after around 2 bar of pressure are reached. This figure also provides an indication on the planet's clouds and hazes. Figure 3.3 shows the cloud structure retrieved from methane absorption data at 30° S (solid line), the equator (dotted line), and 30° N (dashed line). Cavalié et al. (2020) state that Uranus' atmospheric opacity increases exponentially as depth increases, especially beyond depths of 15 bar.

All knowledge on Uranus' opacity distribution is thus not accurate and can often be contradicted from one study to another. This is because the data on the planet's opacity is taken from different data and models, which each contain their margins of uncertainties, assumptions, and which each use different analysis methods. Moreover, models often show the atmosphere down to pressure levels of a few bars, while some of the measurement phases of the mission at hand here will have to take place much deeper in the atmosphere, at $30 - 50$ bar, or even at around 200 bar for the detection of oxygen.

## 3.4. Atmospheric Temperature, Pressure, and Density Profiles

Uranus' atmospheric temperature and pressure profiles were primarily retrieved from the Voyager 2 radio occultation measurements of refractivity versus altitude (Lindal, 1992), and were further constrained by thermal infrared (Flasar et al., 1987), solar (Herbert et al., 1987; J. Bishop et al., 1990; Stevens et al., 1993; Broadfoot et al., 1989) and stellar occultation (Lane et al., 1986; West et al., 1987) observations. They depend however, on the assumption of a specific atmospheric bulk composition and more specifically on knowledge of the atmosphere's mean molecular mass. Besides, knowing that the Voyager 2 radio occultation experiment probed a pressure range of 0.25 mbar to 2.3 bar (Lindal et al., 1987), the temperature and pressure profiles

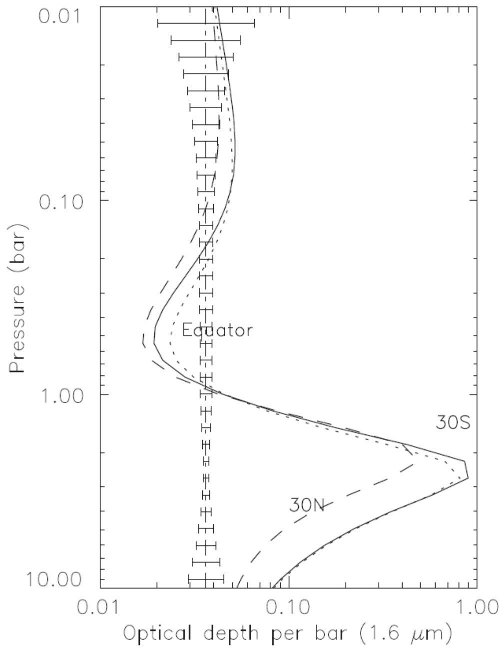


**Figure 3.3:** Cloud structure of Uranus retrieved from methane absorption data at 30° S (solid line), the equator (dotted line), and 30° N (dashed line) (Irwin et al., 2010).

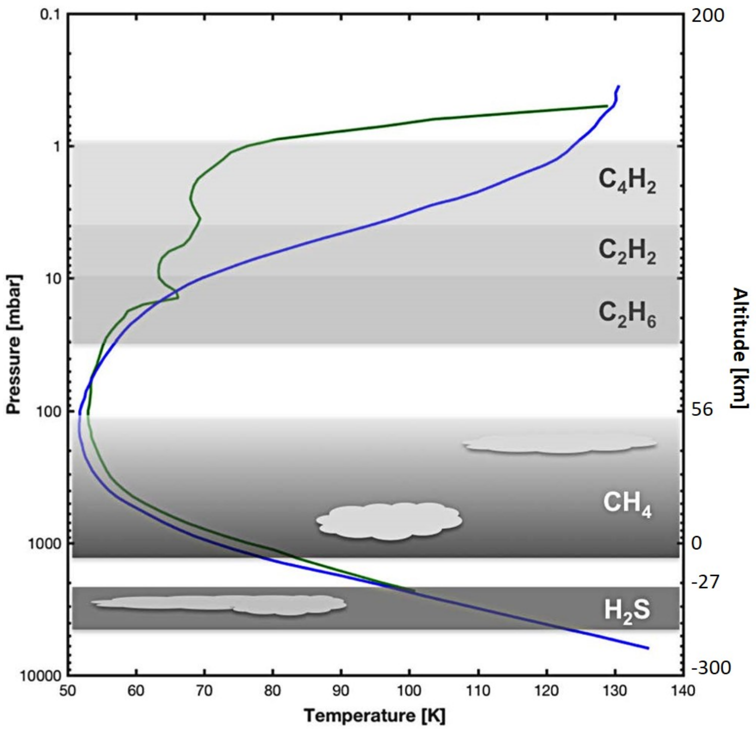


**Figure 3.4:** Uranus' and Neptune's atmospheric structure (Ferri et al., 2020) with temperature profile taken from Voyager 2 radio occultation for Uranus (green) and Neptune (blue) (Lindal, 1992), and scheme of the haze and cloud structure as observed by, or inferred from remote sensing (Baines and Hammel, 1994; Irwin, 2003; Karkoschka and Tomasko, 2011).

are strongly model-dependent as pressure increases. Figure 3.4 shows Uranus' (green) and Neptune's (blue) temperature and pressure profile, from a combination of Voyager 2's radio occultation data, and observed or inferred schemes of hazes and clouds from remote sensing. An altitude scale was added on the right-hand side.

In Figure 3.4, the lower portion of the graph where the temperature increases with increasing pressure (negative temperature gradient) is referred to as the troposphere. It is the region that is interesting to study the presence and quantity of relevant molecules such as methane, hydrogen sulfide, ammonia, and water. The

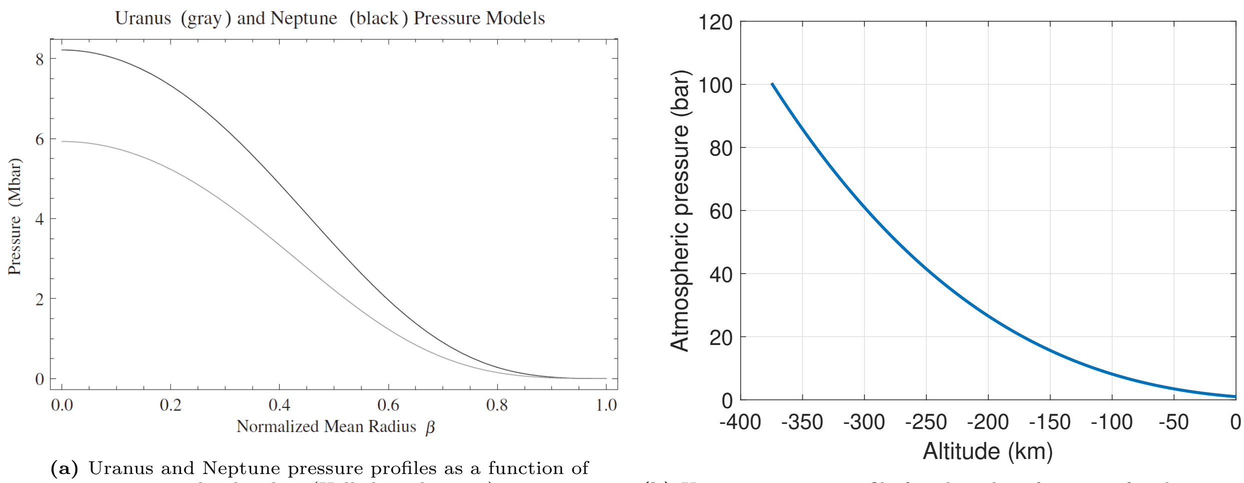


**(a)** Uranus and Neptune pressure profiles as a function of normalised radius (Helled et al., 2011).

**(b)** Uranus pressure profile for altitudes of interest for the mission.

**Figure 3.5:** Uranus atmospheric pressure profile.

slope across that region could suggest that a constantly increasing pressure (taking into account the fact that the y-axis is log-scaled) with increasing temperature would be a valid assumption for the planet's temperature and pressure model.

Similarly to the density profile, the pressure profile used for this thesis was communicated by Prof. Dr. Ravit Helled. The calculation of the atmospheric depends on the normalised mean radius of Uranus $\beta_U$:

$$\begin{aligned} p_U =& 5.927292600897025 - 17.543881478838355{\beta_U}^2 + 92.9835701421597{\beta_U}^6 - 112.28171430116535{\beta_U}^7 \\ &+ 36.04248792784944{\beta_U}^8 - 186.69724035429894{\beta_U}^{10} + 465.8660186609074{\beta_U}^{11} \\ &- 444.9407536600727{\beta_U}^{12} + 192.46620445658272{\beta_U}^{13} - 31.821982994020956{\beta_U}^{14} \end{aligned} \tag{3.4}$$

Here, all the significant figures have to be included for the pressure calculation to work as intended. Otherwise, if less significant figures are included, the pressure value is negative from roughly $\beta_U = 0.975$ to $\beta_U = 1.0$. The logarithm can then not be computed, as it is undefined. Figure 3.5 presents both the model from the work of Helled et al. (2011), and its reproduction for the altitudes of interest for this mission: from $h = 0$ km to the target altitude of $h = -375$ km. With both models provided by Prof. Dr. Ravit Helled, a relationship between the atmospheric density, pressure, and altitude can be established.

Lindal (1992) also provides tabulated data for the pressure and temperature profiles, ranging from 0.50 mbar to 2308.81 mbar. This was used for the atmospheric temperature model, extrapolating the pressure data in bar until a temperature of 300 K by following the relation in Equation (3.5) and interpolating between data points when necessary:

$$p = (54.572 \cdot e^{0.0376T}) \cdot 10^{-3} \tag{3.5}$$

For the atmospheric density profile, data from Helled et al. (2011) is used, see Figure 3.6a. The equation describing the Uranus curve (gray) was communicated by Prof. Dr. Ravit Helled[4] and used as Uranus' density model. The calculation of the atmospheric density depends on the normalised mean radius of Uranus $\beta_U$, as follows:

$$\rho_U = 4424.907684145567 - 49167.82872027526{\beta_U}^4 + 71977.30436154245{\beta_U}^5 - 27234.032598490125{\beta_U}^6 \tag{3.6}$$

Here, all the significant digits have to be included for the model to work as intended. For the mission at hand, the density model is shown in Figure 3.6b from the altitude of $h = 0$ km to the target altitude of $h = -375$ km where the atmospheric pressure is 100 bar.

## 3.5. Atmospheric Dynamics: Heating, Winds

Uranus has a mean global internal heat flux of at most 14% of the mean solar flux it receives. Its atmospheric circulation is thus dominated by the solar flux, which is an uneven distribution of sunlight from pole to equator

[4]Personal communication with Ravit Helled, 23/03/2021

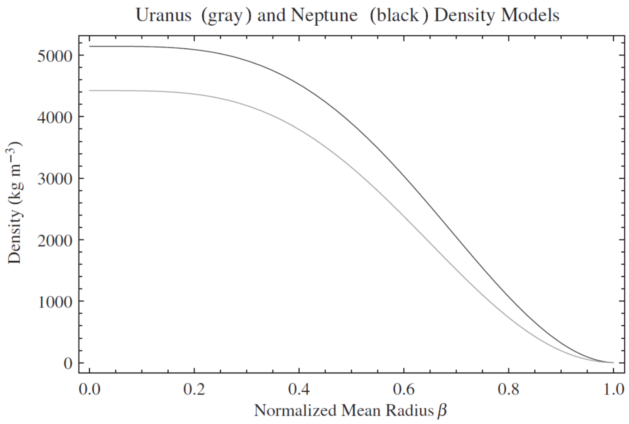


**(a)** Uranus and Neptune density profiles as a function of normalised radius (Helled et al., 2011).

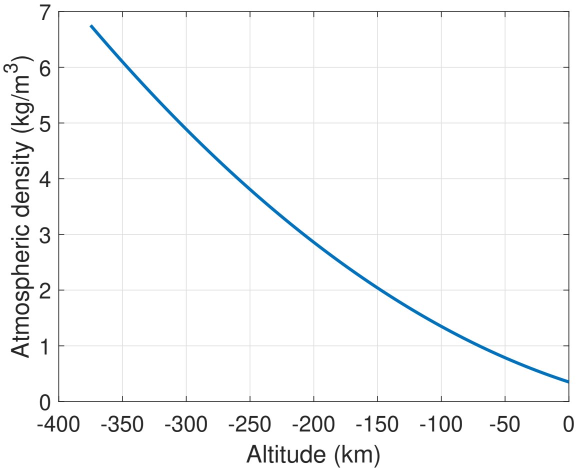


**(b)** Uranus density profile for altitudes of interest for the mission.

**Figure 3.6:** Uranus atmospheric density profile.

(Baines, 1997). The wind profile on Uranus is the least constrained, as compared to the other giant planets of our Solar System. This is mainly due to the lack of cloud features that can easily be observed from Earth. At the moment, its most used wind model relies on temperature field data measured by Voyager 2's Infrared Interferometer Spectrometer (IRIS) instrument, which was used to determine the magnitude of the circulation system through the thermal wind equation (Hanel et al., 1986). Baines (1997) states that this equation relates "measured meridional temperature gradient (that is, equator-to-pole variations in the longitudinally averaged mean temperature) to vertical variations in the mean zonal winds (that is, the mean variation in altitude of the east—west component of wind speed)". The resulting mean zonal wind speeds and thermal wind shear consist of a system of large-scale zonal jets blowing in the prograde direction at mid-latitudes, while strongly blowing in the retrograde direction at low latitudes.

Soyuer et al. (2020) provide another zonal windspeed profile for Uranus, as seen in Figure 3.7, which confirms the zonal winds behaviour described above, even with data coming from Keck and Hubble space telescopes. The smallest wind speeds are seen around 20° latitude. This location could represent a potential area for the atmospheric vehicle's flight, although the vehicle should not find itself at exactly 20° latitude, as that is where the wind direction changes direction from prograde to retrogade. The equatorial region is seen to be, in general, less prone to high velocity winds.

**Only zonal winds will be considered here.** Effects such as thermal upwelling winds, wind gusts, and turbulence, can be looked into as a further step to this thesis. For the modelling of zonal wind velocity $V_w$, the fitted curve shown in Figure 3.7 will be used, which can be described as follows (Hammel et al., 2001):

$$V_w = 170(0.6\cos\delta - \cos 3\delta) \tag{3.7}$$

Here, the zonal wind velocity $V_w$ is given in m/s, and the parameter $\delta$ represents the latitude, as opposed to the co-latitude $\theta$ shown in Figure 3.7. The relation between latitude $\delta$ and co-latitude $\theta$ is as follows: $90° = \delta + \theta$. Note that Equation (3.7) yields zonal surface winds, defined at 1 bar pressure level. This function is relative to the bulk rotation of 17 hours and 14 minutes of Uranus, as determined from Voyager 2 magnetic field data. Since then, updates have been made to the rotational rate of the planet. For an updated wind profile, the surface wind speeds calculated with Equation (3.7) can be adapted to a new rotating frame using Equation (43) mentioned in the work of Soyuer et al. (2020). The implementation of a wind model into the Simulink software is inspired by the work of Viavattene (2018).

## 3.6. Verification: Environment Module

The following models were thus implemented in the software's environment module: **Uranus' gravity is represented by a central field model without the inclusion of perturbations, Uranus' pressure profile is represented with Equation** (3.4) **(Helled et al., 2011), Uranus' temperature profile is extrapolated from the Voyager 2 observations mentioned in the work of Lindal (1992) with Equation** (3.5)**, Uranus' density profile is represented by Equation** (3.6) **(Helled et al., 2011),**

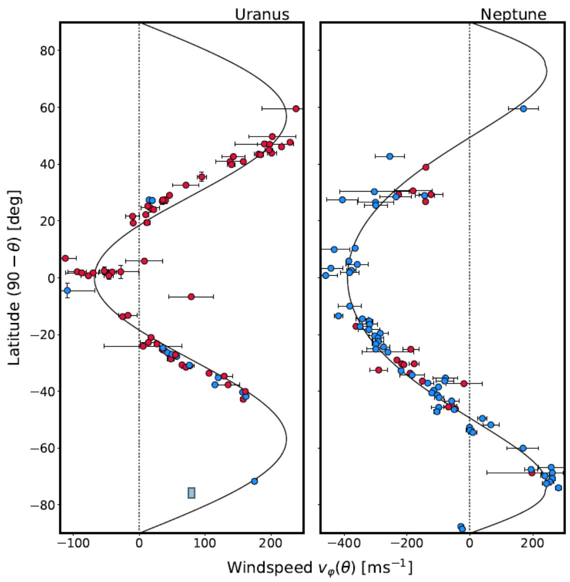


**Figure 3.7:** Uranus and Neptune's zonal windspeeds versus latitude. Keck and Hubble Space telescope measurements are shown as red points (Hammel et al., 2005; Sromovsky and Fry, 2005), while Voyager 2 measurements (Hammel et al., 2001) are displayed as blue points (Soyuer et al., 2020).

**and Uranus' zonal wind speeds are modelled with Equation** (3.7) **(Hammel et al., 2001).** These models were verified by simply comparing their results to their analytical computations. They were computed for random values of altitude, longitude, and latitude and showed to be similar to the values outputted from the simulator. Since the environment module produces the same results as when computing these quantities analytically, this means that the Simulink blocks of that module are correctly connected, and produce intended results. The module is thus considered to be verified.

## 3.7. Mission In-Situ Target Areas

To achieve the science objectives mentioned in Section 2.4, target areas to be probed by the gliders were selected. It was found that the study of Uranus' atmosphere can most effectively be performed in the planet's troposphere, as it presents the most measurable properties mentioned in the science objectives. This target region extends from 0.1 bar to 100 bar (Lunine, 1993), which corresponds to altitudes of approximately 0 km to −375 km. Moreover, as the planet's southern hemisphere was observed by Voyager 2 in 1986, it would strengthen the current knowledge of the planet to study both the day/Summer and night/Winter sides of its northern hemisphere. The target latitudes and longitudes depend on both the planet's Summer/Winter arrangement at arrival, and on its assumed known wind patterns. This is because two types of zones would have to be avoided in terms of the winds: the zones with high zonal winds, and the ones where a transition between prograde and retrograde winds occur, as they might more easily destabilise the vehicles. These target latitudes and longitudes will help determine the number of in-situ vehicles needed. They are chosen as follows, following the information given in the work of Fletcher et al. (2020a):

- **Equatorial Domain:** This area is less challenging in terms of zonal winds, as seen in Figure 3.7. The deep atmosphere is enriched in $CH_4$ and $H_2S$, and possibly other volatiles such as $NH_3$ and $H_2O$ by rising motion from the 100 bar level or deeper. It is better to stay between $0° - 18.5°$ N, so as to avoid the prograde/retrograde wind shift occurring at 18.5° N. However, the atmospheric vehicle should not probe too close to the equator, as it may present a local minimum in volatiles species in the upper troposphere. An off-equatorial entry site might thus be optimal, before encountering the storm bands and strong up-welling of mid-latitudes (Fletcher et al., 2020a). Using Equation (3.7), the zonal wind velocity was calculated for different values of latitude close to the 18.5° N limit. It was decided to keep a 1° separation between the limit 18.5° and the target latitudes to minimise the zonal winds as much as possible, without encountering the wind shift. This 1° separation corresponds to an arc distance of $\approx 446.09$ km at Uranus' equatorial radius of $R_{u,e} = 25,559$ km. This led to choosing an equatorial latitude of 17.5° N, where the zonal wind magnitude is equal to $V_w = 6.21$ m/s blowing in retrograde direction.
- **Polar Domain:** The polar domain enables the measurement of noble gases and of a small-scale con-

**Table 3.3:** Altitude, pressure, density, and temperature ranges to be explored during atmospheric flights.

| Altitude [km] | Pressure [bar] | Density [kg/m$^3$] | Temperature [K] |
|---|---|---|---|
| 0.00 | 1.00 | 0.35 | 71.60 |
| -100.01 | 8.15 | 1.35 | 133.15 |
| -172.07 | 20.00 | 2.38 | 157.10 |
| -200.02 | 26.55 | 2.86 | 164.55 |
| -273.42 | 50.01 | 4.30 | 181.49 |
| -300.03 | 61.02 | 4.89 | 186.69 |
| -374.36 | 100.02 | 6.74 | 199.92 |
| -400.04 | 116.57 | 7.44 | 203.84 |

vective activity leading to potential enhanced humidity of $H_2$ immediately above the clouds. In order to encounter minimal zonal winds without being exactly on top of the planet's north pole to keep a constant latitude, a separation of 1° was again taken between the limit and target latitude. This led to a polar target latitude of 89° N, where the zonal wind magnitude is of $V_w = 10.67$ m/s blowing in prograde direction.

**Two atmospheric vehicles will thus be needed to explore these two domains**, with the equatorial one flying in retrograde direction, and the polar one flying in prograde direction, to always experience tailwind. Considering Uranus' target northern hemisphere, it is clear that the atmospheric vehicles will have to fly in positive longitudes, so as to explore both day/Summer and night/Winter sides of the planet. At the arrival date of May 2043 defined in Section 2.8, the north pole will be illuminated, so the polar glider will find itself on the day side of the planet. The equatorial glider will have to be placed on the night side of the planet, at a longitude higher than 10.5°, where the day/night terminator will be to explore the night side. As a reference, the altitudes, pressures, densities, and temperatures to be explored are listed in Table 3.3 (Helled et al., 2011; Lindal, 1992).

## 3.8. Environment-Related Requirements

Some additional mission, system, and modelling requirements will be listed below, detailing how the mission shall behave in terms of Uranus' environment, and how it should be modelled. These requirements concern the science part of the mission and the feasibility of fulfilling the science objectives in the Uranian atmosphere.

**MIS-5:** There shall be two atmospheric vehicles deployed in Uranus' atmosphere.

**MIS-6:** The scientific measurements performed by instruments on-board the atmospheric vehicles shall fulfil Tier 1, Tier 2A, and Tier 2B science objectives. *Sciences objectives defined in Section 2.4 of this report.*

**MIS-6.1:** The atmospheric vehicles shall glide from a depth with 1 bar pressure to depths of 100 bar of pressure in Uranus' atmosphere. *Tier 1 science objectives and isotope ratio measurements fulfilled at 1 or several bars of pressure. All other science objectives fulfilled when going as deep as* 10 *bar of pressure, except detection of oxygen which can be fulfilled at* 100 *bar.*

**MIS-6.2:** The atmospheric vehicles shall fly in Uranus' northern hemisphere, on both the nigh/Winter and day/Summer sides of the planet.

**MIS-6.3:** The polar atmospheric vehicle shall have an initial target latitude of 89° N at any longitude.

**MIS-6.4:** The equatorial atmospheric vehicle shall have an initial target latitude of 17.5° N at a longitude larger than 10.5°.

**SYS-6.1:** The atmospheric vehicle's scientific instruments shall at least include a mass spectrometer, a helium abundance detector, an atmospheric structure instrument, a nephelometer, a net flux radiometer, a tunable laser spectrometer, a NanoChem, and an ultra high frequency transceiver.

**SYS-6.2:** The atmospheric vehicle and its instruments shall remain within their operational environmental conditions until depths of 100 bar of pressure are reached by the vehicle.

**MIS-7:** The scientific measurements performed by instruments on-board the relay spacecraft shall help fulfil the Tier 2B science objectives. *Sciences objectives defined in Section 2.4 of this report.*

**SYS-7.1:** The relay spacecraft's scientific instruments shall at least include a radio transceiver for the performance of a Doppler wind experiment with the atmospheric vehicles.

**SYS-7.2:** The relay spacecraft shall remain within its operational environmental conditions during the whole mission duration.

**MOD-2.1:** Uranus' gravity shall be represented by a central field model, without the inclusion of any perturbation.

**MOD-2.2:** Uranus' density profile shall be represented by the relationship provided by Figure 3.5b.

**MOD-2.3:** Uranus' temperature-pressure profile shall be represented by the relationship extrapolated from tabulated data given in the work of Lindal et al. (1987).

**MOD-2.4:** Uranus' zonal wind profile shall be represented by Equation (3.7), given in the work of Hammel et al. (2001) and implemented in Simulink following the approach of Viavattene (2018).

# 4

# Flight and Orbital Mechanics

The flight and orbital mechanics of the atmospheric platforms and relay spacecraft will be described here, with aim to model their behaviour and trajectory in Uranus' atmosphere and in space. Section 4.1 provides information on the fundamentals of motion and Section 4.2 on orbital mechanics. The reference frames and transformation matrices that were not tailored to this mission but that are still used in the simulator are specified in Appendix D. Finally, Section 4.3 will provide verification steps on the implementation of the planet's wind model.

## 4.1. Fundamentals of Motion

The required reference frames, state-variables, transformation matrices between the different reference frames, and general formulations of equations of motion will be defined in the following sections.

### 4.1.1. Reference Frames

The motion of an object in space needs to be expressed with respect to a certain reference frame, for it to be understood. Newton's laws of motion are usually expressed with respect to an inertial reference frame, while other reference frame types are typically used for other types of analysis. Here, the reference frame specific to the mission at hand will be presented. The other reference frames to be used for this work are taken from the work of Mooij (1997b) and are defined in Appendix D.

- **Inertial Planetocentric Reference Frame:**
  An inertial reference frame is a reference frame that is not undergoing acceleration. An inertial planetocentric reference frame has its origin located at the centre of mass (c.o.m.) of the central body around which the vehicle is moving. The central body, Uranus in this case, is naturally moving around the Sun, which itself is following the Galaxy's rotation. However, these accelerations experienced by the central body can be neglected for navigational purposes, and the inertial planetocentric reference frame can be considered to be inertial. This reference frame is denoted with the index $I$, and an illustration is given in Figure 4.1. The International Astronomical Union (IAU) provides a definition as to determine the direction of the reference frame's axes. First of all, the planet's north pole is defined as the pole that lies on the north side of the invariable plane (see Section D.1). The peculiarity of Uranus is that this definition induces a retrograde motion, as it rotates around itself from east to west. The direction of the north pole is defined by its right ascension $\alpha_0$ and declination $\delta_0$. For Uranus this yields $(\alpha_0, \delta_0) = (257.311^\circ, -15.175^\circ)$. The two nodes of Uranus' equator are at $\alpha_0 \pm 90^\circ$ on the ICRF equator, with respect to the Earth equinox at J2000 ♈. This leads to points $Q$ and $R$. The prime meridian is defined at shift of $W = 203.81 - 501.1600928d$ where $d$ is the interval in days from the standard epoch, eastward from point $Q$ along the planet's equator, thus passing through point $B$. For example, were the vehicle to arrive on January 1, 2046 at noon, the coordinates of $B$ would be $(347.311^\circ, 2.511^\circ)$ with respect to $(0^\circ, 0^\circ)$. Finally, the inclination of the planet's equator to the ICRF equator should be equal to $90^\circ - \delta_0$ (Archinal et al., 2018). The $Z_I$-axis points north along the central body's axis of rotation (whose rotation is assumed to be constant in magnitude and direction), and the surface spanned by the $X_I$- and $Y_I$-axes coincides with the equatorial plane. The direction of the $X_I$-axis is determined by the prime meridian passing through point $B$, and the $Y_I$-axis completes the right-handed system. The description of this reference frame is important for the interpretation of this thesis' results. **To avoid confusion, Uranus' inertial reference frame will be considered to be right-handed during simulations,**

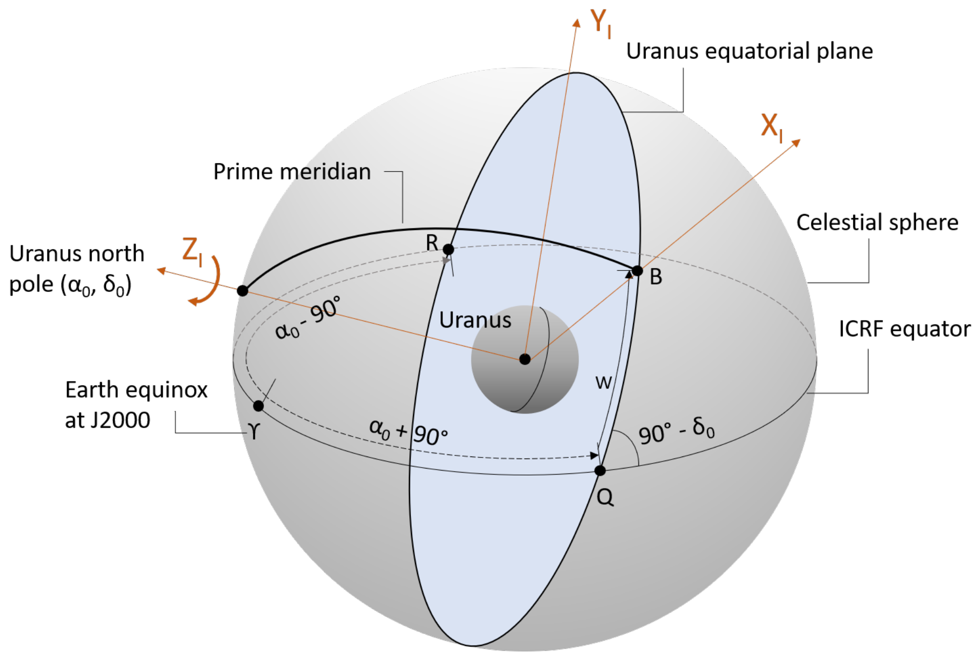


**Figure 4.1:** Inertial planetocentric reference frame definition (Holtkamp, 2014).

**with its rotational rate being positive** (so going in the other direction as the rotation shown on the positive Z-axis of Figure 4.1). The sign of the atmospheric vehicles' heading angle is adjusted for the vehicles to move in prograde or retrograde direction, as constrained by the mission's needs.

### 4.1.2. State-Variable Definitions

To define a dynamic system's state at a given instance in time, state-variables are needed. Coordinate systems are needed to express the atmospheric vehicle and relay spacecraft's position, velocity and attitude in time.

## Position and Velocity

To define the position and velocity of an object, first the necessary orbital elements will be presented. These will be useful to describe and help visualise the motion of the carrier and relay spacecraft. Cartesian and spherical coordinates are then presented, which can be useful to simulate the motion of the atmospheric vehicle. Transformations between these three systems must be defined, to be able to go from one system to another during the calculations.

- **Orbital Elements:**
  Orbital state-variables are needed to describe the motion of the carrier and relay spacecraft. The orbital elements of an orbit are as follows: the semi-major axis $a$, the eccentricity $e$, the inclination $i$, the argument of periapsis $\omega$, the right ascension of the ascending node $\Omega$, and the true anomaly $\theta$. An additional parameter is needed to define the position of a spacecraft in its orbit: the time of periapsis passage $\tau$. It is often replaced by the mean anomaly at the time $t_0$ following: $M_0 = n(t_0 - \tau)$ with $n = \sqrt{\frac{\mu^3}{a}}$. Here $n$ is the mean motion, and $\mu$ is the gravitational parameter of the central body. The mean anomaly $M$ can then be expressed as follows: $M = M_0 + n(t - t_0) = n(t - \tau)$. These are illustrated in Figure 4.2.

- **Cartesian Components:**
  Cartesian components specify a point's position and velocity with the components $x, y, z$ and $\dot{x}, \dot{y}, \dot{z}$ respectively, with respect to either the $I$- or $R$-frame. It is a very common orthogonal system. An illustration of these components is given in Figure 4.3.

- **Spherical Components:**
  Using spherical components, the position of an object is expressed in terms of components $r, \tau, \delta$, where $r$ is the distance from the object to the origin of the chosen reference frame, $\tau$ the longitude measured positively to the east ($0^\circ \leq \tau < 360^\circ$), and $\delta$ the latitude, which is measure positively in the northern

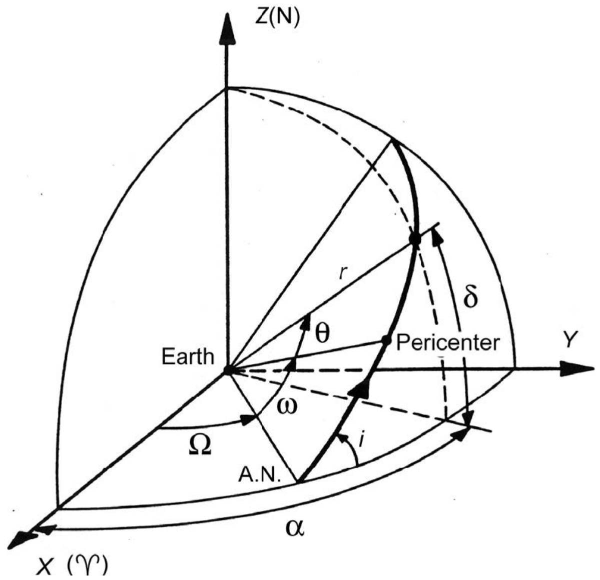


**(a)** Definition of the orbital elements $i$, $\omega$, and $\Omega$ (Wakker, 2015).

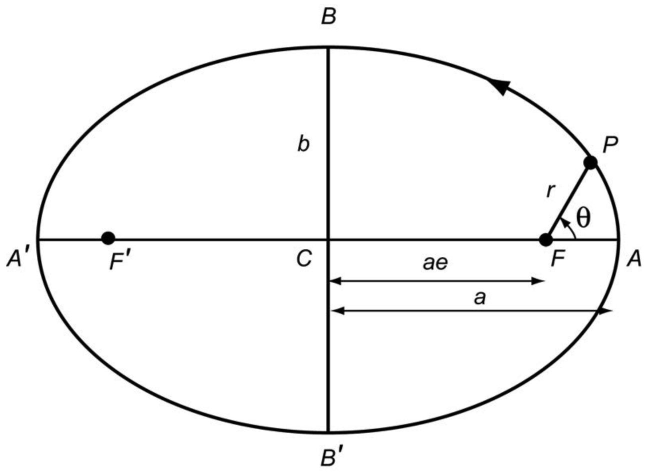


**(b)** Definition of the orbital elements $a$, and $e$ with the spacecraft moving at a distance $r$ at a true anomaly $\theta$ (Wakker, 2015).

**Figure 4.2:** Definition of orbital elements.

direction ($-90^{\circ} \leq \delta \leq 90^{\circ}$) and negatively in the southern direction along the appropriate meridian starting at the equator. The object's velocity is expressed in terms of the components $V_g, \gamma_g, \chi_g$, where $V_g$ is the groundspeed, $\gamma_g$ the flight-path angle, and $\chi_g$ the heading angle. These velocity components are typically expressed with respect to the rotating planetocentric reference frame.

## Attitude and Angular Rates

Aerodynamics attitude angles are described here, as they are commonly used to describe the attitude of a body with respect to the groundspeed or airspeed, and are a good tool for visualisation. Similarly to position and velocity systems, transformations will be necessary to define, to be able to go from one representation to another. Quaternions are also introduced as they do not contain any singularity and can be used in the simulation of the equations of motion.

- **Aerodynamic Attitude Angles:**
  The aerodynamic attitude angles are made up of the vehicle's angle-of-attack $\alpha$ positive for a "nose-up" attitude ($-180^{\circ} \leq \alpha < 180^{\circ}$), the angle of side-slip $\beta$ positive for a "nose-left" attitude ($-90^{\circ} \leq \beta \leq 90^{\circ}$), and the bank angle $\sigma$ positive when banking to the right ($-180^{\circ} \leq \sigma < 180^{\circ}$). These angles can define the vehicle's attitude with respect to the groundspeed and will be denoted with the subscript $g$ when used in the equations of motion. They can also define the vehicle's attitude with respect to the air-speed,

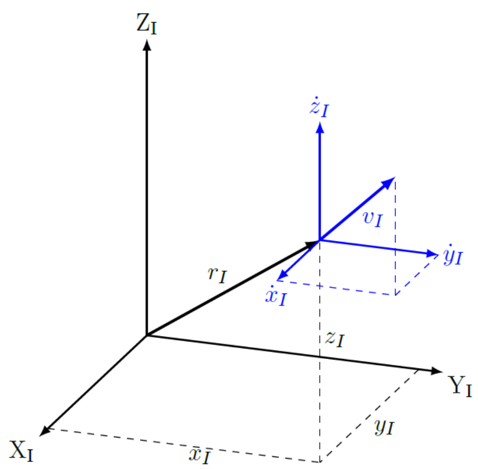


**Figure 4.3:** Position and velocity of an object in an inertial frame using Cartesian components (Holtkamp, 2014).

in which case they shall be denoted with a subscript $a$ in the equations of motion. The aerodynamic attitude angles have a singularity at pitch angles of $\theta = \pm 90°$, however that would not voluntarily happen for the vehicles considered in this study, so they can be used for flight mechanics.

- **Quaternions:**
  A quaternion consists of one real and three imaginary numbers. They are computationally more efficient and do not suffer from any singularities. In the simulator, a general quaternion $Q$ is defined as follows:

$$Q = \mathbf{Q} + Q_0 = \mathbf{i}Q_1 + \mathbf{j}Q_2 + \mathbf{k}Q_3 + Q_0 \tag{4.1}$$

Here, $Q_0, Q_1, Q_2$, and $Q_3$ are real numbers or scalars, and $\mathbf{i}, \mathbf{j}$, and $\mathbf{k}$ are the standard orthonormal imaginary basis in three-dimensional space (Kuipers, 1999). They obey the following rule:

$$\mathbf{i}^2 = \mathbf{j}^2 = \mathbf{k}^2 = \mathbf{ijk} = -1 \tag{4.2}$$

The vector part of a quaternion can be expressed in terms of the Euler axis $\mathbf{a}$ and Euler angle $\phi$:

$$\mathbf{Q} = \begin{pmatrix} Q_1 \\ Q_2 \\ Q_3 \end{pmatrix} = \mathbf{a} \sin\left(\frac{\phi}{2}\right) \tag{4.3}$$

Its scalar part can be expressed as: $Q_0 = \cos\left(\frac{\Phi}{2}\right)$.

### 4.1.3. External Forces and Moments

The external forces and moments exerted on the atmospheric platforms will be detailed here. Two different external forces acting on an un-propelled atmospheric platform can be distinguished: aerodynamic, and gravitational forces.

## Aerodynamic Forces:

Only aerodynamic moments are of interest since the gravitational force acts on the vehicle's c.o.m. The planet's atmospheric density and the vehicle's velocity with respect to the atmosphere influence both aerodynamic forces and moments. Mooij (1997b) describes the aerodynamic forces as follows:

$$\mathbf{F_{A,AA}} = \begin{pmatrix} -D \\ -S \\ -L \end{pmatrix} = \begin{pmatrix} -C_D \bar{q} S_{ref} \\ -C_S \bar{q} S_{ref} \\ -C_L \bar{q} S_{ref} \end{pmatrix} \tag{4.4}$$

Here, the drag $D$, side force $S$, and lift $L$ are dependent on their respectful aerodynamic coefficients $C_D$, $C_S$ and $C_L$, as well as the dynamic pressure expressed as in Equation 4.5, where $\rho$ is the atmospheric density, $V_A$ the airspeed, and $S_{ref}$ the reference area. The wind speed is taken into account in the drag component's dynamic pressure term. The aerodynamic coefficients are dependent on the Mach number $M$, the angle-of-attack $\alpha$, and side-slip angle $\beta$. The Mach number is defined below, where $V_a$ is the airspeed and $a$ the local speed of sound, which itself is expressed below, where $\gamma$ is the air's specific heat ratio, $R$ the air's specific gas constant, and $T$ the air temperature, which varies with altitude.

$$\bar{q} = \frac{1}{2} \rho V_A^2 \tag{4.5}$$

$$M = \frac{V_A}{a} \tag{4.6}$$

$$a = \sqrt{\gamma R T} \tag{4.7}$$

The aerodynamic moments can be expressed in the body frame as follows:

$$\mathbf{M^M_{A,B}} = \begin{pmatrix} \mathcal{L} \\ \mathcal{M} \\ \mathcal{N} \end{pmatrix} = \begin{pmatrix} C_l \bar{q} S_{ref} b_{ref} \\ C_m \bar{q} S_{ref} c_{ref} \\ C_n \bar{q} S_{ref} b_{ref} \end{pmatrix} \tag{4.8}$$

In Equation (4.8), $\mathcal{L}$ represent the rolling moment, $\mathcal{M}$ the pitching moment, and $\mathcal{N}$ the yawing moment, with their respective coefficients $C_l$, $C_m$, and $C_n$. The two variables $b_{ref}$ and $c_{ref}$ correspond to aerodynamic reference lengths: for an aircraft, $b_{ref}$ denotes the wingspan while $c_{ref}$ the mean aerodynamic chord. Taking into account the arm $\mathbf{r_{cm}}$ that defines the distance between the centre of mass of the vehicle and the acting point of a force, an arbitrary moment expressed in the B-frame can be described as follows:

$$\mathbf{M^F_{A,B}} = \mathbf{r^b_{cm}} \times \mathbf{F_{A,B}} = \mathbf{r^b_{cm}} \times (\mathbf{C_{B,AA}F_{A,A}}) \tag{4.9}$$

The total aerodynamic moment is thus expressed as the sum of the aerodynamic moment and aerodynamic moment induced by the aerodynamic forces as follows:

$$\mathbf{M_{A,B}} = \mathbf{M^M_{A,B}} + \mathbf{M^F_{A,B}} \tag{4.10}$$

## Gravitational Forces:

Considering the assumptions made in Section 3.2, the gravitational force $F_g$ acting on the atmospheric vehicle and relay spacecraft will be expressed as follows:

$$\mathbf{F_g} = m\mathbf{g} \tag{4.11}$$

Here, $m$ is the mass of the vehicle considered, and $\mathbf{g}$ represents the acceleration vector. This vector $\mathbf{g}$ will simply be modelled as follows, where $\mu$ is Uranus' standard gravitational parameter, and $\mathbf{r}$ represents the vehicle's position vector:

$$\mathbf{g} = \frac{\mu}{||\mathbf{r}||^2}\hat{\mathbf{r}} \tag{4.12}$$

### 4.1.4. Non-Linear Equations of Motion

Newtonian mechanics can be used to describe the motion of a vehicle flying in a planetary atmosphere, as well as one orbiting a planet or performing a fly-by next to it. This kind of motion is based on Newton's Three Laws of Motion, as well as on Galileo's principle of relativity. The motion of a non-elastic body can be divided into two movements: the motion of the centre of mass, and the motion around the centre of mass, also known as translational and rotational motions, respectively.

## Translational Motion

The equations describing a vehicle's translational motion can be derived by applying Newton's second law to the vehicle's motion in an inertial frame as follows (Mooij, 1997b):

$$\mathbf{F_I} = m\frac{d^2\mathbf{r_{cm}}}{dt^2} \tag{4.13}$$

Here, $\mathbf{F_I}$ represents the summation of all external forces acting on the vehicle in the I-frame [N], $m$ is the vehicle's mass [kg], and $\frac{d^2r_{cm}}{dt^2}$ the vehicle's acceleration in the inertial frame [m/s$^2$] with $r_{cm}$ being the vehicle's position vector with respect to the centre of the inertial frame [m]. An additional equation, the kinematic equation, is given below to describe the corresponding change in position with $\mathbf{V_I}$ representing the vehicle's velocity in the inertial frame [m/s]:

$$\frac{d\mathbf{r_{cm}}}{dt} = \mathbf{V_I} \tag{4.14}$$

For a rotating spherical Earth, the dynamic equations of translational motion are given as follows:

$$\begin{aligned}
\dot{V} &= -\frac{D}{m} - g\sin\gamma + \omega_{cb}^2 R\cos\delta(\sin\gamma\cos\delta - \cos\gamma\sin\delta\cos\chi) \\
\dot{\gamma} &= \frac{L\cos\sigma}{mV} - \frac{g}{V}\cos\gamma + 2\omega_{cb}\cos\delta\sin\chi + \frac{V}{R}\cos\gamma + \omega_{cb}^2\frac{R}{V}\cos\delta(\cos\delta\cos\gamma + \sin\gamma\sin\delta\cos\chi) \\
\dot{\chi} &= \frac{L\sin\sigma}{mV\cos\gamma} + 2\omega_{cb}(\sin\delta - \cos\delta\tan\gamma\cos\chi) + \frac{V}{R}\cos\gamma\tan\delta\sin\chi + \omega_{cb}^2\frac{R}{V\cos\gamma}\cos\delta\sin\delta\sin\chi
\end{aligned} \tag{4.15}$$

The associated kinematic relations are given by:

$$\begin{aligned}
\dot{R} &= \dot{h} = V\sin\gamma \\
\dot{\tau} &= \frac{V\sin\chi\cos\gamma}{R\cos\delta} \\
\dot{\delta} &= \frac{V\cos\chi\cos\gamma}{R}
\end{aligned} \tag{4.16}$$

Here, $D$ and $L$ represent the aerodynamic drag and lift forces, $g$ is the gravitational acceleration, and $\omega_{cb}$ the rotational rate of the Earth.

- **Wind Equations**
  As mentioned in Section 3.5, only zonal winds will be considered in this work. When taken into account, the windspeed influences the aerodynamic forces and moments acting on the vehicle as they are dependent on airflow parameters, influencing the trajectory that it follows. The following theory is taken from (Mooij, 1997b): The velocity of the vehicle with respect to Uranus' surface can be expressed as the vectorial summation of the vehicle's velocity with respect to the air and the velocity of the air with respect to the ground:

$$\mathbf{V_{vehicle/ground}} = \mathbf{V_{vehicle/air}} + \mathbf{V_{air/ground}} \Leftrightarrow \mathbf{V_g} = \mathbf{V_a} + \mathbf{V_w} \tag{4.17}$$

If the groundspeed $\mathbf{V_g}$ and wind speed $\mathbf{V_w}$ are known in spherical coordinates, then the airspeed $\mathbf{V_a}$ can be computed as follows:

$$\begin{aligned} V_a &= \sqrt{V_g^2 + V_w^2 - 2V_gV_w\left(\cos\gamma_g\cos\gamma_w\cos\left(\chi_w - \chi_g\right) + \sin\gamma_g\sin\gamma_w\right)} \\ \gamma_a &= \text{asin}\left(\frac{V_g\sin\gamma_g - V_w\sin\gamma_w}{V_a}\right) \\ \chi_a &= \text{atan}\left(\frac{V_g\sin\chi_g\cos\gamma_g - V_w\sin\chi_w\cos\gamma_w}{V_g\cos\chi_g\cos\gamma_g - V_w\cos\chi_w\cos\gamma_w}\right) \end{aligned} \tag{4.18}$$

Here, the subscript $g$ corresponds to groundspeed parameters, and $w$ to wind parameters. The airspeed must be positive and from the second equation, a singularity exists at $\gamma \pm 90°$. The corresponding airspeed-based aerodynamic angles are calculated from the airspeed and groundspeed-based parameters defined above, as well as from the groundspeed-based aerodynamic angles. The transformation matrix $\mathbf{C_{B,V}}$ from vertical to body reference frame is defined as follows, with the three $X$-, $Y$-, and $Z$-axes of a particular reference frame denoted with subscripts $1, 2, 3$ as further explained in Appendix D:

$$\mathbf{C_{B,V}} = \mathbf{C_2}(\alpha_g)\mathbf{C_3}(\beta_g)\mathbf{C_1}(-\sigma_g)\mathbf{C_2}(\gamma_g)\mathbf{C_3}(\chi_g) = \mathbf{C_{B,TA}}\mathbf{C_{TA,V}} \tag{4.19}$$

With the transformation matrix $\mathbf{C_{B,TA}}$ being formulated as follows:

$$\mathbf{C_{B,TA}} = \mathbf{C_2}(\alpha_a)\mathbf{C_3}(-\beta_a)\mathbf{C_1}(-\sigma_a) \tag{4.20}$$

From this expression, we know that $\mathbf{C_{V,TA}} = \mathbf{C_z}(-\chi_a)\mathbf{C_2}(-\gamma_a)$ so we can solve for $\mathbf{C_{B,TA}}$ from $\mathbf{C_{B,TA}} = \mathbf{C_{B,V}}\mathbf{C_{V,TA}}$ yielding the following transformation matrix:

$$\mathbf{C_{B,TA}} = \begin{bmatrix} \cos\alpha_a\cos\beta_a & -\cos\alpha_a\sin\beta_a\cos\sigma_a + \sin\alpha_a\sin\sigma_a & \cos\alpha_a\sin\beta_a\sin\sigma_a + \sin\alpha_a\cos\sigma_a \\ \sin\beta_a & \cos\beta_a\cos\sigma_a & -\cos\beta_a\sin\sigma_a \\ \sin\alpha_a\cos\beta_a & -\sin\alpha_a\sin\beta_a\cos\sigma_a + \cos\alpha_a\sin\sigma_a & \sin\alpha_a\sin\beta_a\sin\sigma_a + \cos\alpha_a\cos\sigma_a \end{bmatrix} \tag{4.21}$$

From this transformation matrix, the airspeed-based aerodynamic angles can be derived as follows:

$$\alpha_a = \text{atan}\left(\frac{\mathbf{C_{B,TA}}(3,1)}{\mathbf{C_{B,TA}}(1,1)}\right), \quad \beta_a = \text{asin}\left(\mathbf{C_{B,TA}}(2,1)\right), \quad \sigma_a = \text{atan}\left(-\frac{\mathbf{C_{B,TA}}(2,3)}{\mathbf{C_{B,TA}}(2,2)}\right) \tag{4.22}$$

These are defined within the following bounds: $\alpha_a = [-\frac{\pi}{2}, \frac{\pi}{2}]$, $\beta_a = [-\pi, \pi]$, $\sigma_a = [-\pi, \pi]$.

## Rotational Motion

The rotational equations of motion can be formulated with help of the Euler equations. Their non-linear equations are as follows:

$$\frac{d\boldsymbol{\omega}}{dt} = \mathbf{I}^{-1}\left(\tilde{\mathbf{M}}_{\mathbf{cm}} - \boldsymbol{\omega} \times \mathbf{I}\boldsymbol{\omega}\right) \tag{4.23}$$

In Equation (4.23), the variables are defined as follows: $\tilde{\mathbf{M}}_{\mathbf{cm}} = \left(M_x, M_y, M_z\right)^T$ is the sum of external, Coriolis, and relative moments about the c.o.m. along the body axes, $\boldsymbol{\omega} = (p, q, r)^T$ is the rotation vector of the body frame with respect to the inertial frame along the body axes, and $I$ represents the inertia tensor of the vehicle referenced to the body frame expressed as follows:

$$\mathbf{I} = \begin{bmatrix} I_{xx} & -I_{xy} & -I_{xz} \\ -I_{xy} & I_{yy} & -I_{yz} \\ -I_{xz} & -I_{yz} & I_{zz} \end{bmatrix} \tag{4.24}$$

The equations of motion are linearised for the definition of their state-space form for the control module. The linearisation process described by Mooij (1997a) is applied.

## 4.2. Orbital Mechanics

Kepler's First Law states that the orbits of celestial objects are conic sections (Wertz, 2001). This means that they represent figures produced by the intersection of a plane and a cone, or any quadratic function. This enables the possibility of yielding a circular orbit, an elliptic one, a parabolic one, or a hyperbolic one. The orbital elements used to describe such orbits are defined in Section 4.1.2.
All orbits can be expressed with the Vis-Viva equation (Wertz, 2001):

$$\epsilon = \frac{V^2}{2} - \frac{\mu}{r} = -\frac{\mu}{2a} \tag{4.25}$$

Here, $\epsilon$ represents the total specific energy, $\frac{V^2}{2}$ is the spacecraft's kinetic energy with $V$ being the relative velocity, and $\frac{\mu}{r}$ is the spacecraft's potential energy with $\mu$ being the central body's standard gravitational parameter and $r$ the instantaneous distance separating the spacecraft from the central body. For a circular or elliptic orbit the following relations are true where $T$ is the orbital period, $r$ is the radius, $r_p$ is the periapsis distance, $r_a$ is the apoapsis distance, and $e$ is the eccentricity of the orbit:

$$T = 2\pi\sqrt{\frac{a^3}{\mu}} \tag{4.26}$$

$$r = \frac{a(1-e^2)}{1+e\cos\theta} \quad ; \quad r_p = a(1-e) \quad ; \quad r_a = a(1+e) \tag{4.27}$$

A circular orbit has zero eccentricity and its semi-major axis is a chosen radius. Its total energy is negative. Equation (4.25) can be used to determine the spacecraft's circular velocity $V_c$ along such an orbit by setting the semi-major axis equal to the orbit's radius $a = R$:

$$V_c = \sqrt{\frac{\mu}{R}} \tag{4.28}$$

Knowing, the orbit's radius and the spacecraft's circular velocity and assuming it to be constant can thus enable to calculate the communication window available for the atmospheric vehicle to send its scientific data to the spacecraft, and the spacecraft to relay it back to the Earth.

## 4.3. Verification: Flight Dynamics

The equations of motion and their propagation are considered verified, as they were adapted from the verified model of Mooij and Ellenbroek (2011). The steps taken towards the verification of the wind model are presented below.

### 4.3.1. Wind Model

The wind model used to represent zonal winds on Uranus was verified in 3 DoF by running a test simulation and comparing the quantities on which the wind force has an influence, namely airspeed, flight-path angle, and heading angle. When the equatorial glider is flying at a quasi-constant latitude of 17.5 °, it experiences a wind-speed with magnitude of 6.2103 m/s.

Equation (4.18) was used with the following initial conditions: $V_g$ = 52.8 m/s, $\gamma_g = -1.25°$, $\chi_g = -90°$, $V_w$ = 6.2103 m/s, $\gamma_w = 0°$, $\chi_w = -90°$ to yield analytical airspeed, flight-path angle, and heading angle. The simulator's wind model's was then used with the same initial conditions. Results are shown in Table 4.1. It can be seen here, that for the simulation's initial conditions at $t = 0$ s, the analytical and simulated airspeed parameters are very similar. The analytically calculated initial conditions thus correspond to the simulated ones when the wind model is included in the simulator. Conditions at $t = 1,000$ s of simulation were then taken to see if these results would still compare later in the simulation. The ground-speed parameters at that time stamp are as follows: $V_g$ = 52.0622596 m/s, $\gamma_g = -1.08283055°$, $\chi_g = -90.00080846$. The same wind parameters as previously mentioned are used. Analytical and simulated results are listed in Table 4.1 as well. When comparing these values, it can be seen that they are very similar as well. Following these tests, the implemented wind model is considered to be verified.

**Table 4.1:** Comparison of analytical and simulated wind-speed parameters for verification of wind model.

| **Simulation time** | | $t = 0$ **s** | $t = 1,000$ **s** |
|---|---|---|---|
| Ground-speed velocity parameters | $V_g$ (m/s) | 52.8 | 52.0622596 |
| | $\gamma_g$ (°) | -1.25 | -1.08283055 |
| | $\chi_g$ (°) | -90.0 | -90.00080846 |
| Wind-speed parameters | $V_w$ (m/s) | 6.2103 | 6.2103 |
| | $\gamma_w$ (°) | 0.0 | 0.0 |
| | $\chi_w$ (°) | -90.0 | 90.0 |
| Analytical airspeed parameters | $V_{A,ana}$ (m/s) | 59.00899158 | 58.27158277 |
| | $\gamma_{A,ana}$ (°) | -1.11845592 | -0.96743430 |
| | $\chi_{A,ana}$ (°) | -90.0 | -90.00072229 |
| Simulated airspeed parameters | $V_{A,sim}$ (m/s) | 59.00899124 | 58.27158277 |
| | $\gamma_{A,sim}$ (°) | -1.11845596 | -0.96743430 |
| | $\chi_{A,sim}$ (°) | -90.00000250 | -90.00072229 |

# 5
# Vehicle Design Cycle

This chapter will present design elements of both the atmospheric vehicles and the spacecraft orbiting Uranus. Section 5.1 presents the choice and scaling of an atmospheric reference vehicle, the generation of its aerodynamic coefficients and their verification, as well as the gliders' reference trajectory design. Section 5.2 presents the orbiter's mass budget and its reference trajectory design. Finally, the communication windows between the different vehicles will be investigated in Section 5.3 with aim of having the orbiter perform a continuous trajectory tracking of the atmospheric vehicles, as well as to relay the measured scientific data to an Earth ground station.

## 5.1. Reference Vehicle

The conclusion of the discussion made in Section 2.6 was that a multiple un-propelled winged vehicles concept was chosen for the mission at hand. Moreover, it was mentioned in Section 3.7 that it would be interesting and relevant to the mission's science objectives to study two regions of the planet's atmosphere: the equatorial and polar domains, both being probed from 1 bar to 100 bar pressure levels. This means that two vehicles would be needed to achieve this.

### 5.1.1. Choice of Reference Vehicle

According to the constraints listed in Section 5.1, a reference glider was chosen from literature to serve as the in-situ platform for the simulations of this thesis work. This vehicle is the GL-1 glider from Amalia et al. (2018) and Pratama (2015). A first attempt in the generation of the vehicle's aerodynamic coefficients was done with the 3D vortex lattice program Tornado (Melin, 2001). This method was quickly discarded however, due to the generation of induced drag only, and the complicated aspect of the deflected configurations' coefficients. The software XFLR5 (Deperrois, 2003) was later chosen as it satisfied all the requirements of the aerodynamic coefficients' generation. This software is limited to low Reynolds number applications ($10^5 - 10^9$)[1], which is the case for this mission ($4.71 \cdot 10^6 - 7.66 \cdot 10^6$). Its 3D application also makes the assumption of inviscid flow and merely interpolates 2D viscous drag from local wing lift, which leads to an overall underestimation of total drag. More limitations and shortcomings of this software include the use of flat quad panels to approximate the surfaces' shape which leads to an error of small magnitude, the modelling of a flat wake which can lead to an over-estimation of wing lift (the error can be in the order of magnitude of 1 to 10%), and incomplete modelling of body and wing interactions for which reason it is recommended to omit the fuselage from any analysis in XFLR5. These are further explained in Deperrois (2019).

The vehicle and the reproduction of its geometry can be seen in Figure 5.1 and Figure 5.2. The presence of a fuselage yielded very small changes in the aerodynamic coefficients (around 1%), so it was chosen to be neglected, as suggested in the XFLR5 documentation. Indeed, the intersection between body-lifting surfaces is not fully modelled in XFLR5, so bodies should preferably be omitted from analyses. A static margin (distance between centre of gravity and neutral point) of 15 % of the mean aerodynamic chord was included to increase the aircraft's stability. This GL-1 glider was not originally designed with the aim of being folded to fit in a descent probe, but it was assumed that by folding its wings and its fuselage, it would fit in a descent probe such as the Mars Science Laboratory (MSL) entry vehicle, which has an interior space of 3.7 m in diameter and 1.2 m in height. The chosen Atlas V541 launch vehicle has a capacity of 5.4 m in diameter, which allows

[1] `https://sourceforge.net/p/xflr5/discussion/679396/thread/79403cc6aa/?limit=25`, accessed on 03/05/2022.

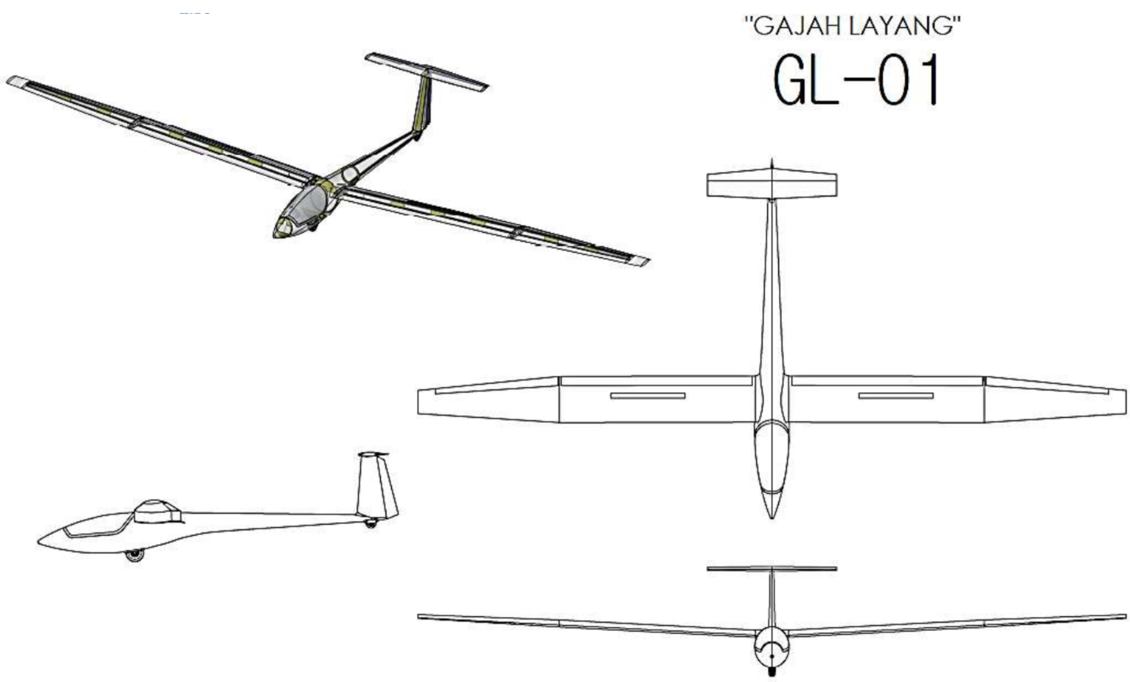


**Figure 5.1:** Three view of GL-1 glider drawing (Pratama, 2015).

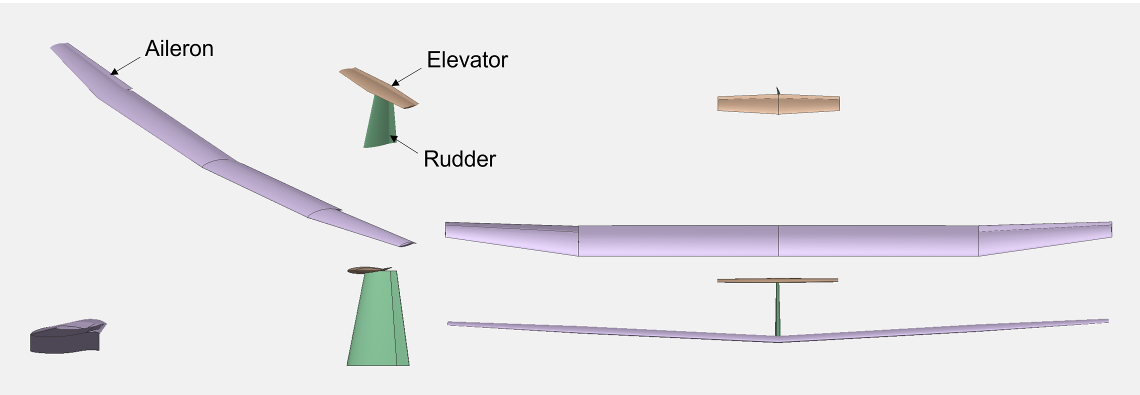


**Figure 5.2:** GL-1 glider reproduced with XFLR5.

for a larger descent probe than the MSL. By folding both the vehicle's wings and fuselage three times, the folded configuration could fit in a 4 m wide and 1.2 m high descent probe.

The GL-1 glider possesses three types of control surfaces: a right and left aileron on both sections of its main wings, an elevator on its horizontal tail, and a rudder on its vertical tail. The ailerons deflect asymmetrically, while the elevator's flaps deflect symmetrically. It was chosen to include ailerons on the outer partitions of the main wings only, to have one type of coefficient increment from the ailerons' deflection. Having ailerons on the outer portion of a glider's main wing is also what is traditionally opted for in glider design. The GL-1 design was scaled down, to yield a more realistic wing loading $W/S$ in Uranus' atmosphere.
To achieve this, the wing loading of all documented gliders with necessary information from the year 1980 until 2021 was averaged[2], to yield $W/S_{avg} = 224.482$ N/m$^2$. This comes very close to the original GL-1 wing loading of $W/S_{GL-1} = 221.75$ N/m$^2$ when flying in Earth's atmosphere, and considering the glider's empty mass of $m_{empty} = 190$ kg and a maximum payload mass of 110 kg, which consists of a pilot and their parachute. The glider's dimensions were then scaled down according to the change in wing loading, by keeping the empty mass constant. This yielded properties are mentioned in Table 5.1. The large final wing span of $b = 12$ m corresponds to the 12 m wing span of the Large Uranus Glider designed in the work of LeBeau et al. (2015).

[2] `https://www.j2mcl-planeurs.net/dbj2mcl/planeurs-index_0.php`, accessed on 16/04/2021.

**Table 5.1:** Scaled down GL-01 glider properties.

| | | | |
|---|---|---|---|
| Empty mass [kg] | 190 | Aspect ratio | 17.0 |
| Payload mass [kg] | 25 | Span $b_{ref}$ [m] | 12.0 |
| Wing loading [N/m$^2$] | 224.3588 | Main wing airfoil | FX62-K-153/20 |
| Wing surface area $S_{ref}$ [m$^2$] | 8.479 | Vertical & horizontal tail airfoil | FX71-L-150/25 |
| Angle-of-attack range [°] | [-8.0,9.5] | $\alpha_{opt}$ for maximum range [°] | 2.3 |
| Root chord $c_{ref}$ [m] | 0.785 | $I_{xx}$, $I_{yy}$, $I_{zz}$ [kg/m$^2$] | 625.3693, 218.2010, 818.9555 |

**Table 5.2:** Range of parameters explored in XFLR5 to generate the vehicle's aerodynamic coefficients.

| | |
|---|---|
| Altitude [km] | [0, -100, -200, -300, -375] |
| Velocity [m/s] | [9, 25, 50, 70] |
| Angle-of-attack [°] | (-8, 9.5, 0.5) for clean configuration; (-0.5, 3.5, 0.5) for deflected configuration |
| Aileron deflection [°] | [-25, -20, -15, -5, 0, 5, 15, 20, 25] |
| Rudder deflection [°] | [-25, -20, -15, -5, 0, 5, 15, 20, 25] |
| Elevator deflection [°] | [-30, -20, -15, -5, 0, 5, 15, 20, 30] |

**Table 5.3:** Dependency of parameters used for interpolation of aerodynamic coefficients Lookup tables.

| | $C_L$ | $C_D$ | $C_S$ | $C_{S_\beta}$ | $C_l$ | $C_{l_\beta}$ | $C_m$ | $C_n$ | $C_{n_\beta}$ |
|---|---|---|---|---|---|---|---|---|---|
| $\alpha$ | ✓ | ✓ | ✓ | ✓ | ✓ | ✓ | ✓ | ✓ | ✓ |
| $V$ | | ✓ | | | | | ✓ | ✓ | |
| $h$ | | ✓ | | | | | ✓ | ✓ | |

### 5.1.2. Generation of Aerodynamic Coefficients

Concerning the generation of the vehicle's aerodynamic coefficients, two configurations were considered: a so-called *clean configuration* with zero control surface deflection, and a *deflected configuration* where each control surface is gradually deflected while keeping all other deflections null. The aerodynamics are assumed to be decoupled and the contribution of each control surface is added together to yield the total aerodynamic coefficients at all times of the flight. The stored aerodynamic coefficients were the following: the lift force coefficient $C_L$, the drag force coefficient $C_D$, the side force coefficient $C_S$, the pitching moment coefficient $C_m$, the rolling moment coefficient $C_l$, and the yawing moment coefficient $C_n$. The pitching, rolling, and yawing moment coefficients are also computed for two values of side-slip angles, and their derivatives are calculated and multiplied by the current side-slip angle during the simulations. The total pitching, rolling, and yawing moment coefficients are obtained by adding this $\beta$-gradient contribution to the clean configuration contribution.

The range of parameters explored in the generation of the aerodynamic coefficients is shown in Table 5.2. The choice of explored ranges is explained here. Concerning the altitude, increments of 100 km were taken, except for the last interval which is of 75 km until the final altitude of $-400$ km. These intervals were simply chosen to explore the travelled altitude. To determine the range of velocities explored, a fixed lift analysis was run with XFLR5 at different locations of the gliders' flight, and thus for different atmospheric conditions. The velocity curve over time was then plotted and strategic increments were selected for the generation of the coefficients, such that interpolation between the increments would later yield accurate values. Concerning the control surface deflection angles, the minimum and maximum values were determined from GL-1 literature, and the increments were also strategically selected, by looking at the behaviour of the coefficients over the selected range. It is important to note that the aerodynamic coefficients were generated for a nominal elevator deflection of $-1.5°$, for the glider to be longitudinally stable when in clean configuration ($C_{m_0} > 0$).

The data is stored in Lookup tables in Simulink and linear interpolation is performed to retrieve the aerodynamic coefficients corresponding to the current flight conditions during the simulations. Linear interpolation is used because the data points are neither sparse nor rapidly changing. The behaviour of the lift coefficient with respect to the parameters listed in Table 5.2 was found to be linear, with a gradient of 0.1022 /° of angle-of-attack. The dependency of each aerodynamic coefficient on angle-of-attack, velocity, and altitude is summarised in Table 5.3, for the vehicle's clean configuration. In deflected configuration, all aerodynamic coefficients depend on the deflection angles of all three control surfaces as well.

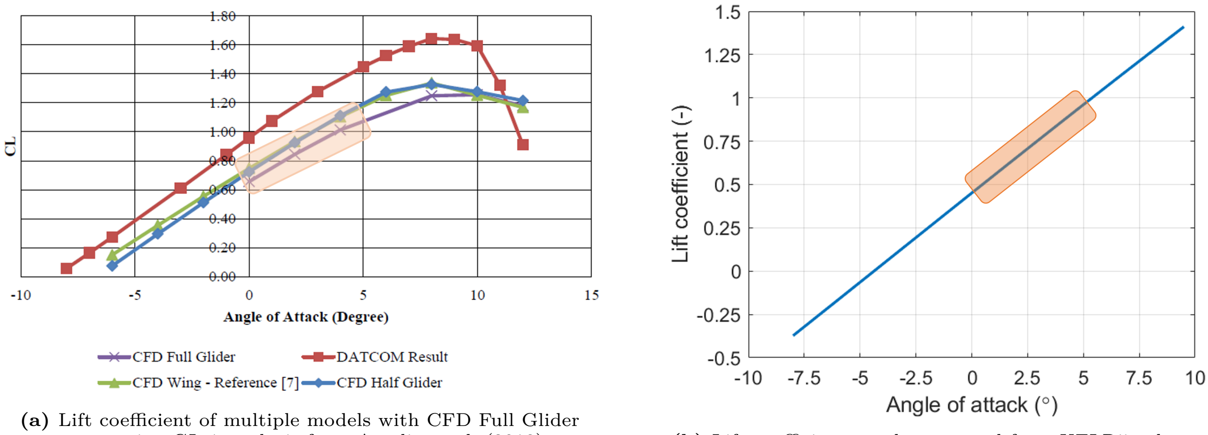


**(a)** Lift coefficient of multiple models with CFD Full Glider representing GL-1 analysis from Amalia et al. (2018).

**(b)** Lift coefficient graph generated from XFLR5 values.

**Figure 5.3:** Lift coefficient comparison between values from literature and those generated with XFLR5.

### 5.1.3. Verification: Aerodynamic Coefficients

The aerodynamic coefficients generated with XFLR5 were compared to the ones provided in the work of Amalia et al. (2018) and the comparative graphs shown in Figure 5.3 were yielded for the lift coefficient. The orange boxes represent the parameter space where both models result in similar lift coefficient behaviours for the same angles of attack. In Figure 5.3a, the curve that should be looked at is the one labeled as “CFD Full Glider”, as the “CFD Wing” and “CFD Half Glider” curves only represent parts of the vehicle, and the “DATCOM Result” curve corresponds to a less accurate estimate of the glider’s aerodynamic coefficient, due to it being based on empirical data. It was found that below an angle-of-attack of $\alpha = -4°$, the lift coefficient generated with XLFR5 was negative.

As can be seen in Figure 5.3, the lift coefficient values generated with XFLR5 do not lead to a stalling behaviour. This is a distinctiveness of the software. It can, however, be verified that the values have a similar behaviour for a certain range of angle-of-attack: from $\alpha = 0°$ to nearly $\alpha = 5°$, which contains the range of angles of attack explored during the simulation: from $\alpha = 0°$ to $\alpha = 1.5°$. These low angle-of-attack values ensure that the vehicle stays far away from the angles of attack at which stall could occur, as these are not generated by XFLR5. As described in Section 5.1.4, the optimal angle-of-attack at which the gliders should stay during the majority of their flights is $\alpha = 1.5°$, to stay in maximum range configuration (at $\left(\frac{C_L}{C_D}\right)_{max}$).

It must be noted that the generated aerodynamic coefficients’ values do not exactly match the graphs provided by Amalia et al. (2018), even when generated for the same velocity and atmospheric density values. The XFLR5 lift coefficients are slightly lower (by $0.15 - 0.2$), while the XFLR5 drag coefficients have even lower values (around 4 times lower). These differences are attributed to the different software used: Amalia et al. (2018) performed a Computational Fluid Dynamics (CFD) analysis on a full glider meshing, including its fuselage and a $k - \epsilon$ turbulence model. This turbulence model is the most commonly used model to simulate mean flow characteristics for turbulent flow conditions. The analysis performed in XFLR5 did not include any turbulence model, which leads to different aerodynamic coefficients, and especially much lower drag coefficients.

### 5.1.4. Gliders: Reference Trajectory Design

The gliders’ initial conditions were chosen with aim to minimise the flight’s oscillations at the beginning of the simulation, as well as to be able to fulfil the mission’s scientific objectives. It was mentioned in Section 3.7 that the equatorial glider would have to be initially placed at a longitude higher than 10.5°, where the day/night terminator will be at arrival in year 2043, in order to explore the night side of the planet (with the polar glider already exploring the day side of the planet). After simulating the equatorial glider’s flight with the initial conditions shown in Table 5.4, it was found that it would travel around 45° of longitudes until it reaches the end-of-mission altitude of $-375$ km. The equatorial glider can thus travel around 45° of longitude between longitudes of 10.5° and $-169.5°$ to stay on the planet’s night side. To avoid the transition regions between day and night sides, the middle part of that range is chosen, yielding an initial longitude of 70° and letting the glider travel to around 25° of longitude. The polar glider’s initial longitude does not matter, as it will rotate multiple times around the planet, at constant latitude of 89° (see Section 3.7 for the choice of target latitudes) and thus always stay on the planet’s day side. For the equatorial glider to fly retrograde with respect to Uranus’ rotation,

**Table 5.4:** Initial conditions of gliders' flight.

| | |
|---|---|
| Altitude [km] | 0.0 |
| Velocity [m/s] | 52.8 |
| Longitude and latitude ($\tau$, $\delta$) [°] | Equatorial glider: (-70.0, 17.5); Polar glider: (0.0, 89.0) |
| Flight-path angle $\gamma$ [°] | $-1.25°$ |
| Heading angle $\chi$ [°] | Equatorial glider: $-90$; Polar glider: $+90$ |
| Aerodynamic angles ($\alpha$, $\beta$, $\sigma$) [°] | (0.0, 0.0, 0.0) |

its initial heading angle is set to $\chi = -90°$ and kept constant for the whole flight duration. Similarly, the polar glider's initial heading angle is set to $\chi = +90°$ for it to fly in prograde direction, to always experience tailwind.

The rest of the trajectory was optimised for maximum range to reach the final altitude of $-375$ km (100 bar pressure level) by travelling the longest distance, to explore as much as possible, while keeping each glider's latitude constant. To do this, an optimal angle-of-attack of 1.5° was found at the $(C_L/C_D)_{max}$ condition of the flight, at all altitudes. The velocity and flight-path angle profiles were retrieved and stored at every 25 km by simulating the flight of one of the gliders at a forced constant heading angle. These profiles will then be used by the guidance module.

## Entry Corridor Analysis

An entry corridor analysis was performed to check whether the designed reference trajectory respects thermal and mechanical loads allowed by the vehicle, as well as equilibrium glide conditions which are seen as the theoretical ceiling under which no skipping flight will occur. A velocity-altitude plot is constructed, with the equilibrium glide constraint velocity $V_{eq}$, the thermal load constraint velocity $V_{q,c}$, and the mechanical load constraint velocity $V_g$ being calculated as follows:

$$V_{eq} = \sqrt{\frac{1}{\frac{\rho C_L S_{ref}}{2mg} + \frac{1}{V_c^2}}} \tag{5.1}$$

$$V_{q,c} = \frac{V_c}{\left(\frac{\rho}{\rho_0}^{\frac{1}{n-1}} \cdot \frac{c^*}{q_{c,max} R_n^n}\right)^{\frac{1}{m}}} \tag{5.2}$$

$$V_g = \sqrt{\frac{2mg \cdot n_{g,max}}{\rho S_{ref}\sqrt{C_D^2 + C_L^2}}} \tag{5.3}$$

Here, $V_c$ corresponds to the circular velocity calculated with $V_c = \sqrt{gR}$, and the other variables are as follows: $c^*$ is a constant coming from Chapman's equation taken as $2 \cdot 10^8\sqrt{m}$ here to represent the worst case scenario, $n$ is the value which determines a laminar ($n = 0.5$) or a turbulent ($n = 0.2$) boundary layer, $m$ is an empirical constant ($m = 3$) which was set here to represent a gas with viscosity proportional to the square root of the atmospheric temperature as is the case for Uranus as seen in Figure 5.4a, $R_n$ is the vehicle's nose radius measured as 0.11494 m from the designed fuselage in XFLR5, $q_{c,max}$ is the maximum thermal flux experienced which was defined at 100 kW/m$^2$, $n_{g,max}$ is the maximum g-load experienced which was defined as $5.6 \cdot g_{Uranus}$ as transformed from the Earth-specific maximum g-load constrained by the chosen reference vehicle. Both $n$ and $m$ are atmosphere dependent. Earth-specific values are used here but using Uranus-specific ones should increase the results' accuracy and is left as a recommendation for future work because such values are unknown at the moment.

The low value of maximum thermal load shows that this factor is not a driving constraint in the design of the entry corridor, which shows that the vehicle is not in need of a thermal protection system. The plotted entry corridor is shown in Figure 5.4b. It can be seen that neither the thermal nor the g-load constraint come close to the followed trajectory. This was to be expected as the gliders are simply gliding in Uranus' atmosphere, and not experiencing extreme loads as a descent probe would during atmospheric entry. This analysis should, however, be performed for the ballistic entry of the two probes delivering each glider to their target latitudes. However, this analysis is out of the scope of this thesis. It can be seen that the followed trajectory is very close to the equilibrium glide condition. It remains below the constraint, which ensures that no skipping flight will occur.

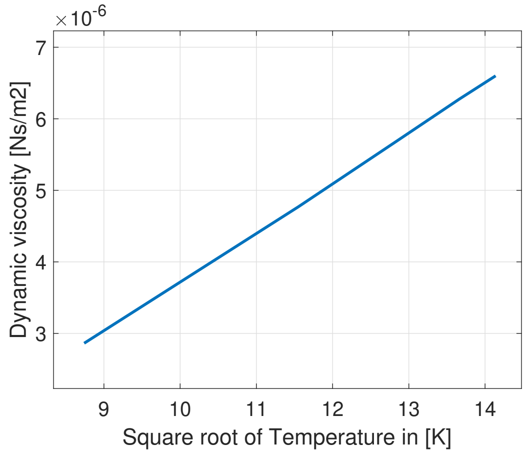


**(a)** Uranus' dynamic viscosity versus square root of temperature.

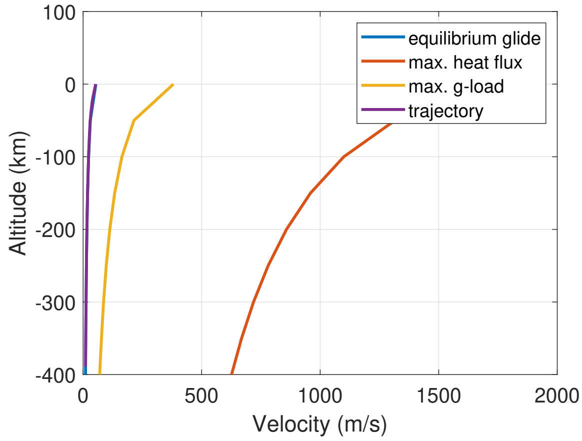


**(b)** Entry corridor of gliders' flight inside Uranus' atmosphere.

**Figure 5.4:** Atmospheric dynamic viscosity and temperature relation, and entry corridor for the gliders' flight.

## 5.2. Orbiter

The orbiter has multiple objectives during the mission. Firstly, it has to carry and deliver the two descent probes containing the equatorial and polar gliders to their target initial latitudes and longitudes. Secondly, it has to be in an orbit where continuous line-of-sight is possible with the two gliders, for trajectory tracking and communications purposes. Lastly, it should be able to communicate the gliders' scientific measurements to Earth.

### 5.2.1. Mass Budget

A mass budget was established to make sure that the two gliders and their respective descent probes would fit in the Atlas V541 suggested by Hofstadter et al. (2019). This launch vehicle has an injected mass capacity of 4,450 kg to launch C3 (launch characteristic energy) of 11.9 km$^2$/s$^2$.

- **Orbiter:** Hofstadter et al. (2019) mention an orbiter dry mass of 1,220.0 kg including the 36.7 kg of scientific instruments on-board the orbiter, consisting of a narrow angle camera, a magnetometer, and a Doppler imager. The following elements contribute to the orbiter's mass: command and data handling (21.6 kg), power (216.6 kg), telecommunications (59.4 kg), structures (451.1 kg), the harness system (86.3 kg), the thermal subsystem (113.1 kg), propulsion (171.7 kg), and guidance navigation and control modules (63.5 kg). Specific contingency percentages are applied to each of these elements to yield a total orbiter dry mass of 1,442.3 kg. A system margin of 224.9 kg is then added to that, yielding a total dry mass of 1,667.2 kg. Hofstadter et al. (2019) then recommend a propellant mass of 2,357.0 kg, which results in the orbiter's total wet mass to 4,024.2 kg.
- **Descent probes:** Concerning the descent probes, Hofstadter et al. (2019) mention a dry mass of 90 kg for a 1.2 m diameter, 45° sphere conic structure. To yield a 4 m diameter structure as mentioned in Section 5.1.1, this value is multiplied by 3 to yield a 270.7 kg structure.
- **Gliders:** Amalia et al. (2018) mentions a dry mass of 190 kg for the GL-1 glider. Taking into account the 25 kg of payload mass, this yields a total glider mass of 215 kg.

More information on the orbiter, descent probes, and gliders' mass are available in the work of Hofstadter et al. (2019) and Amalia et al. (2018). Elements related to the mission's cost budget are also mentioned there.

So in summary, adding together the orbiter's wet mass, two probe structures, and two gliders, with each vehicle containing their respective payload suite, a total mission mass of 4,995.6 kg is yielded. This value is 545.6 g higher than the allowable mass of 4,450 kg on-board the Atlas V541 payload fairing. Two solutions exist to this problem: either another launch vehicle is chosen (for example the Atlas V HLV). The choice of launch vehicle has no other influence on the mission analysis. The launch window might change, but as long as the launch occurs in 2031, then the mission analysis of this thesis is still applicable.

### 5.2.2. Orbiters: Reference Trajectory Design

A circular orbit was chosen for the carrier and relay spacecraft of this mission. This choice was implemented to respond to the criteria of having continuous trajectory tracking of both gliders. In terms of telecommunications, Sayanagi et al. (2020) suggest to have the atmospheric vehicle remain within a 30° communication cone and 100,000 km distance of the relay spacecraft, as well as in the relay spacecraft's antenna beam footprint, while the planet is rotating. A spacecraft in a circular, equatorial, and synchronous orbit can meet these trajectory tracking and telecommunication criteria. The orbiter's trajectory is designed to be synchronous with the equatorial glider's expected path.

To do so, first the expected number of degrees of longitude $\tau_{gl,exp}$ covered by the equatorial glider, as well as the expected time of flight $t_{gl,exp}$ are retrieved from simulating the glider's flight from $h = 0$ km to $h = -375$ km altitude. Knowing these two quantities, as well as the sidereal rotation period of Uranus of $T_{u,rot} = -17.24$ h, the number of degrees of longitude travelled by the orbiter $\tau_{orb}$ can be computed as follows, with $\tau_U = 360°$:

$$\tau_{orb} = \tau_U - \tau_{gl,exp} \cdot \frac{T_{u,rot}}{t_{gl,exp}} \tag{5.4}$$

The period of the orbiter's circular, equatorial, and glider-synchronous orbital period can then be computed following:

$$T_{orb} = \frac{2\pi T_{u,rot}}{\tau_{orb}} \tag{5.5}$$

Following this, the orbiter's semi-major axis is computed with Equation (4.26). With a longitude of 89°, the polar glider is nearly at the north pole of Uranus, and so it is assumed that an equatorial orbiter can achieve radio signal with it, as the planet's curvature is negligible for 1° of latitude.

The different orbit manoeuvres necessary for the orbiter to reach target areas above Uranus is kept as a recommendation for future work. Values for an insertion $\Delta V$, an entry flight-path angle, velocity and altitude of the descent probes, as well as timeline guidelines for the sequence of operations to be followed by the orbiter are available in the work of Hofstadter et al. (2017), for Mission Option 5.

## 5.3. Communication Window

A challenging aspect for telecommunications is Uranus' atmospheric opacity, which increases exponentially with depth, especially beyond the 15 bar pressure level (Cavalié et al., 2020). It is a reason for having a relay spacecraft operate as close to the atmospheric vehicle as possible during its measurement and telecommunication phase. Cavalié et al. (2020) suggest to use optical laser instead of radio frequencies for communication as a possibility to overcome the opacity issue. However, considering the very high pointing accuracy that such a method requires (around $\pm 1°$), and the fact that the gliders' state variables are estimated with yet an unknown accuracy, the implementation of this telecommunication system is deemed unfeasible. The communication instruments suggested in the work of Hofstadter et al. (2017) will thus be considered. They consist of two X-band and Ka-band radio transponders, two UHF receivers, and antennas that can support these types of communications: X-band and Ka-band high, medium, and low gain antennas, as well as an UHF patch array. Finally, as suggested by Sayanagi et al. (2020), the orbiter should stay within a 30° communication cone, and a 100,000 km distance from the gliders, for radio transmission to occur. This is achieved with the circular orbit described in Section 5.2.2.

Concerning the mission's data rate of 1,493 bps mentioned in Table 2.2, and the orbiter's uplink and downlink respective data rates of 3 Mbps and 15,000 bps (Hofstadter et al., 2017), the communication window duration can be determined once both gliders' flight times are known. Considering that the measurement phase lasts for the whole flight duration $t_{flight}$, starting at the 1 bar pressure level, and finishing at 100 bar of pressure, the communication window time $t_{com}$ is calculated as follows for both uplink and downlink communications:

$$t_{com,uplink} = \frac{(t_{flight} \cdot 1493)}{3 \cdot 10^6} \quad ; \quad t_{com,downlink} = \frac{(t_{flight} \cdot 1493)}{15000} \tag{5.6}$$

Figure 5.5 illustrates how the spacecraft orbiting Uranus would be in continuous line-of-sight with the two gliders, by orbiting a circular, equatorial, and synchronous trajectory with the equatorial glider. As seen here, the planet's north pole will be fully illuminated at arrival in 2043, which means that the polar glider's initial longitude has no importance. For continuous line-of-sight to occur between orbiter and gliders, the curvature of

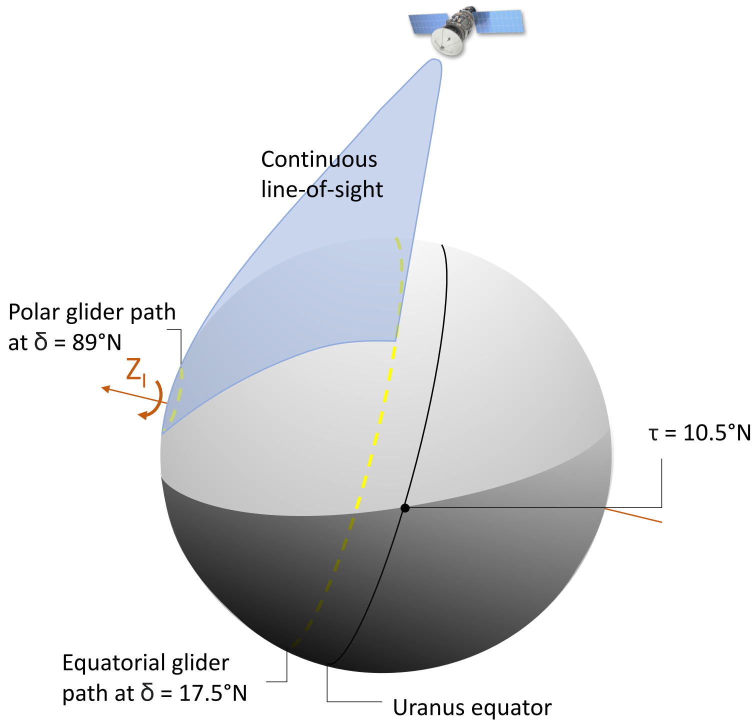


**Figure 5.5:** Communication window for continuous trajectory tracking of both gliders by the orbiter.

Uranus' pole at $\delta = 89°$ is neglected, meaning that the polar glider is assumed to be visible by the orbiter even when on the other side of the pole, as seen in Figure 5.5, where the continuous line-of-sight window extends to the left of the planet's Z-axis. This assumption is reasonable as the vertical distance along the planet's Z-axis from latitude $\delta = 89°$ to the north pole corresponds to $d = 3.867$ km, calculated with the following:

$$d = R_{U,m} - R_{U,m} \sin \delta \tag{5.7}$$

# 6

# Guidance and Control Design

The study of Guidance, Navigation, and Control (GNC) is essential to this research, to be able to follow the atmospheric vehicle's trajectory and relate the measured scientific data to a spatial and temporal reference. To do so, and to stay within the time constraint of this work, **the focus will be on navigation of the atmospheric vehicles during this thesis**. Guidance and control will be modelled with simple models such as a Linear Quadratic Regulator (LQR). The relay spacecraft's GNC is not considered here. Section 6.1 will provide information on the fundamental concepts of GNC. Section 6.2 will provide guidance and control system and modelling requirements. Then, Section 6.3 will detail the guidance aspect of the mission and Section 6.4 will give details on the control module. Verification steps for both the guidance and control modules are explained at the end of their respective sections.

## 6.1. Fundamental Concepts of GNC

During the mission analysis and design phase of an atmospheric mission, a reference trajectory is generated for the atmospheric vehicle, starting from specified initial conditions, and satisfying constraints such as maximal allowable thermal and deceleration loads. It is then verified, whether the vehicle can actually execute the trajectory's required manoeuvres without violating any constraints. Finally, encountering unforeseen disturbances, which force the vehicle away from its nominal path should not disable it from fulfilling its mission. To ensure the successful accomplishment of these actions, the vehicle should posses a GNC system. The individual terms of GNC are defined below:

- **Guidance:** Its function is to define the current or future estimated state. It answers the question "Where am I going?".
- **Navigation:** Its function is to determine the current or future estimated state from the measured state. It answers the question "Where am I?".
- **Control:** Its function is to derive control commands so as to match the current or future estimated state with the desired state. It answers the question "How do I get there?".

A typical GNC system architecture is shown in Figure 6.1. A reference trajectory is defined in the Mission Manager block and fed to the Guidance Logic block. Guidance commands such as angle-of-attack and bank

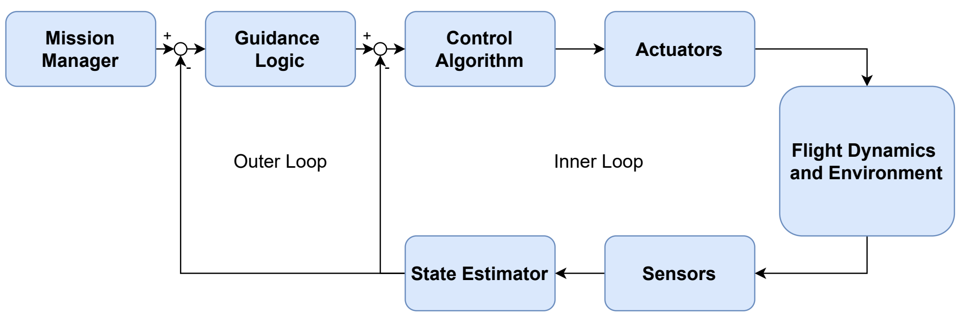


**Figure 6.1:** Guidance, Navigation, and Control system architecture.

angle increments, as well as trimming commands such as elevator deflections are computed by the guidance block and passed to the Control Algorithm block, which converts them to control surface deflection commands. The guidance commands are calculated by comparing the reference trajectory from the Mission Manager to the estimated state from the navigation module's State Estimator. The commands outputted from the Control Algorithm are fed to the Actuators, for them to execute the necessary control surface deflections in this case, to bring the vehicle to the defined reference trajectory. Control forces and moments are yielded and fed to the Flight Dynamics and Environment block, which contains the vehicle's dynamics and atmospheric models. The output of this block is the vehicle's true state, which is inputted to the Sensors block to measure the atmospheric and dynamical quantities that will be passed as inputs to the State Estimator. The inner and outer loops seen in Figure 6.1 can also be referred to as the control loop, which is typically associated with the stability of the complete system, and the guidance loop.

A typical development process of the GNC modules involves first developing the guidance logic. Guidance gains are computed and tuned, and nominal tests are run to check whether the block behaves as intended. In this case, the tracking guidance should output angle-of-attack and bank angle commands which ensure no trajectory oscillations and no deviation from the reference heading angle, and the trimming module should output an elevator deflection which ensures that the gliders remain longitudinally statically stable. A sensitivity analysis is then run to analyse the robustness of the system and a final tuning of the guidance gains takes place. The same process is then followed for the control module's design: development, gain computing, nominal analysis, sensitivity analysis, and final tuning of the gains. Both guidance and control modules are then integrated together, and a sensitivity analysis is again run to evaluate the integration's robustness. In case of failure, the guidance and control designs should be reviewed. The navigation module is then developed, containing the design of its sensors and estimator. It is verified and then integrated with the guidance and control modules. This process is iterated until the desired performance is yielded from the system. The verification steps associated with this development process are mentioned at the end of each module's section. The verification of the integrated modules is explained in Chapter 8.

It is also important to define and tune the frequencies at which each module and the software's integration are running, to yield proper convergence of each module's results before they are passed to the next one. In the case of this thesis' design, an integration frequency of $f_{int} = 50$ Hz is set, with all modules (control, navigation, and sensors) working at that same frequency, except the guidance module which runs at $f_{guid} = 10$ Hz. No sensitivity analysis, however, was run on the guidance and control modules, due to lack of time. The following section provides the guidance and control requirements that drove the system design of these blocks.

## 6.2. Guidance and Control Requirements

System and modelling requirements are listed below, detailing the Guidance and Control systems design.

**SYS-8:** The atmospheric vehicle shall contain an autonomous guidance system.
**SYS-8.1:** The guidance system shall contain a reference trajectory made up of way-points.
**SYS-8.2:** The guidance system shall produce guidance commands to bring the vehicle's actual trajectory to the reference one, without limited deviation and/or trajectory oscillations.
**SYS-8.3:** The guidance system shall contains a trimming module which ensures longitudinal static stability.
**MOD-8.1:** The guidance parameters shall be the vehicle's angle-of-attack and bank angle.
**MOD-8.2:** The guidance system shall be based on a Linear Quadratic Regulator (LQR).

**SYS-9:** The atmospheric vehicle shall contain an autonomous control system.
**SYS-9.1:** The control system shall transform the guidance commands to deflections of the vehicle's control surfaces.
**MOD-9.1:** The control system shall contain a longitudinal controller and a lateral controller.
**MOD-9.2:** The control system shall be based on a LQR.

## 6.3. Guidance

The atmospheric vehicles will enter Uranus' atmosphere in descent probes. When a certain altitude is reached, the winged vehicles will be released from the descent probes. From then on, the guidance system will use a reference trajectory, which it will try to replicate by following a set of pre-defined way-points. With the difference between the reference trajectory and the actual trajectory that the vehicle will be following, the guidance system will compute the necessary steering commands to send to the control system. It will also

**Table 6.1:** Reference trajectory parameters for Mission Manager.

| **Altitude** [m] | **Angle-of-attack** [rad] | **Velocity** [m/s] | **Flight-path angle** [rad] | **Pseudo-altitude** [m] |
|---|---|---|---|---|
| 0.0 | 0.0 | 52.8 | -0.021816615649930 | -34.5575191894891 |
| -25000 | 0.0131 | 36.937004219841924 | -0.020157510229738 | -25022.3367412125 |
| -50000 | 0.0262 | 28.741445505507233 | -0.020409967005816 | -50017.5983586340 |
| -75000 | 0.0262 | 24.876685927870358 | -0.020139583704294 | -75015.0301829559 |
| -100000 | 0.0262 | 21.987237202371603 | -0.020159638783481 | -100013.297642795 |
| -125000 | 0.0262 | 19.732785328111369 | -0.020345729408203 | -125012.044337323 |
| -150000 | 0.0262 | 17.917439835486210 | -0.020385707591499 | -150010.957790678 |
| -175000 | 0.0262 | 16.420834670138259 | -0.020318740045959 | -175010.009520130 |
| -200000 | 0.0262 | 15.163675254361602 | -0.020170835336992 | -200009.175919900 |
| -225000 | 0.0262 | 14.091408751393059 | -0.020150576975414 | -225008.518500502 |
| -250000 | 0.0262 | 13.165198324320404 | -0.020092889287432 | -250007.935806171 |
| -275000 | 0.0262 | 12.356547634788631 | -0.020004898320869 | -275007.415744371 |
| -300000 | 0.0262 | 11.644037603210165 | -0.019892019780266 | -300006.948702790 |
| -325000 | 0.0262 | 11.011228395803904 | -0.019849194239058 | -325006.556920337 |
| -350000 | 0.0262 | 10.314749294375051 | -0.019797279903742 | -350006.126119368 |
| -375000 | 0.0262 | 9.935983525649835 | -0.019766567640427 | -375005.892008713 |

output the trimming commands (deflection of elevator for trim in pitch). The flight is said to be trimmed when no rotational accelerations are being experienced around the vehicle's c.o.m.

## 6.3.1. Reference Trajectory

In terms of the reference trajectory, as previously mentioned, the atmospheric vehicles will be performing gliding flights. They are modelled to only experience tailwind from the dominating zonal winds. This means that they will not experience any strong side forces, and thus should not deviate from the specific latitudes at which they will conduct their scientific measurements. A guidance system is used to guide the vehicles through the straight paths they have to follow, at constant latitudes. Way-points of the following variables are defined: angle-of-attack and velocity. The side-slip and bank angle are kept constant at zero and the heading angle is kept constant at either $-90°$ or $+90°$ depending on whether it concerns the equatorial or polar glider's trajectory. The way-points of the reference trajectory are defined every 25 km of altitude. The altitude range goes from $h = 0$ km to $h = -375$ km to reach the 100 bar pressure level, the angle-of-attack is initialised at $\alpha = 0°$ to minimise initial trajectory oscillations and goes up to $\alpha = 1.5°$, which correspond to the maximum range condition at $\left(\frac{C_L}{C_D}\right)_{max}$, and the velocity values go from $V = 52.8$ m/s (initial condition to minimise initial trajectory oscillations) to $V = 9.93$ m/s. The velocity values were generated by hard-coding the vehicle to go from $h = 0$ km to $h = -375$ km following a constant latitude and heading angle. The same was done for the values of flight-path angle, which was designed to range from $\gamma = -1.25°$ to $\gamma = -1.1325°$, as these values are needed for the computation of the pseudo-altitude, further explained in Equation (6.9), which is used as the reference trajectory interpolator. The aim is then for the guidance module to make the vehicle follow this reference trajectory.

## 6.3.2. Trimming Module

To ensure that the gliders remain longitudinally statically stable throughout their flights, a trimming command of the elevator is computed to counter the occurring pitching moment. This is done by computing the current pitching moment coefficient in clean configuration (i.e., without control-surface deflection), as well as the pitching moment coefficients for every elevator deflection interval for the current flight conditions. The necessary elevator command is then yielded by interpolating between all elevator deflection intervals to counter the pitching moment occurring from the clean configuration. This trim command is then added to the value of angle-of-attack of the previous time-step. This sum is considered to be the new commanded angle-of-attack and it is passed to the control module, where commanded and estimated states are further processed.

For verification purposes, it was checked that the produced trimming command indeed leads to a pitching moment with similar magnitude but opposite sign to the naturally occurring pitching moment of the vehicles' clean configuration (no control surface deflection). The *GetTrimde.c* function used in the simulator is considered verified.

### 6.3.3. Tracking Guidance

A vertical and lateral tracking guidance system was included to counter any vertical oscillations that were seen in the flight, as well as any deviation from the constant commanded heading angle. This is done through the implementation of a Linear Quadratic Regulator (LQR) which is based on optimal control theory and is introduced here.

## Optimal Control Theory: LQR

Using the method of a Linear Quadratic Regulator (LQR), a defined cost function must be maximised or minimised. It can be expressed as follows (Mooij, 1997a):

$$\mathbf{J} = \int_0^{\infty} \left(\mathbf{x}^T\mathbf{Q}\mathbf{x} + \mathbf{u}^T\mathbf{R}\mathbf{u}\right) dt \tag{6.1}$$

Here, $\mathbf{x}^T\mathbf{Q}\mathbf{x}$ represents the control deviation, and $\mathbf{u}^T\mathbf{R}\mathbf{u}$ the control effort. Elements $\mathbf{Q}$ and $\mathbf{R}$ are weighting matrices, with $\mathbf{Q}$ being a real positive semi-definite matrix, and $\mathbf{R}$ a real symmetric positive definite matrix. Varying these weighting matrices has a direct effect on the control deviation (resulting in a faster response if more weight is given to it), and on the control effort (resulting in smaller control signals for example). The weighting matrices $\mathbf{Q}$ and $\mathbf{R}$ are calculated following Bryson's Rule (Bryson and Ho, 1975):

$$\begin{aligned} \mathbf{Q} &= \text{diag}\left\{\frac{1}{\Delta x^2_{1,max}} \frac{1}{\Delta x^2_{2,max}} \cdots \frac{1}{\Delta x^2_{n,max}}\right\} \\ \mathbf{R} &= \text{diag}\left\{\frac{1}{\Delta u^2_{1,max}} \frac{1}{\Delta u^2_{2,max}} \cdots \frac{1}{\Delta u^2_{m,max}}\right\} \end{aligned} \tag{6.2}$$

Here, $\Delta x^2_{i,max}$ represents the maximum allowable amplitude of the $i^{th}$ element of the state vector, and $\Delta u^2_{j,max}$ represents the maximum allowable value of the $j^{th}$ control. The linearised state-space of the system to be controlled is expressed as follows:

$$\Delta\dot{\mathbf{x}} = \mathbf{A}\Delta\mathbf{x} + \mathbf{B}\Delta\mathbf{u} \tag{6.3}$$

$$\Delta\mathbf{y} = \mathbf{C}\Delta\mathbf{x} + \mathbf{D}\Delta\mathbf{u} \tag{6.4}$$

Here, $\mathbf{x}$ is a $n \times 1$ state vector, $\mathbf{u}$ is the $m \times 1$ control vector, $\mathbf{A}$ and $\mathbf{B}$ are the $n \times n$ state (or system) and $n \times m$ control coefficient matrices, $\mathbf{y}$ is the $k \times 1$ output vector, and $\mathbf{C}$ and $\mathbf{D}$ are the $k \times n$ output and $k \times m$ direct transmission matrices, respectively. In most applications, $\mathbf{D} = \mathbf{0}$. The matrices $\mathbf{A}$ and $\mathbf{B}$ can be derived from the equations of motion $f_i$ as follows:

$$\mathbf{A} = \begin{bmatrix} \frac{\partial f_1}{\partial x_1} & \dots & \frac{\partial f_1}{\partial x_n} \\ \dots & \dots & \dots \\ \frac{\partial f_n}{\partial x_1} & \dots & \frac{\partial f_n}{\partial x_n} \end{bmatrix}_{\mathbf{x}=\mathbf{x_0},\mathbf{u}=\mathbf{u_0}} \quad \text{and} \quad \mathbf{B} = \begin{bmatrix} \frac{\partial f_1}{\partial u_1} & \dots & \frac{\partial f_1}{\partial u_m} \\ \dots & \dots & \dots \\ \frac{\partial f_n}{\partial u_1} & \dots & \frac{\partial f_n}{\partial u_m} \end{bmatrix}_{\mathbf{x}=\mathbf{x_0},\mathbf{u}=\mathbf{u_0}} \tag{6.5}$$

Here, the conditions of $\mathbf{x} = \mathbf{x_0}$ and $\mathbf{u} = \mathbf{u_0}$ correspond to the nominal trimmed flight conditions. The elements of matrices $\mathbf{A}$ and $\mathbf{B}$ depend on the reference trajectory and vehicle data. For state feedback, the control law is defined as follows:

$$\Delta\mathbf{u} = -\mathbf{K}\Delta\mathbf{x} \tag{6.6}$$

The state feedback matrix $\mathbf{K}$ can then be expressed as:

$$\mathbf{K} = \mathbf{R}^{-1}\mathbf{B}^T\mathbf{P} \tag{6.7}$$

Here, $\mathbf{P}$ is a positive definite matrix and can be obtained from the Riccati equation:

$$\mathbf{A}^T\mathbf{P} + \mathbf{P}\mathbf{A} - \mathbf{P}\mathbf{B}\mathbf{R}^{-1}\mathbf{B}\mathbf{P} + \mathbf{Q} = \mathbf{0} \tag{6.8}$$

This equation can easily be solved using standard algorithms, available in MATLAB's control-system design tools, such as *lqr.m*, which returns the optimal gain matrix $\mathbf{K}$, the solution $\mathbf{P}$ to the Riccati equation, and the closed-loop eigenvalues.

## Vertical and Horizontal Tracking Guidance

For the vertical tracking guidance, the altitude $h$ and flight-path angle $\gamma$ are combined into a pseudo-altitude $h^*$. In Equations (4.15) and (4.16), altitude is a kinematic variable so it cannot be directly controlled. However, it can be indirectly controlled by changing the flight-path angle. That is why those two variables are combined, as suggested by Mooij (2014):

$$h^* = h + K_\gamma \gamma = h + c_\gamma V \gamma \tag{6.9}$$

Here, a value of $c_\gamma = 30$ s/rad was found to work well for the vehicle and mission at hand, although it was seen that as long as this variable is consistently implemented in both the calculation of the tracking guidance gain and the calculation of pseudo-altitude, the chosen value does not matter. The pseudo-altitude is thus calculated from the estimated state variables at every time-step, and used as the interpolator for the reference trajectory definition, to output a reference velocity and angle-of-attack. The reference velocity is then compared to the estimated one from the navigation system, and an angle-of-attack increment $\delta\alpha$ command is yielded from the implementation of the tracking guidance using the first two equations of Equation (4.15).

The state vector considered here is $\mathbf{x} = [V \; h^*]^T$ and the input vector is $\mathbf{u} = [\delta\alpha \; \delta\sigma]^T$. However, no bank angle command $\delta\sigma$ will be yielded from this as the other matrices are constructed only to yield an angle-of-attack increment, with aim to limit vertical oscillations. The system matrix $\mathbf{A}$ and the control or input matrix $\mathbf{B}$ were defined as follows, to yield an increment in angle-of-attack as guidance parameter for the vertical guidance:

$$\mathbf{A} = \begin{bmatrix} \frac{\partial \dot{V}}{\partial V} & 0 \\ \\ \frac{\partial \dot{h}^*}{\partial V} & 0 \end{bmatrix}_{\mathbf{x}=\mathbf{x_0},\mathbf{u}=\mathbf{u_0}} \qquad \text{and} \qquad \mathbf{B} = \begin{pmatrix} \frac{\partial \dot{V}}{\partial \alpha} \\ \\ \frac{\partial \dot{h}^*}{\partial \alpha} \end{pmatrix}_{\mathbf{x}=\mathbf{x_0},\mathbf{u}=\mathbf{u_0}} \tag{6.10}$$

Here, the velocity derivative $\dot{V}$ is taken from Equation 4.15 by assuming zero rotational rate of Uranus, and the pseudo-altitude derivative $\dot{h}^*$ is as follows, where zero rotational rate of Uranus is again assumed:

$$\begin{aligned} \dot{h}^* &= \dot{h} + c_\gamma \dot{V}\gamma + c_\gamma V \dot{\gamma} \\ &= V \sin\gamma + c_\gamma \left[ 2\omega_{cb} V + \frac{V^2}{R}\cos\gamma + \omega_{cb}^2 R \cos\gamma - g\cos\gamma \frac{L}{m}\cos\sigma \right] \\ &+ c_\gamma \gamma \left[ \omega_{cb}^2 R \sin\gamma - g \sin\gamma - \frac{D}{m} \right] \\ &= V \sin\gamma + c_\gamma \left[ \frac{V^2}{R}\cos\gamma - g\cos\gamma\frac{L}{m}\cos\sigma \right] + c_\gamma\gamma\left[ -g\sin\gamma - \frac{D}{m}\right] \end{aligned} \tag{6.11}$$

To derive the partial derivatives necessary here, the dependency of flight-path angle, density, as well as drag and lift forces on velocity and pseudo-altitude must be considered as such:

$$\begin{aligned} \gamma = \frac{h^* - h}{c_\gamma V} &\Rightarrow \frac{\partial \gamma}{\partial V} = \frac{-\gamma}{V} \\ &\Rightarrow \frac{\partial \gamma}{\partial h^*} = \frac{1}{c_\gamma V} \end{aligned} \tag{6.12}$$

$$\begin{aligned} \rho = \rho_0 e^{\frac{h}{H_s}} &\Rightarrow \frac{\partial \rho}{\partial h^*} = \frac{-\rho}{H_s} \\ &\Rightarrow \frac{\partial \rho}{\partial V} = \frac{-\rho c_\gamma \gamma}{H_s} \end{aligned} \tag{6.13}$$

$$\begin{aligned} D = \frac{1}{2}\rho V^2 S C_D &\Rightarrow \frac{\partial D}{\partial V} = \frac{1}{2}\frac{\partial \rho}{\partial V} V^2 S C_D + \frac{1}{2}\rho \frac{\partial V^2}{\partial V} S C_D + \frac{1}{2}\rho V^2 S \frac{\partial C_D}{\partial V} = -D \cdot \frac{c_\gamma \gamma}{H_s} + \rho V S C_D + \bar{q} S \frac{\partial C_D}{\partial V} \\ &\Rightarrow \frac{\partial D}{\partial h^*} = \frac{1}{2}\frac{\partial \rho}{\partial h^*} V^2 S C_D \end{aligned} \tag{6.14}$$

$$\begin{aligned} L = \frac{1}{2}\rho V^2 S C_L &\Rightarrow \frac{\partial L}{\partial V} = \frac{1}{2}\frac{\partial \rho}{\partial V} V^2 S C_L + \frac{1}{2}\rho \frac{\partial V^2}{\partial V} S C_L + \frac{1}{2}\rho V^2 S \frac{\partial C_L}{\partial V} = -L \cdot \frac{c_\gamma \gamma}{H_s} + \rho V S C_L + \bar{q} S \frac{\partial C_L}{\partial V} \\ &\Rightarrow \frac{\partial L}{\partial h^*} = \frac{1}{2}\frac{\partial \rho}{\partial h^*} V^2 S C_L \end{aligned} \tag{6.15}$$

The necessary partial derivatives to construct matrices **A** and **B** can thus be expressed as follows:

$$\frac{\partial \dot{V}}{\partial V} = g \cdot \frac{\gamma}{V}\cos\gamma + \frac{D}{m}\cdot\left(\frac{c_\gamma \gamma}{H_s} - \frac{2}{V}\right) - \frac{\bar{q}S}{m}\frac{\partial C_D}{\partial V} \tag{6.16}$$

$$\begin{aligned}\frac{\partial \dot{h}^*}{\partial V} &= \sin\gamma - \gamma\cos\gamma + 2c_\gamma\frac{V}{R}\cos\gamma + c_\gamma\frac{V}{R}\gamma\sin\gamma + \frac{c_\gamma}{m}\cos\sigma\cdot\left[L\left(\frac{-c_\gamma\gamma}{H_s} + \frac{2}{V}\right) + \bar{q}S\frac{\partial C_L}{\partial V}\right]\\ &+ c_\gamma\gamma\frac{\partial \dot{V}}{V} + c_\gamma\frac{\gamma}{V}\cdot\left(g\sin\gamma + \frac{D}{m}\right)\end{aligned} \tag{6.17}$$

$$\frac{\partial \dot{V}}{\partial \alpha} = \frac{-1}{m}\frac{\partial D}{\partial \alpha} = \frac{-1}{m}\bar{q}S\frac{\partial C_D}{\partial S} \tag{6.18}$$

$$\frac{\partial \dot{h}^*}{\partial \alpha} = c_\gamma\frac{\cos\sigma}{m}\frac{\partial L}{\partial \alpha} - \frac{c_\gamma\gamma}{m}\frac{\partial D}{\partial \alpha} = \frac{c_\gamma}{m}\bar{q}S\cdot\left(\cos\sigma\frac{\partial C_L}{\partial \alpha} - \gamma\frac{\partial C_D}{\partial \alpha}\right) \tag{6.19}$$

The two weighing matrices **Q** and **R** are defined as follows, with $\Delta V_{max}^2$ and $\Delta\delta\alpha_{max}^2$:

$$\mathbf{Q} = \begin{bmatrix} \frac{1}{\Delta V_{max}^2} & 0 \\ 0 & 0 \end{bmatrix} \quad \text{and} \quad \mathbf{R} = \begin{bmatrix} \frac{1}{\Delta\delta\alpha_{max}^2} \end{bmatrix} \tag{6.20}$$

Solving the LQR Riccati equation yields a gain of $K_\alpha$. For the lateral tracking guidance, the third equation of Equation (4.15) is considered and solved for a commanded bank angle $\delta\sigma$, with the addition of a gain of $K_\sigma$. This gain was computed using a LQR with the following components, at trimmed conditions:

$$A = \frac{\partial \dot{\chi}}{\partial \chi}_{\mathbf{x}=\mathbf{x_0},\mathbf{u}=\mathbf{u_0}} \quad \text{and} \quad B = \frac{\partial \dot{\chi}}{\partial \sigma}_{\mathbf{x}=\mathbf{x_0},\mathbf{u}=\mathbf{u_0}} \tag{6.21}$$

$$Q = \frac{1}{\Delta\delta\chi_{max}^2} \quad \text{and} \quad R = \frac{1}{\Delta\delta\sigma_{max}^2} \tag{6.22}$$

The parameters of $Q$ and $R$ were set to $\Delta\delta\chi_{max}$ and $\Delta\delta\sigma_{max}$, and the following partial derivatives were used for $A$ and $B$:

$$\frac{\partial \dot{\chi}}{\partial \chi} = 2\omega_{cb}\cos\delta\tan\gamma\sin\chi + \frac{V}{R}\cos\gamma\tan\delta\cos\chi + \omega_{cb}^2\frac{R}{V\cos\gamma}\cos\delta\sin\delta\cos\chi \tag{6.23}$$

$$\frac{\partial \dot{\chi}}{\partial \sigma} = \frac{L\cos\sigma}{mV\cos\gamma} \tag{6.24}$$

The resulting gains vary in terms of the tuning of the two weighing matrices **Q** and **R** of both Equations (6.20) and (6.22). These weighing matrices were kept constant for the analysis of potential dependency on flight conditions. the altitude and velocity were varied to match the reference profile listed in Table 6.1, thus influencing the values of gravity, Mach number, dynamic pressure, as well as drag and lift forces involved in the computation of the tracking guidance gains. By exploring different altitude and velocity intervals it was concluded that the computed gains do not vary significantly enough for different values to be included in the software. This assumption is supported by the fact that the angle-of-attack gain parameter only varies by 0.077 through the whole flight, while the bank angle gain parameter does not vary with changing altitude and velocity. The gain values of the glider's initial conditions are thus kept for the whole flight, maintaining the possibility of varying them by tuning the **Q** and **R** matrices.

### 6.3.4. Verification & Performance: Guidance

The guidance module is verified in translational 3 Degrees of Freedom (DoF) with and without the inclusion of both oscillations-limiting and heading angle tracking guidance components. A step function is enforced on both the pseudo-altitude $h^*$ and velocity $V$, and the control module is set to ideal. This means that the commanded aerodynamic angles outputted from the guidance module are transformed into control surface deflections and directly passed to the vehicle's actuators. The navigation module is turned off, such that the simulation's real values are used in the simulation loop. The following cases are summarised as **Sim #1** and **Sim #2** in Table 8.2, along with the gain tuning parameters used.

**Table 6.2:** Tracking guidance gain parameters for LQR tuning in 3 DoF (translational).

| $\Delta V_{max}$ [m/s] | $\Delta h_{max}$ [m] | $\Delta\alpha_{max}$ [°] | $\Delta\chi_{max}$ [°] | $\Delta\sigma_{max}$ [°] |
|---|---|---|---|---|
| 0.005 | 500 | 0.5 | 0.5 | 5 |

- **3 DoF (translational) nominal guidance (Sim #1):** With the tracking guidance not being active, two types of deviations are expected from the commanded reference trajectory: oscillations in velocity, flight-path angle, and radius, as well as a deviation from the commanded heading angle. The commanded aerodynamic angles are successfully passed to the control module and transformed to control surface deflections, yielding real aerodynamic angles similar to the commanded ones. Figure 6.2 displays the commanded and real velocity and heading angle values for this situation. The trajectory oscillations seen in Figure 6.2a and the heading angle deviation pictured in Figure 6.2b emphasise the importance of implementing a tracking guidance which can counter these two phenomena.

- **3 DoF (translational) nominal & tracking guidance (Sim #2):** When turning on the tracking guidance, two additional sets of parameters have to be defined: the tracking guidance gains computed with a LQR, as well as minimum and maximum limits on the angle-of-attack and bank angle tracking guidance incremental commands. Those limits are needed to ensure that the produced commands do not diverge from the system's capabilities. For the angle-of-attack increment in particular, these limits also constrain the expected command within a small range, due to the noisiness of the produced signal. In terms of the tracking guidance's performance, Figure 6.3 displays the commanded and real velocity and heading angle values for this situation, as well as the generated tracking guidance commands. With the help of the angle-of-attack and bank angle commands, the actual velocity is much closer to the commanded one, with no more oscillations present. The noise seen in the behaviour of the real heading angle oscillates around the value of $\chi = -90.00008°$ which remains close to the commanded $-90°$ for the equatorial glider, leading to a quasi-constant latitude during the flight. The parameters used to compute the tracking guidance gains are listed in Table 6.2, and the defined angle-of-attack and bank angle limits were set as follows: $\delta\alpha_{min} = -0.04°$, $\delta\alpha_{max} = -0.02°$, $\delta\sigma_{min} = -5°$, and $\delta\sigma_{max} = 5°$. The noise in heading angle displayed in Figure 6.3b is linked to the noisy angle-of-attack command displayed in Figure 6.3c, and is thus constrained by the minimum and maximum limits set on this value. This is because both commands are coupled.

  The pseudo-altitude $h^*$ defined for the tracking guidance is used as interpolator for the reference trajectory's way-points. For verification purposes, a step function is thus implemented on it, to see whether the generated tracking guidance commands can help the real trajectory match the reference one, with the step. A step of around $-20$ m is enforced on the pseudo-altitude at 5 s of the simulation time, yielding a drop in the commanded velocity as seen in Figure 6.4a. Figure 6.4 displays the commanded and real velocity and heading angle values for this situation, as well as the generated tracking guidance

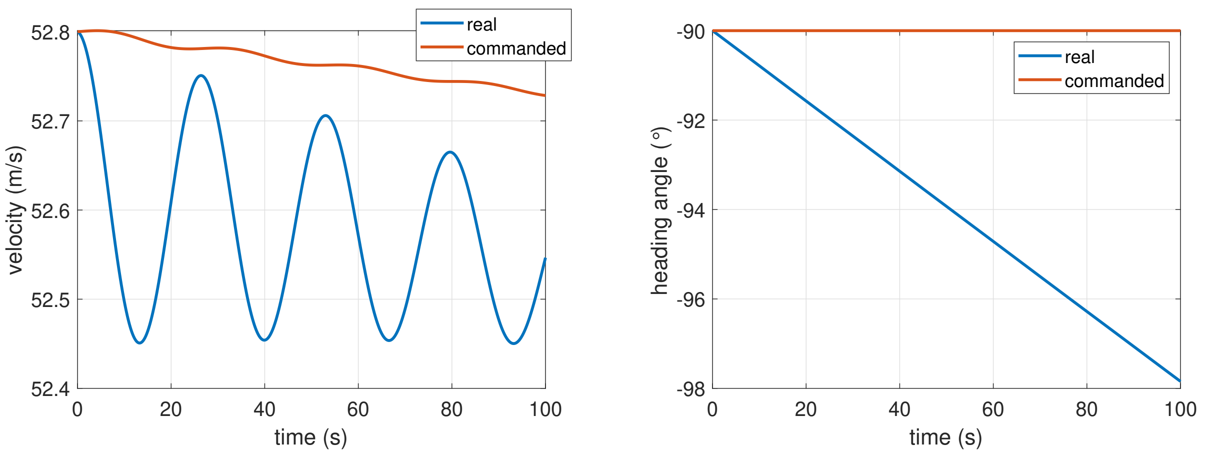


**(a)** Velocity of glider with tracking guidance off. **(b)** Heading angle of glider with tracking guidance off.

**Figure 6.2:** Behaviour of velocity and heading angle of equatorial glider when tracking guidance is off, displaying trajectory oscillations and deviation from constant commanded heading angle of $-90°$.

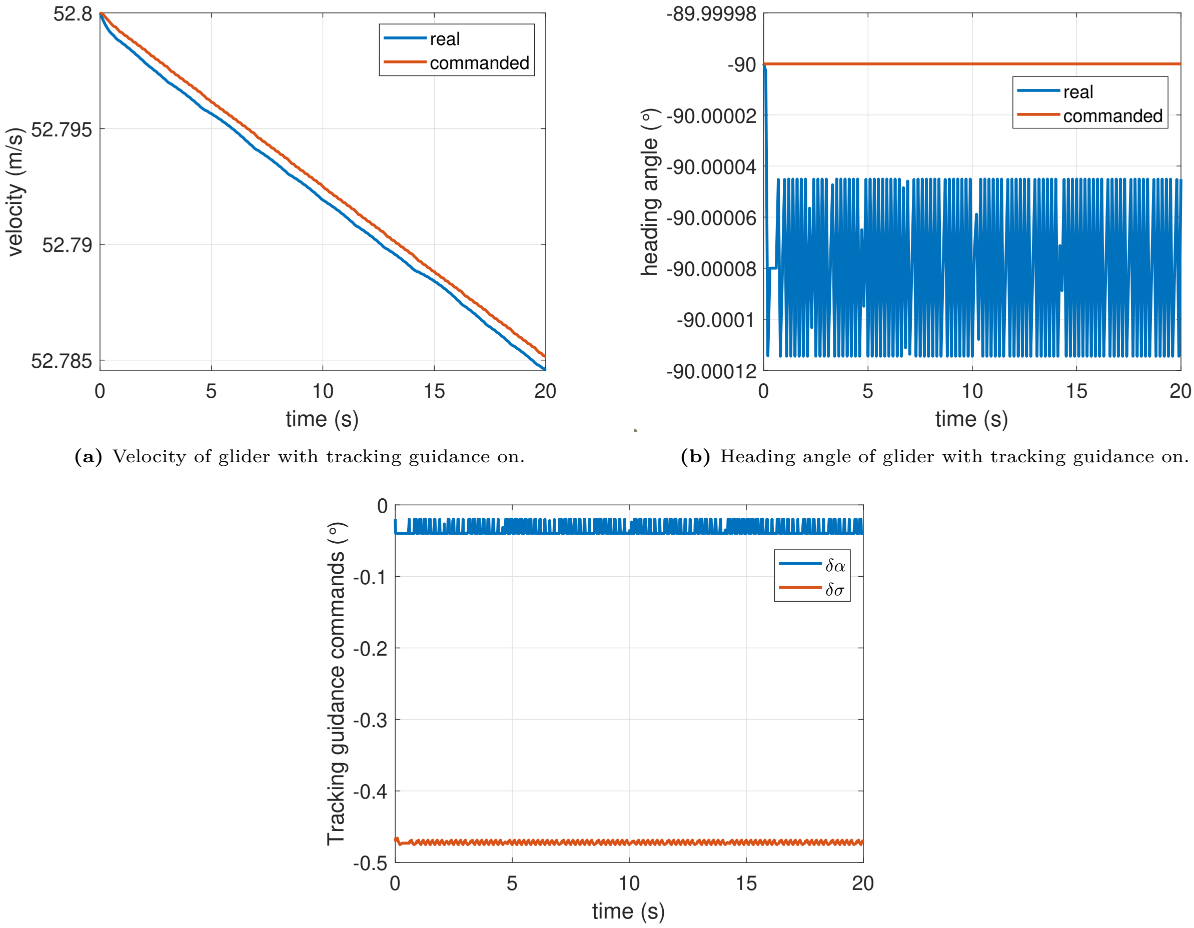


**(a)** Velocity of glider with tracking guidance on.

**(b)** Heading angle of glider with tracking guidance on.

**(c)** Tracking guidance commands of equatorial glider.

**Figure 6.3:** Behaviour of velocity, heading angle, and tracking guidance commands of equatorial glider.

commands. As seen here, the tracking guidance overcomes the step in reference velocity, bringing back the trajectory to a non-oscillating one, following a heading angle similar to the one followed without the step, as seen in Figure 6.3b.

## 6.4. Control

Since the focus of this thesis is on the navigation system, a relatively simple control system is implemented. A Linear Quadratic Regulator (LQR) is chosen, which is based on optimal control theory explained in Section 6.3.3. For this control system, the state vector $\mathbf{x}$ and control vector $\mathbf{u}$ are defined as follows:

$$\mathbf{x} = (\Delta q, \Delta p, \Delta r, \Delta\alpha, \Delta\beta, \Delta\sigma)^T \qquad \text{and} \qquad \mathbf{u} = (\Delta\delta_e, \Delta\delta_a, \Delta\delta_r)^T \tag{6.25}$$

Here, $q$, $p$, $r$ are the pitch, yaw, and roll rate respectively, and $\alpha$, $\beta$, $\sigma$ the aerodynamic angles. The control vector is made up of the deflections in all three control surfaces present on the gliders: elevator, aileron and rudder with their respective subscripts $e$, $a$, and $r$. The $\Delta$ symbol in front of these variables represents the difference between the commanded and the estimated or actual value.

The controller is divided into a longitudinal and a lateral controller, assuming the decoupling of symmetric and asymmetric motions. The longitudinal controller takes care of the pitch movement, while the lateral controller focuses on the coupled motion of roll and yaw. This means that both controllers have different linearised state and control vectors $\Delta\mathbf{x}$ and $\Delta\mathbf{u}$.

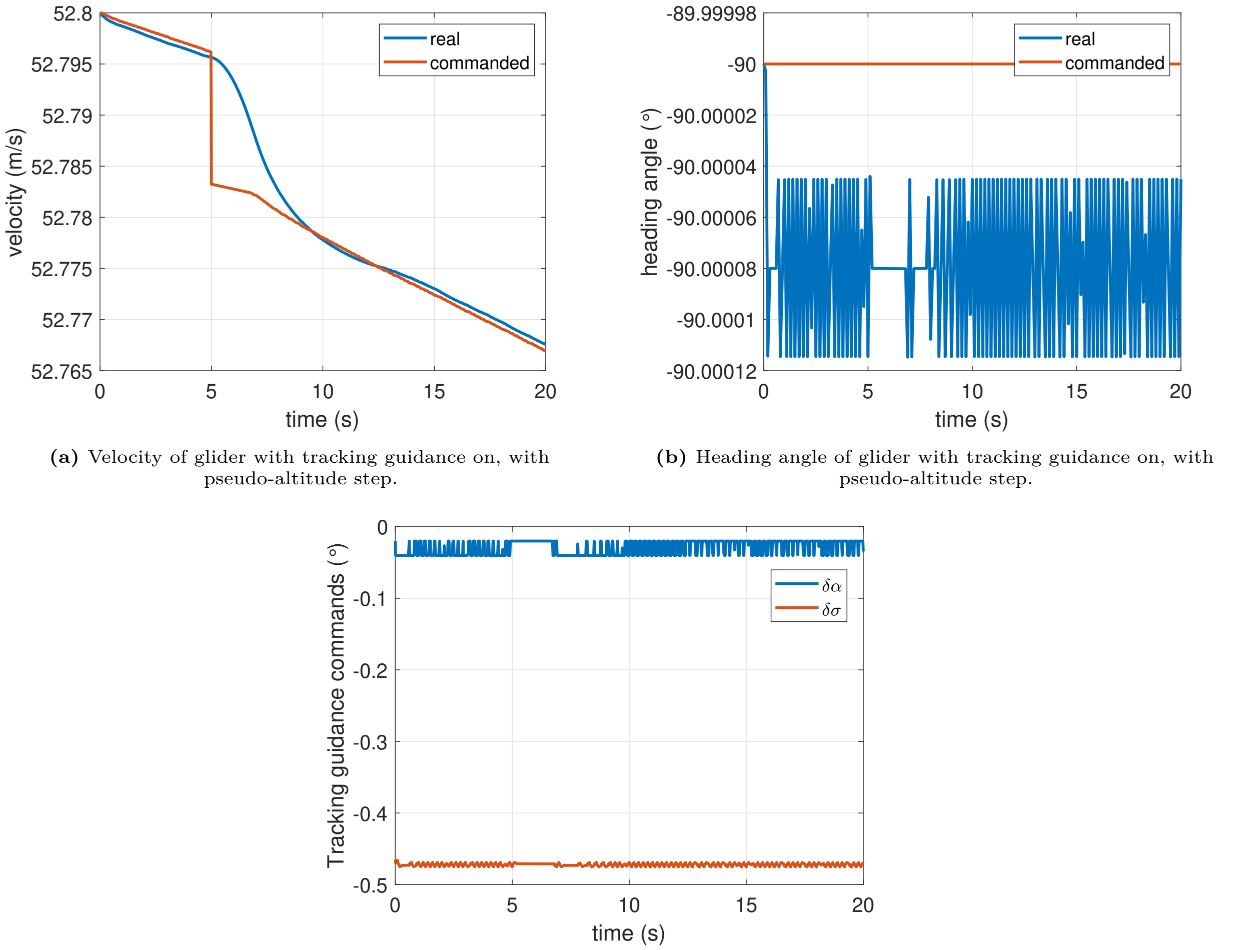


**(a)** Velocity of glider with tracking guidance on, with pseudo-altitude step.

**(b)** Heading angle of glider with tracking guidance on, with pseudo-altitude step.

**(c)** Tracking guidance commands of glider, with pseudo-altitude step.

**Figure 6.4:** Behaviour of velocity, heading angle, and tracking guidance commands of equatorial glider, with pseudo-altitude step.

### 6.4.1. Longitudinal Controller

For the design of the longitudinal controller, $\Delta\beta$ and $\Delta\sigma$ along with their respective rates $\Delta r$ and $\Delta p$ are set to zero. The following system can then be obtained:

$$\begin{pmatrix} \Delta\dot{q} \\ \Delta\dot{\alpha} \end{pmatrix} = \begin{bmatrix} 0 & \frac{1}{I_{yy}}\frac{\partial C_m}{\partial\alpha}\bar{q}S_{ref}c_{ref} \\ 1 & -\frac{1}{mV_0}\frac{\partial C_L}{\partial\alpha}\bar{q}S_{ref} \end{bmatrix} \begin{pmatrix} \Delta q \\ \Delta\alpha \end{pmatrix} + \begin{bmatrix} \frac{1}{I_{yy}}\frac{\partial C_m}{\partial\delta e}\bar{q}S_{ref}c_{ref} \\ 0 \end{bmatrix} (\Delta\delta e) \tag{6.26}$$

The aerodynamic coefficient contributions were interpolated from the aerodynamic coefficient database generated with XLFR5. It was determined that $\frac{\partial C_m}{\partial\alpha}$, $\frac{\partial C_L}{\partial\alpha}$, as well as $\frac{\partial C_m}{\partial\delta e}$ were staying constant or quasi-constant for different values of altitude and velocity. When computing the control module's gains, they were thus kept constant at the following values: $\frac{\partial C_m}{\partial\alpha} = -4.3743\cdot10^{-15}$ 1/rad, $\frac{\partial C_L}{\partial\alpha} = 5.8669$ 1/rad, and $\frac{\partial C_m}{\partial\delta e} = 1.4152$ 1/rad. Here, the pitch rate $\frac{\partial C_m}{\partial\alpha}$ has a value close to zero, because it is retrieved from the pitch moment, which is close to zero in trimmed conditions. The dynamic pressure $\bar{q}$ and velocity $V_0$ are taken from the simulation but all other variables present in Equation (6.26) are kept constant. The weighing matrices $\mathbf{Q}$ and $\mathbf{R}$ are computed using the following relation:

$$\mathbf{Q} = \text{diag}\left\{\frac{1}{\Delta q^2_{\max}}, \frac{1}{\Delta\alpha^2_{\max}}\right\} \quad \text{and} \quad \mathbf{R} = \text{diag}\left\{\frac{1}{\Delta\delta e^2_{\max}}\right\} \tag{6.27}$$

### 6.4.2. Lateral Controller

For the design of the lateral controller, $\Delta\alpha$ and its rate $\Delta q$ are set to zero. The following system can then be obtained from the linearised set of equations of motion:

$$\begin{pmatrix} \Delta\dot{p} \\ \Delta\dot{r} \\ \Delta\dot{\beta} \\ \Delta\dot{\sigma} \end{pmatrix} = \begin{bmatrix} 0 & 0 & \frac{1}{I_{xx}}\frac{\partial C_l}{\partial\beta}\bar{q}S_{ref}b_{ref} & 0 \\ 0 & 0 & \frac{1}{I_{zz}}\frac{\partial C_n}{\partial\beta}\bar{q}S_{ref}b_{ref} & 0 \\ \sin\alpha_0 & -\cos\alpha_0 & -\frac{1}{mV_0}\frac{\partial C_S}{\partial\beta}\bar{q}S_{ref} & -\frac{g_0}{mV_0}\cos\gamma_0\cos\sigma_0 \\ -\cos\alpha_0 & -\sin\alpha_0 & \frac{\tan\gamma_0\cos\sigma_0}{mV_0}\frac{\partial C_S}{\partial\beta}\bar{q}S_{ref} - \frac{L_0}{mV_0} & \tan\gamma_0\cos\sigma_0\frac{L_0}{mV_0} \\ & & +\frac{g_0}{mV_0}\cos\gamma_0\cos\sigma_0 & \end{bmatrix} \begin{pmatrix} \Delta q \\ \Delta\alpha \end{pmatrix}$$

$$+ \begin{bmatrix} \frac{1}{I_{xx}}\frac{\partial C_l}{\partial\delta a}\bar{q}S_{ref}b_{ref} & 0 \\ \frac{1}{I_{zz}}\frac{\partial C_n}{\partial\delta a}\bar{q}S_{ref}b_{ref} & \frac{1}{I_{zz}}\frac{\partial C_n}{\partial\delta r}\bar{q}S_{ref}b_{ref} \\ 0 & 0 \\ 0 & 0 \end{bmatrix} \begin{pmatrix} \Delta\delta a \\ \Delta\delta r \end{pmatrix} \tag{6.28}$$

Similarly to the longitudinal controller, the aerodynamic coefficient contributions were interpolated from the aerodynamic coefficient database generated with XLFR5. The following gradients were kept constant: $\frac{\partial C_S}{\partial\beta} = -0.2258$ 1/rad, $\frac{\partial C_l}{\partial\beta} = -0.0488$ 1/rad, $\frac{\partial C_n}{\partial\beta} = 0.0523$ 1/rad, as well as $\frac{\partial C_l}{\partial\delta a} = 0.3064$ 1/rad, and $\frac{\partial C_n}{\partial\delta r} = 0.0378$ 1/rad. The dynamic pressure $\bar{q}$ and velocity $V_0$ are taken from the simulation but all other variables present in Equation (6.28) are kept constant. The weighing matrices $\mathbf{Q}$ and $\mathbf{R}$ are computed using the following relation:

$$\mathbf{Q} = \text{diag}\left\{\frac{1}{\Delta p_{\max}^2}, \frac{1}{\Delta r_{\max}^2}, \frac{1}{\Delta\beta_{\max}^2}, \frac{1}{\Delta\sigma_{\max}^2}\right\} \quad \text{and} \quad \mathbf{R} = \text{diag}\left\{\frac{1}{\Delta\delta a_{\max}^2}, \frac{1}{\Delta\delta r_{\max}^2}\right\} \tag{6.29}$$

### 6.4.3. Gain Computation and Tuning

The control gains were determined by implementing the necessary **A**, **B**, **Q**, and **R** matrices for both the longitudinal and lateral motions in the MATLAB function *lqr.m*, for trimmed conditions. The software was run in 3 DoF (rotational) to determine and tune its gains. The tracking guidance and navigation modules were turned off, which means that the simulation's real values are used in the simulation, without optimal control to minimise trajectory oscillations and heading angle deviations, which can, in any case, not be simulated in a 3 DoF rotational simulation. Step responses of a few degrees were analysed on all aerodynamic angles to tune the control gains. After turning, the control module successfully brings the aerodynamic angles back to their commanded value after experiencing the step. This process takes about 15 s, which is acceptable for this system, as no sudden change in aerodynamic angles are expected during the flight. Without including the tracking guidance, the expected aerodynamic angle behaviour is as follows: the angle-of-attack should increase from $\alpha = 0°$ to $\alpha = 1.5°$ and remain at the value for most of the flight, and the side-slip angle and the bank angle should stay close to $\beta = 0°$. When including tracking guidance, the aerodynamic angles' behaviour should be similar, expect both angle-of-attack and bank angles should have slightly lower values.

It was noticed, however, that the combination of the guidance and control modules when run in a 6 DoF simulation produced poor results, and that tuning the tracking guidance and the control module's gains simultaneously increased the results' accuracy, as both systems influence each other. The two modules having an influence on each other is a first sign of their low robustness. In a typical GNC system design process, the design of the guidance and control modules would be re-evaluated at this point, and changed to yield more robustness, evaluated with a sensitivity analysis. The time constraint of this thesis, however, did not allow the re-design of those modules. Instead, the tracking guidance and control modules' gains are tuned simultaneously to yield better performance, when integrated together.

The tuning process starts by first using the tracking guidance gains computed with the parameters listed in Table 6.2. Both the tracking guidance and control gain parameters are then modified to yield minimum velocity and aerodynamic angles error, between the commanded and the actual values, using the reference trajectory mentioned in Section 6.3.1 as input. Then, the performance of the chosen gains is assessed by analysing the step response to 1.5° of the aerodynamic angles. The response of the aerodynamic angles is analysed, checking that they indeed follow the commanded ones, and that they do not take too much time to converge to their commanded values. The tuning parameters are altered to optimise this, making sure the deflections of the control surfaces do not diverge and explode over time. The values listed in Table 6.4 are yielded for the control gains after this process. The new tracking guidance gain tuning parameters are listed in Table 6.3.

**Table 6.3:** Tracking guidance gain parameters for LQR tuning in 6 DoF.

| $\Delta V_{max}$ [m/s] | $\Delta h_{max}$ [m] | $\Delta\alpha_{max}$ [°] | $\Delta\chi_{max}$ [°] | $\Delta\sigma_{max}$ [°] |
|---|---|---|---|---|
| 0.01 | 100 | 5 | 5 | 5 |

**Table 6.4:** Control gain parameters for LQR tuning.

| $\Delta q_{max}$ [°/s] | $\Delta\alpha_{max}$ [°] | $\delta e_{max}$ [°] | $\Delta p_{max}$ [°/s] | $\Delta r_{max}$ [°/s] | $\Delta\beta_{max}$ [°] | $\Delta\sigma_{max}$ [°] | $\delta a_{max}$ [°] | $\delta r_{max}$ [°] |
|---|---|---|---|---|---|---|---|---|
| 10 | 6.9 | 30 | 20 | 15 | 5 | 10 | 25 | 25 |

Indeed, when a step of 1.5° is given to each aerodynamic angle individually, their response is influenced by this step, and the tracking guidance manages to bring their value back to the most optimal ones to minimise both trajectory oscillations and heading angle deviation, in the time span of around 1 s.

It is then checked whether altitude and velocity influence the control gains. To achieve this, the values used for the weighing matrices **Q** and **R** are kept constant. It was determined that a change in angle-of-attack had close to no influence on the gains, so all gains were computed at an angle-of-attack of $\alpha = 1.5°$ which is the angle-of-attack at which the vehicles should be flying for the majority of their flights. The flight-path and bank angle were also set constant, as they were seen to converge to two specific values and stay constant during the flight: $\gamma = -1.258°$ and $\sigma = -0.4687°$. The control gains were then computed for different altitudes and velocities. The explored altitudes and velocities are the same ones as the increments taken for the generation of the glider's aerodynamic coefficients, namely $h = [0, -100, -200, -300, -375]$ km and $v = [9, 25, 50, 70]$ m/s. There is no driving factor between altitude and velocity that is making the gains vary the most. Nevertheless, the computed gains are seen to change with varying altitude and velocity. It is thus better to include a range of gains in the simulator, rather than keep them constant, to have specific ones at every instance of the flight. A Lookup table was created for each gain, with the altitude and velocity as interpolators, for the control module to use the right gains at every instance of the gliders' flights. It is not recommended to combine the altitude and velocity as specific energy for the Lookup tables' interpolator, because the gains' data is not evenly distributed, which leads to jumps and peaks in the control surfaces' deflections, leading to peaks in the produced aerodynamic angles, the elevator trimming command, and the aerodynamic coefficients. The change in longitudinal and lateral gains are plotted against the different altitude and velocity values in Appendix E.

### 6.4.4. Verification & Performance: Control

The verification and performance analysis of the control module is done by running it in 3 DoF rotational, with tracking guidance and navigation modules turned off. A step response in the aerodynamic angles is evaluated. Figure 6.5a shows the deflection angles of the three control surfaces to achieve convergence to the commanded aerodynamic angles when a 1.5° step is enforced on the angle-of-attack at 5 s of simulation time, and Figure 6.5b shows the difference between commanded and real angle-of-attack. As mentioned at the beginning of Section 6.4.3, it takes about 15 s for the real angle-of-attack to reach the commanded one after experiencing the step. For the mission at hand, 15 s is acceptable, as no jump in aerodynamic angle is expected. Moreover, when integrated with the guidance module, the behaviour of the controller is seen to increase and it takes around 1 s for the real value to reach the commanded one after a 1.5° step.

The performance of the inclusion of the computed gains in the control module was evaluated by comparing the case where the computed gains are included, to the one where all gains are set to unity. For 20 s of simulation time, both aerodynamic angle errors and control surface deflections explode, as shown in Figure 6.6. Here, the simulation is run in 3 DoF rotational, with the tracking guidance and navigation modules turned off.

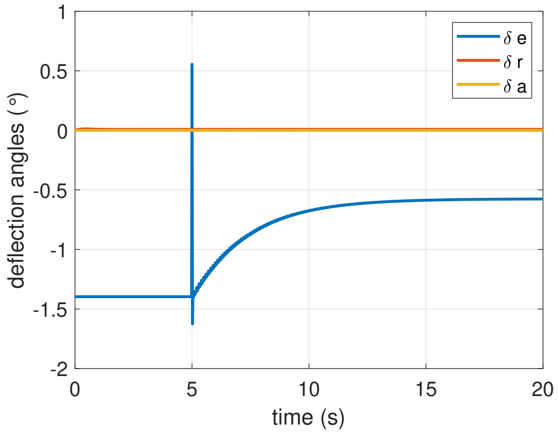


(a) Behaviour of deflection of control surfaces.

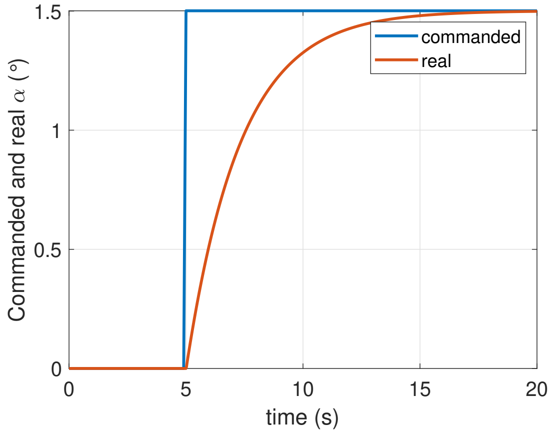


(b) Commanded and real angle-of-attack.

**Figure 6.5:** Behaviour of deflection of control surfaces, commanded and real angle-of-attack during 3 DoF (rotational) analysis for control module verification and performance analysis.

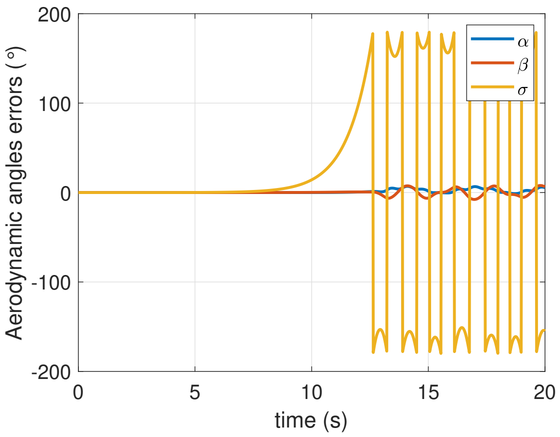


(a) Aerodynamic angles error with unity control gains.

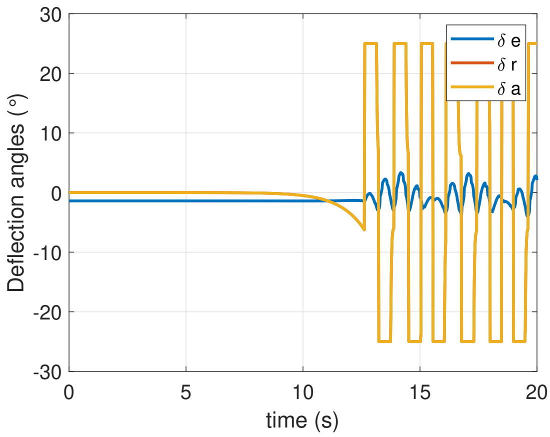


(b) Control surface commands with unity control gains.

**Figure 6.6:** Behaviour of aerodynamic angles error and deflection of control surfaces when unity gains included in control module.

# 7 Navigation Design

Focusing on navigation, it is now understood that the goal will be to accurately estimate the state of the gliders. To do so, the different types of navigation sensors that can be used in Uranus' atmosphere will be detailed in Section 7.1, as well as their benefits, limitations, and implementations. Section 7.2 will then explain the theory of the chosen estimation filter as well as provide a sensor input analysis. Then, Section 7.3 will list additional navigation system and modelling requirements, and Section 7.4 will relate the navigation verification steps.

## 7.1. Navigation Sensors

Different types of sensors can be used to obtain information about a vehicle's state variables. Some of them can, however, be harder to implement for this mission. If these types of sensors were implemented as navigation or relative navigation, care would have to be taken with respect to the accuracy of the results. Margins of errors should be included to tackle this. They are the following:

- **Star and Sun sensors, navigation cameras/imagers:** These can hardly be used for the mission at hand, due to the atmosphere's high opacity, and presence of clouds. A way to implement cameras as navigation sensors would be to have cameras on both the relay spacecraft and the atmospheric vehicle, and be able to position the atmospheric vehicle with respect to certain atmospheric/cloud visual elements observed in orbit and descent at Uranus, so as to be able to retrieve the atmospheric vehicle's relative position with respect to these elements, and thus to the relay spacecraft. That position could then be made inertial, assuming the relay spacecraft's position and velocity is known from its own navigation system.
- **Laser ranging:** Laser ranging seems like a poor candidate for a navigation sensor in Uranus' atmosphere. The distance between the atmospheric vehicle and the relay spacecraft is typically deduced by measuring the time of flight of a short flash of infrared laser radiation, which should reflect on the planet's surface and be sent back to the vehicle. However, there is no proof that Uranus possesses a surface, and performing laser ranging between two vehicles would present a too demanding pointing accuracy.

Due to the limitations mentioned above, four other potential sensors were identified for the mission at hand: an Inertial Measurement Unit (IMU) containing a three-axis accelerometer and gyroscope, an Atmospheric Structure Instrument (ASI) containing an accelerometer, a temperature sensor, and a pressure sensor, an Ultra High Frequency (UHF) transceiver to use radio ranging providing range and range rate measurements between the gliders and the orbiter, and a Flush Air Data Sensor (FADS) measuring atmospheric static pressure, and producing dynamic pressure, velocity, angle-of-attack, and side-slip angle estimates. These four instruments are presented in the following sections.

### 7.1.1. Inertial Measurement Unit (IMU)

IMUs consist of accelerometers and gyroscopes. A set of three non-collinear accelerometers are needed to measure accelerations in three dimensions, with respect to the ambient acceleration due to gravity. Gyroscopes are used to measure angular velocities. There exists a number of errors that can make the IMU's measurements to be different from reality. They are the following: bias, scale factor, saturation, dead zone, non-linearity, sign asymmetry, hysteresis, quantisation, and misalignments. The most realistic IMU is one which incorporates all mentioned errors. However, a simpler model can be used for simulations in atmospheric entry studies. In that

**Table 7.1:** IMU $1\sigma$ errors, taken from Mooij and Chu (2002).

| Accelerometer | | Gyroscope | |
|---|---|---|---|
| $s_x$ | $2 \cdot 10^{-4}$ | $s_p$ | $2 \cdot 10^{-4}$ |
| $s_y$ | $-1.7 \cdot 10^{-4}$ | $s_q$ | $-1.7 \cdot 10^{-4}$ |
| $s_z$ | $2.3 \cdot 10^{-4}$ | $s_r$ | $2.3 \cdot 10^{-4}$ |
| $m_{xy}$ | $10^{-6}$ | $m_{pq}$ | $10^{-6}$ |
| $m_{xz}$ | $-10^{-6}$ | $m_{pr}$ | $-10^{-6}$ |
| $m_{yx}$ | $-10^{-6}$ | $m_{qp}$ | $-10^{-6}$ |
| $m_{yz}$ | $2 \cdot 10^{-6}$ | $m_{qr}$ | $2 \cdot 10^{-6}$ |
| $m_{zx}$ | $-10^{-6}$ | $m_{rp}$ | $-10^{-6}$ |
| $m_{zy}$ | $2 \cdot 10^{-6}$ | $m_{rq}$ | $2 \cdot 10^{-6}$ |
| $b_x$ | $3 \cdot 10^{-4}$ | $b_p$ | $4 \cdot 10^{-6}$ |
| $b_y$ | $-3.5 \cdot 10^{-4}$ | $b_q$ | $-5 \cdot 10^{-6}$ |
| $b_z$ | $3 \cdot 10^{-4}$ | $b_r$ | $3 \cdot 10^{-6}$ |

case, only the bias $b$, scale factor $s$, and misalignments $m$ are taken into account. For the accelerometers, the model is as follows:

$$\mathbf{a_m} = \mathbf{a} + \begin{pmatrix} b_x \\ b_y \\ b_z \end{pmatrix} + \begin{pmatrix} s_x \\ s_y \\ s_z \end{pmatrix} \mathbf{a} + \begin{bmatrix} 0 & m_{xy} & m_{xz} \\ m_{yx} & 0 & m_{yz} \\ m_{zx} & m_{zy} & 0 \end{bmatrix} \mathbf{a} = \mathbf{b_a} + (\mathbf{I} + \mathbf{S_a})\mathbf{a} \quad \text{with} \quad \mathbf{S_a} = \begin{bmatrix} s_x & m_{xy} & m_{xz} \\ m_{yx} & s_y & m_{yz} \\ m_{zx} & m_{zy} & s_z \end{bmatrix} \tag{7.1}$$

The acceleration $\mathbf{a}$ represents the difference between the real acceleration and the acceleration due to gravity expressed with respect to the body frame. The bias, scale factor, and misalignments are commonly modelled as random walks, which can be modelled using normally distributed white noise parameters (Farrell and Barth, 1999). In this work, however, the IMU bias, scale factor, and misalignment errors are kept constant but unknown when estimating them in the navigation filter, so as to represent the values at which they would each converge to after in-flight calibration. It is left as a recommendation for future work to make these errors vary with time as a random-walk process (see Equation (3.171) in the work of Farrell and Barth (1999) for the bias error for example). The gyroscopes are modelled as in the following equation, and the bias, also called gyroscope drift, can be modelled similarly to the acceleration bias. The values of the errors included in this sensor are listed in Table 7.1. For the scope of this study, they are taken from the work of Mooij and Chu (2002), but should be reviewed based on accelerometer and gyroscope specifications from the IMU supplier.

$$\boldsymbol{\omega}_\mathbf{m} = \boldsymbol{\omega} + \begin{pmatrix} b_p \\ b_q \\ b_r \end{pmatrix} + \begin{bmatrix} s_p & m_{pq} & m_{pr} \\ m_{qp} & s_q & m_{qr} \\ m_{rp} & m_{rq} & s_r \end{bmatrix} \boldsymbol{\omega} = \mathbf{b}_\omega + (\mathbf{I} + \mathbf{S}_\omega)\boldsymbol{\omega} \tag{7.2}$$

### 7.1.2. Atmospheric Structure Instrument (ASI)

The ASI consists of an accelerometer, a pressure, and a temperature sensor. It outputs static temperature, pressure, the vehicle's acceleration due to the experienced drag force, as well as the atmospheric density, from which the speed of sound and the ortho- to para-hydrogen ratio can be deduced. The modelling of this sensor is illustrated in Fig. 7.1. The accelerometer determines the vehicle's acceleration due to drag from the drag force retrieved from the software's Flight Dynamics module. The drag coefficient $C_D$ is computed by interpolating through the reference vehicle's drag coefficient database generated with XFLR5, using the angle-of-attack and measured velocity from the FADS instrument, the control surfaces deflection values, as well as the altitude derived from the temperature sensor's measured temperature as inputs to the drag coefficient Lookup tables. The drag coefficients from the vehicle's clean configuration, the deflection of the elevator, rudder, and ailerons are added together to yield the vehicle's total drag coefficient for the current flight conditions. The atmospheric density is then computed as in Equation (7.3), where $m$ is the vehicle's mass, $a_D$ its acceleration due to the drag force, $C_D$ its drag coefficient, $S_{ref}$ its reference area, and $V$ the glider's velocity relative to the atmosphere in the direction of the descent trajectory, which is also taken as the velocity measured with the FADS instrument.

$$\rho = \frac{2ma_D}{C_D S_{\text{ref}} V^2} \tag{7.3}$$

The density measurement is then fed to the pressure sensor module where the static pressure is determined by subtracting the dynamic pressure to a database of total pressures. The temperature and pressure sensors are inspired from those presented by Ferri et al. (2020), where the former uses wire resistance thermometers and the latter consists of a pitot tube surrounded by a Kiel probe shielding. The temperature sensor uses two Resistance Temperature Detectors (RTDs) whose principle is based upon the Callendar-Van Dusen equation, which is used in this study to generate the instrument's data:

$$R_T = R_0\left(1 + AT + BT^2 + (T - 100)CT^3\right) \tag{7.4}$$

Here, $R_T$ represents the resistance in $\Omega$ at temperature $T$ in °C, $R_0$ is the resistance at $T = 0$ °C, and $A$, $B$, and $C$ are material resistance constants. For a typical platinum resistance thermometer (PT 100/15A resistor), these constants are the following: $A = 3.90830 \cdot 10^{-3}$ °C$^{-1}$, $B =$ -5.77500 $\cdot 10^{-7}$ °C$^{-1}$, $C =$ -4.18301 $\cdot 10^{-12}$ °C$^{-1}$, and $R_0 = 100.0\ \Omega$.

Ferri et al. (2020) established the error of the ASI temperature sensor to be of 0.1 K. A sensor noise with standard deviation of 0.05 K was thus included. This error, as well as the FADS one is carried on to the computation of the atmospheric density and pressure, so no additional errors are included in the ASI pressure sensor. For additional scientific value, the ortho to para-hydrogen ratio can be deduced from the speed of sound calculated with the measured temperature, the specific gas constant $R$, the atmosphere's mean molecular weight (from the mass spectrometer), and the planet's adiabatic index $\gamma_{ad}$ using Equation (4.7).

### 7.1.3. Ultra High Frequency (UHF) Transceiver

The design of different Mars approach, entry, descent, and landing phase missions has led to the development of an innovative navigation scheme for state estimation. This scheme relies on radio communication (such as an emitting beacon) as sensor measurements, to retrieve range and relative velocity quantities. NASA has developed the Electra ultrahigh frequency (UHF) transceiver, that enables Doppler measurements between an orbiter and a vehicle in approach of the surface of Mars. It can operate in both one-way or two-way tracking mode, and was demonstrated to be capable of achieving a 300 m or better atmospheric entry knowledge error to enable pinpoint landing (Lightsey et al., 2008). The radiometric measurements can then be combined with the IMU measurements, to yield parameters such as the vehicle's position, velocity, lift-to-drag ratio, and atmospheric density, as shown in the work of Levesque and Lafontaine (2007). Along with a default IMU-based navigation scenario where two out of six state parameters converged, Levesque and Lafontaine (2007) analysed four navigation scenarios based on radio ranging. In the first scenario, radio ranging from a reference beacon is used in addition to the IMU measurements. Compared to the default IMU-based navigation scenario, this augmented system improved the estimation accuracy only slightly: three out of six states converged. The second scenario made use of an additional second radio-ranging measurement, while the third scenario included a third known reference beacon to the system, increasing accuracy on the atmospheric density measurements. Five and six out of six state parameters converged, respectively. In the fourth scenario, a proof-mass is released at the same time as the vehicle, to benefit from the same initial conditions. It follows a free-falling ballistic trajectory and experiences the same initial atmospheric conditions as the vehicle. Knowing the proof-mass' aerodynamic coefficients perfectly (such as the one of a sphere), the following assumption can then be made: any difference between the real and modelled aerodynamics of the vehicle can be observed through the proof-mass range measurement. The measurement accuracy of this fourth scenario showed that a free-falling beacon can replace additional in-orbit spacecraft to provide range measurements.

The UHF transceiver is used to conduct a Doppler wind experiment, yielding Doppler residuals between gliders and the orbiter, as well as between the two gliders, from which wind speeds and the presence of microwave absorbers (clouds, water, hydrogen sulfide, ammonia) can be determined. To yield the pseudo range, the pseudo range rate, but also the Doppler residuals, the wind speed, and the presence of microwave absorbers, this sensor should be modelled as in Fig. 7.2, where the emitting signal source is referred to as 'emitter', and the receiving one as the 'observer'. For this thesis, only the pseudo range and the pseudo range rate were computed. The emitter and observer's location and velocity are provided by the software's Flight Dynamics module. The following equation is used to calculate the pseudo range $\tilde{\rho}$ and pseudo range rate $\dot{\tilde{\rho}}$ of the emitter.

$$\tilde{\boldsymbol{\rho}} = c\,(t_R - t_T) = \sqrt{(\mathbf{r_o} - \mathbf{r_g})^T(\mathbf{r_o} - \mathbf{r_g})} \qquad \text{and} \qquad \dot{\tilde{\boldsymbol{\rho}}} = c\left(1 - \frac{f_T}{f_R}\right) = \frac{(\mathbf{r_o} - \mathbf{r_g})^T(\dot{\mathbf{r_o}} - \dot{\mathbf{r_g}})}{\sqrt{(\mathbf{r_o} - \mathbf{r_g})^T(\mathbf{r_o} - \mathbf{r_g})}} \tag{7.5}$$

Here, the subscripts $T$ and $R$ correspond to transmitter of receiver frequency or clock time, respectively. The variables $\mathbf{r_o}$ and $\mathbf{r_g}$ correspond to the position coordinates of the orbiter and glider, respectively. Their derivatives are denoted as $\dot{\mathbf{r_o}}$ and $\dot{\mathbf{r_g}}$, and $c$ is the speed of light.

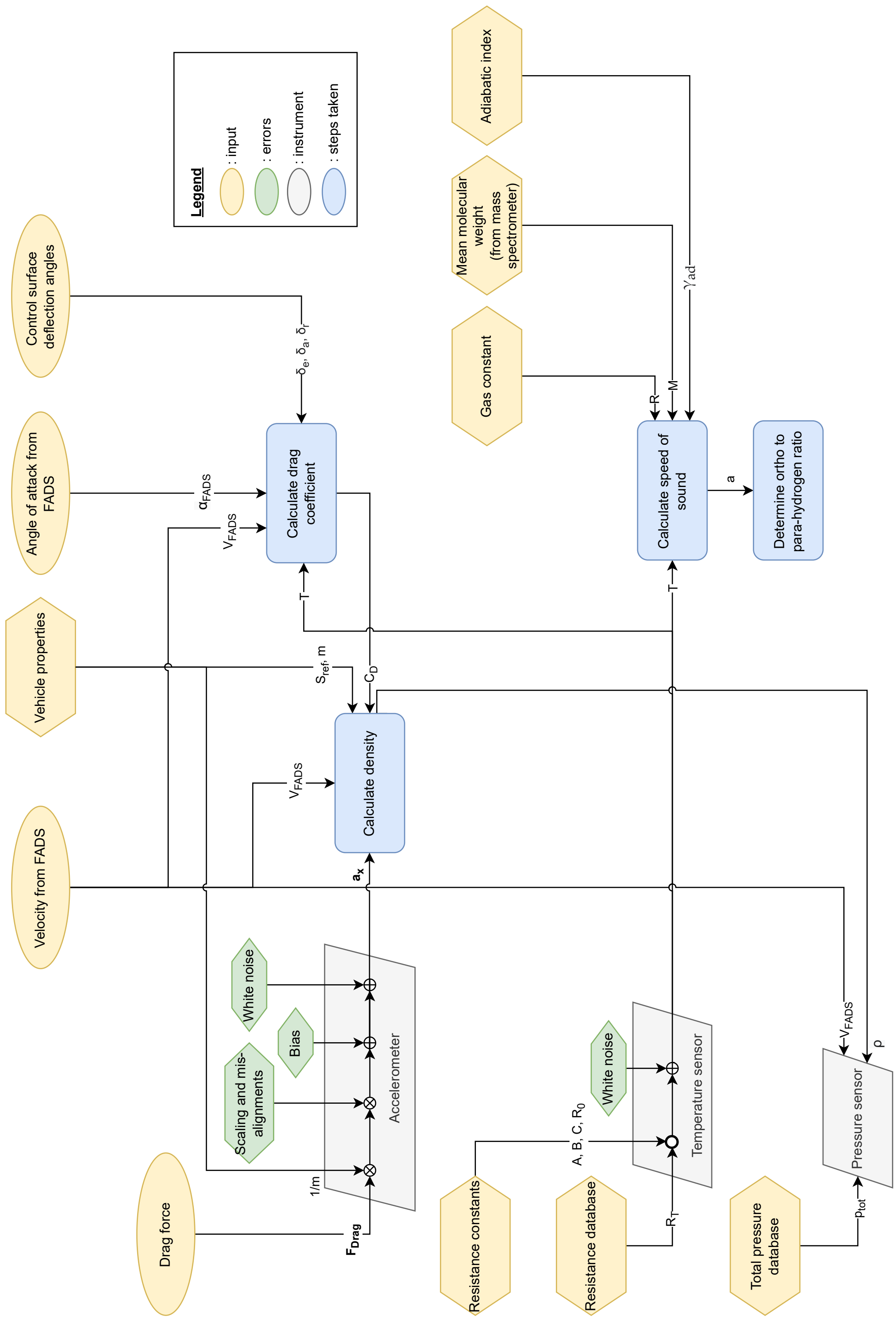


**Figure 7.1:** Block diagram of Atmospheric Structure Instrument.

**Table 7.2:** Locations of eight pressure ports used for FADS measurement (Cobleigh et al., 1999).

| Port number | Clock angle [°] | Cone angle [°] | Primary use |
|---|---|---|---|
| 1 | 16.1 | 0 | $\alpha$, $\beta$ |
| 2 | 38.6 | 0 | $\alpha$, $\beta$ |
| 3 | 61.1 | 0 | $\alpha$ |
| 4 | 6.4 | 180 | $\alpha$, $\beta$ |
| 5 | 28.9 | 180 | $\alpha$ |
| 6 | 45 | 90 | $\beta$ |
| 7 | 45 | -90 | $\beta$ |
| 8 | 90 | 0 | $\alpha$ |

A bias error and a white noise error are introduced both to the pseudo range and pseudo range rate measurements. For the pseudo range, a bias of 1 m is introduced, as well as a white noise with standard deviation of 25 m, while for the pseudo range rate measurements, a drift of 0.4 m/s is added, as well as a white noise error with a standard deviation of 0.1 m/s (Mooij and Chu, 2002).
The Doppler shift is the change in frequency of a wave in relation to an observer who is moving relative to the wave source (Giordano, 2009). Mulder et al. (1999) relates Doppler shift $\Delta f$ and the derivative of the pseudo-range $\dot{\tilde{\rho}}$ as follows:

$$\Delta f = f_T - f_R = \frac{\dot{\tilde{\rho}} f_T}{c} \tag{7.6}$$

Here, $f_T$ and $f_R$ are the transmitted and received signal frequency respectively.

### 7.1.4. Flush Air Data Sensor (FADS)

The FADS system is a non-intrusive sensing system concept defined by Cobleigh et al. (1999), in which air data are inferred from surface pressure measurements on the front side of the body. A mathematical algorithm then relates the measured pressures to the air data state. This system was wind tunnel tested, behaving well from Mach 0.25 to Mach 5, an angle-of-attack extending to greater than 30°, and an angle of side-slip range extending to greater than 15°. It was mentioned at the beginning of this section that the pressure-altitude profile of Uranus is not well known. This type of sensor could thus not be used efficiently for navigation of a single vehicle. However, by comparing the values of pressure measured at different locations on Uranus, this sensor could serve for relative navigation purposes, between multiple atmospheric vehicles. There are two potential solutions to using this instrument with more confidence. First of all, the pressure-altitude profile of Uranus could be studied from the orbiting spacecraft with the use of radio occultation measurements similar to the ones performed by Voyager 2 before the gliders' flight. This could help constrain the pre-defined pressure profile for at least the first few kilometres of atmospheric depth, to better calibrate and interpret the FADS measurements. Another solution could be to correlate the FADS pressure measurements to the ones performed by the pressure sensor of the ASI. With an estimate of both sensors' error margins, a better on-board pressure measurement can be yielded. More information on implementation theory of such a system for both uniform flow over a sphere and modified Newtonian impact theory, can be found in the work of Cobleigh et al. (1999).

This sensor was modelled and verified in the work of Rijnsdorp (2017), and a similar design was implemented for this work. The sensor consist of a first module which generates total pressure measurements at eight defined locations on the aircraft's nose, an angle-of-attack estimator, a side-slip angle estimator, a total and dynamic pressure estimator, and a Mach number calculating module. The same pressure ports locations as in Cobleigh et al. (1999), Rijnsdorp (2017), and Ellsworth and S. Whitmore (2007) were implemented, as listed in Table 7.2 and shown in Table 7.2.

In his work, Rijnsdorp (2017) only used the static pressure measurement outputs as navigation sensor input. In this work, however, the outputted Mach number is translated to a velocity measurement by multiplying it by Equation (4.7), where the measured temperature from the ASI sensor is used. It is used as an input to the calculation of both the atmospheric density and pressure of the ASI sensor. This sensor's estimated angle-of-attack is also used as an input to the calculation of the atmospheric density in the ASI sensor.

A complete explanation of the equations used in the sensor's different modules, as well as their verification and performance is present in the work of Rijnsdorp (2017). Potential errors that can be included to make the modelling of this instrument more realistic include: an upwash correction in angle-of-attack, a sidewash

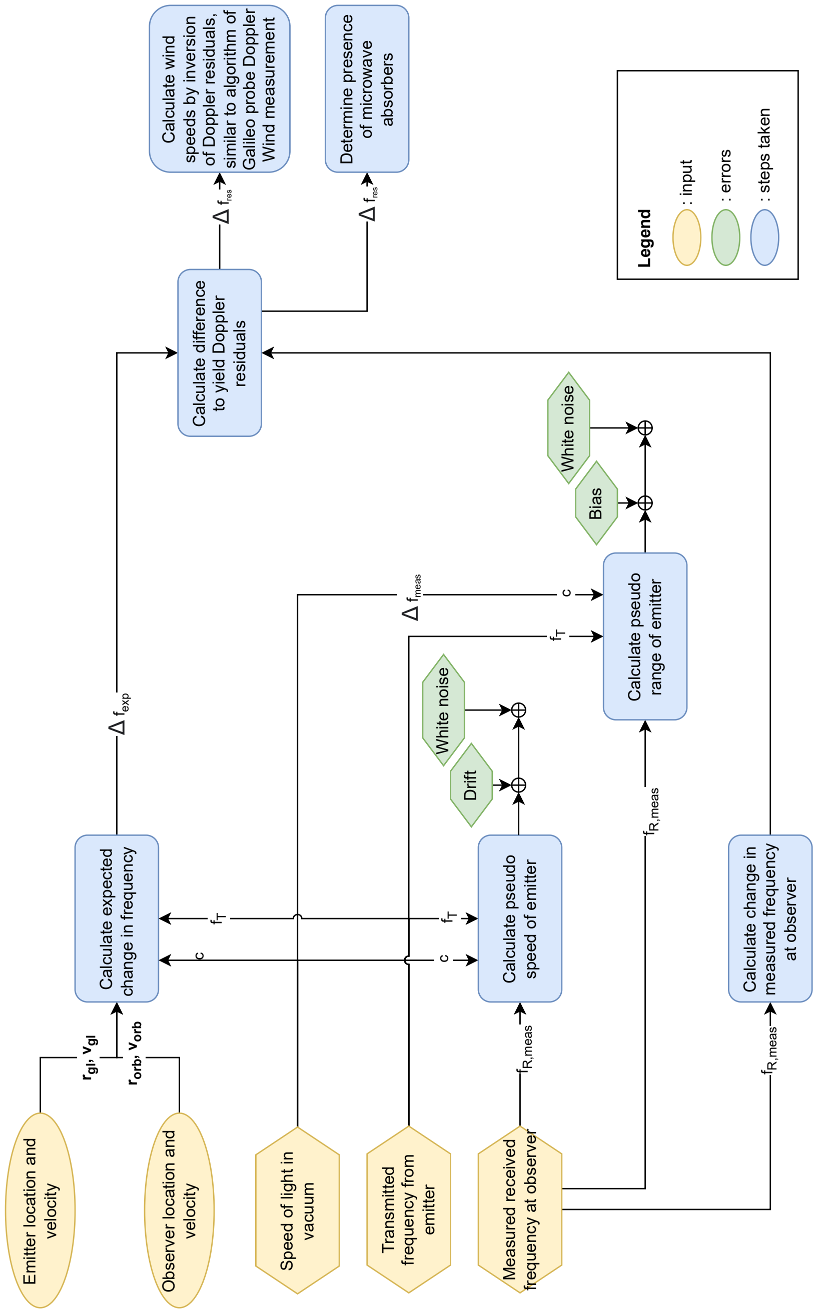


**Figure 7.2:** Block diagram of Ultra High Frequency transceiver.

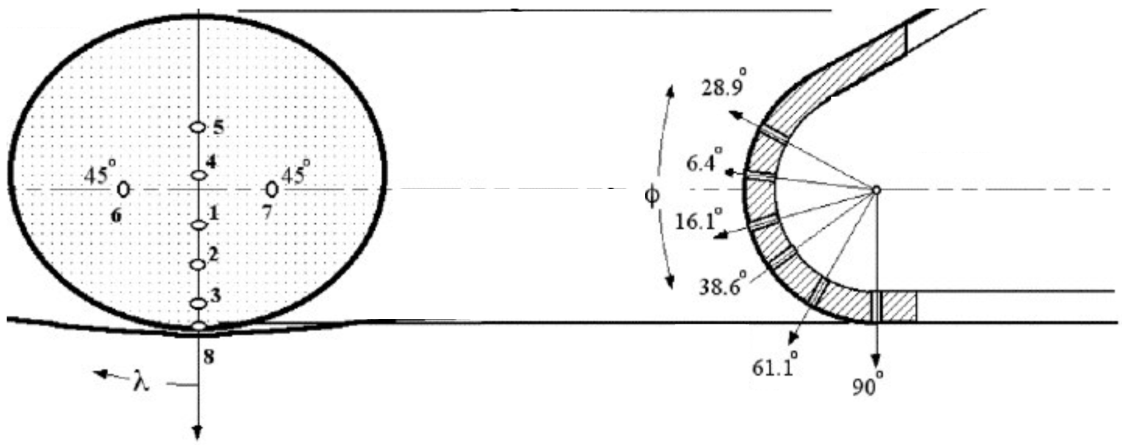


**Figure 7.3:** Vehicle nose showing locations of FADS pressure ports (Ellsworth and S. Whitmore, 2007).

correction in side-slip angle, a misalignment in both the clock and cone angles which define the position of the pressure inlets on the vehicle's nose, changing the value of measured static pressure to account for viscous interactions, drag experienced by the air stream in the tubes of the sensor's hardware, thermodynamic effects in the tubes, and including errors due to quantization inaccuracies of the instrument's transducers (S. A. Whitmore and Moes, 1994). Out of all errors mentioned by S. A. Whitmore and Moes (1994), none were included in the work of (Rijnsdorp, 2017), as all of them were considered negligible for low Mach number applications. A sensor noise is still considered in the generation of the static pressure measurement, with standard deviation of 1 N/m$^2$ (Rijnsdorp, 2017).

### 7.1.5. Benefits, Limitations, and Implementation of Sensor Outputs

Before explaining how the outputs of every sensor are used as inputs to the navigation filter, a short summary of their benefits and limitations is given below:

## IMU

- **Benefits:** Most navigation filter designs are based on IMU measurements, which means that this kind of filter design was supported by a lot of mission heritage.
- **Limitations:** An acceleration and acceleration rate measurement must be produced for every axis, but that is what a typical IMU usually produces.

## ASI

- **Benefits:** The temperature and pressure measurements can be translated to an altitude measurement, using the atmospheric models described in Section 3.4. The speed of sound calculation made with this sensor's outputs can contribute to Uranus' wind model, as well as to the calculation of the vehicle's Mach number.
- **Limitations:** Translating the measured temperature and pressure to an altitude before passing it to the navigation filter creates a loosely-coupled system, which could be outperformed by a tightly-coupled system (Mooij and Chu, 2002), where temperature and pressure data are directly used in the navigation filter. This also leads to different errors than the ones expected by a tightly-coupled system, as the data used as input to the navigation filter is already processed, thus prone to carrying a processing error to the filter. Moreover, as the deduced altitude is interpolated from Lookup tables containing theoretical pre-flight data, this introduces a small error, resulting in an altitude which does not perfectly match the real one. However, it contributes to represent any sensor measurement error.

## UHF

- **Benefits:** The pseudo range and pseudo range rate measurements can be implemented the same way as GPS measurements would. This makes the filter design more accessible as most navigation filters used for Earth-based vehicles rely on GPS measurements, so heritage of this application could be used for this mission's filter design. With the orbiter's position being known inertially, this sensor can contribute to knowing the gliders' relative and inertial position.

- **Limitations:** The orbiter's position and velocity must be accurately known, which means that a reliable GNC suite must be present on-board the orbiter. This can be tackled by making use of the NASA Deep Space Network and ground segment support.

### FADS

- **Benefits:** The sensor's estimators are very powerful and yield results very similar to the real values, with just the pressure inlets' positions and measured pressure values as inputs. The angle-of-attack and side-slip angle errors are in the order of $10^{-11}$ degrees when no errors are included in the system. The Mach number error is of $10^{-7}$ m/s, the dynamic pressure error of $10^{-9}$ kg/m$^3$, the static pressure error of $10^{-9}$ Pa, and the deduced velocity error is of $10^{-4}$ m/s.
- **Limitations:** It is recommended for the nose of the chosen reference vehicle to be blunt. A fuselage was not included in the generation of the GL-1 vehicle's aerodynamic coefficients, as recommended in the XLFR5 documentation. A dummy fuselage was however included to have an estimate of the pressure inlet locations on the vehicle's nose. Another limitation of this sensor concerns its computation time: it is the instrument which takes the most time to run, mainly due to the implementation of its angle-of-attack and side-slip angle estimators.

The sensor measurements used as navigation inputs are the following: **the altitude from the ASI pressure and temperature sensors, the pseudo range and pseudo range rate between orbiter and glider from the UHF transceiver, and the glider's velocity from the FADS**. The acceleration and rotational rates measured by the IMU are integrated in the navigation filter, and their bias and drift errors are estimated.

## 7.2. Navigation Estimator

Estimators are used to fuse together data from different measurement sensors, to yield the best estimate of state variables, thereby reducing the errors that are present in each of the individual sensor data components. A Linear Kalman Filter (LKF) is most commonly used to do so, but cannot be applied to most real-life situations, which are typically non-linear. Other types of estimators can be used for non-linear applications: Extended Kalman Filters (EKF), Unscented Kalman Filters (UKF), Particle Filters, and Divided Difference Filters for example. An Extended Kalman Filter (EKF) uses a first-order Taylor series approximation of the non-linear system around the current estimate. It is the most used system for non-linear applications. On the other hand, Unscented Kalman Filters use multiple points (called sigma points, which are weighted) instead of using only the mean, yielding a more accurate approximation. A Particle Filter uses a sequential Monte Carlo method. Instead of deriving analytic equations, the Particle Filter uses simulation methods to generate estimates of the state. It gives more accurate results for applications with non-linear and/or non-gaussian environments, at the price of additional computational effort. Finally, the advantage of Divided Difference Filters is that no calculation of the Jacobian is needed as for the Extended Kalman Filters, and it does not need to use several parameters, as for the Unscented Kalman Filters and Particle Filters.

Due to its high accuracy and especially its fastest computation time out of the filters mentioned above, **an EKF was implemented in the navigation system design of this thesis**. Moreover, it was found that an UKF only showcases a slightly better performance, as compared to an EKF, when used to estimate position of an integrated navigation information system (St-Pierre and Gingras, 2004). It is also demonstrated that for the navigation design of St-Pierre and Gingras (2004), an UKF is less performant than an EKF when no GPS measurements are used, which is the case for this thesis' mission. Finally, potential linearisation errors of an EKF were also deemed negligible. The accuracy of an EKF can thus satisfy the mission requirements.

### 7.2.1. Extended Kalman Filter (EKF)

The theoretical modelling of an EKF will be described below (Welch and G. Bishop, 1995). The non-linear system is expressed as follows:

$$\mathbf{x}_{k+1} = \mathbf{f}(\mathbf{x}_k, \mathbf{u}_k, \mathbf{w}_k) \tag{7.7}$$

With the following measurement:

$$\mathbf{z}_k = \mathbf{h}(\mathbf{x_k}, \mathbf{v_k}) \tag{7.8}$$

Here, $\mathbf{x}$ is the state vector, $\mathbf{u}$ the input vector, $\mathbf{z}$ is the measurement vector, and $\mathbf{v}$ and $\mathbf{w}$ are noise vectors. Subscript $k$ denotes the current time step, while subscript $k+1$ denotes the next time step. The noises included in these equations can be related to covariance matrices. They can be modeled as probability functions with a normal distribution, as shown by the following notation:

$$\begin{aligned} p(\mathbf{v}_k) &\sim N(0, \mathbf{R_k}) \\ p(\mathbf{w}_k) &\sim N(0, \mathbf{Q_k}) \end{aligned} \tag{7.9}$$

The matrices $\mathbf{R}_k$ and $\mathbf{Q}_k$ represent the measurement noise and process noise matrices. They are diagonal, so that for each probability element of vectors $\mathbf{v}_k$ and $\mathbf{w}_k$, a normal distribution holds, with a mean of zero and a variance from the matrices $\mathbf{R}_k$ and $\mathbf{Q}_k$. In the prediction step of the filter, the so-called *a priori* estimate $\hat{\mathbf{x}}_{k+1}^-$ can be derived from the previous *a posteriori* estimate $\hat{\mathbf{x}}_k$ and is expressed as follows:

$$\hat{\mathbf{x}}_{k+1}^- = \mathbf{f}(\hat{\mathbf{x}}_k, \mathbf{u}_{k+1}, 0) \tag{7.10}$$

The measurement can then be estimated as follows:

$$\hat{\mathbf{z}}_k = \mathbf{h}(\hat{\mathbf{x}}_k^-, 0) \tag{7.11}$$

Equations for both the state and the measurements can then be obtained by linearising an estimate about Equations (7.10) and (7.11):

$$\begin{aligned} \mathbf{x}_{k+1} &\approx \hat{\mathbf{x}}_{k+1}^- + \mathbf{A}_k(\mathbf{x}_k - \hat{\mathbf{x}}_k) + \mathbf{W}_k\mathbf{w}_k \\ \mathbf{z}_k &\approx \hat{\mathbf{z}}_k + \mathbf{H}_k(\mathbf{x}_k - \hat{\mathbf{x}}_k^-) + \mathbf{V}_k\mathbf{v}_k \end{aligned} \tag{7.12}$$

Here, $\mathbf{A}$, $\mathbf{H}$, $\mathbf{V}$, and $\mathbf{W}$ are Jacobians used to linearise the system. Their coefficients are obtained by differentiating functions $\mathbf{f}$ and $\mathbf{h}$ with respect to the state and noise variables, as follows:

$$\begin{aligned} \mathbf{A}_k &= \left.\frac{\partial \mathbf{f}}{\partial \mathbf{x}}\right|_{(\hat{\mathbf{x}}_k, \mathbf{u}_k, \mathbf{0})} \\ \mathbf{W}_k &= \left.\frac{\partial \mathbf{f}}{\partial \mathbf{w}}\right|_{(\hat{\mathbf{x}}_k, \mathbf{u}_{k+1}, \mathbf{0})} \\ \mathbf{H}_k &= \left.\frac{\partial \mathbf{h}}{\partial \mathbf{x}}\right|_{(\hat{\mathbf{x}}_k^-, \mathbf{0})} \\ \mathbf{V}_k &= \left.\frac{\partial \mathbf{h}}{\partial \mathbf{v}}\right|_{(\hat{\mathbf{x}}_k^-, \mathbf{0})} \end{aligned} \tag{7.13}$$

Then the errors generated during the approximation of the state and the measurements in Equation (7.12) can be described as follows:

$$\begin{aligned} \hat{\mathbf{e}}_{xk}^- &\equiv \mathbf{x}_k - \hat{\mathbf{x}}_k^- \approx \mathbf{A}_{k-1}\left(\mathbf{x}_{k-1} - \hat{\mathbf{x}}_{k-1}\right) + \boldsymbol{\epsilon}_k \\ \hat{\mathbf{e}}_{zk}^- &\equiv \mathbf{z}_k - \hat{\mathbf{z}}_k \approx \mathbf{H}_k\left(\hat{\mathbf{e}}_{xk}^-\right) + \boldsymbol{\eta}_k \end{aligned} \tag{7.14}$$

The variables $\boldsymbol{\epsilon}$ and $\boldsymbol{\eta}$ are linear approximations of the noise parameters $\mathbf{w}$ and $\mathbf{v}$. The distribution of these variables is as follows:

$$\begin{aligned} p\left(\boldsymbol{\epsilon}_k\right) &\sim N\left(\mathbf{0}, \mathbf{W}_{k-1}\mathbf{Q}_{k-1}\mathbf{W}_{k-1}^T\right) \\ p\left(\boldsymbol{\eta}_k\right) &\sim N\left(\mathbf{0}, \mathbf{V}_k\mathbf{R}_k\mathbf{V}_k^T\right) \end{aligned} \tag{7.15}$$

The prediction error estimate is found from the difference between the *a priori* and *a posteriori* errors, and should be equivalent to the state update:

$$\hat{\mathbf{e}}_k \equiv \hat{\mathbf{x}}_k - \hat{\mathbf{x}}_k^- \equiv \mathbf{K}(\hat{\mathbf{e}}_{zk}^-) = \mathbf{K}(\mathbf{z}_k - \hat{\mathbf{z}}_k^-) \tag{7.16}$$

The *a posteriori* state estimate can be expressed as follows, with $\mathbf{K}$ being a Kalman gain:

$$\hat{\mathbf{x}}_k = \hat{\mathbf{x}}_k^- + \mathbf{K}(\mathbf{z}_k - \hat{\mathbf{z}}_k^-) \tag{7.17}$$

The covariance matrix $\mathbf{P}$ can be propagated as follows:

$$\mathbf{P}_{k+1}^- = \mathbf{A}_k\mathbf{P}_k\mathbf{A}_k^T + \mathbf{W}_k\mathbf{Q}_k\mathbf{W}_k^T \tag{7.18}$$

With the gain matrix being calculated as follows:

$$\mathbf{K}_k = \mathbf{P}_k^-\mathbf{H}_k^T(\mathbf{H}_k\mathbf{P}_k^-\mathbf{H}_k^- + \mathbf{V}_k\mathbf{R}_k\mathbf{V}_k^T)^{-1} \tag{7.19}$$

### 7.2.2. Implementation of EKF in 3 DoF and 6 DoF

An EKF was designed for both the 3 DoF (translational) and 6 DoF cases of this simulator. It must be noted that for both cases, the same sensor suite is used as a basis (IMU, ASI, FADS, and UHF transceiver), with the addition of a position measurement in x-direction for both cases, and quaternion measurements for the 6 DoF case. The importance of these additional fictional measurements is explained in Section 7.2.3. The sate vectors for both cases are as follows:

$$\mathbf{x_{3DoF}} = [X, Y, Z, V_X, V_Y, V_Z, b_X, b_Y, b_Z]^T \tag{7.20}$$

$$\mathbf{x_{6DoF}} = [X, Y, Z, V_X, V_Y, V_Z, Q_1, Q_2, Q_3, Q_4, b_X, b_Y, b_Z, d_X, d_Y, d_Z]^T \tag{7.21}$$

Here, the position coordinates $X, Y, Z$ and velocity coordinates $V_X, V_Y, V_Z$ are expressed in the rotating reference frame, $Q_1, Q_2, Q_3, Q_4$ represent the quaternions, $b_X, b_Y, b_Z$ the IMU bias components, and $d_X, d_Y, d_Z$ the IMU drift components. The measurement matrix $\mathbf{H}$ given in Equation (7.13) is computed at every time step, with only the first six elements of the state vectors (position and velocity components) having an influence on the needed partial derivatives. The $\mathbf{H}$ measurement matrix of every designed navigation sensor will thus be given here for the first six elements of the sate vector:

$$\mathbf{H_{ASI}} = \begin{bmatrix} \frac{\partial h}{\partial X} & \frac{\partial h}{\partial Y} & \frac{\partial h}{\partial Z} & 0 & 0 & 0 & \dots \end{bmatrix} = \begin{bmatrix} \frac{X}{R} & \frac{Y}{R} & \frac{Z}{R} & 0 & 0 & 0 & \dots \end{bmatrix} \tag{7.22}$$

$$\mathbf{H_{FADS}} = \begin{bmatrix} 0 & 0 & 0 & \frac{\partial V}{\partial V_X} & \frac{\partial V}{\partial V_Y} & \frac{\partial V}{\partial V_Z} & \dots \end{bmatrix} = \begin{bmatrix} 0 & 0 & 0 & \frac{V_X}{V} & \frac{V_Y}{V} & \frac{V_Z}{V} & \dots \end{bmatrix} \tag{7.23}$$

$$\mathbf{H_{UHF}} = \begin{bmatrix} \frac{\partial \rho}{\partial X} & \frac{\partial \rho}{\partial Y} & \frac{\partial \rho}{\partial Z} & 0 & 0 & 0 & \dots \\ \frac{\partial \dot\rho}{\partial X} & \frac{\partial \dot\rho}{\partial Y} & \frac{\partial \dot\rho}{\partial Z} & \frac{\partial \dot\rho}{\partial V_X} & \frac{\partial \dot\rho}{\partial V_Y} & \frac{\partial \dot\rho}{\partial V_z} & \dots \end{bmatrix} \tag{7.24}$$

$$= \begin{bmatrix} -\frac{X_o - X}{\partial \rho} & -\frac{Y_o - Y}{\partial \rho} & -\frac{Z_o - Z}{\partial \rho} & 0 & 0 & 0 & \dots \\ -\frac{V_{X,o} - V_X}{\partial \rho} - \frac{\dot\rho}{\rho} \cdot \frac{\partial \rho}{\partial X} & -\frac{V_{Y,o} - V_Y}{\partial \rho} - \frac{\dot\rho}{\rho} \cdot \frac{\partial \rho}{\partial Y} & -\frac{V_{Z,o} - V_Z}{\partial \rho} - \frac{\dot\rho}{\rho} \cdot \frac{\partial \rho}{\partial Z} & \frac{\partial \rho}{\partial X} & \frac{\partial \rho}{\partial Y} & \frac{\partial \rho}{\partial Z} & \dots \end{bmatrix} \tag{7.25}$$

Here, $R$ and $V$ represent the norm of the position and velocity coordinates in rotating frame, respectively. The variables $\rho$ and $\dot\rho$ represent the pseudo range and pseudo range rate outputted by the UHF transceiver. The measurement matrix contribution of each sensor is taken into account by including as new rows of the main measurement matrix $\mathbf{H}$, in the order in which the different sensors' measurements are included in the navigation filter. The position, velocity, and quaternion components are given an initial error $e$ at the beginning of the simulation, as follows: $e_{pos} = [5.0, -4.0, 3.0]$ m, $e_{vel} = [0.5, -0.4, 0.3]$ m/s, $e_Q = [0.05, -0.05, -0.05]$. The *a priori* estimate $\hat{\mathbf{x}}^-_{k+1}$ is found by propagating the states using a forward Euler method. The tuning matrices $\mathbf{P}$, $\mathbf{Q}$, and $\mathbf{R}$ are different for both the 3 DoF and 6 DoF cases, as well as for the different applications studied (see Table 8.2).

### 7.2.3. Sensor Input Analysis

An analysis was conducted on the observability of the system, using "fake" position and velocity Cartesian components as navigation sensor inputs. Real position and velocity values were used, and small errors of a few meters and meters/second were added to simulate measurements. This was done to evaluate the rank of the observability matrix in order to determine how many different measurements are needed for all desired state variables to be accurately estimated, for the mission at hand. Indeed, a system is said to be observable if, and only if, there is a time $k$ for which the rank of the observability Gramian is equal to the number of state variables. The observability Gramian $\mathbf{W}$ at index $k$ is defined as follows:

$$\mathbf{W(0, k)} = \sum_{j=0}^{k-1} \boldsymbol{\phi}_j^T \mathbf{H}_j^T \mathbf{H}_j \boldsymbol{\phi} \tag{7.26}$$

Here, $\boldsymbol{\phi}$ corresponds to the system transition matrix and $\mathbf{H}$ to the measurement matrix. It was found that the mentioned six position and velocity measurements are enough to accurately estimate the nine desired state variables (position, velocity, and IMU bias components), as the observability matrix has an initial rank of 6 but reaches 9 after ten time-steps. However, the position error estimates in x-direction and y-direction were seen to stay constant at their initial value, with their covariance bounds not converging, as seen in Figure 7.4a. This phenomenon was seen to be mission-dependent, as when the glider's initial longitude coordinates were changed, the non-converging behaviour was seen in other state variables. For example, when the initial longitude was set to $\tau = 0°$ instead of $\tau = 70°$, the non-converging behaviour was seen to occur for position estimate

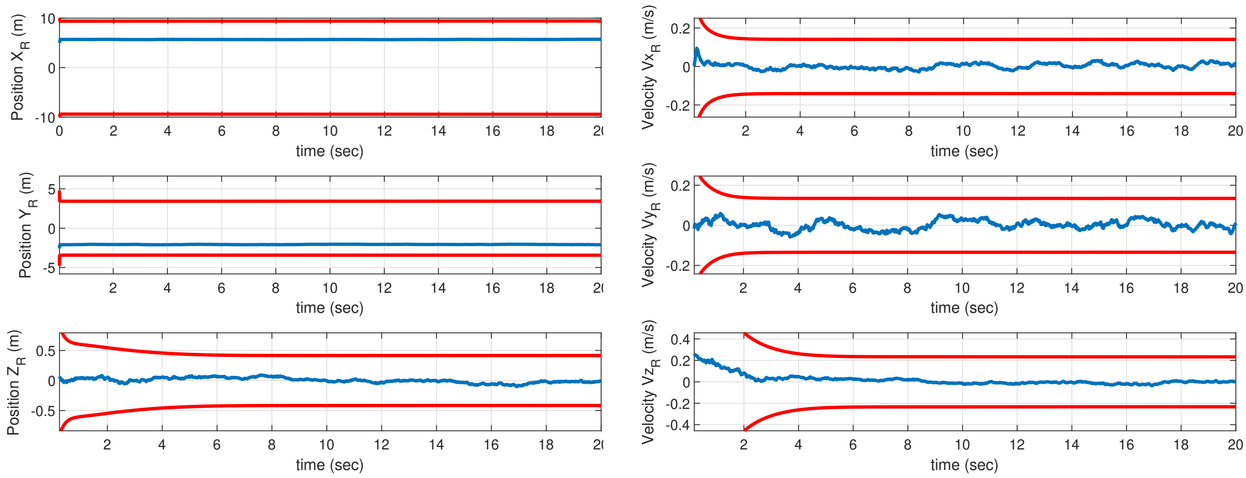


**(a)** Position error estimates without inclusion of x-position additional measurement, and initial longitude of $\tau = 70°$.

**(b)** Velocity error estimates without inclusion of x-position additional measurement, and initial longitude of $\tau = 70°$.

**Figure 7.4:** Position and velocity error estimates, no additional x-direction measurement, initial longitude of $\tau = 70°$.

in y-direction only, as shown in Figure 7.5a. The behaviour of the velocity estimates is not affected much by a change in initial longitude, as seen in Figure 7.4b and Figure 7.5b, which yield very similar results.

Four navigation sensors were designed and modelled for the purpose of this thesis: an IMU, an ASI, an UHF transceiver, and a FADS. The inclusion of their measurements in the navigation filter, however, did not lead accurate state estimates, at first. As mentioned above, the problem of having some position estimates not converging is related to the sensors' measurements not providing enough information to estimate all state variables accurately from the start of the simulation. When only including the designed sensors' measurements, the system's observability matrix has an initial rank of 4 and reaches 9 after ten time-steps as well. This, however, does not seem to suffice in making the EKF produce converging state estimations.

An analysis was thus conducted in 3 DoF, to check which additional measurement to the ones provided by the four designed sensors, would be needed to yield convergence of the state variables' error estimates and respective covariance bounds. It was found that, for the mission at hand, including an additional position measurement in x-direction yielded convergence of all state variables, as seen in Figure 7.6. When doing so, the observability matrix has an initial rank of 5, and reaches 9 after ten time-steps.

For this mission's initial conditions, an additional measurement is thus needed in x-direction, for the navigation filter to yield converging error estimates for all position and velocity variables. Multiple ways were investigated to yield a position measurement in x-direction $p_x$ from the other measurements' data and pre-existing mission knowledge. The distance $p_x$ corresponds to the radial distance between the glider and the centre of Uranus, along the x-axis of the rotating frame. They are as follows:

- First, knowledge on the geometry between both gliders, the orbiting spacecraft, and Uranus was used to retrieve a $p_x$ measurement. The formula used was as follows, with $R_{U,m}$ being Uranus' mean radius, $h_{ASI}$ the altitude retrieved from pressure and temperature measurements of the ASI data, and $\tau_{gl}$ and $\delta_{gl}$ representing the glider's longitude and latitude coordinates, respectively:

$$p_x = (R_{U,m} + h_{ASI}) \cos \tau_{gl} \cos \delta_{gl} \tag{7.27}$$

  This formula can be used because even though the orbiting spacecraft's trajectory was designed to follow the equatorial glider synchronously, their longitudes will not always be the same because of differences in estimated and real values. There thus exists a small difference between the orbiter and glider's longitudes. However, considering the different longitudes and latitudes at which each vehicle is operating, the geometry was deemed too complicated to solve for $\tau_{gl}$, and thus $p_x$ analytically.

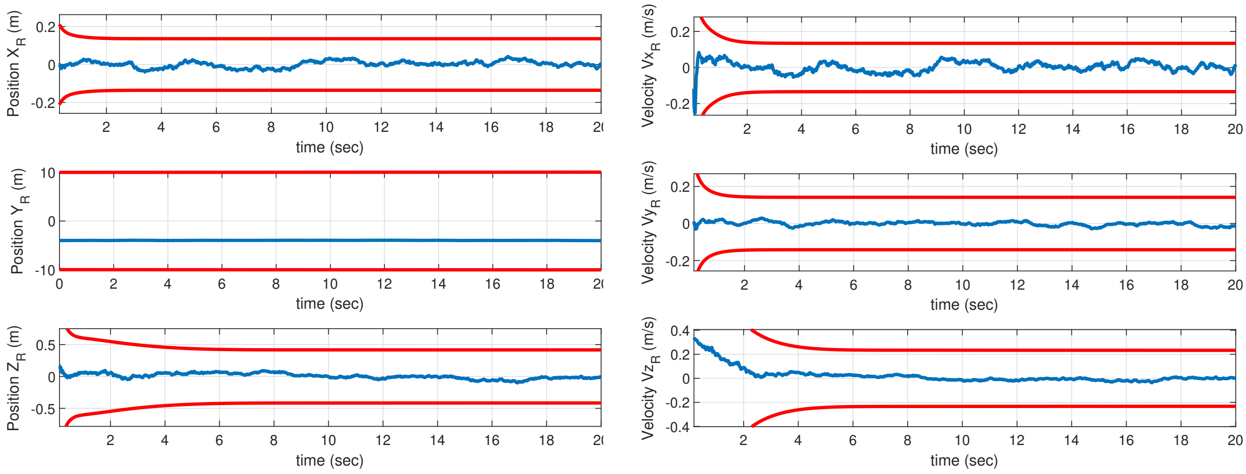


**(a)** Position error estimates without inclusion of x-position additional measurement, and initial longitude of $\tau = 0°$.

**(b)** Velocity error estimates without inclusion of x-position additional measurement, and initial longitude of $\tau = 0°$.

**Figure 7.5:** Position and velocity error estimates, without additional x-direction measurement, initial longitude of $\tau = 0°$.

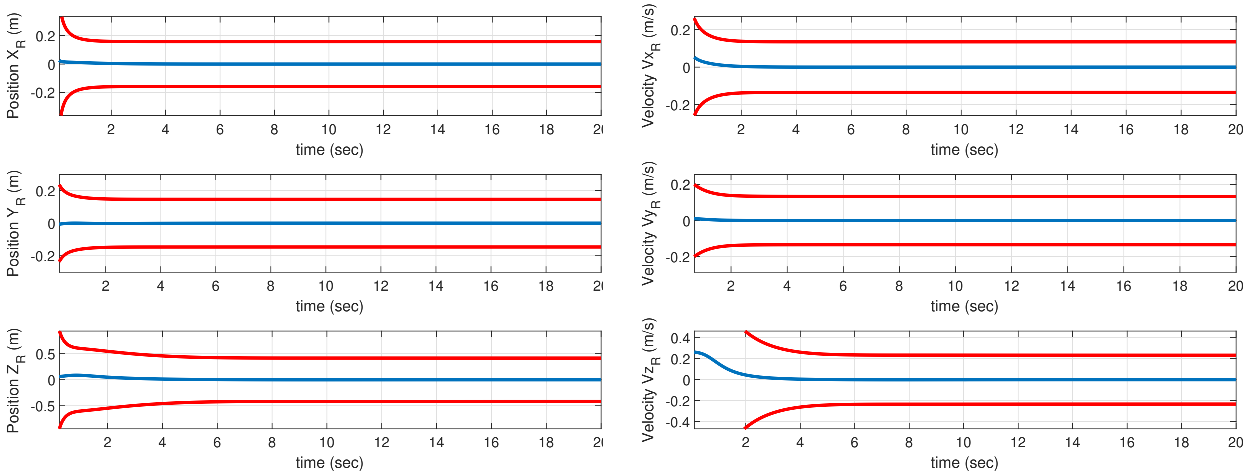


**(a)** Position error estimates with inclusion of x-position additional measurement, and initial longitude of $\tau = 70°$.

**(b)** Velocity error estimates with inclusion of x-position additional measurement, and initial longitude of $\tau = 70°$.

**Figure 7.6:** Position and velocity error estimates, with additional x-direction measurement, initial longitude of $\tau = 70°$.

- Another way to find $p_x$ was to integrate the glider's velocity components in rotating frame as follows:

$$p_x = \int_0^{t_f} \mathbf{C_{RV}} \cdot \begin{pmatrix} V_R \cos\gamma \cos\chi \\ V_R \cos\gamma \sin\chi \\ -V_R \sin\gamma \end{pmatrix} dt \tag{7.28}$$

  To solve this equation however, real values of flight-path angle $\gamma$ and transformation matrix $C_{RV}$ are needed, because they are not available from other sensors' measurements and simply using the initial values of these two quantities does not yield an accurate result for $p_x$.

- The last method that was investigated to yield a $p_x$ measurement was to integrate the IMU's acceleration measurement in x-direction twice, as follows:

$$p_x = \iint_0^{t_f} a_{x,IMU} \; dt^2 \tag{7.29}$$

  This equation was too complicated to solve analytically however, due to the inclusion of both position and velocity in y-direction, to solve for a position in x-direction, as seen in the x- and y-direction acceleration components of the equations of motion:

$$\frac{\mathrm{d}a_x}{\mathrm{d}t} = a_x + g_x + \omega_{cb}^2 x + 2\omega_{cb} v_y \tag{7.30}$$

$$\frac{\mathrm{d}a_y}{\mathrm{d}t} = a_y + g_y + \omega_{cb}^2 y - 2\omega_{cb} v_x \tag{7.31}$$

For this case as well, some real data was needed, which deceived the purpose of finding a $p_x$ measurement from other measured quantities and geometry.

**With none of these methods yielding an accurate $p_x$ measurement, it was decided to include a "fake" $p_x$ measurement, by using the real value from the simulator and adding an error to it.** This error is modelled as a white noise error with standard deviation of 0.3 m. The development of such a sensor is left as a recommendation and is explained in more detail in Section 10.3.

In 6 DoF, three additional quaternion measurements were required for the proper convergence of all state variables' error estimates and covariance bounds, as the combination of the four designed sensors and the additional $p_x$ measurement was not enough to yield accurate filter estimates. The inclusion of these three quaternion variables is done the same way as for the inclusion of a "fake" $p_x$ measurement: **the real values of the first three quaternions are included as sensor measurements, and an error is added to them.** Similarly to the fictitious $p_x$ measurement error, the quaternion errors are modelled as white noise errors with standard deviation of 0.001. The fourth quaternion is computed by taking the norm of the following expression:

$$Q_4 = \sqrt{1 - Q_1^2 - Q_2^2 - Q_3^2} \tag{7.32}$$

The inclusion of accurate quaternion measurements is all the more important, considering the fact that the other estimations rely on them through their use in the computation of the estimated $\mathbf{C_{IB}}$ transformation matrix. As a recommendation for future work, a sensor producing at least three quaternion measurements should thus be included in this mission's navigation sensor suite. This recommendation is further elaborated in Section 10.3.

## 7.3. Navigation Requirements

Additional system and modelling requirements will be listed below, detailing the Navigation system.

**SYS-10:** The atmospheric vehicle shall contain an autonomous navigation system.
**SYS-10.1:** The navigation system shall contain the following sensors: IMU, ASI, FADS, UHF transceiver.
**SYS-10.2:** The navigation estimator shall be an EKF.

## 7.4. Verification: Navigation

Both the designed navigation sensors and estimator will be verified here. The sensor outputs are compared with real values from the simulator, and tests are run on the estimator to verify it.

### Navigation Sensors

The navigation sensors include an Inertial Measurement Unit (IMU), an Atmospheric Structure Instrument (ASI), an Ultra-High Frequency (UHF) transceiver, and a Flush Air Data Sensor (FADS).

The IMU and FADS designs were taken from the work of Rijnsdorp (2017). To consider them verified, acceptance tests are run. The IMU's outputs are calculated analytically for a random set of non-gravitational forces and compared to the one of the simulator, which compare exactly. For the verification of the FADS, it was noticed that the side-slip angle estimator designed by Rijnsdorp (2017) was not working. The mistake was that only pressure ports aligned on the vehicle's nose's vertical meridian were included, which is discouraged by the FADS designers (Cobleigh et al., 1999). This was fixed by changing the first input pressure port to one of the two that lie on the nose's horizontal median (pressure port number 6 from Table 7.2 and shown in Figure 7.3).

To further verify the FADS and verify the ASI, all sensor errors were first excluded to check that their outputted values were equal to the ones outputted by the simulator's atmospheric module concerning the temperature and pressure value of the ASI, and the dynamic pressure and static pressure measurements of the FADS. The

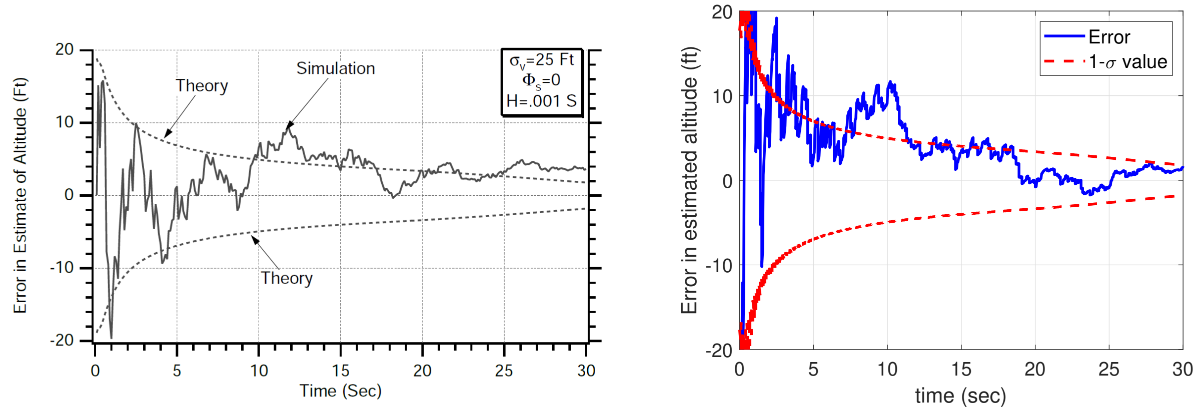


**(a)** Altitude estimate from Zarchan (2005). **(b)** Altitude estimate of EKF using inputs from Zarchan (2005).

**Figure 7.7:** Altitude estimate from Zarchan (2005) and from designed EKF, for EKF verification.

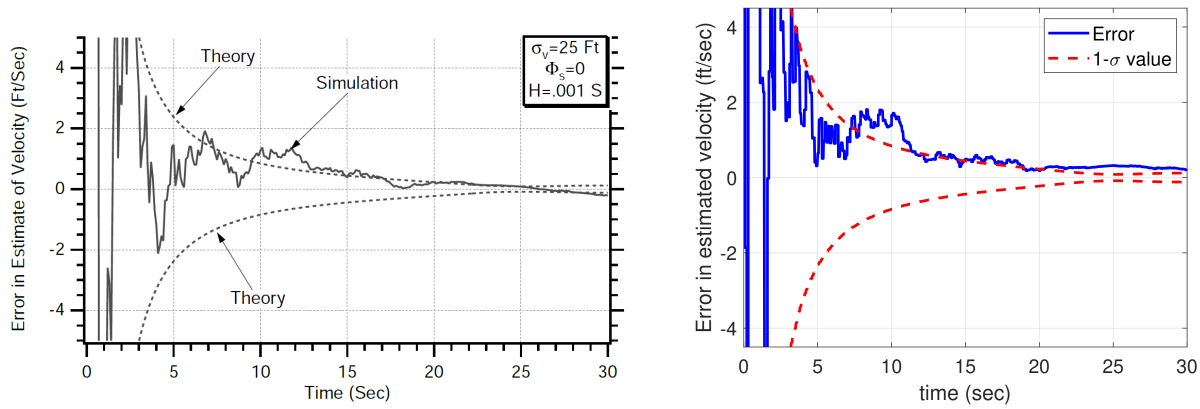


**(a)** Velocity estimate from Zarchan (2005). **(b)** Velocity estimate of EKF using inputs from Zarchan (2005).

**Figure 7.8:** Velocity estimate from Zarchan (2005) and from designed EKF, for EKF verification.

outputted Mach number, angle-of-attack, angle of side-slip, and velocity measurements of the FADS were compared to the ones outputted from the flight dynamics module. The UHF transceiver was verified by conducting the pseudo range and pseudo range rate computations analytically, and comparing the results with the modelled instrument. All four modelled sensors are thus considered verified.

## Navigation Estimator

For the verification of the navigation filter, a one-dimensional test explained in the work of Zarchan (2005) was run. It consists of the estimation of the altitude and velocity of a falling object experiencing gravity and drag. A range measurement is provided by a tracking radar. The inclusion of drag makes the equations describing the object's motion non-linear. The initial conditions, equation of motions, and matrices related to this case (**P**, **Q**, **R**, **H**, **F**, and **K**) were implemented in the simulator's filter to check the outcomes. This resulted in similar results as in the work of Zarchan (2005), as seen in the comparative graphs shown in Figure 7.7 and Figure 7.8. By doing this, the structure of the filter is verified. Here, the original and generated altitude and velocity estimates do not correspond exactly, mainly due to the different seeds used in the the two computations' random number generator when including noise to the range measurement. A seed of 23 of the MATLAB *randn* function was seen to approximate the results found in Zarchan (2005) the best.

The other components of the filter were then verified analytically. State propagation was performed separate from the estimation process, setting the IMU frequency to 50 Hz. It was seen that the position errors, due to propagation only, were higher (in the order of 0.03 - 0.3 m) than the velocity ones (in the order of $10^{-4}$ m/s) when simulated for a simulation time of 500 s. This position error was taken into account when designing the filter, to make sure that it would estimate the gliders' position variables with enough accuracy.

# 8

# Software Design and Verification

This chapter will describe the software architecture including a description of every block in Section 8.1, and a strategy to perform verification of the software's integrated modules in Section 8.2. The following combinations of modules are verified: guidance and control first, as well as guidance, control, and navigation modules second.

## 8.1. Software Architecture

A description of the function, inputs, and outputs of each block composing the developed software is given below. A figure of the software's top-level architecture can be seen in Figure 8.1, where each described block is illustrated, along with its inputs and outputs, and the relations between each of them. The sensor and navigation blocks, which are illustrated in more detail, are explained below. This architecture was mainly inspired by the work of Rijnsdorp (2017), and Mooij and Ellenbroek (2011). Table 8.1 summarises whether each software module is re-used, adapted from literature, or fully developed. The software is run at an integration frequency of 50 Hz, with all modules running at the same frequency, except the guidance module which is running at 10 Hz, as it is better to have it first converge before passing the data to the next blocks.

- **Environment:** The environment module takes the vehicle's state vector as an input, with information on the vehicle's position and velocity magnitudes. Atmospheric properties such as the atmosphere's pressure, density, and temperature are derived from the models mentioned in Chapter 3. These quantities are then used to compute the current speed of sound, Mach number, dynamic pressure, and specific energy (the sum of specific potential and kinetic energy). The computed dynamic pressure is fed back to the actuator module, for the computation of the control forces and moments.
- **Aerodynamics:** The aerodynamics module takes dynamic pressure $\bar{q}$ from the environment module, as well as the real state (angle-of-attack, side-slip angle, velocity, and altitude) from the flight dynamics modules, which will be described below, as inputs. The deflections of the control surfaces, as well as the guidance commands are also provided to the aerodynamics module. The vehicle-related aerodynamic coefficients are then interpolated from tabulated values (generated by reproducing the geometry of the GL-1 glider (Amalia et al., 2018) in XFLR5 with Uranus atmospheric conditions). Here, linear interpolation is used, as the data is not sparsely distributed nor completely different from one tabulated entry to the next. Aerodynamic coefficients are computed for both a clean glider configuration (no deflection of control surfaces) and a deflected configuration. The resulting control forces and moments are added together. The aerodynamics module then outputs the aerodynamic forces and moments in the body frame, to feed them to the flight dynamics module.
- **Flight Dynamics:** The flight dynamics module takes as input the guidance commands and the control forces and moments outputted from the control module. Wind and gravitational forces are computed in this block. In this module, the equations of motion of the glider are also propagated in time, to yield the gliders' real state variables at the next time-step. This real state is fed to both the atmospheric module and to the sensors block.
- **Guidance module:** The guidance system consists of three blocks: the mission manager which outputs the pre-defined reference trajectory components that the gliders should follow (velocity, altitude, flight-path angle, aerodynamic angles, and heading angle), the trimming module which makes sure that the vehicle is longitudinally stable by outputting a elevator deflection command for the pitching moment to

remain null, and the tracking guidance block which produces both an angle-of-attack and a bank angle command to reduce the initial trajectory oscillations and make sure that the vehicle does not deviate from its reference heading angle. The block takes the reference and estimated trajectory parameters as inputs (velocity, altitude, flight-path angle, aerodynamic angles, heading angle, and roll, pitch, and yaw rates). It outputs the aerodynamic angles commands and the trimming elevator deflection command, to feed to the control module.

- **Control system:** The control module takes the guidance commands, as well as the navigation module's estimated state as input. The estimated state variables from the navigation module are then compared to the commanded ones from the guidance module, and the difference vectors are used as inputs to both the longitudinal and lateral controllers. The controllers use optimal gains computed with a LQR. The output of the control module is yielded: the control surface deflections for the ailerons, elevator, and rudder, which are passed to the aerodynamics module for the interpolation of the aerodynamic coefficients.
- **Sensor module:** The sensor module contains the four developed navigation sensors: IMU, ASI (with accelerometer, pressure sensor, and temperature sensor), UHF transceiver, and FADS. They take the real state variables as input from the flight dynamics module, as well as non-gravitational forces, the orbiter's state, and the placement constants of the FADS pressure ports, to produce the following measurements: acceleration $a_{IMU}$ and acceleration rate $\omega_{IMU}$ from the IMU, temperature $T_{ASI}$ and pressure $p_{ASI}$ from the ASI, pseudo range $\rho_{UHF}$ and pseudo range rate $\dot{\rho}_{UHF}$ between the gliders and the orbiting spacecraft from the UHF transceiver, and velocity $V_{FADS}$ from the FADS. The temperature and pressure measurements are transformed into an altitude measurement $h_{ASI}$, using the atmospheric models described in Chapter 3. These measurements are then fed to the navigation estimator.
- **Navigation module:** The navigation module's EKF uses the sensors' measured quantities as inputs, along with the simulation time and IMU frequency, and constants such as the planet's mean radius, rotational rate, and standard gravitational parameter. The filter estimates position and velocity components in rotating frame, the quaternions, as well as the IMU's bias and drift errors. These quantities are then transformed to quantities of interest for the guidance and control modules: velocity $V$, flight-path angle $\gamma$, heading angle $\chi$, altitude $h$, aerodynamic angles $\alpha$, $\beta$ and $\sigma$, and angular rates $p$, $q$, and $r$.

**Table 8.1:** Indication for re-use, adaptation, or development of software modules.

| Software Block | Re-used, Adapted, or Generated/Developed |
|---|---|
| Atmospheric Model | This module was developed fully, by implementing the Uranian density, pressure, and temperature models mentioned in Chapter 3. |
| Aerodynamics | This block was adapted from the work of Rijnsdorp (2017), and Mooij and Ellenbroek (2011), by only considering the chosen atmospheric vehicle's control surfaces, and removing the thrusters' moments. The chosen atmospheric vehicle was taken from literature, its aerodynamic coefficients were generated with XLFR5, and included as Lookup tables that use linear interpolation. |
| Flight Dynamics | This block was adapted from the work of Rijnsdorp (2017), and Mooij and Ellenbroek (2011), and a wind model inspired by the work of Viavattene (2018) was included. Parameters relevant to Uranus were included here, namely the planet's radius, rotational rate, and standard gravitational parameter. |
| Guidance Module | The trimming module adapted from the work of Rijnsdorp (2017), and Mooij and Ellenbroek (2011). The tracking guidance module was developed fully. |
| Control Module | This block was adapted from the work of Rijnsdorp (2017), and Mooij and Ellenbroek (2011), by only considering the chosen reference vehicle's control surfaces, and removing the thrusters' moments. LQR gains relevant to the mission at hand were generated for different flights conditions and included as Lookup tables using linear interpolation. |
| Navigation Module | This block was fully developed. |
| Sensors | The IMU and FADS design were re-used from the work of Rijnsdorp (2017), and Mooij and Ellenbroek (2011). The ASI and UHF transceiver were fully developed. |

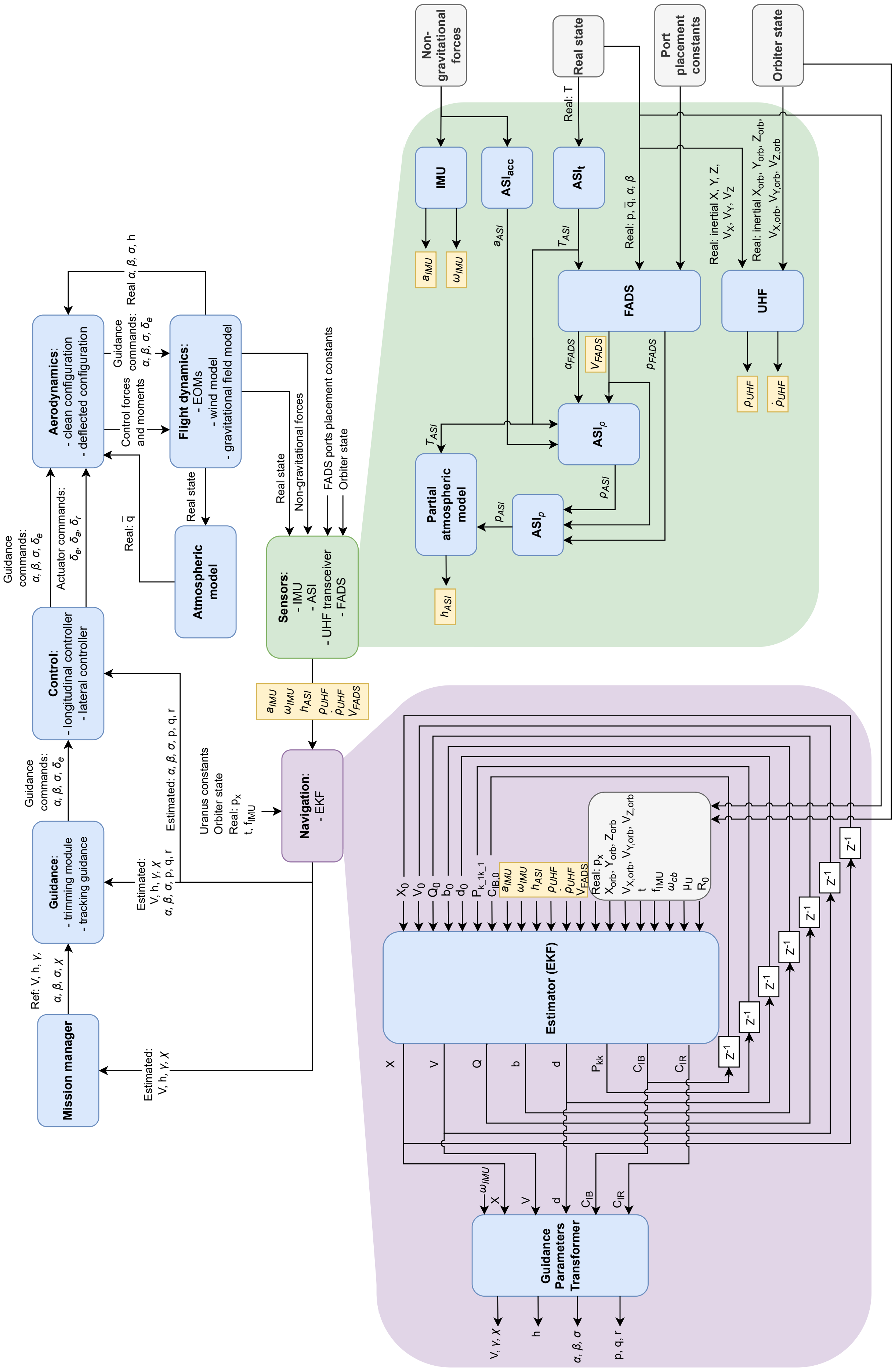


**Figure 8.1:** Block diagram of software architecture

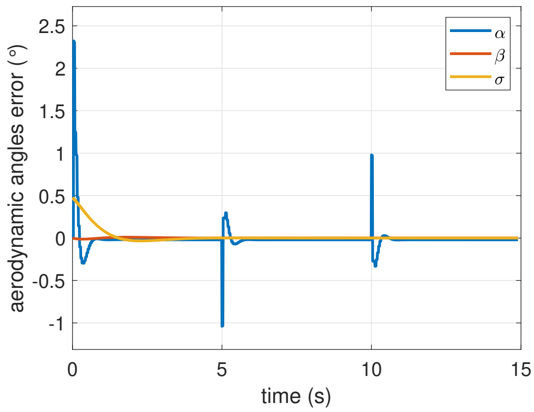


**(a)** Aerodynamic angles errors.

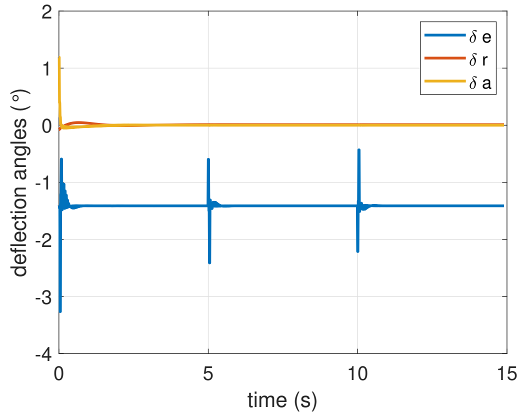


**(b)** Control module commands.

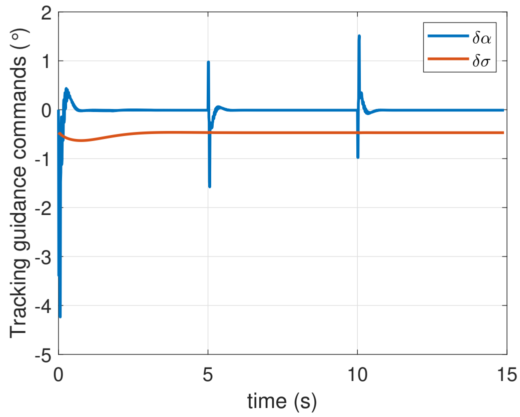


**(c)** Angle-of-attack and bank angle tracking guidance commands.

**Figure 8.2:** Behaviour of aerodynamic angles error, deflection angles of control surfaces, and tracking guidance commands of equatorial glider when tracking guidance is on, for guidance and control module performance analysis, in 6 DoF.

## 8.2. Software Verification

The software's different modules were verified individually, as well as together when relevant. The verification of the atmospheric model, aerodynamics block, flight dynamics block, and navigation sensors is explained in Section 3.6, Section 5.1.3, Section 4.3, and Section 7.4, respectively. Concerning the verification of the guidance, navigation, and control modules, a simulation plan was drafted, so as to explore all relevant combinations of these modules, be it in 3 DoF or in 6 DoF. The tracking guidance, control, and navigation filter gains' parameters are shown in Table 8.2. The individual testing of both the guidance and control modules are also mentioned in this table, with their corresponding tuning parameters.

### 8.2.1. Guidance and Control

As mentioned in Section 6.4.3, running the guidance and control modules together in 6 DoF with their individually generated gains yielded poor simulator results. The tracking guidance and control modules' gains had to be tuned again, yielding the parameters listed in Table 8.2 for **Sim #4**.

Testing the combination of guidance with tracking guidance and control consists in the following: verifying that a reference trajectory provided by the guidance module can be altered by the tracking guidance module, so that trajectory oscillations are minimised and the commanded heading angle is followed. The yielded new aerodynamic angle profiles should be transformed to control surface deflections by the control module to pass to the actuators module, all while trimming the vehicle for longitudinal stability and including the trim command. This can be tested by imposing both a positive and negative pulse change in angle-of-attack for example, and checking how the control module manages to bring the angle-of-attack back to the one dictated by the reference trajectory. A negative pulse of $\alpha = -1°$ is enforced at 5 s of the simulation time, and a positive one of $\alpha = -1°$ at 10 s. Figure 8.2a shows the behaviour of the angle-of-attack when under the influence of these two pulses. Figure 8.2b shows how the elevator, rudder, and aileron behave to bring the

**Table 8.2:** Simulation plan for GNC verification, with 3T = 3 DoF (translational), 3R = 3 DoF (rotational), TG = tracking guidance, ideal control = using guidance commands, ideal navigation = using measurement with noise, real navigation = using measurements with errors and noise.

| **Sim #** | **DoF** | **G** | **C** | **N** | **Guidance gains** | | | | | **Control gains** | | | | | | | | |
|---|---|---|---|---|---|---|---|---|---|---|---|---|---|---|---|---|---|---|
| | | | | | $\Delta V$ [m/s] | $\Delta h$ [m/ | $\Delta\alpha$ [°] | $\Delta\chi$ [°] | $\Delta\sigma$ [°] | $\Delta q$ [°/s] | $\Delta\alpha$ [°] | $\Delta\delta e$ [°] | $\Delta p$ [°/s] | $\Delta r$ [°/s] | $\Delta\beta$ [°] | $\Delta\sigma$ [°] | $\Delta\delta a$ [°] | $\Delta\delta r$ [°/s] |
| **1** | 3T | yes but no TG | ideal | no | - | - | - | - | - | - | - | - | - | - | - | - | - | - |
| **2** | 3T | yes | ideal | no | 0.005 | 500 | 0.5 | 0.5 | 5 | - | - | - | - | - | - | - | - | - |
| **3** | 3R | yes but no TG | yes | no | - | - | - | - | - | 10 | 6.9 | 30 | 20 | 10 | 5 | 10 | 25 | 25 |
| **4** | 6 | yes | yes | no | 0.01 | 100 | 5 | 5 | 5 | 10 | 6.9 | 30 | 20 | 10 | 5 | 10 | 25 | 25 |
| **5** | 6 | yes | yes | ideal | 0.01 | 100 | 5 | 15 | 5 | 10 | 6.9 | 30 | 20 | 10 | 5 | 10 | 25 | 25 |
| **6** | 6 | yes | yes | yes | 0.01 | 100 | 15 | 15 | 5 | 10 | 6.9 | 30 | 20 | 10 | 5 | 10 | 25 | 25 |

**Table 8.3:** Navigation gains for simulations 5 and 6.

| **Sim #** | **Navigation gains** | |
|---|---|---|
| | **P** | diag([10 10 10 1 1 1 1 1 1 1 50 3e-4 50 -3.5e-4 50 3e-4 50 4e-6 50 -5e-6 50 3e-6]$^2$) |
| **5** | **Q** | diag([1, 1, 1, 1, 1, 1, 1, 1, 1, 1, 1e-5, 1e-5, 1e-5, 1e-8, 1e-8, 1e-8]) |
| | **R** | diag([1, 1, 1, 1, 1e-2, 1e-3, 1e-3, 1e-3]) |
| | **P** | diag([10 10 10 1 1 1 1 1 1 1 50 3e-4 50 -3.5e-4 50 3e-4 50 4e-6 50 -5e-6 50 3e-6]$^2$) |
| **6** | **Q** | diag([1e-3, 1e-3, 1e-3, 1e-3, 1e-3, 1e-3, 1e3, 1e3, 1e3, 1e-3, 1e-5, 1e-5, 1e-5, 1e-8, 1e-8, 1e-8]) |
| | **R** | diag([1e2, 1e4, 1e1, 1e4, 1e3, 1e-3, 1e-3, 1e-3]) |

angle-of-attack back to its reference value after each pulse. Finally, Figure 8.2c shows the behaviour of the angle-of-attack and bank angle increments needed for the tracking guidance to ensure minimised trajectory oscillations and constant heading angle. When turning on the tracking guidance modules, the derivative term of the tracking guidance component producing an angle-of-attack command is included with a gain of $-10$ to yield less oscillations. The parameters listed in Table 8.2 for **Sim #4** are used to compute the gains.

It can be seen that the angle-of-attack, deflection angles, and tracking guidance commands remain stable after countering the pulses, with the angle-of-attack converging back to the value prescribed by the reference trajectory in less than 1 s, so the combination of these two modules together is considered verified as it is performing as intended. A convergence of 1 s for a pulse of $1^\circ$ is acceptable as no big aerodynamic angle deflections are expected during the gliders' flight. The angle of attack should gradually increase, without experiencing any pulse, while both the side-slip angle and the bank angle should remain constant.

### 8.2.2. Guidance, Navigation, and Control

Verification of the guidance, control and navigation modules together, consists in making sure that the estimation of the navigation system stays stable over time, and does not hinder the performance of the already verified integration of guidance and control modules. The flight of one glider, the equatorial glider in this case, was simulated for a portion of the flight time, to see if it remained stable. No navigation sensor error or noise were included for the purpose of this verification step.

With the current guidance, control, and navigation modules integrated together, a 6 DoF simulation was run for $30,000$ s. The performance of the simulator was poor. The reason for this is as follows: **Although the navigation module's estimator performs well (X- and Z-position error estimates in the order of $10^{-2}$ m, Y-position error estimate of $10^{-3}$ m, and X-velocity error estimate in the order of $10^{-2}$ m/s, Y- and Z-velocity error estimates in the order of $10^{-3}$ m/s), the guidance module is not robust enough to receive different data than the real ones, to yield stable tracking guidance commands to pass to the control module**. Indeed, when receiving the navigation module's estimates, the tracking guidance commands ($\delta\alpha$ and $\delta\sigma$) explode. They were then kept constrained between $-0.04^\circ$ and $-0.02^\circ$ for the angle-of-attack increment, and $-0.5^\circ$ and $0.0^\circ$ for the bank angle increment. As a result, the angle of attack and bank angle increments are either staying constant at one of the defined limits, or oscillating very rapidly between the defined minimum and maximum. This is limiting the tracking guidance's performance and both trajectory oscillations and deviation from the commanded heading angle are yielded. As mentioned in bold, the navigation estimator produces good position and velocity estimates in this configuration. However, when these variables are transformed to guidance quantities (altitude, velocity, flight-path angle, heading angle, and aerodynamic angles), the aerodynamic angles' estimates are noisy for the first $11,800$ s of the simulation, with the following amplitudes: $0.05^\circ$ for the angle-of-attack, $0.2^\circ$ for the side-slip angle, and $0.1^\circ$ for the bank angle. This makes the control surfaces' deflections be noisy as well, with the elevator deflection oscillating between its minimum and maximum values of $30^\circ$ and $30^\circ$. Noise can then also be seen in the behaviour of the aerodynamic angles, for that first portion of the flight. It was investigated whether the noise in the estimated aerodynamic angles was due to the guidance module operating at a lower frequency than the rest of the software, but running all the modules at the same frequency yielded the same results.

From this analysis, it is clear that the tracking guidance needs to be more robust, in particular with the angle-of-attack increment calculation. The design of a LQR with proportional and derivative terms for the angle-of-attack increment, and a proportional term for the bank angle increment is not enough to provide confidence that the module can accept and respond to estimated data, while still fulfilling its purpose of reducing trajectory oscillations and keeping a constant heading angle. For the design of this LQR, the three expressions of Equation Equation 4.15 were used separately, with the two first ones contributing to the angle-of-attack increment, and the third one being used for the bank angle increment command. As a recommendation for future work, these equations should be used together, linking vertical and horizontal guidance together.

Accepting that the guidance module cannot receive the navigation module's outputs, it was decided to feed real data to the guidance and control modules, and have the navigation module operate in parallel to evaluate its performance. Error estimates produced by the navigation estimator are shown in Figure 8.3 for the first $30,000$ s. X- and Y-position error estimates are in the order of $10^{-5}$ m, Z-position error estimate is in the order of $10^{-4}$ m, and velocity error estimates in the order $10^{-6}$ m/s. Using real data for the guidance feedback enables the navigation estimates to be more accurate, thus not leading to noisy aerodynamic angles. The performance of the navigation system with sensor errors and noise is shown in Section 9.2 and Section 9.3.

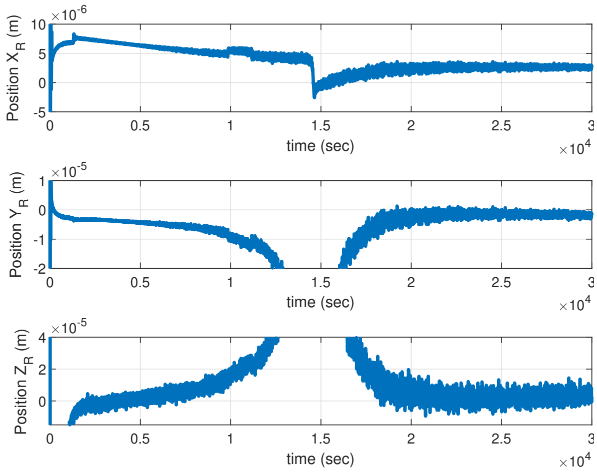


**(a)** Position error estimate.

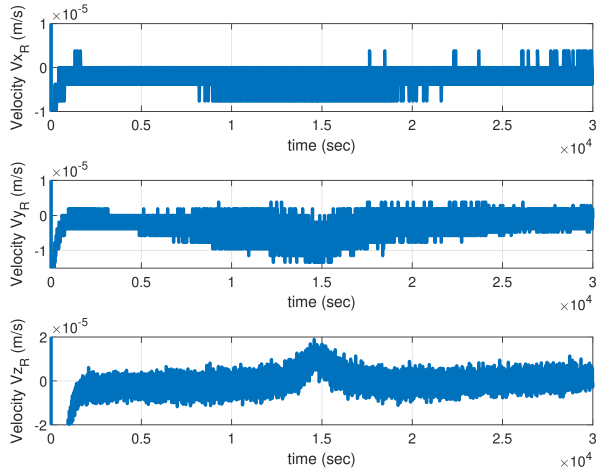


**(b)** Velocity error estimate.

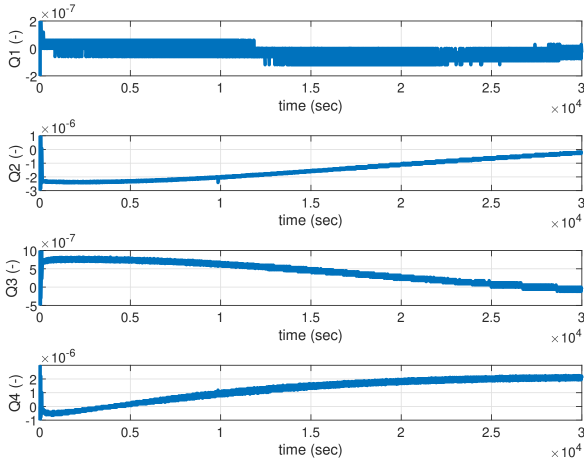


**(c)** Quaternion error estimate.

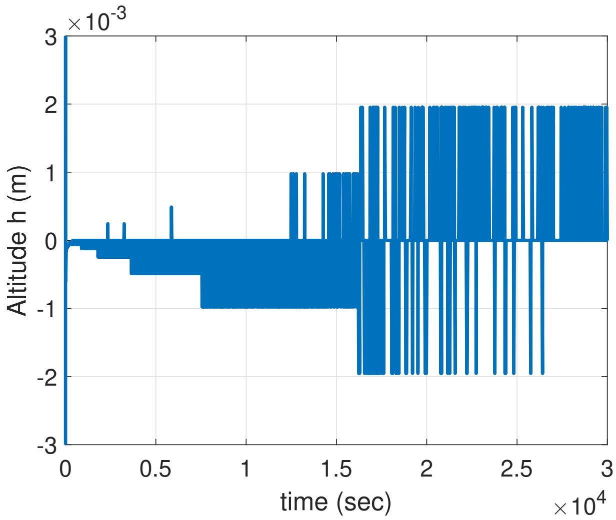


**(d)** Altitude error estimate.

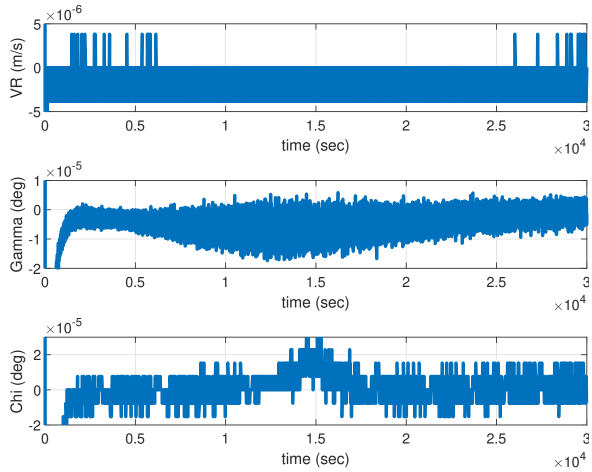


**(e)** Velocity, flight-path angle, and heading angle error estimates.

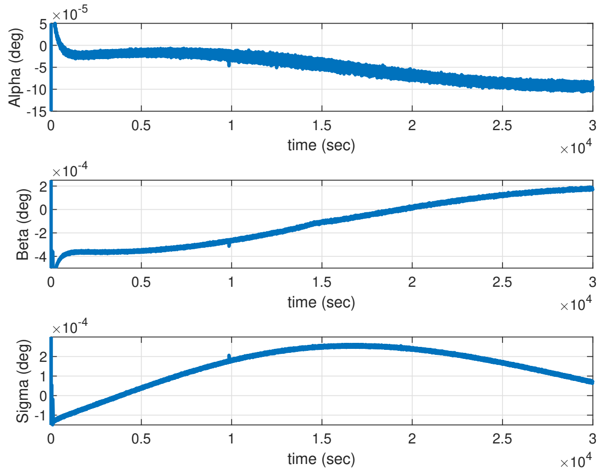


**(f)** Aerodynamic angles error estimates.

**Figure 8.3: Sim #5**: State variables error estimates with navigation system working in parallel to the main simulation using real state variables, for the first 30.000 s, with no sensor noise. All estimates are within covariance bounds.

# 9

# Results

This chapter presents the results of the three last simulations listed in Table 8.2 and Table 8.3. Section 9.1 presents the results of **Sim #4**, where the guidance and control modules are active but the navigation one is not. Results are presented with respect to flight dynamics, Uranus' environment, the aerodynamics, guidance, and control. Section 9.2 then presents navigation results for **Sim #5**, where both guidance and control modules are active, and where the navigation block is run in parallel with the presence of sensor noise. Section 9.3 presents the navigation results for **Sim #6**, which is the same as **Sim #5** with sensor errors included as well. Section 9.4 then summarises the navigation results of these last two simulations, and Section 9.5 mentions the results related to the relay spacecraft's orbit, to ensure continuous line-of-sight with both gliders.

## 9.1. Sim #4: G, C, no N

The simulator was run in 6 DoF with the guidance and control modules active, but using the real state data from the flight dynamics module as a feedback to close the simulation loop. The reason for this is twofold: first, it is important to evaluate the performance of the guidance, tracking guidance, and control modules, without being influenced by the use of estimated data from the navigation module, which can be inaccurate. Second, this is the best case to run to retrieve mission data such as time of flight and range achieved by the gliders, to compare to typical mission data of a conventional descent probe. The tracking guidance and control gain parameters used are mentioned in Table 8.2 for **Sim #4**.

### 9.1.1. Flight Dynamics

Each glider's flight was simulated with a terminal altitude of −375 km, where the pressure is equal to 100 bar. Both simulations were run at an integration frequency of 50 Hz, with all modules' frequencies being equal to that, except the guidance module's frequency which was set to 10 Hz. The initial altitude was set to 0 km altitude, corresponding to the defined 1 bar pressure level. Both gliders' initial velocity was set to $V_0 = 52.8$ m/s, and their initial flight-path angle and aerodynamic angles were set as follows: $\gamma_0 = -1.25°$, $\alpha_0 = \beta_0 = \sigma_0 = 0°$. Other glider-dependent initial parameters and final time of flight, range, and accumulated scientific data are shown in Table 9.1.

Both gliders have a time of flight close to 13 Earth days, which is significantly larger than the measurement time of a few hours (3.5 h for the Huygens probe) offered by using conventional descent probes as the in-situ atmospheric platform of such a mission. This enables the scientific instruments to be active for longer periods of time, yielding more science data. Moreover, with a range of around 19,000 km, it becomes possible for both gliders to explore a larger region than a descent probe would. This allows for the detection of spatially variable species, both laterally as both gliders are exploring different latitudes, and longitudinally thanks to the 19,000 km of distance explored along constant respective latitudes. The equatorial glider's range corresponds to 44.62° of explored longitude, by starting at $\tau_{eq,0} = 70°$ and reaching $h = -375$ km at $\tau_{eq,f} = 25.38°$. The polar glider goes around Uranus' north pole around six and half times. Considering this longer mission time, a total scientific data of 3.29 Gb was computed taking into account the 1,493 bps data rate calculated in Table 2.2. Taking both gliders' measured data into account, and using the relations described in Section 5.3, this leads to a total uplink time of 18.26 min to the relay spacecraft and a total downlink time of 62.88 h for the relay spacecraft to transmit the data to Earth.

**Table 9.1:** Initial and final conditions of both equatorial and polar gliders' flight simulations.

| Glider | Equatorial | Polar |
|---|---|---|
| Initial longitude $\tau_0$ [°] | 70 | 70 |
| Initial latitude $\delta_0$ [°] | 17.5 | 89.0 |
| Initial heading $\chi_0$ [°] | $-90$ | $+90$ |
| Time of flight [Earth days] | 12.80 | 12.69 |
| Range [km] | 18,741.108 | 18,784.844 |
| Scientific data [Gb] | 1.65 | 1.64 |

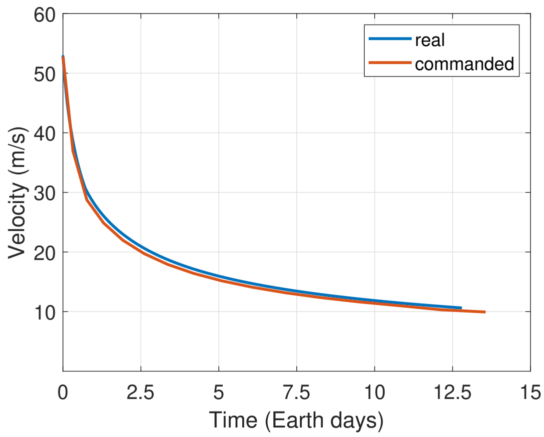


**(a)** Velocity profile during glider's flight.

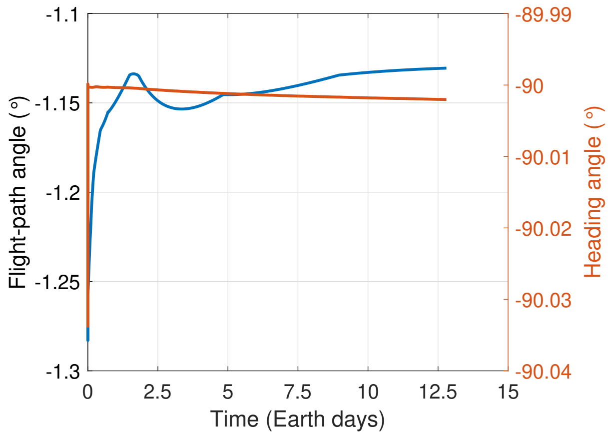


**(b)** Flight-path and heading angle profiles during glider's flight.

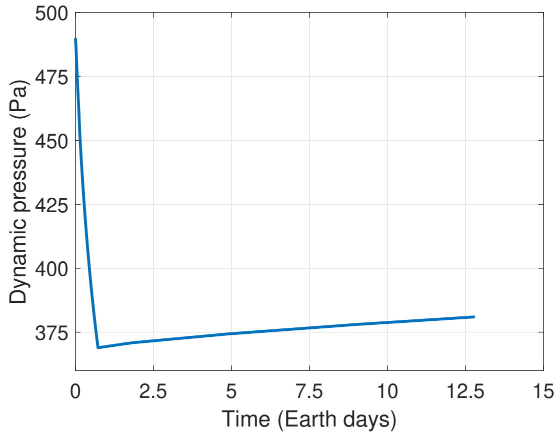


**(c)** Dynamic pressure profile during glider's flight.

**Figure 9.1:** Velocity, flight-path angle, heading angle, and dynamic pressure profiles during glider's flight.

Figure 9.1 displays the velocity, flight-path angle, heading angle, and dynamic pressure profiles experienced during the equatorial glider's flight. The glider's velocity is seen to decrease to about 10 m/s, following the velocity profile imposed by the reference trajectory listed in Table 6.1. The flight-path angle stays quasi-constant between $-1.1534°$ and $-1.1305°$. The heading angle stays quasi-constant as well, going down to $-90.0020370°$, with a constant imposed reference heading angle of $-90.0°$. These results demonstrate that the equatorial glider is indeed following a downwards gliding path, respecting the commanded velocity and heading angle profiles with limited deviation. The dynamic pressure shown in Figure 9.1c stays quasi-constant from $\overline{q} = 369$ Pa to $\overline{q} = 381$ Pa, which is much smaller than the dynamic pressure a glider would experience during cruise, as typical values range between 675 Pa (at an altitude of 4 km and at typical speed of 80 knots) and $1,037$ Pa (at sea-level and at typical speed of 80 knots)[1]. This implies less load on the glider's structure.

[1]`https://www.faa.gov/regulations_policies/handbooks_manuals/aviation/glider_handbook/media/gfh_ch05.pdf`, accessed on 27/05/2022.

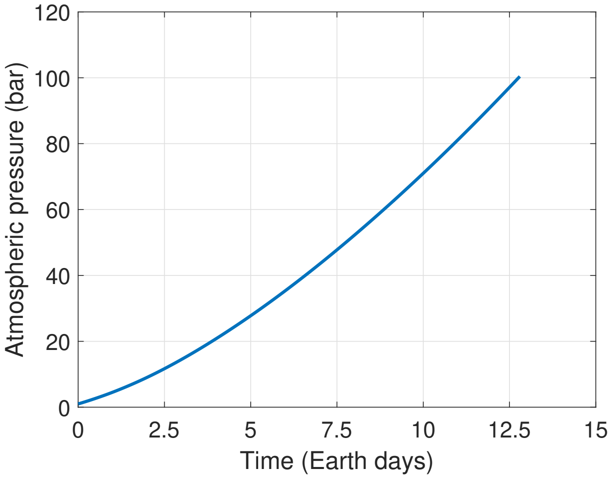


**(a)** Pressure profile explored during glider's flight.

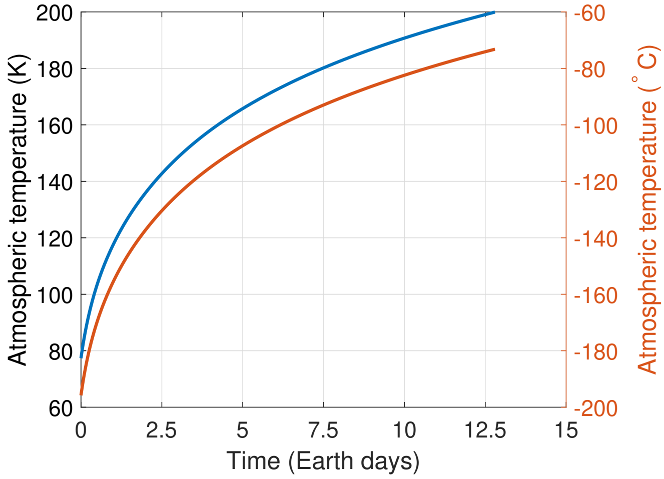


**(b)** Temperature profile explored during glider's flight.

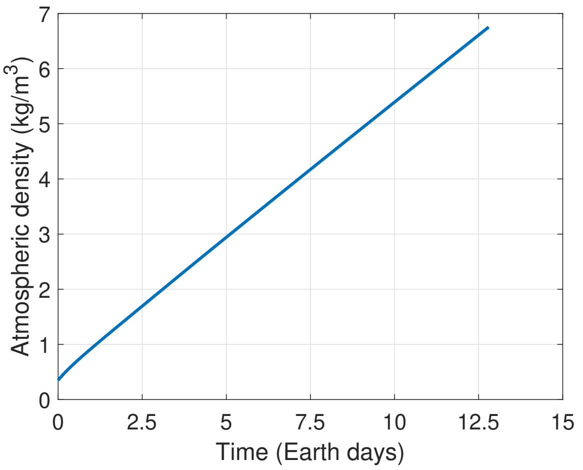


**(c)** Density profile explored during glider's flight.

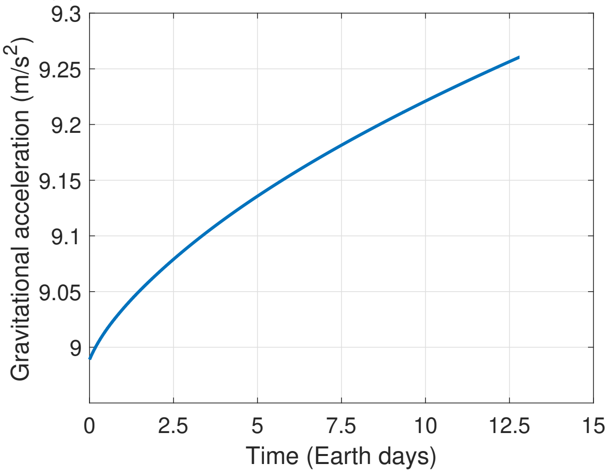


**(d)** Gravitational attraction profile explored during glider's flight.

**Figure 9.2:** Atmospheric pressure, temperature, density, and gravity profiles explored during glider's flight.

## 9.1.2. Environmental Module

Uranus' environmental models described in Chapter 3 were used to model the planet's atmospheric density, pressure, temperature, and gravity. Both gliders' flight-paths yielded similar explored atmospheric conditions, which are shown in Figure 9.2, until each glider reaches the 100 bar pressure level at an altitude of −375 km. These experienced atmospheric conditions are important for the design of the gliders, as they should structurally sustain the high experienced pressures, the very low temperatures, and thick atmosphere. The on-board scientific payload should also survive and perform well under these conditions. The selection of the vehicles' structural components and materials goes beyond the scope of this thesis and is left as a recommendation. A robust on-board thermal system will be needed to maintain the gliders' subsystems and instruments operative. Considering the high density and opacity of Uranus' atmosphere, an active thermal control system, such as heaters, is recommended.

The total pressure load experienced by the vehicle can be calculated by adding the dynamic and static pressure profiles together. When comparing the dynamic pressure plotted in Figure 9.1c to the static pressure shown in Figure 9.2a, it is clear that the static pressure is much higher and thus dominates the total pressure load experienced by the gliders. The behaviour of the total pressure load profile experienced by the glider is thus similar to the one of the static pressure.

## 9.1.3. Aerodynamics

The behaviour of the aerodynamic coefficients interpolated from the XFLR5-generated Lookup tables is shown in Figure 9.3a. Both the drag coefficient $C_D$ and side-slip coefficient $C_S$ remain quite low. This is expected for the side-slip, as no side force is experienced during the flight. For the drag coefficient, the reason for

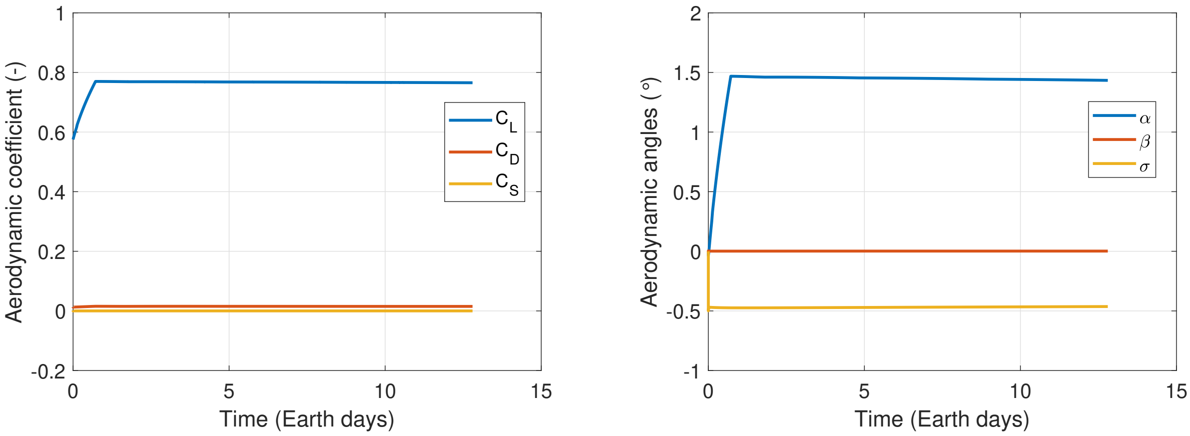


**(a)** Behaviour of aerodynamic coefficients $C_L$, $C_D$, and $C_S$.

**(b)** Behaviour of aerodynamic angles $\alpha$, $\beta$, and $\sigma$.

**Figure 9.3:** Behaviour of aerodynamic coefficients and angles during the gliders' flight.

its low value was explained in Section 5.1.3: no turbulence model was included. Moreover, as the glider is experiencing tailwind, its relative velocity is decreasing, which decreases the drag force it is experiencing. The lift coefficient is seen to remain quite constant around $C_L = 0.77$. The constant behaviour of this coefficient is expected, as it is composed of the lift coefficient experienced at the nominal angle-of-attack of $\alpha = 1.5°$ provided in the reference trajectory, and of the constant lift coefficient provided by the tracking guidance's angle-of-attack command of $\delta\alpha = -0.02°$, as seen in Figure 9.4b.

### 9.1.4. Guidance

The guidance contains a trimming module and a tracking guidance module. The trimming command of the elevator deflection ensures that the glider's pitching moment remains null. The objective of the tracking guidance is twofold: first ensure minimal trajectory oscillations by enforcing an angle-of-attack increment command $\delta\alpha$, and secondly, it makes sure that the glider is following the heading angle given in the reference trajectory by commanding the bank angle with $\delta\sigma$. Both the trimming and the tracking guidance commands can be seen in Figure 9.4. The trimming command is seen to remain quite constant around $\delta_e = 0.6°$, which corresponds to the constant behaviour of the lift coefficient shown in Figure 9.3a. Concerning the behaviour of the tracking guidance commands, it can be seen in Figure 9.4b that the angle-of-attack increment $\delta\alpha$ remains constant, constrained at the upper limit set at $\delta\alpha_{max} = -0.02°$. The bank angle increment $\delta\sigma$ is seen to stay quasi-constant around $\delta\sigma = -0.47°$. It must be noted here, that without the strict limits set on the angle-of-attack increment ($\delta\alpha_{min} = -0.04°$ and $\delta\alpha_{max} = -0.02°$), the command would oscillate very rapidly between a less strict set of limits, leading to non-effective tracking guidance and thus non-countered oscillations in the gliders' trajectories. As previously shown in Figure 6.3, the implementation of the mentioned limits in this software's design leads to successful countering of the experienced trajectory oscillations. This is because those limits were carefully chosen, constraining the optimal angle-of-attack increment of $\delta\alpha_{opt} = -0.03°$ by $\pm 0.01°$. This optimal value was calculated by running the guidance module in 3 DoF (translational) with ideal control module (the commanded aerodynamic angles outputted from the guidance module are transformed into control surface deflections and directly passed to the vehicle's actuators), and no navigation.

### 9.1.5. Control

The control module's performance is shown in Figure 9.5a, with the plot of the error in aerodynamic angles. This corresponds to the difference between the commanded and actual aerodynamic angles. It can be seen that both the side-slip and bank angle errors stay close to zero, while the angle-of-attack error is changing behaviour, with a maximum error of $e(\alpha) = -0.0476362°$ by the end of the flight. This small error most probably arises because of the constrained tracking guidance command at $\delta\alpha_{max} = -0.02°$. The control surface deflections computed by both the longitudinal and lateral controllers are shown in Figure 9.5b, where the rudder and aileron deflections stay close to zero as expected because no side-slip or rolling motion is occurring during the flight. The elevator command accounts for both the vehicle's trimming and the oscillation-limiting action of the tracking guidance, following a quasi-constant behaviour around $\delta_e = -0.6°$, corresponding to the trimming command, as the other contributing tracking guidance command is small ($\delta\alpha = -0.02°$).

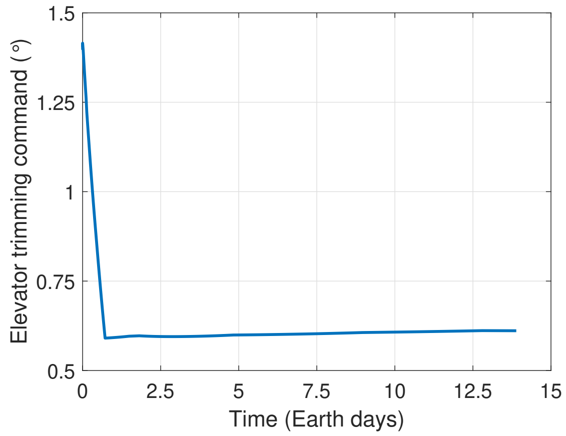


**(a)** Behaviour of trimming command $\delta_e$.

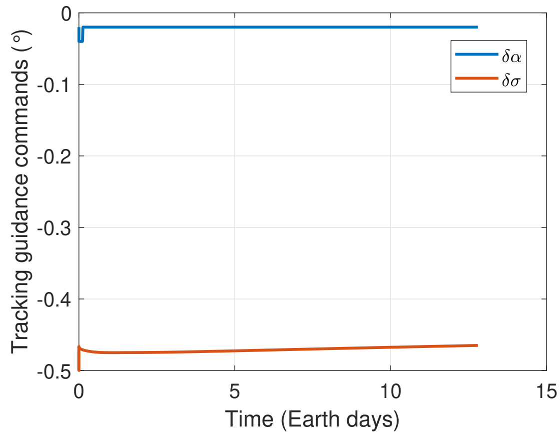


**(b)** Behaviour of tracking guidance commands $\delta\alpha$, $\delta\sigma$.

**Figure 9.4:** Behaviour of guidance commands $\delta_e$, $\delta\alpha$, and $\delta\sigma$ during the gliders' flight.

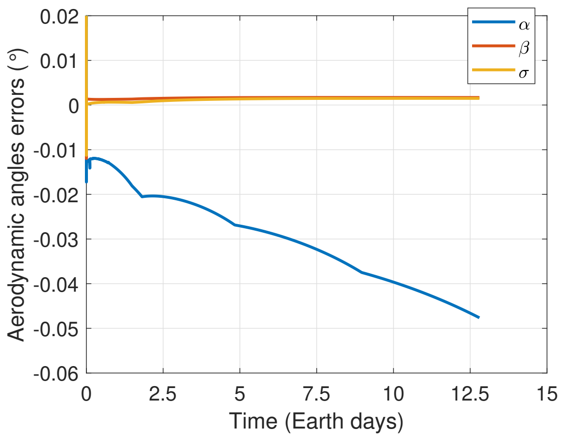


**(a)** Behaviour of aerodynamic angles errors.

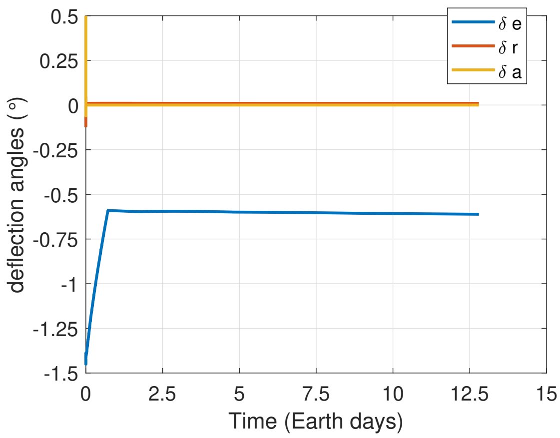


**(b)** Behaviour of control surface deflections $\delta_e$, $\delta_a$, $\delta_r$.

**Figure 9.5:** Behaviour of aerodynamic angles errors and deflections of control surfaces during the gliders' flight.

**Table 9.2:** White noise standard deviations used in navigation sensors

| Navigation Sensor | White Noise Standard Deviation | Value |
|---|---|---|
| ASI | $\sigma_{ASI}$ (m) | 0.001 |
| UHF transceiver | $\sigma_{\rho}$ (m) | 0.5 |
| | $\sigma_{\dot{\rho}}$ (m/s) | 0.2 |
| FADS | $\sigma_V$ (m) | 0.1 |
| Additional measurements | $\sigma_{p_x}$ (m) | 0.3 |
| | $\sigma_Q$ (-) | 0.001 |

## 9.2. Sim #5: G, C, N with Noise in Parallel

The simulator was then run in 6 DoF with the guidance and control modules active, still using the real data from the flight dynamics module as a feedback, but running the navigation module in parallel to assess its performance. White noise was added to the navigation sensors' measurements, with the standard deviations listed in Table 9.2. This noise was included to simulate more realistic signals. Although it is not possible to know the amplitude of a signal's noise prior to measuring it, it is better to still include noise in those sensor measurements. Their standard deviation values were chosen to be less than 1 m and 1 m/s for the position and velocity measurements, respectively. A small white noise standard deviation is attributed to the quaternion measurement, as the quaternion estimates are used within the filter to evaluate the $\mathbf{C_{IB}}$ transformation matrix, which is also continuously used and updated for the state variable estimations.

**Table 9.3:** Navigation sensor errors included in each modelled instrument.

| Navigation Sensor | **Error** | **Value** |
|---|---|---|
| ASI | $\sigma_T$ (K) | 0.05 |
| UHF transceiver | $\sigma_\rho$ (m) | 25.0 |
| | $b_\rho$ (m) | 1.0 |
| | $\sigma_{\dot{\rho}}$ (m/s) | 0.1 |
| | $d_{\dot{\rho}}$ (m/s) | 0.4 |
| FADS | $\sigma_p$ (N/m$^2$) | 1.0 |

### 9.2.1. Navigation

The navigation module's performance was thus evaluated by running it in parallel to the main simulation loop, for the beginning of the mission. Here, a total simulation time of 30,000 s was run in this configuration. The yielded error estimates were as follows: $e(X) = 0.01$ m, $e(Y) = 0.01$ m, $e(Z) = 0.05$ m, $e(V_X) = 0.01$ m/s, $e(V_Y) = 0.005$ m/s, $e(V_Z) = 0.005$ m/s, $e(Q_1) = 2 \cdot 10^{-4}$, $e(Q_2) = -1 \cdot 10^{-4}$, $e(Q_3) = 1 \cdot 10^{-4}$, $e(Q_4) = -2 \cdot 10^{-3}$, which led to the following guidance parameters errors: $e(h) = 0.01$ m, $e(\alpha) = 0.2°$, $e(\beta) = 0.1°$, $e(\sigma) = 0.05°$, $e(V) = 0.02$ m/s, $e(\gamma) = 0.01°$, $e(\chi) = 0.02°$, and Euler angles error from transforming the quaternion errors: $e(\phi) = 0.2°$, $e(\theta) = 28°$, $e(\psi) = 0.3°$. The convergence plots of the error estimates and covariance bounds are displayed in Figure 9.6. It can be seen in those plots that including noise in the sensor measurements reduces the performance of the estimator. A filter will be needed on the estimator's outputs, to pass noise-free signals to the guidance module. A band-pass filter inspired by the work of Mooij (2020) was implemented but did not yield noise-free result. Indeed, using the gains of Mooij (2020), the signal was merely shifted downward without being filtered. The choice, design, and implementation of a noise-filtering module is left as a recommendation for future work.

## 9.3. Sim #6: G, C, N with Errors and Noise in Parallel

Finally, as a last simulation case, the simulator was run in 6 DoF with the guidance and control modules active, still using the real data from the flight dynamics module as a feedback, but running the navigation module with sensor errors and noise in parallel, to assess its performance. The same standard deviation values as for **Sim #5** were used for the included white noise. The sensor errors are explained in the description of each navigation instrument in Section 7.1, and are summarised in Table 9.3.

### 9.3.1. Navigation

The navigation module was again run in parallel to the main simulation loop for the beginning of the mission, this time including errors in the sensor measurements used as inputs to the filter. A total simulation time of 30,000 s was run in this configuration. The yielded error estimates were as follows: $e(X) = -0.02$ m, $e(Y) = 6.5$ m, $e(Z) = -26$ m, $e(V_X) = 0.01$ m/s, $e(V_Y) = 0.05$ m/s, $e(V_Z) = -0.2$ m/s, $e(Q_1) = 2 \cdot 10^{-4}$, $e(Q_2) = 2 \cdot 10^{-4}$, $e(Q_3) = 2 \cdot 10^{-4}$, $e(Q_4) = 1 \cdot 10^{-3}$, which led to the following guidance parameters errors: $e(h) = 4$ m, $e(\alpha) = 0.2°$, $e(\beta) = -0.5°$, $e(\sigma) = 0.05°$, $e(V) = -0.03$ m/s, $e(\gamma) = 0.1°$, $e(\chi) = -0.4°$, and Euler angles error from transforming the quaternion errors: $e(\phi) = 0.06°$, $e(\theta) = 28°$, $e(\psi) = 0.1°$. The convergence plots of the error estimates and covariance bounds are displayed in Figure 9.7. It can be seen in those plots that including sensor errors in the sensor measurements reduces the performance of the estimator, with its estimations being less accurate. This is to be expected, as instruments errors complicate the filter's task of yielding estimates that are close to the real values. The EKF should be improved, possibly through better tuning, to yield more accurate estimates even when erroneous measurements are used as input.

## 9.4. Summary of Navigation Results

The navigation system's results will be summarised in Table 9.4, showing state variable estimates at the end of the 30,000 s test simulations. As can be seen here and as expected, the navigation filter's performance decreases once sensor noise is included, and decreases even more when both sensor noise and sensor errors are included. This is especially seen in the y-position and z-position estimates, as well as in the altitude variable derived from those. The filter is thus quite sensitive to altitude measurement errors, induced by including errors in the ASI sensor, as the altitude measurement is derived from this instrument's outputs. It must be noted here that, were the estimated variables' noise be filtered, the estimator's results would be better, as they are seen to be noisy around zero (see Figure 9.7d, where the altitude is estimated for the case where sensor

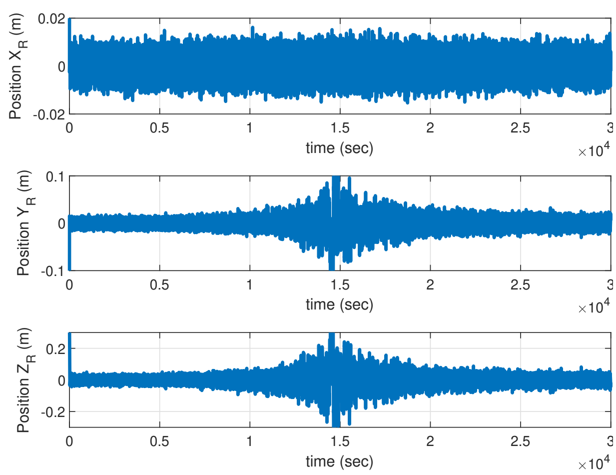


**(a)** Position error estimate.

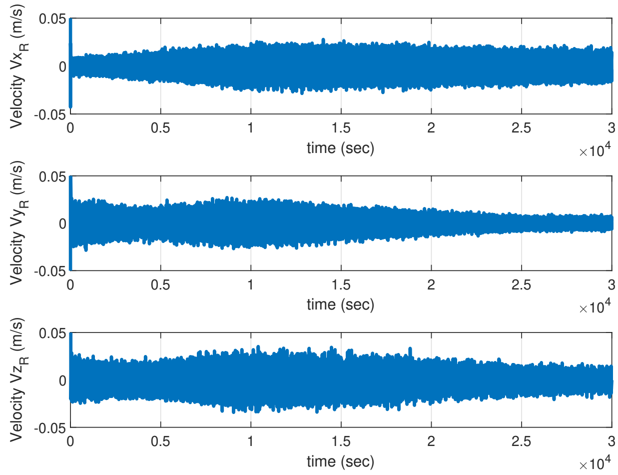


**(b)** Velocity error estimate.

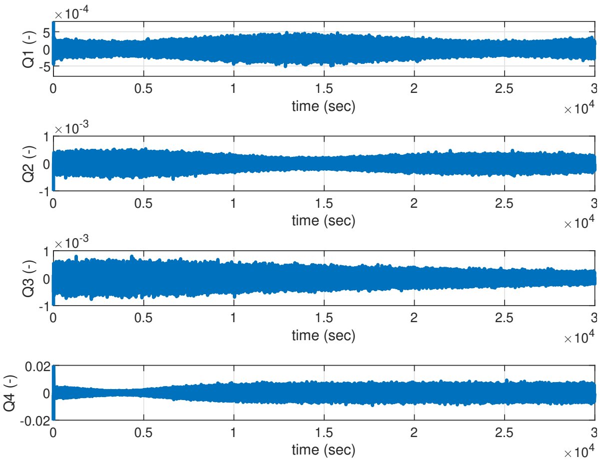


**(c)** Quaternion error estimate.

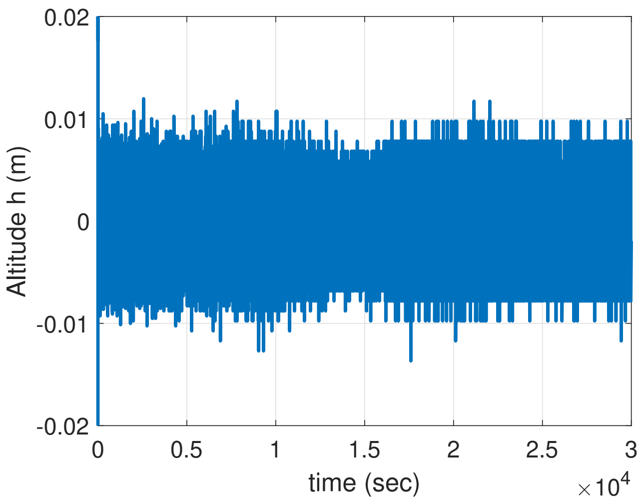


**(d)** Altitude error estimate.

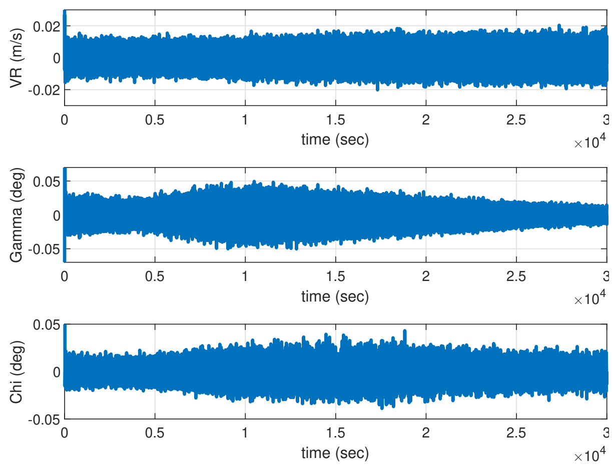


**(e)** Velocity, flight-path angle, and heading angle error estimates.

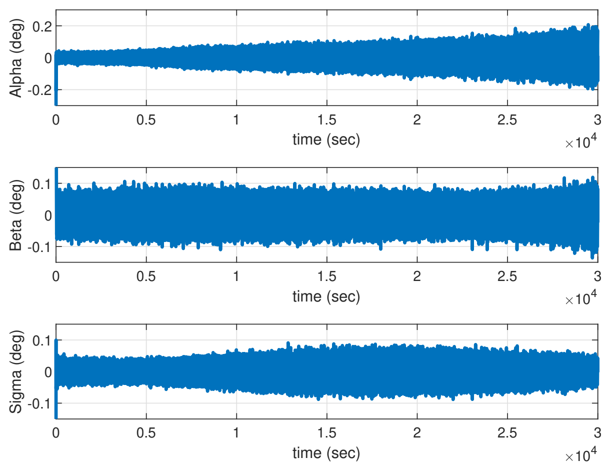


**(f)** Aerodynamic angles error estimates.

**Figure 9.6: Sim #5**: State variables error estimates with navigation system working in parallel to the main simulation using real state variables, for the first 3.000 s of the simulation, with sensor noise.. All estimates are within covariance bounds.

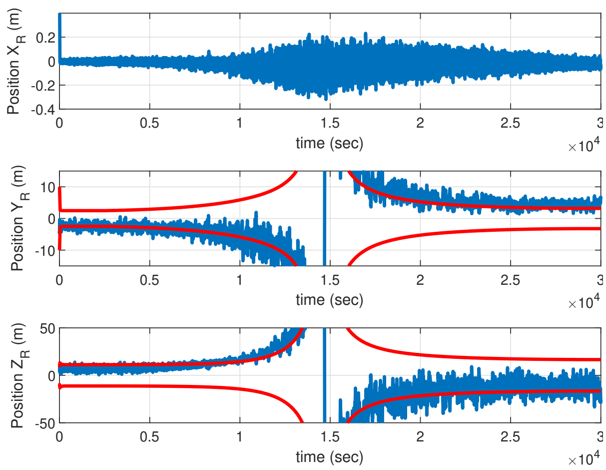


**(a)** Position error estimate.

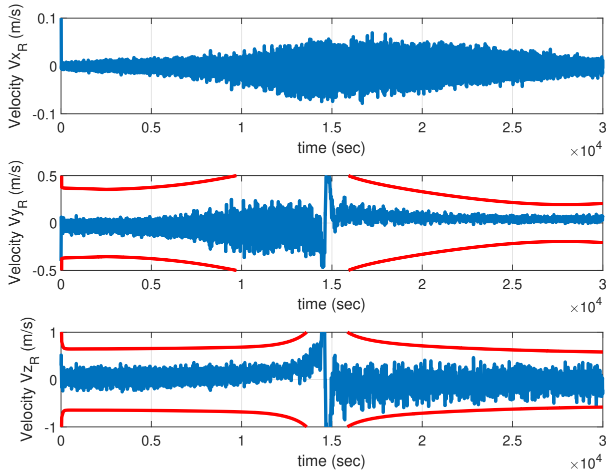


**(b)** Velocity error estimate.

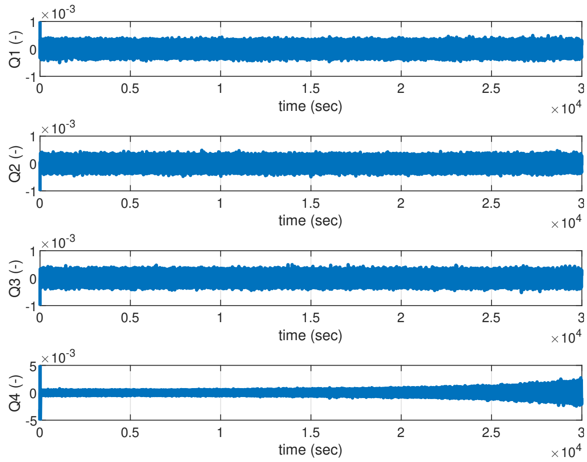


**(c)** Quaternion error estimate.

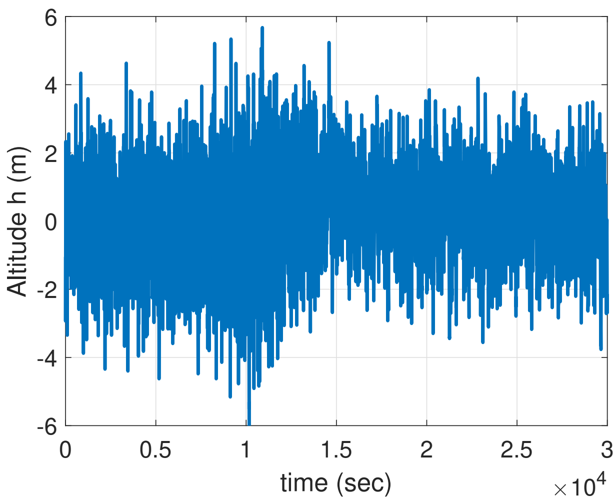


**(d)** Altitude error estimate.

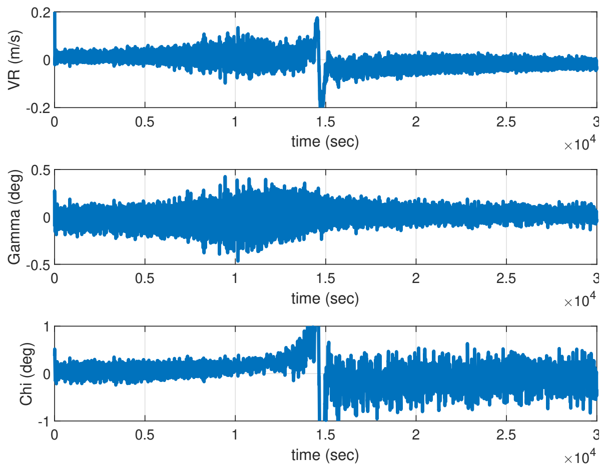


**(e)** Velocity, flight-path angle, and heading angle error estimates.

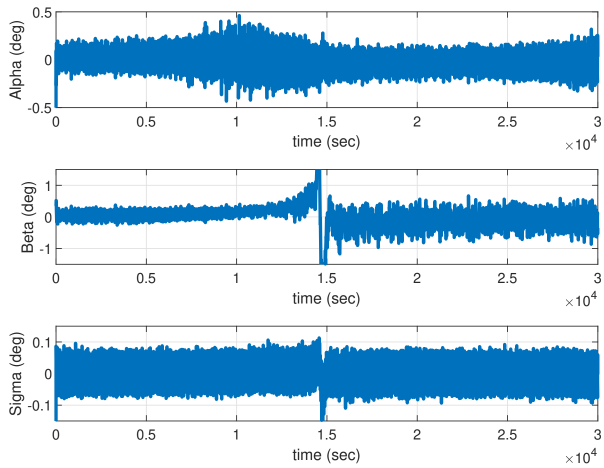


**(f)** Aerodynamic angles error estimates.

**Figure 9.7: Sim #6**: State variables error estimates with navigation system working in parallel to the main simulation using real state variables, for the first 3.000 s of the simulation, with sensor errors and noise. All estimates are within covariance bounds.

**Table 9.4:** Summary of navigation system's error estimates for **Sim #5** without sensor noise, **Sim #5**, and **Sim #6**.

| State Variable Error | Sim #5 no noise | Sim #5 | Sim #6 |
|---|---|---|---|
| $e(X)$ (m) | $2.6 \cdot 10^{-6}$ | 0.01 | -0.02 |
| $e(Y)$ (m) | $-1.8 \cdot 10^{-6}$ | 0.01 | 6.5 |
| $e(Z)$ (m) | $2 \cdot 10^{-6}$ | 0.05 | -26.0 |
| $e(V_X)$ (m/s) | $-4 \cdot 10^{-6}$ | 0.01 | 0.01 |
| $e(V_Y)$ (m/s) | $-3 \cdot 10^{-6}$ | 0.005 | 0.05 |
| $e(V_Z)$ (m/s) | $-2 \cdot 10^{-6}$ | 0.005 | -0.2 |
| $e(Q_1)$ (-) | $-3 \cdot 10^{-8}$ | $2 \cdot 10^{-4}$ | $2 \cdot 10^{-4}$ |
| $e(Q_2)$ (-) | $-2 \cdot 10^{-7}$ | $-1 \cdot 10^{-4}$ | $2 \cdot 10^{-4}$ |
| $e(Q_3)$ (-) | $-5 \cdot 10^{-8}$ | $1 \cdot 10^{-4}$ | $2 \cdot 10^{-4}$ |
| $e(Q_4)$ (-) | $2.1 \cdot 10^{-6}$ | $-2 \cdot 10^{-3}$ | $1 \cdot 10^{-3}$ |
| $e(h)$ (m) | $2 \cdot 10^{-3}$ | 0.01 | 4.0 |
| $e(V)$ (m/s) | $-4 \cdot 10^{-6}$ | 0.02 | -0.03 |
| $e(\gamma)$ (°) | $-2 \cdot 10^{-6}$ | 0.01 | 0.1 |
| $e(\chi)$ (°) | $-8 \cdot 10^{-6}$ | 0.02 | $-0.4$ |
| $e(\alpha)$ (°) | $-9.2 \cdot 10^{-5}$ | 0.2 | 0.2 |
| $e(\beta)$ (°) | $1.8 \cdot 10^{-4}$ | 0.1 | $-0.5$ |
| $e(\sigma)$ (°) | $6.8 \cdot 10^{-5}$ | 0.05 | 0.05 |

noise and errors are included). This comes as a recommendation for future work: to filter out the estimations' noise before passing them to the guidance module. This can be done with the use of a low-pass, high-pass, or band-pass filter (Mooij, 2020).

## 9.5. Orbiter Parameters Results

As mentioned in Section 5.2.2, the orbiting spacecraft will follow a circular, equatorial, and synchronous orbit with respect to the equatorial glider. This way, continuous trajectory tracking of both gliders is ensured, as the spacecraft is in line-of-sight of both during their measurement phase. Using the relations developed in Section 5.2.2, an orbital period of $T_{orb} = 62,072.398$ s $\approx 17.2423$ h is obtained, which is very similar to Uranus' rotational period of 17.24 h. This calculated orbital period is then used in Equation (4.26) yielding a semi-major axis of $a_{orb} = 82,693.320$ km, which corresponds to an orbital altitude of $h_{orb} = 57,305.120$ km.

# 10
# Conclusions and Recommendations

This chapter will first detail the conclusions that can be drawn from this thesis' results, answering the research questions in Section 10.1. A requirements compliance check of the deemed most important mission, system, and modelling requirements is performed in Section 10.2, followed by a list of recommendations for future work in Section 10.3. The Main Research Question that was mentioned in this work is as follows:

Main Research Question

**How can knowledge about Uranus' current atmosphere help us understand the formation and evolution of the Ice Giants, and in a broader sense, those of the Solar System?**

As mentioned in the Introduction, an Intermediate Research Question was defined to stay within the scope of a MSc thesis. It relates which atmospheric quantities are essential to the identification of new science return related to Uranus' formation and evolution, and on how to feasibly measure them. It reads as follows:

Intermediate Research Question

**Which mission profile and GNC design can enable the measurement of essential Uranian atmospheric properties to help answer the Main Research Question?**

This research question was split into four sub-questions:

1. **Which trajectory should be followed by the atmospheric vehicles to measure physical and chemical properties of Uranus' atmosphere?**
2. **Which orbit should the relay spacecraft follow, so as to deliver the atmospheric platforms, track their trajectory, and relay scientific data to the Earth?**
3. **Which is the most appropriate autonomous navigation architecture for atmospheric probing of Uranus?**
4. **What are the limitations and shortcomings of a standard GNC design that allows robust and autonomous mission performance?**

Answers and conclusions to these questions will be provided below.

## 10.1. Conclusions

The relevance of this thesis' Main Research Question lies in the fact that, as of today, none of the current formation and evolution models developed for Uranus can explain all of its chemical and dynamical aspects. Its last close-up observation dates back to 1986 with the Voyager 2 probe's observation of the first layer of its atmosphere, until around −30 km depth. The Intermediate Research Question was formulated so as to provide means to tackle the Main Research Question. In-situ observations until the 100 bar pressure level, or until −375 km of depth could help provide answers to the formation and evolution of Uranus, by analysis of its atmospheric properties' profile, at different locations of the planet. The mission profile and GNC design to achieve such a flight were thus looked into, through the answering of the four previously mentioned sub-questions. The first sub-question to help answer the Intermediate Research Question is repeated here:

1. **Which trajectory should be followed by the atmospheric vehicles to measure physical and chemical properties of Uranus' atmosphere?**

Considering the planet's spatially variable species, it is important to probe different locations of its atmosphere. This can also ensure that an anomalous region is not solely probed, as it inadvertently happened with the Galileo probe at Jupiter. Two target latitudes were thus selected: 17.5° and 89° of its northern atmosphere, to not only complement Voyager 2's measurement of the planet's southern hemisphere, but also to take advantage of the planet's low wind-speed regions, and to probe spatially variable species: the equatorial deep atmosphere is enriched in $CH_4$ and $H_2S$, and possibly other volatiles such as $NH_3$ and $H_2O$ by rising motion from the 100 bar level or deeper, while the polar region enables the measurement of noble gases and of small-scale convection activity leading to potential enhanced humidity of $H_2$ immediately above the clouds. Two atmospheric vehicles are thus required, with one at each defined target latitude. A down-going trajectory, from the 1 bar (0 km) to the 100 bar (−375 km) pressure level, along constant latitudes, ensures the exploration of Uranus' troposphere, while experiencing a more or less constant tailwind, as zonal winds are believed to be dominant in Uranus' atmosphere. Gliders were selected to perform this flight. To fulfil the Tier 1, Tier 2A, and Tier 2B science objectives defined in Section 2.4.1, the necessary payload suite needed on-board the atmospheric vehicles consists of a mass spectrometer, a tunable laser spectrometer, a Helium abundance detector, an atmospheric structure instrument containing an accelerometer, a pressure sensor, and a temperature sensor, a NanoChem instrument, an ultra high frequency transceiver, a nephelometer, and a net flux radiometer. Answers to the following sub-questions provide more information on the established communication link between the atmospheric platforms and the orbiting spacecraft.

The second sub-question is as follows:

2. **Which orbit should the relay spacecraft follow, so as to deliver the atmospheric platforms, track their trajectory, and relay scientific data to the Earth?**

Continuous trajectory tracking of both gliders is essential to the mission, especially to relate the gliders' measurements to Uranus' geometry. Moreover, as the gliders' navigation system relies on relative position and velocity, it is key for the relaying spacecraft to be in continuous line-of-sight of both of them. As suggested by Sayanagi et al. (2020), the orbiter will remain within a 30° telecommunication cone at a distance of no more than $100,000$ km of the atmospheric vehicles to ensure that radio communication can take place with the telecommunication instruments described in Section 5.3. These criteria are ensured by following an equatorial, circular, and synchronous orbit with the equatorial glider. By having the spacecraft orbit at a semi-major axis of $a_{orb} = 82,693.32$ km, with an orbital period of $T_{orb} = 17.2423$ h, it can respect the 30° telecommunication cone requirement, and orbit at $h_{orb} = 57,305.12$ km from Uranus's 1 bar pressure level, defined at 0 km altitude. The spacecraft should also deliver the two descent probes containing each glider, at their respective target latitudes and longitudes. This can be done by performing specific manoeuvres, with the descent probes separating from the relay spacecraft 50 days before their interface altitude of $1,000$ km is reached.

The third sub-question is:

3. **Which is the most appropriate autonomous navigation architecture for atmospheric probing of Uranus?**

Due to Uranus' opaque atmosphere at the foreseen altitudes of the gliders, optical sensors such as star sensors, Sun sensors, and imagers are avoided. Instead of these typical navigation sensors, measurements from the scientific payload's instruments are used as input to the navigation filter. The modelled sensors include an Inertial Measurement Unit (IMU) producing acceleration and acceleration rate measurements, an Atmospheric Structure Instrument (ASI) which comprises an accelerometer, a pressure sensor, and a temperature sensor, whose measurements' combination can relate to the atmospheric vehicle's altitude, an Ultra High Frequency (UHF) transceiver which can provide pseudo range and pseudo range rate measurements with respect to the orbiter, and a Flush Air Data Sensor (FADS) providing pressure, velocity, and aerodynamic angles measurement. Two additional "fake" measurements were included in the navigation sensor suite: a position in the x-direction and the first three quaternion measurements. These were modelled by including the real data and adding noise to them. With these sensors, the Extended Kalman Filter (EKF) estimator was seen to perform well and autonomously, for the atmospheric probing of Uranus.

Finally, the fourth and last sub-question is formulated as follows:

4. **What are the limitations and shortcomings of a standard GNC design that allows robust and autonomous mission performance?**

Ensuring robustness of the GNC system is the main challenge of this thesis. Concerning guidance, a tracking guidance system was necessary to ensure that no trajectory oscillations would occur, as well as no deviation from the commanded reference heading angles of both gliders. A Linear Quadratic Regulator (LQR) was used for both the computation of an angle-of-attack increment and a bank angle increment to ensure this. Both a proportional and a derivative term were needed for the angle-of-attack increment, while only a proportional term was included for the bank angle increment computation. Shortcomings of this design include an unstable response when using navigation estimates that are different than the real simulated values, as feedback to the guidance module. A solution to this was to constrain the tracking guidance's response between a very tight range of values, to always have the produced commands be close to their theoretical optimal values. This did not hinder the software's performance in the simulated case of a downwards gliding flight where only zonal winds are included. Were meridional winds, wind gusts, and turbulence be included, or were the gliders to perform turns, then the tracking guidance response might have to be different than the current one, and the imposed strict limits might hinder the overall performance.

The link between guidance and control was done smoothly, with both the control module's longitudinal and lateral controllers transforming the guidance commands to control surface deflections, by the use of a LQR system as well. This current design showed no shortcomings. Limitations include the generation of gains for multiple altitudes and velocities, as they were seen to vary in terms of the flight conditions.

The navigation system required detailed design of all the necessary navigation sensors, as well as extensive tuning of its gains to reach accurate state estimations. Limitations of the design include the fact that the currently used sensor inputs are tailored for the mission at hand. Indeed, it was shown in Section 7.2.3 that an additional position measurement in x-direction was needed for state estimations convergence, due to the equatorial glider's initial longitude of $\tau = 70°$. The measurement inputs to the navigation estimator would have to be reviewed if another initial longitude were to be chosen. A shortcoming of the navigation filter was the production of noisy aerodynamic angles estimates, which hindered the performance of the guidance system. This issue can be tackled by including a noise-filtering element on the estimates' path to the guidance module, which is left as a recommendation for future work. In this work, the navigation module was run in parallel to the simulation loop in order to assess its performance, but real values were fed back to the guidance module. Another drawback of the navigation filter was the poor performance it demonstrated when sensor noise and errors were included.

The integration of these three modules with the rest of the simulator thus posed a problem. This concerns the guidance module not being robust enough to accept noisy navigation estimates that deviate from the real state variables. It is important to design a tracking guidance system which can both keep the gliders' trajectories stable and directed towards their target heading, as well as accept state estimates different than the real values. Moreover, the estimated aerodynamic angles derived from position and velocity estimates were seen to be quite noisy, which decreases the performance of the guidance system as well. Finally, the chosen Extended Kalman Filter (EKF) did not perform well when sensor errors were included.

This thesis' Intermediate Research Question is repeated here:

Intermediate Research Question

**Which mission profile and GNC design can enable the measurement of essential Uranian atmospheric properties to help answer the Main Research Question?**

To better understand the formation and evolution of the Solar System, it is essential to understand the composition and internal structure of its planets. Uranus and Neptune, commonly referred to as the Ice Giants, are the only Solar System planets that have only been visited by a single fly-by, and which have no actively on-going mission planning to visit them. It is thus crucial for us to study these worlds, in order to link their formation and evolution to that of the Solar System as a whole. Studying Uranus' current atmosphere, and especially its variation with depth is key to the unveiling of its physical and chemical properties. An atmosphere's bulk composition can provide evidence for how and where a planet was formed, as well as the associated protosolar nebula conditions.

It is thus through the in-situ probing of Uranus' atmosphere, both at different locations (at an off-equatorial latitude and a polar latitude of its northern hemisphere) and depths (going from the 1 bar to the 100 bar pressure level), that the best science return can be achieved concerning the uncovering of the planet's mysteries. Such a mission's science objectives can be divided into three parts: Tier 1, Tier 2A, and Tier 2B science objectives, in order of decreasing importance (see Section 2.4.1). Tier 1 and Tier 2A science objectives can be performed with the same instruments and consist in measuring atmospheric constituents well beneath the tropopause, to alleviate the possibility of cold trapping of the heavy noble gases or possible adsorption onto methane ice aerosols. The precise depth required to achieve the Tier 1 and Tier 2A science objectives depends on the sensitivity of the on-board instruments, and the number of atmospheric samples required. Tier 2B science objectives require an even deeper atmospheric probing and are much more sensitive to the chosen entry and descent location. This is because the measurements are more sensitive to local weather and therefore likely not representative of the entire planet.

The instrument suite chosen to be included on-board the gliders to meet these science objectives consists of the following: a mass spectrometer, a tunable laser spectrometer, a Helium abundance detector, an atmospheric structure instrument containing an accelerometer, a pressure sensors, and a temperature sensor, a Nanochem instrument, an ultra high frequency transceiver, a nephelometer, and a net flux radiometer, for a total payload mass of 23.15 kg. The science traceability matrix shown in Table A.1 presents how each instrument can contribute to measuring the quantities mentioned in the science objectives to be achieved. As seen in this table, the chosen payload instruments allow for the fulfilment of Tier 1, Tier 2A, and Tier 2B science objectives, given that the gliders go down until the 100 bar pressure level, at −375 km altitude.

A mission architecture comprising of an orbiting spacecraft can also undeniably increase the science return, as continuous trajectory tracking can take place, as well as the relay of the in-situ vehicles' scientific data to Earth. An orbiter can also perform science measurements with the use of the selected instrument suite in the case of this mission: a narrow angle camera for the potential imaging of the gliders themselves, but also of Uranus and any visual properties it may present, a Doppler imager to perform the Doppler wind experiment and enable the measurement of pseudo range and pseudo range rate with the gliders, and a magnetometer to study the planet's complex magnetic field, for a total orbiter payload mass of 36.7 kg.

With the selected payload suite of both the gliders and the orbiter, undeniable new science data will become available, whose interpretation and analysis can help understand Uranus's mysteries: its active atmospheric dynamics, its low internal energy, its extreme obliquity, its complex magnetic field, and its ring and satellite system containing possible ocean worlds. With this, one can better understand the Ice Giants' formation and evolution, and consequently link it to the Solar System's development.

In terms of this mission's GNC design, it can be concluded that a robust guidance system is needed in the design of such a mission's software. The coupling of the angle-of-attack and bank angle incremental commands of the needed tracking guidance should be investigated. Since the vehicles' flight-path consists of a down-going gliding trajectory, a trimming module in pitch is enough. Finally, for maximum control of the gliders' velocity profiles, a reference trajectory with pseudo-altitude (dependent on altitude, velocity, and flight-path angle) as interpolator was shown to be a good option for the Mission Manager module. A simple controller divided into a longitudinal and lateral controller, and using a LQR is deemed sufficient for this design. For the navigation system, this thesis' design showed that it is possible to include measurements from the science payload to perform state estimations.

## 10.2. Requirements Check

The deemed most important mission, system, and modelling requirements are mentioned again in Table 10.1, along with a verification method, and whether they have been met or not. They were selected for this compliance check, as they drive the mission design. Other requirements were seen to often derive from these ones. As can be seen here, they are all met, through analysis (simulations) or inspection (research on every science instrument for the science traceability matrix shown in Table A.1 for the case of **MIS-6**). For **MOD-1.8**, the current mission design allows for a total of 3.88 Earth days spent between 0 bar and 20 bar, which is more than the suggested minimum of 2 h.

**Table 10.1:** Mission, system, and modelling requirements check.

| Req ID | Requirement | Verification method | Compliance |
|---|---|---|---|
| **MIS-1** | Communication shall be possible between the atmospheric vehicles and the relay spacecraft during the atmospheric vehicles' measurement phase. | Analysis | ✓ |
| **MOD-1.8** | The chosen reference atmospheric vehicle shall stay at least 2 h between the 0 bar and 20 bar pressure levels[a] | Analysis | ✓ |
| **MIS-6** | The scientific measurements performed by instruments on-board the atmospheric vehicles shall fulfil Tier 1, Tier 2A, and Tier 2B science objectives. | Inspection | ✓ |
| **SYS-8** | The atmospheric vehicle shall contain an autonomous guidance system. | Analysis | ✓ |
| **SYS-9** | The atmospheric vehicle shall contain an autonomous control system. | Analysis | ✓ |
| **SYS-10** | The atmospheric vehicle shall contain an autonomous navigation system. | Analysis | ✓ |

[a]Personal communication with Olivier Mousis, 18/01/2021.

## 10.3. Recommendations

This section will discuss recommendations for future work, some of which have already been touched upon in this report. With one of the objectives of this thesis being to identify the limitations and shortcomings of a standard GNC design to fit to the mission at hand, most of the following recommendations are related to that, with a focus on improving the simulator's performance.

- **Mission analysis:** The following point was deemed out of the scope of this thesis, but is crucial to consider for the planning of a mission to Uranus. It consists in performing a thorough analysis concerning the approach of Uranus with the orbiting spacecraft, the release of the two descent probes and their respective glider releases, as well as the probes' entry and descent in Uranus' atmosphere. The orbiter's manoeuvres should be defined, with an estimation of their respective $\Delta V$s. An example of such a mission's orbital manoeuvres is given in Hofstadter et al. (2019). There is mission heritage concerning the release of a descent probe from an orbiter (the Galileo and Huygens probes), but no flown heritage as to the release of a winged vehicle from a descent probe. Mentioned in Section 2.2.1, the NASA ARES mission study provides the theoretical deployment steps to be followed (see Figure 2.2). The probes' coast time should be defined, with a budget for its power usage during that time and the associated power and other concerned sub-system requirements. Concerning the probes' entry and descent, parameters such as the probes' interface altitude, entry velocity, entry flight-path angle, maximum g-load, and maximum thermal load should be calculated more thoroughly, as only values taken from Sayanagi et al. (2020) and Hofstadter et al. (2019) were mentioned in this report.
- **Entry corridor analysis:** To strengthen the entry corridor analysis performed on the gliders' flight until $h = -375$ km, Uranus-specific constants can be used for the constant $c^*$ coming from Chapman's equation, the value $n$ which determines a laminar or turbulent flow, and the empirical constant $m$.
- **Wind model:** The implemented wind model only simulates Uranus' zonal winds, as they dominate meridional ones. By including meridional winds, the gliders' response to lateral loads can be explored, and a better representation of Uranus's wind model can be reached. For this aim, thermal upwelling, wind gusts, and turbulence models can also be included. Viavattene (2018) provides a model for wind gusts and turbulence, using a Dryden wind turbulence model, which could be implemented to this thesis' wind model. The implementation of the wind model in 6 DoF also has to be done.
- **Navigation sensors:** As mentioned in Section 7.2.3, two additional measurement sets were needed to yield convergence of the navigation filter's estimations: a position measurement in x-direction, and the first three quaternions measurements. These were included by taking their real values with added noise. It was attempted to generate the position measurement from other sensors' measurement and knowledge on the mission's geometry, with no success. A recommendation for future work would be to design and include actual sensors that can perform these measurements. A way to determine the gliders' position in x-direction would be to include magnetometer measurements in the navigation filter. Indeed, three-axis

magnetic field measurements can be transformed to a position measurement through the generalised multivariate Gaussian likelihood function from Maybeck (1982) described in the work of Raquet et al. (2013). This measurement can be even more constrained by performing the same measurement on-board the orbiter and comparing relative positions with the gliders.
Concerning the quaternion measurements, they can be derived from either the aerodynamic angle estimates, or measurements from the FADS instrument. Another way to generate these measurements would be to use a Magnetic, Angular Rate, and Gravity (MARG) sensor suite to measure the vehicles' orientation and then transform it to quaternions. A MARG sensor suite can consist of an IMU with a three-axis accelerometer and gyroscope, and a three-axis magnetometer. Inertial orientation components can be computed by integrating the gyroscope measurements, and corrected by using the gravity projection and heading angle estimates derived from acceleration measurements. Besides, the inclusion of a magnetometer in the gliders' payload suite can enhance scientific knowledge on the planet's complex magnetic field.
A final recommendation concerning the navigation sensors would be to implement the angle-of-attack and side-slip angle estimations from the FADS as navigation sensor inputs. This can be done by connecting them to the state estimator block and finding their relation to the estimated state variables for the estimator's measurement matrix $\mathbf{H}$. At the moment, the only FADS-measured quantity used as navigation sensor input is the velocity, but the angle-of-attack is used as an input to the ASI pressure block, as shown in Figure 8.1.

- **Navigation estimator:** The navigation estimator, an Extended Kalman Filter (EKF) in the case of this software, was seen to produce poorer state estimates when sensor noise were included, especially concerning z-position and thus altitude estimates. This sensitivity should be explored, and the filter should be made more robust to this kind of error, as altitude is an important variable towards reaching the mission target altitude of $-375$ km, at the 100 bar pressure level to fulfil the mission's science objectives. The implementation of another kind of filter such as an Unscented Kalman Filter (UKF), or a Particle Filter can be explored to yield more accurate estimations.

- **Tracking guidance:** The coupling of the angle-of-attack and bank angle increments of the tracking guidance should be analysed. At the moment, the two commands are produced separately through a vertical and a lateral tracking guidance system. Nevertheless, the generated angle-of-attack command was seen to have an influence over the bank angle one. This relation should be further explored and taken into account into a re-design of the tracking guidance module.

- **Integration of GNC modules:** The main recommendation concerning the integration of the Guidance, Navigation, and Control (GNC) modules concerns the guidance: it should be made more robust. It is important to design a tracking guidance system which can both keep the gliders' trajectories stable and directed towards their target heading angles, as well as accept state estimates different than the real values. Moreover, the estimated aerodynamic angles derived from position and velocity estimates were seen to be quite noisy, which decreases the performance of the guidance system as well. This noise should thus be filtered out before passing the signals to the guidance module for the comparison with the reference trajectory.
Finally, as mentioned in Section 6.1, a typical GNC development process involves sensitivity analyses of the guidance and control modules, which were not performed in this work. They should be carried out to assess the robustness of each module and of their integration. In particular, a sensitivity analysis on the guidance module can help identify which variables are making the guidance module less robust than expected. For the guidance module's sensitivity analysis, parameters of interest include initial conditions and constants such as the vehicle's mass, inertia matrix, initial velocity, flight-path angle, heading angle, and aerodynamic angles. The influence of the tracking guidance's gains can also be analysed, as well as that of the aerodynamic coefficients. To analyse the system's robustness, relative and absolute errors can be enforced on these parameters, through their addition and subtraction to, or multiplication of the variables' original values. A Monte Carlo analysis can then be run, by repeatedly and randomly changing these error values. The guidance's response can then by analysed, and it can be identified, whether some parameters have more influence on the module's behaviour than others.

- **Simulator frequencies:** In this work, the software is run at an integration frequency of 50 Hz, with all modules running at the same frequency, except the guidance module which is running at 10 Hz, as it is better to have it first converge before passing the data to the next blocks. The implementation of other frequencies did not yield good performance of the software. As a recommendation, other combinations of frequencies should be investigated, as it is common to have the software's integration frequency, the guidance module's frequency, the control module's frequency, the navigation module's frequency, and the sensors' frequency be different. This can be done with the use of Zero-Order Hold blocks in Simulink.

- **Glider's structure and components:** Uranus is the Solar System's coldest planet, with temperatures ranging from $-80^{\circ}$ C to $-200^{\circ}$ C at the explored altitudes of this mission, as seen in Figure 9.2b. The experienced pressure levels are also very extreme, as the aim is to fly from the planet's 1 bar to its 100 bar pressure level. The elements composing the glider's structure thus require an in-depth study, so as to survive these harsh atmospheric conditions. Moreover, a robust thermal control system should be included, to make sure that all the gliders' subsystems remain within their temperature and pressure operational ranges.

# References


Altwegg, K. et al. (2015). "67P/Churyumov-Gerasimenko, a Jupiter Family Comet with a High D/H Ratio". In: *Science* 347.6220, p. 1261952. DOI: 10.1126/science.1261952.

Amalia, E., Moelyadi, M. A., and Putra, C. A. (2018). *Aerodynamics Characteristics of Glider GL-1 based on Computational Fluid Dynamics.* Tech. rep. Bandung, Indonesia: Institute of Technology Bandung.

Archinal, B. A. et al. (2018). "Report of the IAU Working Group on Cartographic Coordinates and Rotational Elements: 2015". In: *Celestial Mechanics and Dynamical Astronomy* 130.3, p. 22. DOI: 10.1007/s10569-017-9805-5.

Aslam, S., Amato, M., Atkinson, D. H., Hewagama, T., Jennings, D. E., Nixon, C. A., and Mousis, O. (2017). "A Compact, Multi-view Net Flux Radiometer for Future Uranus and Neptune Probes". In: EPSC2017–772.

Atkinson, D. H., Mousis, O., Spilker, T. R., and Ferri, F. (2020). "Reference Model Payload for Ice Giant Entry Probe Missions". In: *Space Sci. Rev.* 216.8, p. 120. DOI: 10.1007/s11214-020-00738-y.

Atkinson, D. H., Pollack, J. B., and Seiff, A. (1998). "The Galileo Probe Doppler Wind Experiment: Measurement of the Deep Zonal Winds on Jupiter". In: *J. Geophys. Res.* 103.E10, pp. 22911–22928. DOI: 10.1029/98JE00060.

Baines, K. H. (1997). *Uranus: Atmosphere.* Dordrecht: Encyclopedia of Planetary Science. Encyclopedia of Earth Science. Springer. DOI: 10.1007/1-4020-4520-4_426.

Baines, K. H. and Hammel, H. B. (1994). "Clouds, Hazes, and the Stratospheric Methane Abundance in Neptune". In: *Icarus* 109.1, pp. 20–39. DOI: 10.1006/icar.1994.1075.

Balsiger, H. et al. (2007). "Rosina: Rosetta Orbiter Spectrometer for Ion and Neutral Analysis". In: *Space Sci. Rev.* 128.1-4, pp. 745–801. DOI: 10.1007/s11214-006-8335-3.

Balsiger, H. et al. (2015). "Detection of Argon in the Coma of Comet 67P/Churyumov-Gerasimenko". In: *Science Advances* 1.8, e1500377. DOI: 10.1126/sciadv.1500377.

Banfield, D. and Dissly, R. (2012). "Mars Acoustic Anemometer". In: *AGU Fall Meeting Abstracts* 2012, P23A–1916.

Banfield, D., Gierasch, P., and Dissly, R. (2005). "Planetary Descent Probes: Polarization Nephelometer and Hydrogen Ortho/Para Instruments". In: *IEEE Aerospace Conference Proceedings* 2005, pp. 691–697. DOI: 10.1109/AERO.2005.1559359.

Banfield, D., Schindel, D. W., Tarr, S., and Dissly, R. W. (2016). "A Martian Acoustic Anemometer". In: *Acoustical Society of America Journal* 140.2, pp. 1420–1428. DOI: 10.1121/1.4960737.

Barnes, J. W. et al. (2012). "AVIATR - Aerial Vehicle for in-situ and Airborne Titan Reconnaissance. A Titan Airplane Mission Concept". In: *Experimental Astronomy* 33.1, pp. 55–127. DOI: 10.1007/s10686-011-9275-9.

Batygin, K. and Brown, M. E. (2010). "Early Dynamical Evolution of the Solar System: Pinning Down the Initial Conditions of the Nice Model". In: *The Astrophysical Journal* 716.2, pp. 1323–1331. DOI: 10.1088/0004-637X/716/2/1323.

Batygin, K., Brown, M. E., and Betts, H. (2012). "Instability-Driven Dynamical Evolution Model of a Primordially Five-planet Outer Solar System". In: *The Astrophysical Journal* 744.1, p. L3. DOI: 10.1088/2041-8205/744/1/L3.

Bird, M. K. et al. (2003). *The Huygens Doppler Wind Experiment.* Ed. by Christopher T. Russell. Dordrecht: Springer Netherlands, pp. 613–640. ISBN: 978-94-017-3251-2. DOI: 10.1007/978-94-017-3251-2_16.

Bishop, J., Atreya, S. K., Herbert, F., and Romani, P. (1990). "Reanalysis of Voyager 2 UVS Occultations at Uranus: Hydrocarbon Mixing Ratios in the Equatorial Stratosphere". In: *Icarus* 88.2, pp. 448–464. DOI: 10.1016/0019-1035(90)90094-P.

Boese, R. W., Twarowski, R. J., Gilland, J., Hassig, R. E., and Brown, F. G. (1980). "The Infrared Radiometer on the Sounder Probe of the Pioneer Venus Mission". In: *IEEE Transactions on Geoscience and Remote Sensing* 18, pp. 97–100. DOI: 10.1109/TGRS.1980.350289.

Braun, R., Croom, M., Levine J.and Spencer, D., and Wright, H. (2006). "Design of the ARES Mars Airplane and Mission Architecture". In: *Journal of Spacecraft and Rockets* 43.5, pp. 1026–1034. DOI: 10.2514/1.17956.

Broadfoot, A. L. et al. (1989). "Ultraviolet Spectrometer Observations of Neptune and Triton". In: *Science* 246.4936, pp. 1459–1466. DOI: 10.1126/science.246.4936.1459.

Bryson, A. E. and Ho, Y. C. (1975). "Applied Optimal Control". In: *John Wiley & Sons* 59.8, p. 402. DOI: 10.1002/zamm.19790590826.

Calvin, W. M., Miralles, C., Clark, B. C., and Wilson, G. R. (2000). "Mars Science with Small Aircraft". In: *Concepts and Approaches for Mars Exploration*, p. 55.

Cavalié, T., Venot, O., Miguel, Y., Fletcher, L. N., Wurz, P., Mousis, O., Bounaceur, R., Hue, V., Leconte, J., and Dobrijevic, M. (2020). "The Deep Composition of Uranus and Neptune from In Situ Exploration and Thermochemical Modeling". In: *Space Sci. Rev.* 216.4, p. 58. DOI: 10.1007/s11214-020-00677-8.

Cobleigh, B., Whitmore, S., Haering, E., Borrer, J., and Roback, V. (1999). "Flush Airdata Sensing (FADS) System Calibration Procedures and Results for Blunt Forebodies". In: DOI: 10.2514/6.1999-4816.

Colozza, A. and Landis, G. A. (2005). "Long Duration Solar Flight on Venus". In: *American Institute of Aeronautics and Astronautics*. DOI: 10.2514/6.2005-7156.

Deboer, D. R. and Steffes, Paul G. (1994). "Laboratory Measurements of the Microwave Properties of $H_2S$ Under Simulated Jovian Conditions With an Application to Neptune". In: *Icarus* 109.2, pp. 352–366. DOI: 10.1006/icar.1994.1099.

Deperrois, A. (2003). *XFLR5: Analysis of Foils and Wings Operating at Low Reynolds Numbers*. Tech. rep.

— (2019). *Part IV: Theoretical Limitations and Shortcomings of XFLR5*. Tech. rep.

Dormand, J. R. and Prince, P. J. (1980). "A Family of Embedded Runge-Kutta Formulae". In: *Journal of Computational and Applied Mathematics* 6.1, pp. 19–26. DOI: 10.1016/0771-050X(80)90013-3.

Ellsworth, J. and Whitmore, S. (2007). "Reentry Air Data for a Sub-orbital Spacecraft Based on X-34 Design". In: *Collection of Technical Papers - 45th AIAA Aerospace Sciences Meeting and Exhibit* 20. DOI: 10.2514/6.2007-1200.

Farrell, J.A. and Barth, M. (1999). *The Global Positioning System & Inertial Navigation*. McGraw-Hill Education.

Ferri, F. et al. (2020). "The Atmospheric Structure of the Ice Giant Planets from in Situ Measurements by Entry Probes". In: *Space Sci. Rev.* 216.8, p. 118. DOI: 10.1007/s11214-020-00749-9.

Flasar, F. M., Conrath, B. J., Gierasch, P. J., and Pirraglia, J. A. (1987). "Voyager Infrared Observations of Uranus' Atmosphere: Thermal Structure and Dynamics". In: *J. Geophys. Res.* 92.A13, pp. 15011–15018. DOI: 10.1029/JA092iA13p15011.

Fletcher, L. N., de Pater, I., Orton, G. S., Hofstadter, M. D., Irwin, P. G. J., Roman, M. T., and Toledo, D. (2020a). "Ice Giant Circulation Patterns: Implications for Atmospheric Probes". In: *Space Sci. Rev.* 216.2, p. 21. DOI: 10.1007/s11214-020-00646-1.

Fletcher, L. N., Orton, G. S., Teanby, N. A., and Irwin, P. G. J. (2009). "Phosphine on Jupiter and Saturn from Cassini/CIRS". In: *Icarus* 202.2, pp. 543–564. DOI: 10.1016/j.icarus.2009.03.023.

Fletcher, L. N. et al. (2020b). "Ice Giant Systems: The Scientific Potential of Orbital Missions to Uranus and Neptune". In: *Planet. Space Sci.* 191, p. 105030. DOI: 10.1016/j.pss.2020.105030.

Fulchignoni, M. et al. (1997). "The Huygens Atmospheric Structure Instrument". In: ESA Special Publication 1177. Ed. by A. Wilson, p. 163.

Gilmore, M. S., Beauchamp, P. M., Lynch, R., and Amato, M. J. (2020). *Venus Flagship Mission Decadal Study Final Report*. Tech. rep. Pasadena, California: Jet Propulsion Laboratory California Institute of Technology.

Giordano, N. (2009). *College Physics: Reasoning and Relationships*. Cengage Learning. ISBN: 9780534424718.

Givens, J. J., Nolte, L. J., and Pochettino, L. R. (1983). "Galileo Atmospheric Entry Probe System: Design, Development, and Test". In: *AIAA: 21st Aerospace Sciences Meeting*. DOI: 10.2514/6.1983-98.

Gomes, R., Levison, H. F., Tsiganis, K., and Morbidelli, A. (2005). "Origin of the Cataclysmic Late Heavy Bombardment Period of the Terrestrial Planets". In: *Nature* 435.7041, pp. 466–469. DOI: 10.1038/nature03676.

Guillot, T. (2019). *Uranus and Neptune Are Key to Understand Planets with Hydrogen Atmospheres*. Tech. rep. Nice, France: Université Côte d'Azur, Laboratoire Lagrange, OCA, CNRS UMR 7293, pp. 1–23.

Gulkis, S. and Depater, I. (1984). "A Review of the Millimeter and Centimeter Observations of Uranus." In: NASA Conference Publication 2330. Ed. by J. T. Bergstralh, pp. 225–262.

Hammel, H. B., de Pater, I., Gibbard, S., Lockwood, G. W., and Rages, K. (2005). "Uranus in 2003: Zonal winds, Banded Structure, and Discrete Features". In: *Icarus* 175.2, pp. 534–545. DOI: 10.1016/j.icarus.2004.11.012.

Hammel, H. B., Rages, K., Lockwood, G. W., Karkoschka, E., and de Pater, I. (2001). "New Measurements of the Winds of Uranus". In: *Icarus* 153.2, pp. 229–235. DOI: 10.1006/icar.2001.6689.

Hanel, R. et al. (1986). "Infrared Observations of the Uranian System". In: *Science* 233.4759, pp. 70–74. DOI: 10.1126/science.233.4759.70.

Hassanalian, M., Rice, D., and Abdelkefi, A. (2018). "Evolution of Space Drones for Planetary Exploration: A Review". In: *Progress in Aerospace Sciences* 97, pp. 61–105. DOI: 10.1016/j.paerosci.2018.01.003.

Hassig, M., Libardoni, M., Mandt, K., Miller, G., and Blase, R. (2015). "Performance Evaluation of a Prototype Multi-Bounce Time-of-Flight Mass Spectrometer in Linear Mode and Applications in Space Science". In: *Planet. Space Sci.* 117, pp. 436–443. DOI: 10.1016/j.pss.2015.09.006.

Hassig, M. et al. (2017). "Isotopic Composition of $CO_2$ in the Coma of 67P/Churyumov-Gerasimenko Measured with ROSINA/DFMS". In: *A&A* 605, A50. DOI: 10.1051/0004-6361/201630140.

Helled, R., Anderson, John D., Podolak, M., and Schubert, Gerald (2011). "Interior Models of Uranus and Neptune". In: *The Astrophysical Journal* 726.1, p. 15. DOI: 10.1088/0004-637X/726/1/15.

Helled, R., Nettelmann, N., and Guillot, T. (2020). "Uranus and Neptune: Origin, Evolution and Internal Structure". In: *Space Sci. Rev.* 216.3, p. 38. DOI: 10.1007/s11214-020-00660-3.

Herbert, F., Sandel, B. R., Yelle, R. V., Holberg, J. B., Broadfoot, A. L., Shemansky, D. E., Atreya, S. K., and Romani, P. N. (1987). "The Upper Atmosphere of Uranus: EUV Occultations Observed by Voyager 2". In: *J. Geophys. Res.* 92.A13, pp. 15093–15109. DOI: 10.1029/JA092iA13p15093.

Hofstadter, M., Simon, A., Reh, K., Elliot, J., Niebur, C., and Colangeli, L. (2017). *NASA Ice Giants Pre-Decadal Study Final Report.* Tech. rep. Pasadena, California: Jet Propulsion Laboratory California Institute of Technology.

Hofstadter, M. et al. (2019). "Uranus and Neptune Missions: A Study in Advance of the Next Planetary Science Decadal Survey". In: *Planet. Space Sci.* 177, p. 104680. DOI: 10.1016/j.pss.2019.06.004.

Holtkamp, G. C. (2014). "Descent, Touchdown and Repositioning of a Hopping Planetary Lander on Enceladus". MSc Thesis. Delft, The Netherlands: Delft University of Technology.

Husseyin, S. (2016). "Design Considerations for a Stopped-Rotor Cyclocopter for Venus Exploration". In: *NASA Technical Reports Server.* DOI: https://ntrs.nasa.gov/citations/20160012563.

Irwin, P. G. J. (2003). *Giant Planets of our Solar System: Atmospheres Compositions, and Structure.* Berlin, Germany: Springer. DOI: 10.1007/3-540-37713-1.

Irwin, P. G. J., Teanby, N. A., and Davis, G. R. (2010). "Revised Vertical Cloud Structure of Uranus from UKIRT/UIST Observations and Changes Seen During Uranus' Northern Spring Equinox From 2006 to 2008: Application of New Methane Absorption Data and Comparison with Neptune". In: *Icarus* 208.2, pp. 913–926. DOI: 10.1016/j.icarus.2010.03.017.

Karkoschka, E. and Tomasko, M. G. (2011). "The Haze and Methane Distributions on Neptune from HST–STIS Spectroscopy". In: *Icarus* 211, pp. 780–797. DOI: 10.1016/j.icarus.2010.08.013.

Kay, J., Mason, W. H., Durham, W., Lutze, F, and Benoliel, A. (1993). *Control Authority Issues in Aircraft Conceptual Design: Critical Conditions, Estimation Methodology, Spreadsheet Assessment, Trim and Bibliography.* Virginia Polytechnic Institute and State University.

Kuipers, Jack B. (1999). *Quarternions and Rotation Sequences: A Primer with Applications to Orbits, Aerospace, and Virtual Reality.* Princeton: Princeton University Press.

Landis, G. A. (2006). "Robotic Exploration of the Surface and Atmosphere of Venus". In: *Acta Astron.* 59.7, pp. 570–579. DOI: 10.1016/j.actaastro.2006.04.011.

Landis, G. A., Colozza, A., and Lamarre, C. M. (2003). "Atmospheric Flight on Venus: A Conceptual Design". In: *Journal of Spacecraft and Rockets* 40.5, pp. 672–677. DOI: 10.2514/2.6916.

Lane, A. L. et al. (1986). "Photometry from Voyager 2: Initial Results from the Uranian Atmosphere, Satellites, and Rings". In: *Science* 233.4759, pp. 65–70. DOI: 10.1126/science.233.4759.65.

Le Barbu, T., Vinogradov, I., Durry, G., Korablev, O., Chassefière, E., and Bertaux, J. -L. (2006). "TDLAS a Laser Diode Sensor for the in Situ Monitoring of $H_2O$, $CO_2$ and their Isotopes in the Martian Atmosphere". In: *Advances in Space Research* 38.4, pp. 718–725. DOI: 10.1016/j.asr.2005.04.049.

LeBeau, R. P., Bramesfeld, G., Warning, S., Palotai, C., Dreas, J., Krofta, J., Kirwen, J., and Reyes, P. (2015). "Examining Conditions to Explore the Atmosphere of Uranus with Autonomous Gliders". In: *Technical Soaring* 39, pp. 18–29.

Lebonnois, S. and Schubert, G. (2017). "The Deep Atmosphere of Venus and the Possible Role of Density-Driven Separation of $CO_2$ and $N_2$". In: *Nature Geoscience* 10, pp. 473–477. DOI: 10.1038/ngeo2971.

Leconte, J., Selsis, Franck, Hersant, Franck, and Guillot, T. (2017). “Condensation-Inhibited Convection in Hydrogen-Rich Atmospheres. Stability Against Double-Diffusive Processes and Thermal Profiles for Jupiter, Saturn, Uranus, and Neptune”. In: *A&A* 598, A98. DOI: 10.1051/0004-6361/201629140.

Levesque, J. F. and Lafontaine, J. D. (2007). “Innovative Navigation Schemes for State and Parameter Estimation During Mars Entry”. In: *Journal of Guidance Control Dynamics* 30.1, pp. 169–184. DOI: 10.2514/1.25107.

Levine, J. S. and ARES Science and Engineering Teams (2005). “The Aerial Regional-Scale Environmental Survey (ARES) Mission to Mars”. In: Lunar and Planetary Science Conference. Ed. by S. Mackwell and E. Stansbery, p. 1258.

Levison, H. F. and Stewart, G. R. (2001). “Remarks on Modelling the Formation of Uranus and Neptune”. In: *Icarus* 153.1, pp. 224–228. DOI: 10.1006/icar.2001.6672.

Li, J. and Lu, Y. (2009). “Carbon Nanotube Based Chemical Sensors for Space and Terrestrial Applications”. In: *ECS Transactions* 19.6. DOI: 10.1149/1.3118533.

Li, J., Lu, Y., Ye, Q., Cinke, M., Han, J., and Meyyappan, M. (2003). “Carbon Nanotube Sensors for Gas and Organic Vapor Detection”. In: *Nano Letters* 3.7, pp. 929–933. DOI: 10.1021/nl034220x.

Li, Y. (2009). “Information Gathering Strategies for a Combined Martian System of Aerobots and Rovers”. MSc Thesis. Lulea, Sweden: Lulea University of Technology.

Lightsey, E. G., Mogensen, A. E., Burkhart, P. D., Ely, T. A., and Duncan, C. (2008). “Real-Time Navigation for Mars Missions Using the Mars Network”. In: *Journal of Spacecraft and Rockets* 45.3, pp. 519–533. DOI: 10.2514/1.30974.

Lindal, G. F. (1992). “The Atmosphere of Neptune: An Analysis of Radio Occultation Data Acquired With Voyager 2”. In: *The Astronomical Journal* 103, p. 967. DOI: 10.1086/116119.

Lindal, G. F., Lyons, J. R., Sweetnam, D. N., Eshleman, V. R., Hinson, D. P., and Tyler, G. L. (1987). “The Atmosphere of Uranus: Results of Radio Occultation Measurements with Voyager 2”. In: *J. Geophys. Res.* 92.A13, pp. 14987–15001. DOI: 10.1029/JA092iA13p14987.

Lodders, K., Palme, H., and Gail, H. -P. (2009). “Abundances of the Elements in the Solar System”. In: *Landolt-Bornstein* 4B, pp. 560–630. DOI: 10.1007/978-3-540-88055-4_34.

Lorenz, R. D. (1998). “Speed of Sound in Outer Planet Atmospheres”. In: *Planet. Space Sci.* 47.1-2, pp. 67–77. DOI: 10.1016/S0032-0633(98)00099-3.

Lunine, J. I. (1993). “The Atmospheres of Uranus and Neptune.” In: *ARA&A* 31, pp. 217–263. DOI: 10.1146/annurev.aa.31.090193.001245.

Mahaffy, P. R., Donahue, T. M., Atreya, S. K., Owen, T. C., and Niemann, H. B. (1998). “Galileo Probe Measurements of D/H and 3He/4He in Jupiter’s Atmosphere”. In: *Space Sci. Rev.* 84, pp. 251–263.

Mahaffy, P. R. et al. (2012). “The Sample Analysis at Mars Investigation and Instrument Suite”. In: *Space Sci. Rev.* 170.1-4, pp. 401–478. DOI: 10.1007/s11214-012-9879-z.

Mallama, A., Krobusek, B., and Pavlov, H. (2017). “Comprehensive Wide-Band Magnitudes and Albedos for the Planets, with Applications to Exo-Planets and Planet Nine”. In: *Icarus* 282, pp. 19–33. DOI: 10.1016/j.icarus.2016.09.023.

Marley, M. S. and McKay, C. P. (1999). “Thermal Structure of Uranus’ Atmosphere”. In: *Icarus* 138.2, pp. 268–286. DOI: 10.1006/icar.1998.6071.

Marty, B. et al. (2017). “Xenon Isotopes in 67P/Churyumov-Gerasimenko Show that Comets Contributed to Earth’s Atmosphere”. In: *Science* 356.6342, pp. 1069–1072. DOI: 10.1126/science.aal3496.

Mathews, J. H. and Fink, K. D. (1999). *Numerical Methods Using MATLAB*. 3rd. Prentice Hall.

Maybeck, P. S. (1982). *Stochastic Models, Estimation, and Control*. Academic press.

Melin, T. (2001). *User’s Guide and Reference Manual: Tornado 1.0*. Stockholm, Sweden.

Melkert, J., Brugemann, V., Simao Ferreira, C., Mooij, E., Sinke, J., and Verhagen, W. (2003). *Delft Aerospace Design Projects 2003: Inspiring Designs in Aeronautics, Astronautics and Wind Energy*. Hilversum, The Netherlands: B.V. Uitgeversbedrijf Het Goede Boek.

— (2008). *Delft Aerospace Design Projects 2003: Inspiring Designs in Aeronautics, Astronautics and Wind Energy*. Hilversum, The Netherlands: B.V. Uitgeversbedrijf Het Goede Boek.

Mooij, E. (1997a). *Linear Quadratic Regulator Design for an Unpowered, Winged Re-Entry Vehicle*. Delft: Delft University Press.

— (1997b). *The Motion of a Vehicle in a Planetary Atmosphere*. Delft: Delft University Press.

Mooij, E. (2014). “Adaptive Heat-Flux Tracking for Re-Entry Guidance”. In: *AIAA/AAS Astrodynamics Specialist Conference* (4142).

— (2020). “Robust Control of a Conventional Aeroelastic Launch Vehicle”. In: *AIAA Scitech 2020 Forum*.

Mooij, E. and Chu, Q. P. (2002). “Tightly-coupled IMU/GPS Re-entry Navigation System”. In: *AIAA Guidance, Navigation, and Control Conference* (5005).

Mooij, E. and Ellenbroek, M. H. J. (2011). “Multi-Functional Guidance, Navigation and Control Simulation Environment - Rapid Prototyping of Space Simulations”. In: *Rapid Prototyping Technology - Principles and Functional Requirements*. Ed. by Muhammad Enamul Hoque. InTech. Chap. 15, pp. 315–338. DOI: 10.5772/23006.

Morbidelli, A., Tsiganis, K., Crida, A., Levison, H. F., and Gomes, R. (2007). “Dynamics of the Giant Planets of the Solar System in the Gaseous Protoplanetary Disk and Their Relationship to the Current Orbital Architecture”. In: *The Astrophysical Journal* 134.5, pp. 1790–1798. DOI: 10.1086/521705.

Moses, J. I., Cavalie, T., Fletcher, L. N., and Roman, M. T. (2020). “Atmospheric Chemistry on Uranus and Neptune”. In: *Philosophical Transactions of the Royal Society A: Mathematical, Physical and Engineering Sciences* 378.2187, p. 20190477. DOI: 10.1098/rsta.2019.0477.

Mousis, O. et al. (2014). “Scientific Rationale of Saturn’s in Situ Exploration”. In: *Planet. Space Sci.* 104, pp. 29–47. DOI: 10.1016/j.pss.2014.09.014.

Mousis, O. et al. (2016). “The Hera Saturn Entry Probe Mission”. In: *Planet. Space Sci.* 130, pp. 80–103. DOI: 10.1016/j.pss.2015.06.020.

Mousis, O. et al. (2018). “Scientific Rationale for Uranus and Neptune in Situ Explorations”. In: *Planet. Space Sci.* 155, pp. 12–40. DOI: 10.1016/j.pss.2017.10.005.

Mousis, O. et al. (2019). *In Situ Exploration of the Giant Planets*. Tech. rep. Marseille, France. DOI: 10.1007/s10686-021-09775-z.

Mulder, J. A., Chu, Q. P., Sridhar, J. K., Breeman, J. H., and Laban, M. (1999). “Non-Linear Aircraft Flight Path Reconstruction Review and New Advances”. In: *Progress in Aerospace Sciences* 35.7, pp. 673–726. DOI: 10.1016/S0376-0421(99)00005-6.

National Academy of Sciences (2022). *Origins, World, and Life: A Decadal Strategy for Planetary Science and Astrobiology 2023-2032*. Tech. rep. Washington, DC: The National Academies of Sciences, Engineering, Medicine.

Nesvorný, D. (2011). “Young Solar System’s Fifth Giant Planet?” In: *The Astrophysical Journal* 742.2, p. L22. DOI: 10.1088/2041-8205/742/2/L22.

Niemann, H. B. et al. (1998). “The Composition of the Jovian Atmosphere as Determined by the Galileo Probe Mass Spectrometer”. In: *J. Geophys. Res.* 103.E10, pp. 22831–22846. DOI: 10.1029/98JE01050.

Niemann, H. B. et al. (2002). “The Gas Chromatograph Mass Spectrometer for the Huygens Probe”. In: *Space Sci. Rev.* 104.1, pp. 553–591. DOI: 10.1023/A:1023680305259.

Pearl, J. C., Conrath, B. J., Hanel, R. A., Pirraglia, J. A., and Coustenis, A. (1990). “The Albedo, Effective Temperature, and Energy Balance of Uranus, as Determined from Voyager IRIS Data”. In: *Icarus* 84.1, pp. 12–28. DOI: 10.1016/0019-1035(90)90155-3.

Perez-Ayucar, M. et al. (2016). “Science Data Volume Management for the Rosetta Spacecraft”. In: *SpaceOps 2016 Conference*. DOI: 10.2514/6.2016-2489.

St-Pierre, M. and Gingras, D. (2004). “Comparison Between the Unscented Kalman Filter and the Extended Kalman Filter for the Position Estimation Module of an Integrated Navigation Information System”. In: *IEEE Intelligent Vehicles Symposium, Proceedings*, pp. 831–835. DOI: 10.1109/IVS.2004.1336492.

Podolak, M., Helled, R., and Schubert, Gerald (2019). “Effect of Non-Adiabatic Thermal Profiles on the Inferred Compositions of Uranus and Neptune”. In: *MNRAS* 487.2, pp. 2653–2664. DOI: 10.1093/mnras/stz1467.

Pratama, H. A. (2015). *Conceptual Design of Indonesian National Glider GL-01*. Tech. rep. Bandung, Indonesia: Institute of Technology Bandung.

Ragent, B., Privette, C. A., Avrin, P., Waring, J. G., Carlston, C. E., Knight, T. C. D., and Martin, J. P. (1992). “Galileo Probe Nephelometer Experiment”. In: *Space Sci. Rev.* 60.1-4, pp. 179–201. DOI: 10.1007/BF00216854.

Raquet, J. F., Shockley, J. A., and Fisher, K. (2013). *Determining Absolute Position Using 3-Axis Magnetometers and the Need for Self-Building World Models*. Tech. rep. NATO/OTAN.

Reh, K., Erd, C., Matson, D., Coustenis, A., Lunine, J. I., and Lebreton, J. P. (2009). *Titan Saturn System Mission NASA/ESA Joint Summary Report*. Tech. rep., pp. 1–8. DOI: 10.1109/AERO.2009.4839316.

Reinhardt, C., Chau, A., Stadel, J., and Helled, R. (2020). "Bifurcation in the History of Uranus and Neptune: The Role of Giant Impacts". In: *MNRAS* 492.4, pp. 5336–5353. DOI: 10.1093/mnras/stz3271.

Rijnsdorp, J. (2017). "Performance of a Flush Airdata Sensor in a Particle Filter-Based Re-entry Navigation System". MSc Thesis. Delft, The Netherlands: Delft University of Technology.

Rubin, M. et al. (2017). "Evidence for Depletion of Heavy Silicon Isotopes at Comet 67P/Churyumov-Gerasimenko". In: *A&A* 601, A123. DOI: 10.1051/0004-6361/201730584.

Sayanagi, K. M. et al. (2020). "Small Next-Generation Atmospheric Probe (SNAP) Concept to Enable Future Multi-Probe Missions: A Case Study for Uranus". In: *Space Sci. Rev.* 216.4, p. 72. DOI: 10.1007/s11214-020-00686-7.

Seiff, A., Kirk, Donn B., Knight, Tony C. D., Young, R. E., Mihalov, J. D., Young, L. A., Milos, F. S., Schubert, G., Blanchard, R. C., and Atkinson, D. H. (1998). "Thermal Structure of Jupiter's Atmosphere Near the Edge of a 5- m Hot Spot in the North Equatorial Belt". In: *J. Geophys. Res.* 103.E10, pp. 22857–22889. DOI: 10.1029/98JE01766.

Seiff, A. and Knight, T. C. D. (1992). "The Galileo Probe Atmosphere Structure Instrument". In: *Space Sci. Rev.* 60.1-4, pp. 203–232. DOI: 10.1007/BF00216855.

Simon, A., Nimmo, F., and Anderson, R. C. (2022). *Uranus Orbiter & Probe: A Journey to an Ice Giant System.* Tech. rep.

Smith, S., Guynn, M., Parks, R., and Gelhausen, P. (2004). "Evolution of a Mars Airplane Concept for the ARES Mars Scout Mission". In: *2nd AIAA "Unmanned Unlimited" Conf. and Workshop & Exhibit.* DOI: 10.2514/6.2003-6578.

Souami, D. and Souchay, J. (2012). "The Solar System's Invariable Plane". In: *A&A* 543.A133. DOI: 10.1051/0004-6361/201219011.

Soyuer, D., Soubiran, F., and Helled, R. (2020). "Constraining the Depth of the Winds on Uranus and Neptune via Ohmic Dissipation". In: *MNRAS* 498.1, pp. 621–638. DOI: 10.1093/mnras/staa2461.

Sromovsky, L. A., Collard, A. D., Fry, P. M., Orton, G. S., Lemmon, M. T., Tomasko, M. G., and Freedman, R. S. (1998). "Galileo Probe Measurements of Thermal and Solar Radiation Fluxes in the Jovian Atmosphere". In: *J. Geophys. Res.* 103.E10, pp. 22929–22978. DOI: 10.1029/98JE01048.

Sromovsky, L. A. and Fry, P. M. (2005). "Dynamics of Cloud Features on Uranus". In: *Icarus* 179.2, pp. 459–484. DOI: 10.1016/j.icarus.2005.07.022.

Stevens, M. H., Strobel, D. F., and Herbert, F. (1993). "An Analysis of the Voyager 2 Ultraviolet Spectrometer Occultation Data at Uranus: Inferring Heat Sources and Model Atmospheres". In: *Icarus* 101.1, pp. 45–63. DOI: 10.1006/icar.1993.1005.

Szulagyi, J., Cilibrasi, M., and Mayer, L. (2018). "In Situ Formation of Icy Moons of Uranus and Neptune". In: *The Astrophysical Journal* 868.1, p. L13. DOI: 10.3847/2041-8213/aaeed6.

Tomasko, M. G. et al. (2002). "The Descent Imager/Spectral Radiometer (DISR) Experiment on the Huygens Entry Probe of Titan". In: *Space Sci. Rev.* 104.1, pp. 469–551. DOI: 10.1023/A:1023632422098.

Tyler, G. L., Sweetnam, D. N., Anderson, J. D., Campbell, J. K., Eshleman, V. R., Hinson, D. P., Levy, G. S., Lindal, G. F., Marouf, E. A., and Simpson, R. A. (1986). "Voyager 2 Radio Science Observations of the Uranian System: Atmosphere, Rings, and Satellites". In: *Science* 233.4759, pp. 79–84. DOI: 10.1126/science.233.4759.79.

Viavattene, G. (2018). "Flying Qualities and Controllability of Hypersonic Spaceplanes". MSc Thesis. Delft, The Netherlands: Delft University of Technology.

Von Zahn, U. and Hunten, D. M. (1992). "The Jupiter Helium Interferometer Experiment on the Galileo Entry Probe". In: *Space Sci. Rev.* 60.1-4, pp. 263–281. DOI: 10.1007/BF00216857.

Von Zahn, U., Hunten, D. M., and Lehmacher, G. (1998). "Helium in Jupiter's Atmosphere: Results from the Galileo Probe Helium Interferometer Experiment". In: *J. Geophys. Res.* 103.E10, pp. 22815–22830. DOI: 10.1029/98JE00695.

Wakker, K. F. (2015). *Fundamentals of Astrodynamics.* Tech. rep., p. 682.

Webster, C. R. and Mahaffy, P. R. (2011). "Determining the Local Abundance of Martian Methane and its $^{13}C/^{12}C$ and D/H Isotopic Ratios for Comparison with Related Gas and Soil Analysis on the 2011 Mars Science Laboratory (MSL) Mission". In: *Planet. Space Sci.* 59.2-3, pp. 271–283. DOI: 10.1016/j.pss.2010.08.021.

Welch, G. and Bishop, G. (1995). *An introduction to the Kalman Filter.* Tech. rep.

Wertz, J. R. (2001). *Orbit and Constellation Design and Management*. 2nd ed. United States of America: Microcosm Press and Sringer.

West, R. A., Lane, A. L., Hord, C. W., Esposito, L. W., Simmons, K. E., Nelson, R. M., and Wallis, B. D. (1987). "Temperature and Aerosol Structure of the Nightside Uranian Stratosphere from Voyager 2 Photopolarimeter Stellar Occultation Measurements". In: *J. Geophys. Res.* 92.A13, pp. 15030–15036. DOI: 10.1029/JA092iA13p15030.

Whitmore, S. A. and Moes, T. R. (1994). "Measurement Uncertainty and Feasibility Study of a Flush Airdata System for a Hypersonic Flight Experiment". In: *NASA Technical Memorandum 4627* H-2010.

Zarchan, P. (2005). *Fundamentals of Kalman Filtering: A Practical Approach*. Vol. 208. Progress in Astronautics and Aeronautics. AIAA, Incorporated.

# A

# Science Traceability Matrix

The following table details how the mission's research question is divided into three science objective groups (Tier 1, Tier 2A, and Tier 2B), and how each of their measurement requirement can be fulfilled with the selected payload suite. Tier 1 and Tier 2A science objectives can be performed with the same instruments and consist in measuring atmospheric constituents well beneath the tropopause. The depth required to achieve the Tier 1 and Tier 2A science objectives corresponds to one where the pressure is of 10 bar or more. Tier 2B science objectives require a deeper atmospheric probing and are much more sensitive to the entry and descent location chosen. It can be seen here, that the mass spectrometer can help fulfil the majority of measurement requirement, with the tunable laser spectrometer confirming some measurements.

**Table A.1:** Mission science traceability matrix.

| Intermediate Research Question | Mission Science Objectives | Measurement Requirements | Measurement Mode: Mass Spectrometer | Tunable Laser Spectrometer | Helium Abundance Detector | Atmospheric Structure Instrument | NanoChem | Ultra Stable Oscillator (Doppler Wind Experiment) | Nephelometer | Net Flux Radiometer |
|---|---|---|---|---|---|---|---|---|---|---|
| Which mission profile and GNC design can enable the measurement of essential Uranian atmospheric properties to help answer the Main Research Question ? | Tier 1 | Measure the atmospheric helium abundance with an accuracy comparable to measurements made by the Galileo probe helium abundance detector at Jupiter, about 2%[a] | ✓ | | ✓ | | | | | |
| | | Measure the abundance of the noble gases Ne, Xe, Kr, and Ar with an accuracy close to current uncertainties in measured solar abundances, approximately 10%[b] | ✓ | | | | | | | |
| | | Measure the isotopic ratio of nitrogen $^{15}N/^{14}N$ with an accuracy of ±5%[c] | ✓ | ✓ | | | | | | |
| | | Measure the D/H ratio of hydrogen with an accuracy of ±5% or better[d] | ✓ | ✓ | | | | | | |
| | | Measure the helium isotope ratio $^{3}He/^{4}He$ with an accuracy at least commensurate with measurements made by the Galileo neutral mass spectrometer, ±3%[e] | ✓ | | | | | | | |
| | | Measure key noble gas isotope ratios $^{20}Ne/^{22}Ne$, $^{36}Ar/^{38}Ar$, $^{132}Xe$/total Xe, $^{131}Xe$/total Xe, and $^{129}Xe$/total Xe with an accuracy of ±1% to enable direct comparison with other known Solar System values[c] | ✓ | | | | | | | |
| | | Measure atmospheric pressure and temperature during the atmospheric vehicle's descent with an accuracy comparable to the Galileo probe measurements at Jupiter, Pressure: 0.5%; Temperature: ±0.1° K in the upper troposphere, ±1° K at deeper levels[f] | | | | ✓ | | | | |
| | | Measure the speed of sound in the atmosphere (used to reconstruct the profile of ortho to para hydrogen along the atmospheric vehicle's descent trajectory) with an accuracy of at least 1%[g] | | | | ✓ | | | | |
| | Tier 2A | Measure the isotope ratios of carbon $^{13}C/^{12}C$ and oxygen $^{18}O/^{17}O/^{16}O$ with accuracies of ±1%[c] | ✓ | ✓ | | | | | | |
| | | Measure the tropospheric abundances of CO and $PH_3$ with an accuracy equivalent to Jupiter and Saturn, ±5%[h,i] | ✓ | ✓ | | | | | | |
| | | Detect and measure the abundances of other disequilibrium species in the troposphere such as $AsH_3$ and $GeH_4$ with an accuracy of ±10%[c] | ✓ | ✓ | | | | | | |
| | Tier 2B | Measure the vertical (altitude) profiles of elemental abundances (relative to hydrogen) of the cosmogenically abundant species carbon, nitrogen, sulfur, and oxygen from their primary host molecules $CH_4$, $NH_3$, $H_2S$, and $H_2O$, respectively with an accuracy of ±10%, approximately equal to solar abundances measured from photospheric and meteoritic data[b,c] | ✓ | ✓ | | | ✓ | ✓ | | ✓ |
| | | Measure the altitude structure and properties of clouds and haze layers, including determination of the aerosol optical properties, size distributions, number/mass densities, and possibly composition | | | | | | | ✓ | |
| | | Measure the altitude profile of atmospheric dynamics along the atmospheric vehicle's descent path, including horizontal winds, waves, and convection | | | | | | ✓ | | |
| | | Measure altitude profile of the net radiative balance between solar visible insolation and upwelling thermal infrared radiation | | | | | | | | ✓ |

[a](Von Zahn et al., 1998) [b](Lodders et al., 2009) [c](Mousis et al., 2018) [d](Mousis et al., 2016) [e](Mahaffy et al., 1998) [f](Seiff et al., 1998) [g](Banfield et al., 2005) [h](Fletcher et al., 2009) [i](Mousis et al., 2014)

# B

# Detailed Science Instruments

This appendix includes a detailed description of the scientific payload instruments that were not used as navigation sensors. Understanding them in detail is of relevance to the completion of each science objective.

## Mass Spectrometer

The mission's mass spectrometer should perform measurements of the chemical composition and isotope abundances in the atmosphere, such as H, C, N, S, P, Ge, As, noble gases He, Ne, Ar, Kr, and Xe, and the isotopes D/H, $^{13}C/^{12}C$, $^{15}N/^{14}N$, $^{17}O/^{16}O$, $^{18}O/^{16}O$, $^{3}He/^{4}He$, $^{20}Ne/^{22}Ne$, $^{38}Ar/^{36}Ar$, $^{36}Ar/^{40}Ar$, and those of Kr and Xe. It is important for the instrument to be able to distinguish between different molecular species with the same nominal mass. For example, $N_2$, CO, and $C_2H_4$, all have nominal mass of 28, but differ in their actual mass by about 0.01 amu. Two solutions can help solve this issue: using a high-resolution mass spectrometer, or applying chemical pre-separation of the sample followed by low- resolution mass spectrometry. So far, previous space missions have made use of the chemical pre-separation technique, except for the Rosetta Orbiter Spectrometer for Ion and Neutral Analysis (ROSINA) instrument aboard the Rosetta orbiter (Balsiger et al., 2007). On top of the complexity of such a system, the disadvantage of using chemical pre-separation is that a pre-selection of the species to be investigated must be done through the choice of chromatographic columns. On the other hand, no chemical composition needs to be assumed when using high mass spectrometry (Mousis et al., 2018).

For this mission, a high-resolution mass spectrometer will be used, as suggested in the work of Mousis et al. (2018). It is made of a Double Focusing Mass Spectrometer (DFMS) with a mass resolution of about $m/\Delta m = 9,000$, a Reflectron Time-Of-Flight (RTOF) instrument with a mass resolution of about $m/\Delta m = 5,000$ both at 50% peak height, and two pressure gauges. Isotope ratios were determined with percent-level accuracy for gases in the cometary coma for H/D (Altwegg et al., 2015), for $^{13}C/^{12}C$ and $^{18}O/^{16}O$ (Hassig et al., 2017), for the silicon isotopes (Rubin et al., 2017), $^{38}Ar/^{36}Ar$ (Balsiger et al., 2015), and Xe isotopes (Marty et al., 2017).

Since this instrument was developed before Rosetta's 2004 launch, it is expected that this thesis' mission's mass spectrometer can achieve higher accuracy with a smaller instrument mass and power requirement. ROSINA's final design has a mass of 34.8 kg and consumes 49 W, but a similar state-of-the-art instrument such as Europa Clipper's Mass Spectrometer for Space Exploration (MASPEX), is expected to weigh 8 kg and consume around 36 W, for a resolving power of more than $m/\Delta m = 30,000$. This instrument is now at a Technology Readiness Level (TRL) of 4.

## Tunable Laser Spectrometer:

A tunable laser spectrometer (TLS) would be used here to achieve accuracies of about 0.1 % on the isotopic abundances of D/H, $^{13}C/^{12}C$, $^{18}O/^{16}O$, and $^{17}O/^{16}O$ (Mousis et al., 2018), and $^{15}N/^{14}N$ (Atkinson et al., 2020). It can also be used for the measurement of abundances of targeted species such as CO, $PH_3$, $AsH_3$, $SiH_4$, $GeH_4$, $NH_3$, $CH_4$, $H_2S$ (Atkinson et al., 2020). This instrument employs an ultra-high spectral resolution of 0.0005 $cm^3$ tunable laser absorption spectroscopy in the near infra-red (NIR) to mid-infra-red regions (MID).

An interesting instrument to implement here, is the Sample Analysis at Mars (SAM) suite from NASA's 2011 Mars Science Laboratory (MSL) mission with the Curiosity rover. Its TLS uses two laser sources: a NIR tunable laser, which accesses lines of carbon dioxide, water and their isotopic forms, and a JPL-built interband cascade IC laser at 3.27 μm that operates at 245 K with a two-stage thermoelectric cooler (TEC) for methane and its isotopic forms $^{13}CH_4$ and $CH_3D$ (Webster and Mahaffy, 2011). This instrument's methane laser channel could thus be activated especially in the expected region of methane cloud at 1.2 bar.

## Helium Abundance Detector

This instrument measures the atmosphere's refractive index, which is a function of the composition of the sampled gas. Since Uranus' atmosphere is mostly composed of $H_2$ and He (to more than 99.5%), the measured refractive index is a direct measure of the $He/H_2$ ratio. A two-beam interferometer is used, with one beam passing through a reference gas, and the other through the measured atmospheric gas. It is the difference in optical path, which gives the difference in refractive index between the two gases (Mousis et al., 2018).

The Helium Abundance Detector (HAD) instrument used for the Galileo mission made use of a Jamin-Mascart interferometer, which was designed for an accuracy of $\pm 0.0015$ for the $He/H_2$ ratio. The accomplished measurement actually yielded an accuracy of $0.1350 \pm 0.0027$ (Von Zahn et al., 1998), which is lower than expected, but still better than what is achievable by a mass spectrometer. The reference gas used consisted of a mixture of argon and neon, with refractive index of 11.1% He and 88.9% $H_2$ (Von Zahn and Hunten, 1992). The same instrument can be used for this mission.

## NanoChem

The NanoChem instrument would be used as an addition to the vehicle's mass spectrometer, to detect the presence and measure the abundances of molecules such as $CH_4$, $H_2S$, $NH_3$, and $H_2O$. It consists of the following elements: a set of carbon nanotube-based sensing elements, a temperature sensor, and a pressure sensor (J. Li and Lu, 2009; J. Li et al., 2003). In Uranus' atmosphere, Sayanagi et al. (2020) give expected volume concentrations as follows: $CH_4$ with 1 ppm – 5%, $H_2S$ with 10 ppb – 0.1%, and $NH_3$ with 10 ppb – 0.1%. It is also predicted that the low temperatures encountered in Uranus' troposphere (50 K to 350 K)[1] will not be an issue as the instrument's ingested air will be heated to ensure the instrument deck to maintain temperatures above 0° C. To achieve the required sensitivity, it currently takes a NanoChem instrument approximately 30 seconds of integration time to measure the resistivity curve. The sensing head is then cleaned using an ultra-violet (UV) light emitting diode (LED) for a few seconds, which is deemed practically instantaneous. It is important to note that this response time would be slowed down when exposed to lower temperatures. It is believed, however, that a sample integration period of 10 seconds is short enough to allow multiple measurements per scale height. A complete list of detectable species is made available by Sayanagi et al. (2020).

## Nephelometer

A nephelometer will be used in this mission to characterise Uranus' atmospheric clouds, aerosols, and condensates. This is done by illuminating haze and cloud aerosols with a light source and measuring the flux and degree of polarisation of light scattered in several directions, by studying individual particles. Measurement of the angular spectrum and polarisation of scattered light can then help determine properties of aerosols. The flux and polarisation of sunlight diffusing through the atmosphere can also be measured, yielding the visible optical depth and spectral variation for all atmospheric layers explored by the vehicle (Atkinson et al., 2020). Two instrument modules can be used: Light Optical Aerosol Counter (LOAC) which helps retrieve the size distribution of particles in the $0.2 - 50$ mm range, and Polarimetric Aerosol Versatile Observatory (PAVO) to measure their shape and composition (Mousis et al., 2016). Simultaneous measurements can be conducted, at up to 10 scattering angles in the 20–170° range (Mousis et al., 2019). The LOAC technology can thus also help distinguish between solid and liquid particles of methane and other hydrocarbons, that might be present in Uranus' atmosphere, due to the low temperatures (Mousis et al., 2018). For Earth applications, with often took the form of an atmospheric balloon, a pump is usually used to inject the atmospheric particles into the optical chamber and the laser beam. For a winged vehicle, this pump can be omitted, and a collecting inlet can simply be mounted so as to inject the particles inside the chamber naturally (Mousis et al., 2018).

The 1970 nephelometer design of the Galileo probe was calibrated to measure at scattering angles of 5.8°, 16°, 40°, 70°, and 178°, with estimates of mean particle radii being inferred from about 0.2 to 20 micro (mu). It was decided to take this instrument as the reference nephelometer for this mission, by halving its mass, power, and dimensions requirements, considering the technology advancements that occurred since 1970.

[1] https://en.wikipedia.org/wiki/Uranus#/media/File:Tropospheric_profile_Uranus_new.svg,accessedon09/04/2021.

### Net Flux Radiometer

A net flux radiometer (NFR) will be used to measure upward and downward radiative fluxes. This is important to locate sinks and sources of radiation within the atmosphere by measuring radiative heating or cooling, identify cloudy and more opaque regions, and identify elements such as methane, ammonia, and water vapor (Mousis et al., 2019). The results of this instrument can only be exploited in the presence of other instruments such as a mass spectrometer, an atmospheric structure instrument, a nephelometer, and a radio science instrument (Atkinson et al., 2020).

A NFR was already present on the sounder probe of the Pioneer Venus mission (Boese et al., 1980), on the Galileo probe (Sromovsky et al., 1998), and on the Huygens probe (Tomasko et al., 2002). The most recent version of such an instrument, designed for a Uranus mission, was designed by Goddard Space Flight Center. It is a two-channel NFR and can measure upward and downward radiation flux in a $5^{\circ}$ field-of-view at five distinct look angles ($\pm 80^{\circ}$, $\pm 45^{\circ}$, and $0^{\circ}$) relative to zenith/nadir. The first spectral channel is a solar channel (0.4 to 3.5 μm), and the second one is thermal (4 to 300 μm). The sampling rate is once every 2 seconds at each angle (Aslam et al., 2017).

# C

# Numerical Methods

This chapter will present the choice of software as well as numerical methods which were used for the simulations of the atmospheric vehicles in Uranus' environment.

## C.1. Software Design Choices

The choice of software tool depends on the applicability to the simulations that were conducted during this thesis, as well as the availability of libraries and toolboxes, which can help in the project. Several tools are available such as: MATLAB/Simulink, the TU Delft Astrodynamics Toolbox (Tudat) which uses C++ libraries, and Python[1]. They each work in different programming languages.

The Tudat environment is most commonly used to simulate various astrodynamic applications such as interplanetary flight, re-entry dynamics, specialised orbit design, etc. MATLAB/Simulink is most commonly used to design and simulate control systems, because it offers a large number of toolboxes for that purpose. It also looks more visually practical to use when constructing software, as the software architecture can easily be visualised by looking at how blocks are connected to each other. That is why MATLAB/Simulink will be chosen as the programming software for this thesis.

The simulation of the atmospheric vehicle's trajectory was obtained by propagating the equations of motion over time. Thus, numerical integration will be discussed below. Interpolation methods will also be described, to use to retrieve results from tabulated databases.

## C.2. Integration

A numerical method needs to be chosen to perform the task of propagating the equations of motion over time. Here, the numerical integration process refers to the method used to find numerical approximations to the solutions of Ordinary Differential Equations (ODEs). The concept of ODEs is described by the following equation where $i$ goes from 1 to $n$:

$$\frac{d\mathbf{y}_i(\mathbf{x})}{d\mathbf{x}} = \mathbf{f}_i(\mathbf{x}, \mathbf{y}_1, ..., \mathbf{y}_n) \tag{C.1}$$

Boundary conditions are needed to numerically tackle an ODE. They are algebraic conditions on the value of the functions $\mathbf{y}_i$, and can be divided into two different sets: initial value problems and two-point boundary problems. A specific initial condition is given for initial value problems, in the following form:

$$\mathbf{y}(\mathbf{x}_0) = \mathbf{y}_0 \tag{C.2}$$

On the other hand, two-point boundary problems have their boundary conditions defined as follows:

$$\mathbf{g}(\mathbf{y}(\mathbf{x}_0), \mathbf{y}(\mathbf{x}_n)) = \mathbf{0} \tag{C.3}$$

A linear ODE can be solved analytically. It consists of a linear combination of derivatives of the state. However, most real-life cases are described by non-linear equations that have to be solved numerically. For this purpose,

[1] `https://docs.tudat.space/en/stable/index.html`, accessed on 24/05/2022.

the exact solution can, for instance, be approximated using Euler's method, where a small step-size $\Delta\mathbf{x}$ results in a more accurate approximation:

$$\mathbf{y}(\mathbf{x} + \Delta\mathbf{x}) \approx \mathbf{y}(\mathbf{x}) + \dot{\mathbf{y}}\Delta\mathbf{x} \tag{C.4}$$

Other numerical integration methods than the Euler method are available to find solutions to ODEs. The choice of a specific integration method depends on several aspects. First, the computational speed is to be taken into account. The use of a complex integration method will often increase the computational time. A trade must thus be performed between the expected accuracy of the results, and the computational time necessary to yield those results. To do this, the accuracy of the integration method, or error, should be known. It can be defined in two aspects: local truncation error, which represents the error in one integration step, and the final error (or global truncation error), which represents the accumulated errors over the whole simulation. Next, the robustness of the integration method should be evaluated, in order to know how the solution would behave if small changes were made in the problem's initial condition. If such changes induce large final errors, the integration method chosen is said to be unstable. The step size of an integration method is also to be considered. It should be easily adjustable. It can be divided into two aspects: fixed step size methods and variable step size methods. The latter offers the possibility to adjust the step size to optimise the computation: a large step size can be set for certain instances to decrease the computational time, and more importantly the step size can be adjusted with respect to the error. This means that if the error tends to get out of bounds, the step size can be reduced to avoid that.

During this thesis' simulations, both variable step and fixed step methods were explored, namely focusing on the Runge-Kutta 45 and Runge-Kutta 4 algorithms. A fixed step method was used for the final simulations: Runge-Kutta 4, with an integration frequency of 50 Hz to ensure both accuracy of the results and limited computational time. This yields a time step of 0.02 s for the whole simulation. Note that the guidance module was operated at a lower frequency of 10 Hz to yield convergence before passing the guidance commands to the control module. The Runge-Kutta 45 algorithm was used in the propagation of the orbiting spacecraft's orbit.

### C.2.1. Runge-Kutta Method

Related to Euler's integration method is the family of Runge-Kutta methods. They do not require excessive computation time and are relatively easy to use as they are present in most software environment and libraries. The Runge-Kutta-Fehlberg (RKF45) method is the most widely used and has been proven to be superior to Euler and Trapezoidal integration methods for instance. It offers the possibility of varying the step size and has its truncation terms in the fifth order. This method yields two solutions for each integration step, defined as follows:

$$\begin{aligned}
k_1 &= hf\left(t_n, y_n\right) \\
k_2 &= hf\left(t_n + a_2 h, y_n + b_{21}k_1\right) \\
k_3 &= hf\left(t_n + a_3 h, y_n + b_{31}k_1 + b_{32}k_2\right) \\
k_4 &= hf\left(t_n + a_4 h, y_n + b_{41}k_1 + b_{42}k_2 + b_{43}k_3\right) \\
k_5 &= hf\left(t_n + a_5 h, y_n + b_{51}k_1 + b_{52}k_2 + b_{53}k_3 + b_{54}k_4\right) \\
k_6 &= hf\left(t_n + a_6 h, y_n + b_{61}k_1 + b_{62}k_2 + b_{63}k_3 + b_{64}k_4 + b_{65}k_5\right)
\end{aligned} \tag{C.5}$$

The fifth-order solution is as follows:

$$y_{n+1} = y_n + c_1k_1 + c_2k_2 + c_3k_3 + c_4k_4 + c_5k_5 + c_6k_6 + \mathcal{O}\left(h^6\right) \tag{C.6}$$

The so-called embedded fourth order solution is as follows:

$$y^*_{n+1} = y_n + c^*_1k_1 + c^*_2k_2 + c^*_3k_3 + c^*_4k_4 + c^*_5k_5 + \mathcal{O}\left(h^5\right) \tag{C.7}$$

The difference between the two solutions is used to calculate the truncation error. The step size $h$ can be decreased when the error does not meet the predefined truncation error requirements, and it can be increased when the error results in a too accurate system, with respect to the predefined requirements. The truncation error is estimated as follows:

$$\Delta \equiv y_{n+1} - y^*_{n+1} = \sum_{i=1}^{6}\left(c_i - c^*_i\right)k_i \tag{C.8}$$

MATLAB offers multiple numerical integrators. They are divided in three problem type categories: stiff, non-stiff, and fully implicit. The equations of motions are of the explicit form $y' = f(t, y)$ so the integrators for fully implicit problems can be ignored. In terms of the stiffness of the problem at hand, it cannot be determined before simulation. A stiff and a non-stiff integrator will thus be selected here, so as to be able to

| $i$ | $a_i$ | $b_{ij}$ | | | | | | $c_i$ | $c_i^*$ |
|---|---|---|---|---|---|---|---|---|---|
| 1 | | | | | | | | $\frac{35}{384}$ | $\frac{5179}{57600}$ |
| 2 | $\frac{1}{5}$ | $\frac{1}{5}$ | | | | | | 0 | 0 |
| 3 | $\frac{3}{10}$ | $\frac{3}{40}$ | $\frac{9}{40}$ | | | | | $\frac{500}{1113}$ | $\frac{7571}{16695}$ |
| 4 | $\frac{4}{5}$ | $\frac{44}{45}$ | $-\frac{56}{15}$ | $\frac{32}{9}$ | | | | $\frac{125}{192}$ | $\frac{393}{640}$ |
| 5 | $\frac{8}{9}$ | $\frac{19372}{6561}$ | $-\frac{25360}{2187}$ | $\frac{64448}{6561}$ | $-\frac{212}{729}$ | | | $-\frac{2187}{6784}$ | $-\frac{92097}{339200}$ |
| 6 | 1 | $\frac{9017}{3168}$ | $-\frac{355}{33}$ | $\frac{46732}{5247}$ | $\frac{49}{176}$ | $-\frac{5103}{18656}$ | | $\frac{11}{84}$ | $\frac{187}{2100}$ |
| 7 | 1 | $\frac{35}{384}$ | 0 | $\frac{500}{1113}$ | $\frac{125}{192}$ | $-\frac{2187}{6784}$ | $\frac{11}{84}$ | 0 | $\frac{1}{40}$ |
| $j =$ | | 1 | 2 | 3 | 4 | 5 | 6 | | |

**Figure C.1:** Integration parameters used in adaptive step-size RK45 approach (Dormand and Prince, 1980; Rijnsdorp, 2017).

compare the accuracy of the results and computational time of the simulation. MATLAB offers three non-stiff integrators ($ode45$, $ode23$, and $ode113$) and four stiff integrators ($ode15s$, $ode23s$, $ode23t$, and $ode23tb$). The most commonly used non-stiff integrator is $ode45$, which uses the constants shown in Figure C.1, found by Dormand and Prince (1980). It is the solver that will first be used in the simulations for its better performance compared to $ode23$ and $ode113$ in terms of accuracy and speed. Indeed, the $ode23$ solver is based on a third order Runge-Kutta method, while the $ode45$ solver on a fifth order Runge-Kutta method. The solution of the $ode113$ solver is based on multiple previous steps, which might be difficult to implement if only a single initial condition is available in the simulation. If the problem is suspected to be stiff, then $ode15s$ will be used.[2]

## C.3. Interpolation

Interpolation methods will be necessary to interpolate between tabulated values for the control module's gains, the reference trajectory, and the aerodynamic coefficients of the reference vehicle. Different types of interpolation are available, such as the simple linear interpolation, Lagrange polynomial interpolation, cubic spline interpolation, or the Hermite spline interpolation. The latter three methods have the advantage of producing continuous functions that can be differentiated at the control points. This would be preferred for the guidance module, as sudden changes in the angle-of-attack and bank angle are a possibility, as well as for any other database with sparse data points.

The Lagrange polynomial interpolation method, however, has the disadvantage of needing higher degree polynomials for an increasing number of control points, which leads to oscillating polynomials. As a difference to Lagrange polynomial interpolation, where a high-degree polynomial is fitted to all the values at once, spline interpolation uses low-degree polynomials to fit to small subsets of the values. Different low-degree polynomials are thus created between each set of points. Hermite splines are of order 3 and demand the data points to be continuous at their first derivative. Cubic splines are of order 4, and demand the points to be continuous in both their first and second derivatives. Due to their advantage of needing continuity only in the data points' first derivatives, Hermite splines will be used for the interpolation of the reference trajectory fed to the guidance module. Linear interpolation is sufficient and will be used for the interpolation of the tabulated aerodynamic coefficients of the reference vehicle. Both linear and Hermite spline interpolation methods will be explained below.

### C.3.1. Linear Interpolation

The one-dimensional linear interpolation function can be expressed as follows (Mathews and Fink, 1999):

$$s_k(x) = y_k + \frac{y_{k+1} - y_k}{x_{k+1} - x_k}(x - x_k) \tag{C.9}$$

Here, $x$ denotes the input parameter and $y$ corresponds to the tabulated data. The subscript $k$ and $k+1$ define the data point's position in the table. MATLAB/Simulink possess the "Lookup Tables" functionality,

[2] `https://www.mathworks.com/help/matlab/math/choose-an-ode-solver.html`, accessed on 05/03/2021.

which enables linear interpolation to be conducted. It first interpolates over the first dimension, then over the second, up until all dimensions are evaluated. The derivatives $\frac{dy}{dx}$ of the tabulated values can be computed by calculating the slope as follows:

$$\frac{dy}{dx} = \frac{y_{k+1} - y_k}{x_{k+1} - x_k} \tag{C.10}$$

In the case where data outside of the particular tabulated range would be needed, extrapolation should be considered. If no information is available on the behaviour of the aerodynamic coefficients, the last value of the table can be used.

### C.3.2. Hermite Spline Interpolation

Another interpolation method method is the Hermite Spline Interpolation method. For an interval $[x_j, x_{j+1}]$, the interpolated value $s_k(x)$ can be computed as follows:

$$\begin{aligned} s_k(x) = {} & y_k \left(1 + 2\tfrac{x_k - x}{x_k - x_{k+1}}\right)\left(\tfrac{x - x_{k+1}}{x_k - x_{k+1}}\right)^2 + y_{k+1}\left(1 + 2\tfrac{x_{k+1} - x}{x_{k+1} - x_k}\right)\left(\tfrac{x - x_k}{x_{k+1} - x_k}\right)^2 \\ & + d_k (x - x_k)\left(\tfrac{x - x_{k+1}}{x_k - x_{k+1}}\right)^2 + d_{k+1}\left(\tfrac{x - x_k}{x_{k+1} - x_k}\right)^2 \end{aligned} \tag{C.11}$$

Similarly to Equation (C.9), $x$ denotes the input parameter and $y$ corresponds to the tabulated data. The subscript $k$ and $k+1$ define the data point's position in the table. The elements $d_k$ and $d_{k+1}$ correspond to weighted derivatives and can be determined as follows:

$$\frac{w_1 + w_2}{d_k} = \frac{w_1}{\delta_{k-1}} \frac{w_2}{\delta_k} \qquad \text{with} \qquad \begin{aligned} w_1 &= 2h_k + h_{k-1} \\ w_2 &= h_k + 2h_{k-1} \\ h_k &= x_{k+1} - x_k \end{aligned} \tag{C.12}$$

Here, $d_k$ is the slope at point $k$, $\delta_k$ and $\delta_{k+1}$ the slopes left and right of $k$, and $h$ is the width of the interval. If $\delta_k$ and $\delta_{k+1}$ have opposite signs, the element $d_k$ is set to zero to avoid overshoot.

# D

# Reference Frames and Transformation Matrices

## D.1. Reference Frames

The motion of an object in space is expressed with respect to a reference frame. Newton's laws of motion are usually expressed with respect to an inertial reference frame, while other reference frame types are typically used for other types of analysis. Here, the reference frame specific to the mission at hand will be presented.

- **J2000 Reference Frame:**
  J2000 refers to a standard equinox and epoch. The J2000 epoch is defined as the instant at noon (12:00 Terrestrial Time) on January 1, 2000. The prefix "J" corresponds to a Julian epoch. The J2000 equinox refers to a standard direction (the vernal equinox) defined at epoch J2000. This reference is needed because the right ascension and declination of stars are constantly changing due to effects like precession, and/or proper motion. The J2000 reference equinox will be used to define the two nodes of Uranus' equator on the International Celestial Reference Frame (ICRF) equator.
- **International Celestial Reference Frame (ICRF):**
  The ICRF is a quasi-inertial reference frame and is centred at the barycenter of the Solar System. The latest ICRF3 version is defined by the adopted locations of 303 extragalactic radio sources. It has a non-rotating, non-accelerating origin.
- **Invariable Plane of the Solar System:**
  The invariable plane of the solar Solar System is defined as the plane perpendicular to the Solar System's total angular momentum vector, and passing through its barycenter. Its orientiation with respect to the ICRF is given by an inclination of $23°0'31''.9$ and a longitude of the ascending node of $3°51'9''.4$. Its orientation with respect to the ecliptic-equinox of J2000 is given by an inclination of $1°34'43''.3$ and a longitude of the ascending node of $107°34'56''$ (Souami and Souchay, 2012).
- **Heliocentric Reference Frame:**
  A heliocentric reference frame has its origin located at the centre of mass (c.o.m.) of the Sun. It is denoted with the index $H$. The $Z_H$-axis points north along the Sun's axis of rotation (whose rotation is assumed to be constant in magnitude and direction), the solar ascending node on the ecliptic of J2000 forms the $X_H$-axis, and the $Y_H$-axis completes the right-handed system.
- **Rotating Planetocentric Reference Frame:**
  The rotating planetocentric reference frame is denoted with the index $R$ and coincides with the inertial planetocentric reference frame at time $t = t_0$, as well as once every full rotation of the central body. Its origin is located at the central body's c.o.m. The $Z_R$-axis points north along the central body's axis of rotation, the $X_R$-axis passes through the equator at zero longitude, and the $Y_R$-axis completes the right-handed system.
- **Body-Fixed Reference Frame:**
  The body-fixed reference frame typically has its origin located at the c.o.m. of the vehicle, or at a geometrically convenient point at time $t = t_0$. It is denoted with the index $B$. The $X_B$-axis lies in the vehicle's plane of symmetry and is directed towards the vehicle's forward direction. The $Z_B$-axis also lies in the vehicle's plane of symmetry and is directed downwards, while the $Y_B$-axis completes the right-handed system. Rotations around these three axes describe the motions of roll, yaw, and pitch

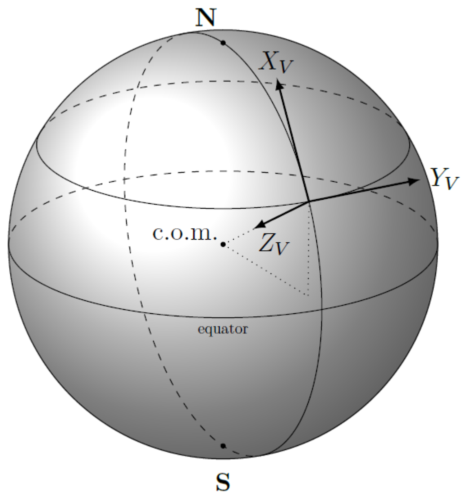


**Figure D.1:** Vertical reference frame definition (Holtkamp, 2014).

respectively. This reference frame is used to describe the orientation and position of a vehicle with respect to another reference frame.

- **Vertical Reference Frame:**
The vertical reference frame is denoted with the index $V$. Its origin is the central point of the vehicle, typically its c.o.m. or a convenient geometric location. The $Z_V$-axis points towards the c.o.m. of the central body, along with the radial component of the body's gravitational attraction. The $X_V$-axis lies perpendicular to the $Z_V$-axis in a meridian plane, and points to the north, while the the $Y_V$-axis points east and completes the right-handed system. In case a perfect sphere is assumed for the central body, then the $X_V - Y_V$- plane is the local horizontal plane. An illustration of this reference frame is given in Figure D.1.

- **Trajectory Reference Frame (groundspeed based):**
The trajectory reference frame is denoted with the index $TG$ and its origin lies at the c.o.m. or at a geometrically convenient point of the vehicle. The $X_{TG}$-axis is positive along the velocity vector relative to the $R$-denoted rotational reference frame, the $Z_{TG}$-axis lies in the vertical plane pointing downwards, and the $Y_{TG}$-axis completes the right-handed system.

- **Trajectory Reference Frame (airspeed based):**
The trajectory reference frame is denoted with the index $TA$ and its origin lies at the c.o.m. or at a geometrically convenient point of the vehicle. The $X_{TA}$-axis is positive along the velocity vector relative to the atmosphere, the $Z_{TA}$-axis lies in the vertical plane, pointing downwards, and the $Y_{TA}$-axis completes the right-handed system.

- **Aerodynamics Reference Frame (groundspeed based):**
The aerodynamics reference frame is denoted with the index $AG$ and its origin lies at the c.o.m. or at a geometrically convenient point of the vehicle. The $X_{AG}$-axis is positive along the velocity vector relative to the $R$-denoted rotational reference frame. This thus implies that the $X_{AG}$-axis is collinear with the $X_{TG}$-axis. The $Z_{AG}$-axis is collinear with the aerodynamic lift vector but in opposite direction, and the $Y_{AG}$-axis completes the right-handed system. The aerodynamic and trajectory reference frames are the same when the vehicle is not banking.

- **Aerodynamics Reference Frame (airspeed based):**
The aerodynamics reference frame is denoted with the index $AA$ and its origin lies at the c.o.m. or at a geometrically convenient point of the vehicle. The $X_{AA}$-axis is positive along the velocity vector relative to the atmosphere. This thus implies that the $X_{AA}$-axis is collinear with the $X_{TA}$-axis. The $Z_{AA}$-axis is collinear with the aerodynamic lift vector but in opposite direction, and the $Y_{AA}$-axis completes the right-handed system. The aerodynamic and trajectory reference frames are the same when the vehicle is not banking.

- **Wind Reference Frame:**
The wind reference frame is denoted with the index $W$. The $X_W$-axis is directed along the wind-velocity vector. For a northern wind, the $X_W$-axis is defined as positive in the northern direction. For a wind

occurring in the local horizontal plane, the $Z_W$-axis is defined as positive downward, and the $Y_W$-axis completes the right-handed system.

# D.2. Frame Transformations

It is crucial to be able to transform elements expressed in one reference frame to another to set up the equations of motion of an object. Based on the work of Mooij (1997b), unit-axis transformations will be explained, as well as all required important transformations related to the systems at hand in this mission. An axis transformation typically consists of a translation and a rotation. If an arbitrary vector $\mathbf{v_A}$ defined in axis system $A$ is expressed in axis system $B$, then we get the following relation:

$$\mathbf{v_B} = \mathbf{T} + \mathbf{C_{B,A}} \cdot \mathbf{v_A} \tag{D.1}$$

Here, $\mathbf{T}$ is a translation vector and $\mathbf{C_{B,A}}$ is the transformation matrix defining the rotation from frame $A$ to frame $B$. As a convention, transformation matrices will always be defined of the sort in this report.

## Unit-Axis Rotations

Any rotation from a (right-handed Cartesian) frame to another can be decomposed into sequential unit-axis rotations. Let us consider arbitrary rotations of angle $\alpha$ about the three $X$-, $Y$-, and $Z$-axes of a particular reference frame denoted with subscripts $1, 2, 3$. Then the three transformation matrices defining the rotations are expressed as follows:

$$\mathbf{C_1}(\alpha) = \begin{bmatrix} 1 & 0 & 0 \\ 0 & \cos\alpha & \sin\alpha \\ 0 & -\sin\alpha & \cos\alpha \end{bmatrix} \tag{D.2}$$

$$\mathbf{C_2}(\alpha) = \begin{bmatrix} \cos\alpha & 0 & -\sin\alpha \\ 0 & 1 & 0 \\ \sin\alpha & 0 & \cos\alpha \end{bmatrix} \tag{D.3}$$

$$\mathbf{C_3}(\alpha) = \begin{bmatrix} \cos\alpha & \sin\alpha & 0 \\ -\sin\alpha & \cos\alpha & 0 \\ 0 & 0 & 1 \end{bmatrix} \tag{D.4}$$

A resulting transformation matrix expressing the rotation from one frame to another can thus be expressed as a combination of the orthonormal $\mathbf{C_1}, \mathbf{C_2}$ and $\mathbf{C_3}$ matrices. This combination should be made in the form of a product. The transformation matrix from frame $A$ to $B$ with successive rotations $a$, $b$, and $c$ is expressed as:

$$\mathbf{C_{B,A}} = \mathbf{C_c}\mathbf{C_b}\mathbf{C_a} \tag{D.5}$$

The following holds for orthonormal matrices:

$$\mathbf{C_{B,A}} = \mathbf{C_{B,A}^{-1}} = \mathbf{C_{B,A}^{T}} \tag{D.6}$$

## Standard Frame Transformations

Here, standard frame transformations between the reference frames defined in Section D.1 will be given. The fully-derived transformation matrices are available in the work of Mooij (1997b).

- **Rotating Planetocentric to Inertial Planetocentric Frame:**
  Both frames coincide at time $t_0$. The rotating planetocentric reference frame rotates around the $Z_R$-axis with the central body's rotational velocity $w_{cb}$. As a function of time, the transformation matrix can thus be expressed as follows:

$$\mathbf{C_{I,R}} = \mathbf{C_3}(-\omega_{cb}t) = \begin{bmatrix} \cos\omega_{cb}t & -\sin\omega_{cb}t & 0 \\ \sin\omega_{cb}t & \cos\omega_{cb}t & 0 \\ 0 & 0 & 1 \end{bmatrix} \tag{D.7}$$

- **Vertical to Rotating Planetocentric Frame:**
  In this case, we consider the vehicle's longitude $\tau$ and latitude $\delta$. The corresponding transformation matrix is expressed as follows:

$$\mathbf{C_{R,V}} = \mathbf{C_3}(-\tau)\mathbf{C_2}(\frac{\pi}{2}+\delta) = \begin{bmatrix} -\cos\tau\sin\delta & -\sin\tau & -\cos\tau\cos\delta \\ -\sin\tau\sin\delta & \cos\tau & -\sin\tau\cos\delta \\ \cos\delta & 0 & -\sin\delta \end{bmatrix} \tag{D.8}$$

- **Wind to Vertical Frame:**
  In this case, we consider the wind vector's flight-path angle $\gamma_w$ and heading $\chi_w$. The corresponding transformation matrix is expressed as follows:

$$\mathbf{C_{V,W}} = \mathbf{C_3}(-\chi_w)\mathbf{C_2}(-\gamma_w) = \begin{bmatrix} \cos\chi_w\cos\gamma_w & -\sin\chi_w & \cos\chi_w\sin\gamma_w \\ \sin\chi_w\cos\gamma_w & \cos\chi_w & \sin\chi_w\sin\gamma_w \\ -\sin\gamma_w & 0 & \cos\gamma_w \end{bmatrix} \tag{D.9}$$

- **(Groundspeed-based) Trajectory to Vertical Frame:**
  In this case, we consider the flight-path angle for groundspeed $\gamma_g$ and heading $\chi_g$. The corresponding transformation matrix is expressed as follows, and is similar to the one expressed for the Wind to Vertical Frame transformation, but with a different index:

$$\mathbf{C_{V,TG}} = \mathbf{C_3}(-\chi_g)\mathbf{C_2}(-\gamma_g) \tag{D.10}$$

- **(Airspeed-based) Trajectory to Vertical Frame:**
  In this case, we consider the flight-path angle for airspeed $\gamma_a$ and heading $\chi_a$. The corresponding transformation matrix is expressed as follows, and is similar to the one expressed for the Wind to Vertical Frame transformation, but with a different index:

$$\mathbf{C_{V,TA}} = \mathbf{C_3}(-\chi_a)\mathbf{C_2}(-\gamma_a) \tag{D.11}$$

- **(Airspeed-based) Aerodynamic to (airspeed-based) Trajectory Frame:**
  In this case, we consider the bank angle based on airspeed $\sigma_a$. The corresponding transformation matrix is expressed as follows:

$$\mathbf{C_{TA,AA}} = \mathbf{C_1}(\sigma_a) = \begin{bmatrix} 1 & 0 & 0 \\ 0 & \cos\sigma_a & \sin\sigma_a \\ 0 & -\sin\sigma_a & \cos\sigma_a \end{bmatrix} \tag{D.12}$$

- **(Airspeed-based) Aerodynamic to Vertical Frame:**
  This transformation matrix can be derived from the combination of the previously-mentioned $\mathbf{C_{V,TA}}$ and $\mathbf{C_{TA,AA}}$ matrices as follows:

$$\begin{aligned} \mathbf{C_{V,AA}} &= \mathbf{C_{V,TA}}\mathbf{C_{TA,AA}} = \mathbf{C_3}(-\chi_a)\mathbf{C_2}(-\gamma_a)\mathbf{C_1}(\sigma_a) \\ &= \begin{bmatrix} \cos\chi_a\cos\gamma_a & -\sin\chi_a\cos\sigma_a - \cos\chi_a\sin\gamma_a\sin\sigma_a & -\sin\chi_a\sin\sigma_a + \cos\chi_a\sin\gamma_a\cos\sigma_a \\ \sin\chi_a\cos\gamma_a & \cos\chi_a\cos\sigma_a - \sin\chi_a\sin\gamma_a\sin\sigma_a & \cos\chi_a\sin\sigma_a + \sin\chi_a\sin\gamma_a\cos\sigma_a \\ -\sin\gamma_a & -\cos\gamma_a\sin\sigma_a & \cos\gamma_a\cos\sigma_a \end{bmatrix} \end{aligned} \tag{D.13}$$

- **(Airspeed-based) Aerodynamic to (groundspeed-based) Trajectory Frame:**
  This transformation matrix can be derived from the combination of the previously-mentioned $\mathbf{C_{TG,V}}$ and $\mathbf{C_{V,AA}}$ matrices as follows, with $\Delta\chi_{ga} = \chi_g - \chi_a$:

$$\mathbf{C_{TG,AA}} = \mathbf{C_{TG,V}}\mathbf{C_{V,AA}} = \mathbf{C_2}(\gamma_g)\mathbf{C_3}(\Delta\chi_{ga})\mathbf{C_2}(-\gamma_a)\mathbf{C_1}(\sigma_a) \tag{D.14}$$

- **Body to (airspeed-based) Aerodynamic Frame:**
  In this case, we consider the angle-of-attack with respect to the airspeed $\alpha_a$ and angle of side-slip with respect to the airspeed $\beta_a$. The corresponding transformation matrix is expressed as follows:

$$\mathbf{C_{AA,B}} = \mathbf{C_3}(\beta_a)\mathbf{C_2}(-\alpha_a) = \begin{bmatrix} \cos\alpha_a\cos\beta_a & \sin\beta_a & \sin\alpha_a\cos\beta_a \\ -\cos\alpha_a\sin\beta_a & \cos\beta_a & -\sin\alpha_a\sin\beta_a \\ -\sin\alpha_a & 0 & \cos\alpha_a \end{bmatrix} \tag{D.15}$$

- **Body to (groundspeed-based) Aerodynamic Frame:**
In this case, we consider the angle-of-attack with respect to the groundspeed $\alpha_g$ and angle of side-slip with respect to the groundspeed $\beta_g$. The corresponding transformation matrix is expressed as follows:

$$\mathbf{C_{AG,B}} = \mathbf{C_3}(\beta_g)\mathbf{C_2}(-\alpha_g) = \begin{bmatrix} \cos\alpha_g\cos\beta_g & \sin\beta_g & \sin\alpha_g\cos\beta_g \\ -\cos\alpha_g\sin\beta_g & \cos\beta_g & -\sin\alpha_g\sin\beta_g \\ -\sin\alpha_g & 0 & \cos\alpha_g \end{bmatrix} \tag{D.16}$$

- **Vertical to Inertial Planetocentric Frame:**
This transformation matrix can be derived from the combination of the previously-mentioned $\mathbf{C_{I,R}}$ and $\mathbf{C_{R,V}}$ matrices as follows, with the celestial longitude $\tilde{\tau}$ expressed as $\tilde{\tau} = \tau + \omega_{cb}t$:

$$\begin{aligned} \mathbf{C_{I,V}} &= \mathbf{C_{I,R}}\mathbf{C_{R,V}} = \mathbf{C_3}(-\omega_{cb}t)\mathbf{C_3}(-\tau)\mathbf{C_2}(\tfrac{\pi}{2}+\delta) = \mathbf{C_3}(-\tilde{\tau})\mathbf{C_2}(\tfrac{\pi}{2}+\delta) \\ &= \begin{bmatrix} -\cos\tilde{\tau}\sin\delta & -\sin\tilde{\tau} & -\cos\tilde{\tau}\cos\delta \\ -\sin\tilde{\tau}\sin\delta & \cos\tilde{\tau} & -\sin\tilde{\tau}\cos\delta \\ \cos\delta & 0 & -\sin\delta \end{bmatrix} \end{aligned} \tag{D.17}$$

- **(Airspeed-based) Aerodynamic to Rotating Planetocentric Frame:**
This transformation matrix can be derived from the combination of the previously-mentioned $\mathbf{C_{R,V}}$ and $\mathbf{C_{V,AA}}$ matrices as follows:

$$\mathbf{C_{R,AA}} = \mathbf{C_{R,V}}\mathbf{C_{V,AA}} = \mathbf{C_3}(-\tau)\mathbf{C_2}(\frac{\pi}{2}+\delta)\mathbf{C_3}(-\chi_a)\mathbf{C_2}(-\gamma_a)\mathbf{C_1}(\sigma_a) \tag{D.18}$$

- **Body to Rotating Planetocentric Frame:**
This transformation matrix can be derived from the combination of the previously-mentioned $\mathbf{C_{R,V}}$, $\mathbf{C_{V,AG}}$, and $\mathbf{C_{AG,B}}$ matrices as follows:

$$\mathbf{C_{R,B}} = \mathbf{C_{R,V}}\mathbf{C_{V,AG}}\mathbf{C_{AG,B}} = \mathbf{C_3}(-\tau)\mathbf{C_2}(\frac{\pi}{2}+\delta)\mathbf{C_3}(-\chi_g)\mathbf{C_2}(-\gamma_g)\mathbf{C_1}(\sigma_g)\mathbf{C_3}(\beta_g)\mathbf{C_2}(-\alpha_g) \tag{D.19}$$

Basing the transformation on the airspeed yields:

$$\mathbf{C_{R,B}} = \mathbf{C_{R,V}}\mathbf{C_{V,AA}}\mathbf{C_{AA,B}} = \mathbf{C_3}(-\tau)\mathbf{C_2}(\frac{\pi}{2}+\delta)\mathbf{C_3}(-\chi_a)\mathbf{C_2}(-\gamma_a)\mathbf{C_1}(\sigma_a)\mathbf{C_3}(\beta_a)\mathbf{C_2}(-\alpha_a) \tag{D.20}$$

- **(Groundspeed-based) Trajectory to Wind Frame:**
This transformation matrix can be derived from the combination of the previously-mentioned $\mathbf{C_{V,TG}}$, and the inverse of $\mathbf{C_{V,W}}$ matrices as follows, with $\Delta\chi_{wg} = \chi_w - \chi_g$:

$$\mathbf{C_{W,TG}} = \mathbf{C_{W,V}}\mathbf{C_{V,TG}} = \mathbf{C_2}(\gamma_w)\mathbf{C_3}(\chi_w)\mathbf{C_3}(-\chi_g)\mathbf{C_2}(-\gamma_g) = \mathbf{C_2}(\gamma_w)\mathbf{C_3}(\Delta\chi_{wg})\mathbf{C_2}(-\gamma_g) \tag{D.21}$$

- **(Airspeed-based) Aerodynamic to Wind Frame:**
This transformation matrix can be derived from the combination of the previously-mentioned $\mathbf{C_{V,AA}}$, and the inverse of $\mathbf{C_{V,W}}$ matrices as follows, with $\Delta\chi_{wa} = \chi_w - \chi_a$:

$$\begin{aligned} \mathbf{C_{W,AA}} &= \mathbf{C_{W,V}}\mathbf{C_{V,AA}} = \mathbf{C_2}(\gamma_w)\mathbf{C_3}(\chi_w)\mathbf{C_3}(-\chi_a)\mathbf{C_2}(-\gamma_a)\mathbf{C_1}(\sigma_a) \\ &= \mathbf{C_2}(\gamma_w)\mathbf{C_3}(\Delta\chi_{wa})\mathbf{C_2}(-\gamma_a)\mathbf{C_1}(\sigma_a) \end{aligned} \tag{D.22}$$

- **Coordinate System Transformations:**
The **transformation from orbital elements** ($a$, $e$, $i$, $\Omega$, $\omega$, $M$) **to Cartesian components** ($x$, $y$, $z$) (and vice versa) is explained here. A Python script was written and verified for this purpose. These transformations will be used when working with the orbiter or spacecraft performing a fly-by. Orbital elements can help visualise and quantify the change in the spacecraft's orbit, but the orbit will

be simulated in Cartesian component. First the parameters $l_1$, $l_2$, $m_1$, $m_2$, $n_1$, and $n_2$ are computed using the following relationships:

$$\begin{aligned} l_1 &= \cos\Omega\cos\omega - \sin\Omega\sin\omega\cos i \\ l_2 &= -\cos\Omega\sin\omega - \sin\Omega\cos\omega\cos i \\ m_1 &= \sin\Omega\cos\omega + \cos\Omega\sin\omega\cos i \\ m_2 &= -\sin\Omega\sin\omega + \cos\Omega\cos\omega\cos i \\ n_1 &= \sin\omega\sin i \\ n_2 &= \cos\omega\sin i \end{aligned} \tag{D.23}$$

Then, using Kepler's Equation, the eccentric anomaly $E$ is found from:

$$M = E - e\sin E \tag{D.24}$$

The value of the true anomaly $\theta$ can be calculating by re-arranging the following equation:

$$\tan\frac{\theta}{2} = \sqrt{\frac{1+e}{1-e}}\tan\frac{E}{2} \tag{D.25}$$

The distance $r$ from the focal point till the object of interest is then calculated using the following:

$$r = a(1 - e\cos E) \tag{D.26}$$

Then the following vector can be computed:

$$\begin{pmatrix} \xi \\ \eta \end{pmatrix} = \begin{pmatrix} r\cos\theta \\ r\sin\theta \end{pmatrix} \tag{D.27}$$

The $x$, $y$, and $z$ coordinates are then found using the following equation:

$$\begin{pmatrix} x \\ y \\ z \end{pmatrix} = \begin{bmatrix} l_1 & l_2 \\ m_1 & m_2 \\ n_1 & n_2 \end{bmatrix} \begin{pmatrix} \xi \\ \eta \end{pmatrix} \tag{D.28}$$

Then the parameter $H$ is calculated using:

$$H = \sqrt{\mu a\left(1 - e^2\right)} \tag{D.29}$$

This yields to the computation of the velocity components using the following relationships:

$$\begin{aligned} \dot{x} &= \frac{\mu}{H}\left[-l_1\sin\theta + l_2(e + \cos\theta)\right] \\ \dot{y} &= \frac{\mu}{H}\left[-m_1\sin\theta + m_2(e + \cos\theta)\right] \\ \dot{z} &= \frac{\mu}{H}\left[-n_1\sin\theta + n_2(e + \cos\theta)\right] \end{aligned} \tag{D.30}$$

The **transformation from Cartesian components ($x$, $y$, $z$) to orbital elements ($a$, $e$, $i$, $\Omega$, $\omega$,** $M$) can be done by first putting all position components into a vector $\mathbf{r}$ and all velocity components into a vector $\mathbf{V}$. The semi-major axis is first found using the following equation:

$$a = \frac{1}{\left(\frac{2}{r} - \frac{V^2}{\mu}\right)} \tag{D.31}$$

The angular momentum can be calculated by doing the cross product between the vectors $\mathbf{r}$ and $\mathbf{V}$, as such:

$$\mathbf{h} = \mathbf{r} \times \mathbf{V} \tag{D.32}$$

The eccentricity vector is then calculated using:

$$\mathbf{e} = \frac{\mathbf{V} \times \mathbf{h}}{\mu} - \frac{\mathbf{r}}{r} \tag{D.33}$$

The magnitude of the eccentricity can then be found by taking the square root of the sum of the vector's components squared as follows:

$$e = \sqrt{(e_x)^2 + (e_y)^2 + (e_z)^2} \tag{D.34}$$

The inclination angle is then found using:

$$i = \arccos\left(\frac{h_z}{\|\mathbf{h}\|}\right) \tag{D.35}$$

This gives a result expressed in radians. Here $h_z$ denotes the z component of the angular momentum vector found before, and $\|\mathbf{h}\|$ denotes the magnitude of this vector found in a similar way to Equation (D.34). The vector $\mathbf{N}$ is then computed with the following equation:

$$\mathbf{N} = \begin{pmatrix} 0 \\ 0 \\ 1 \end{pmatrix} \times \mathbf{h} \tag{D.36}$$

The $N_{xy}$ component is then computed using the following equation:

$$N_{xy} = \sqrt{(N_x)^2 + (N_y)^2} \tag{D.37}$$

This $N_{xy}$ component is needed to compute the right ascension of the ascending node (abbreviated as RAAN, and denoted as $\Omega$) using the atan2 function, which enables to find a result which lies in the correct quadrant of the unit circle:

$$\Omega = \text{atan2}\left(\frac{N_y}{N_{xy}}, \frac{N_x}{N_{xy}}\right) \tag{D.38}$$

$$\begin{aligned} \omega &= \text{sign} \cdot \text{acos}(\hat{\mathbf{e}}.\hat{\mathbf{N}}) \quad (\text{sign} = +1 \quad \text{if } (\hat{\mathbf{N}} \times \mathbf{e}).\mathbf{h} > 0; \quad -1 \text{ otherwise }) \\ \theta &= \text{sign} \cdot \text{acos}(\hat{\mathbf{r}}.\hat{\mathbf{e}}) \quad (\text{sign} = +1 \quad \text{if } (\mathbf{e} \times \mathbf{r}).\mathbf{h} > 0; \quad -1 \text{ otherwise }) \end{aligned} \tag{D.39}$$

The **transformation from Cartesian components ($x$, $y$, $z$) to spherical components ($r$, $\tau$, $\delta$) and vice versa** will be used during the atmospheric vehicle's simulations. Although quaternions will be preferred during the simulations because they do not present any singularities, Cartesian and spherical components can help visualise the vehicle's movement, especially with respect to Uranus. The steps to be taken are as follows:

$$\begin{aligned} x &= r\cos\delta\cos\tau \\ y &= r\cos\delta\sin\tau \\ z &= r\sin\delta \end{aligned} \qquad ; \qquad \begin{aligned} r &= \sqrt{x^2 + y^2 + z^2} \\ r_{xy} &= \sqrt{x^2 + y^2} \\ \tau &= \text{atan2}\left(\tfrac{y}{r_{xy}}, \tfrac{x}{r_{xy}}\right) \\ \delta &= \arcsin\tfrac{z}{r} \end{aligned} \tag{D.40}$$

Now onto the relation between Cartesian and spherical velocity, retrieved from the work of Mooij (1997b). The Cartesian velocity in the R-frame is defined as $\mathbf{V_R} = (u, v, w)^T$. The influence of wind is not considered here. The modulus of the ground velocity vector is calculated as follows:

$$V_G = \sqrt{u^2 + v^2 + w^2} \tag{D.41}$$

The Cartesian velocity in the V-frame $\mathbf{V_V} = (v_x, v_y, v_z)^T$ is then calculated as follows, using the transformation matrix between vertical and rotating planetocentric frame defined in Equation (D.8) knowing that $\mathbf{C_{V,R}} = \mathbf{C_{R,V}}^{-1} = \mathbf{C_{R,V}}^T$:

$$\mathbf{V_V} = \mathbf{C_{V,R}} \mathbf{V_R} \tag{D.42}$$

The components of $\mathbf{V_V}$ can also be expressed as follows: $\mathbf{V_V} = (v_x, v_y, v_z)^T = (v_\delta, v_\tau, -v_r)^T$. The following relations can then be established:

$$\begin{aligned}
&V_G \cos\gamma_G = \sqrt{v_\delta^2 + v_\tau^2} \\
&\chi_G = \arctan\left(\tfrac{v_y}{v_x}\right) \\
&V_G \sin\gamma_G = -v_z
\end{aligned} \tag{D.43}$$

Since the angle $\gamma_G$ lies between $-90^\circ$ and $+90^\circ$, the third equation of Equation (D.43) can be used as the arcsine is defined for the same interval:

$$\gamma_G = -\arcsin\left(\frac{v_z}{V_G}\right) \tag{D.44}$$

The components of $\mathbf{V_V}$ can then be computed as follows:

$$\begin{aligned}
&v_x = V_G \cos\gamma_G \cos\chi_G \\
&v_y = V_G \cos\gamma_G \sin\chi_G \\
&v_z = -V_G \sin\gamma_G
\end{aligned} \tag{D.45}$$

Finally, the velocity in the R-frame can be found using: $\mathbf{V_R} = \mathbf{C_{R,V}} \mathbf{V_V}$

- **Attitude System Transformations:**
  Going from Euler attitude angles to aerodynamic attitude angles is trivial as both these frames are equivalent, except for the definition of their angles: the Euler attitude angles are defined between the horizontal and longitudinal axis of plane, while the aerodynamic angles are defined between the velocity vector and longitudinal axis of plane. The transformation between Euler attitude angles with rotation sequence $\psi \Rightarrow \theta \Rightarrow \phi$ and quaternions can be done as follows (Kuipers, 1999). For a quaternion $\mathbf{q}$ is defined with its elements $q_0, q_1, q_2$ and $q_3$:

$$q = q_0 + \mathbf{i}q_1 + \mathbf{j}q_2 + \mathbf{k}q_3 \tag{D.46}$$

$$\begin{aligned}
&q_0 = \cos\tfrac{\psi}{2}\cos\tfrac{\theta}{2}\cos\tfrac{\phi}{2} + \sin\tfrac{\psi}{2}\sin\tfrac{\theta}{2}\sin\tfrac{\phi}{2} \\
&q_1 = \cos\tfrac{\psi}{2}\cos\tfrac{\theta}{2}\sin\tfrac{\phi}{2} - \sin\tfrac{\psi}{2}\sin\tfrac{\theta}{2}\cos\tfrac{\phi}{2} \\
&q_2 = \cos\tfrac{\psi}{2}\sin\tfrac{\theta}{2}\cos\tfrac{\phi}{2} + \sin\tfrac{\psi}{2}\cos\tfrac{\theta}{2}\sin\tfrac{\phi}{2} \\
&q_3 = \sin\tfrac{\psi}{2}\cos\tfrac{\theta}{2}\cos\tfrac{\phi}{2} - \cos\tfrac{\psi}{2}\sin\tfrac{\theta}{2}\sin\tfrac{\phi}{2}
\end{aligned} \tag{D.47}$$

Then the Euler angles $\phi, \theta$, and $\psi$ follow from:

$$\begin{aligned}
&\phi = \operatorname{atan2}\left(2\left(q_2q_3 + q_0q_1\right), 2q_0^2 + 2q_3^2 - 1\right) \\
&\theta = -\arcsin\left(2\left(q_1q_3 + q_0q_2\right)\right) \\
&\psi = \operatorname{atan2}\left(2\left(q_1q_2 + q_0q_3\right), 2q_0^2 + 2q_1^2 - 1\right)
\end{aligned} \tag{D.48}$$

A transformation matrix, or direction cosine matrix, can then be constructed for the integration of the equations of motion:

$$\mathbf{T}_q = \begin{bmatrix} 2q_0^2 + 2q_1^2 - 1 & 2\left(q_1q_2 + q_0q_3\right) & 2\left(q_1q_3 - q_0q_2\right) \\ 2\left(q_1q_2 - q_0q_3\right) & 2q_0^2 + 2q_2^2 - 1 & 2\left(q_2q_3 + q_0q_1\right) \\ 2\left(q_1q_3 + q_0q_2\right) & 2\left(q_2q_3 - q_0q_1\right) & 2q_0^2 + 2q_3^2 - 1 \end{bmatrix} \tag{D.49}$$

# E Control Module Gains

For the control module, two controllers were implemented: a longitudinal one with two necessary gains, and a lateral one with eight other gains. These gains were computed for different values of altitude (0 km, −100 km, −200 km, −300 km, and −375 km) and velocity (9.0 m/s, 25.0 m/s, 50.0 m/s, and 70.0 m/s). This appendix presents the control gains, when plotted with constant altitude and velocity mentioned here.

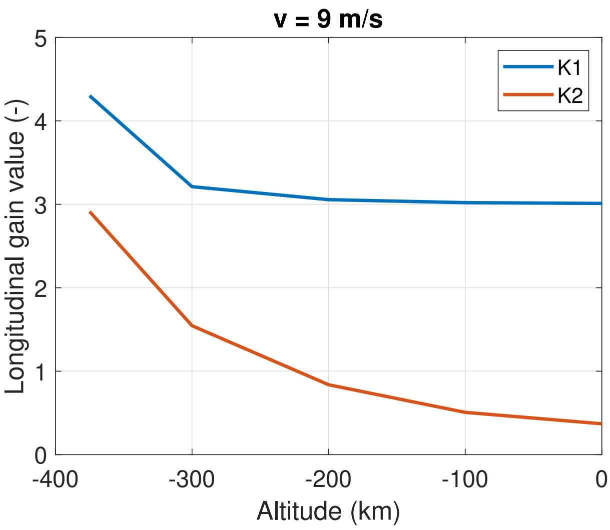


**(a)** Longitudinal control gains at $v = 9$ m/s.

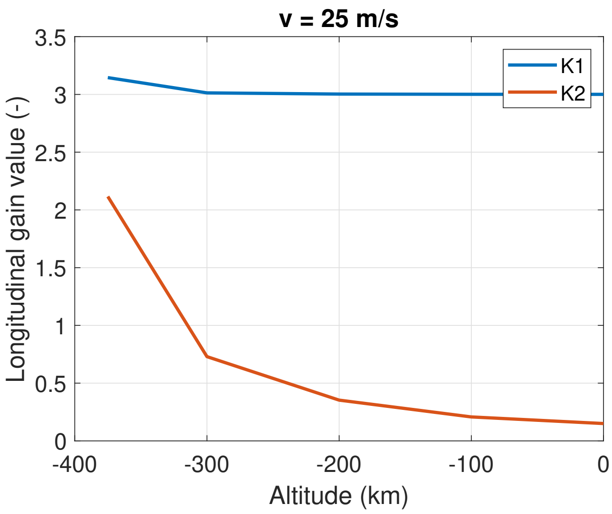


**(b)** Longitudinal control gains at $v = 25$ m/s.

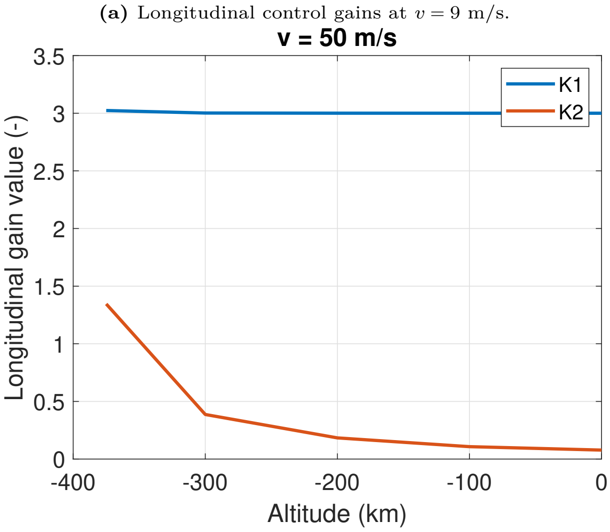


**(c)** Longitudinal control gains at $v = 50$ m/s.

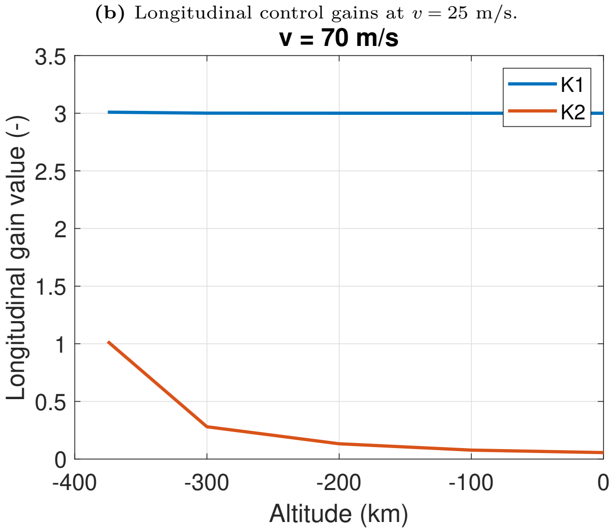


**(d)** Longitudinal control gains at $v = 70$ m/s km.

**Figure E.1:** Behaviour of longitudinal control gains $K_1$ and $K_2$ at constant velocities.

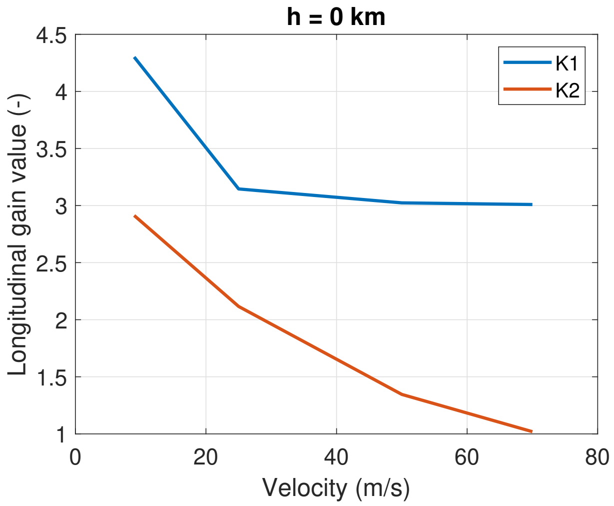


**(a)** Longitudinal control gains at $h = 0$ km.

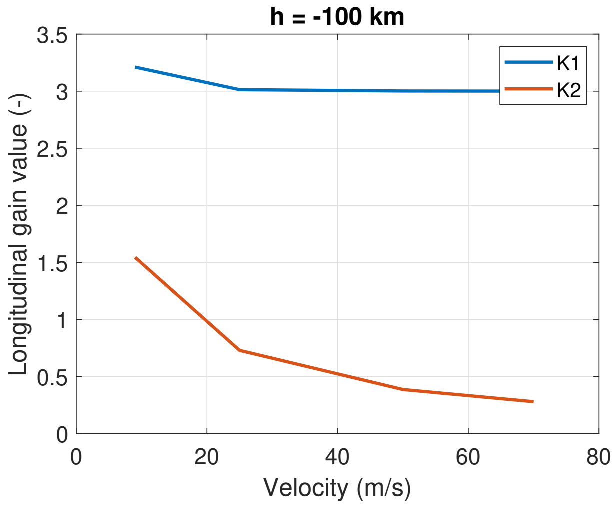


**(b)** Longitudinal control gains at $h = -100$ km.

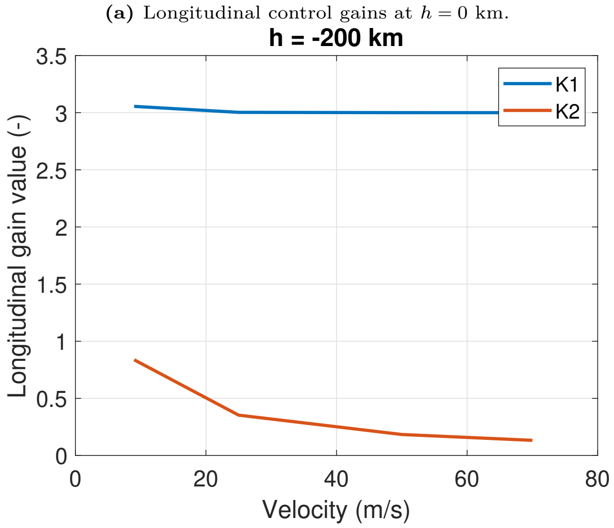


**(c)** Longitudinal control gains at $h = -200$ km.

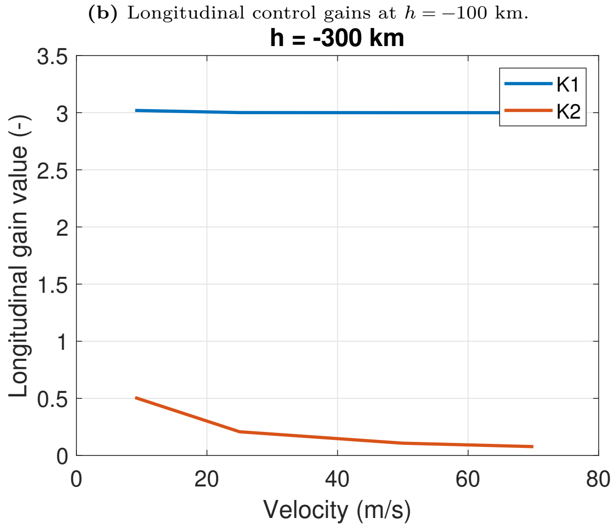


**(d)** Longitudinal control gains at $h = -300$ km.

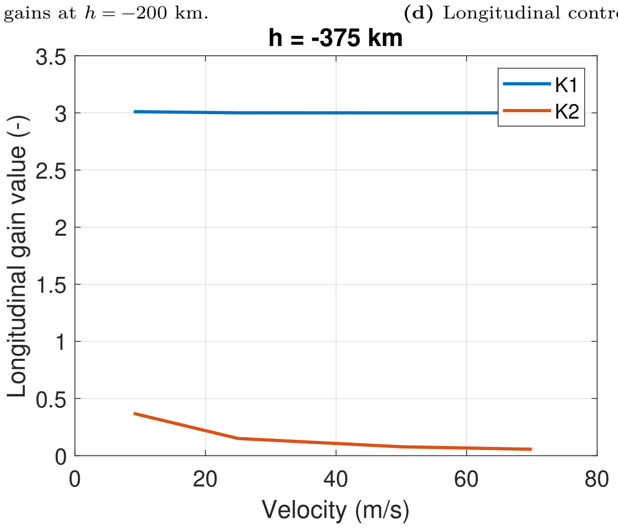


**(e)** Longitudinal control gains at $h = -375$ km.

**Figure E.2:** Behaviour of longitudinal control gains $K_1$ and $K_2$ at constant altitudes.

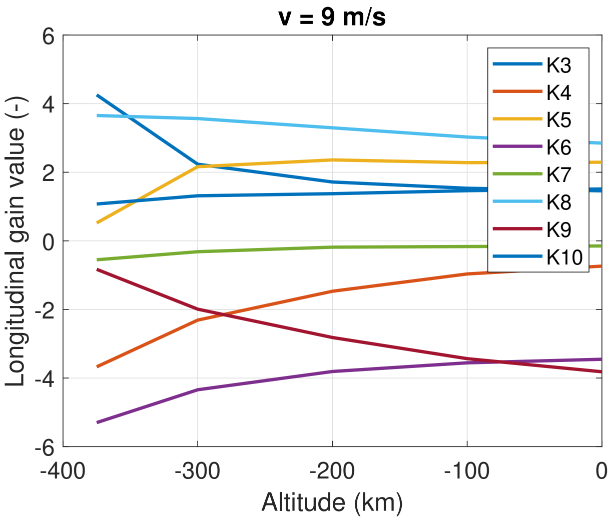


**(a)** Lateral control gains at $v = 9$ m/s.

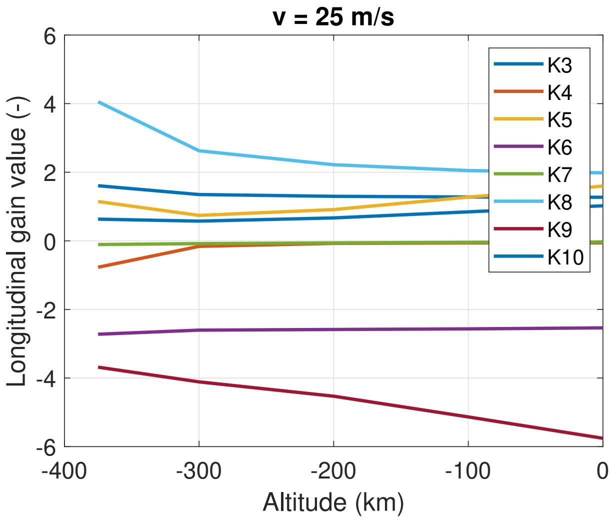


**(b)** Lateral control gains at $v = 25$ m/s.

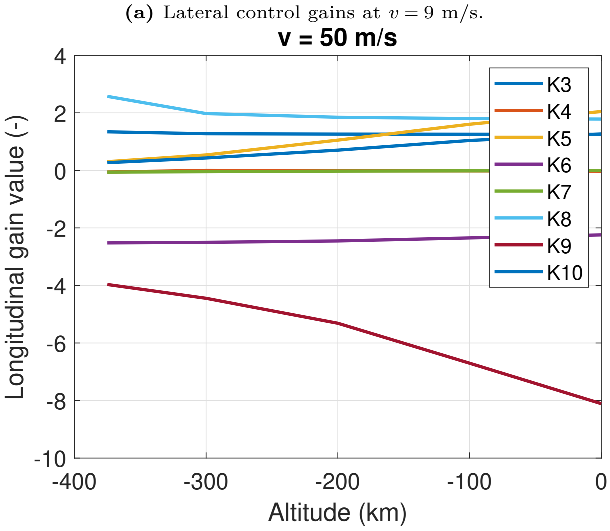


**(c)** Lateral control gains at $v = 50$ m/s.

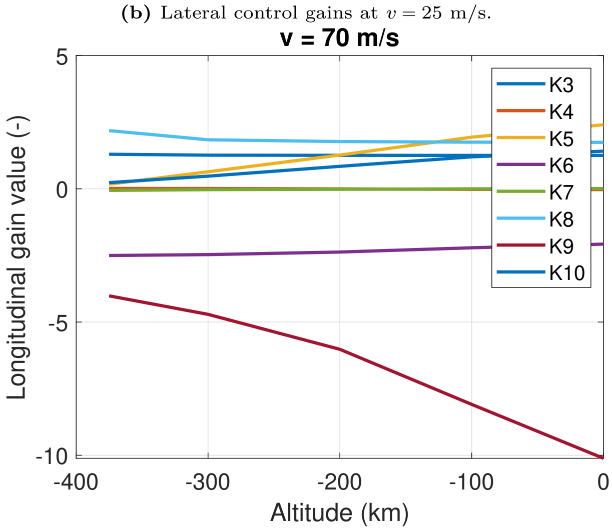


**(d)** Lateral control gains at $v = 70$ m/s km.

**Figure E.3:** Behaviour of lateral control gains $K_3$, $K_4$, $K_5$, $K_6$, $K_7$, $K_8$, $K_9$, and $K_{10}$ at constant velocities.

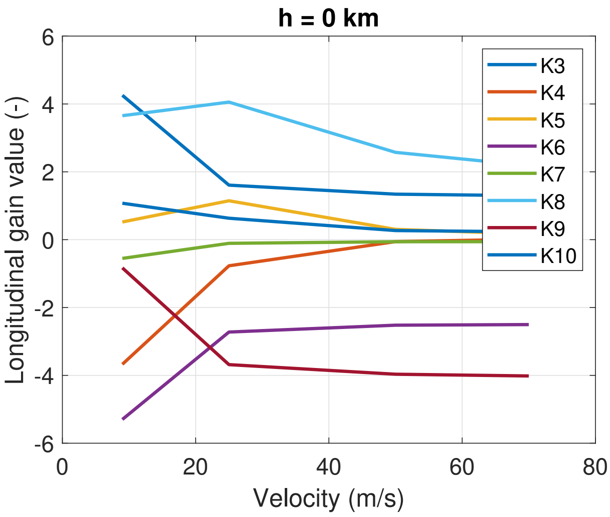


**(a)** Lateral control gains at $h = 0$ km.

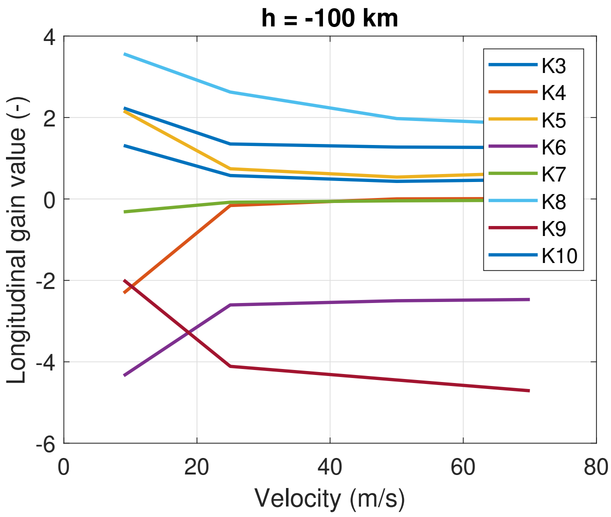


**(b)** Lateral control gains at $h = -100$ km.

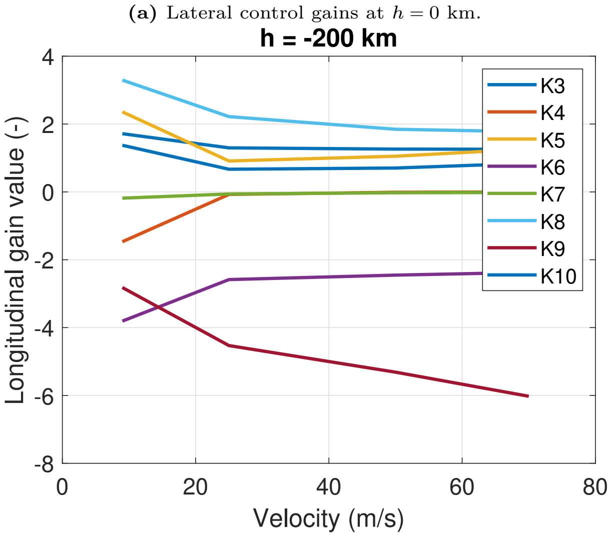


**(c)** Lateral control gains at $h = -200$ km.

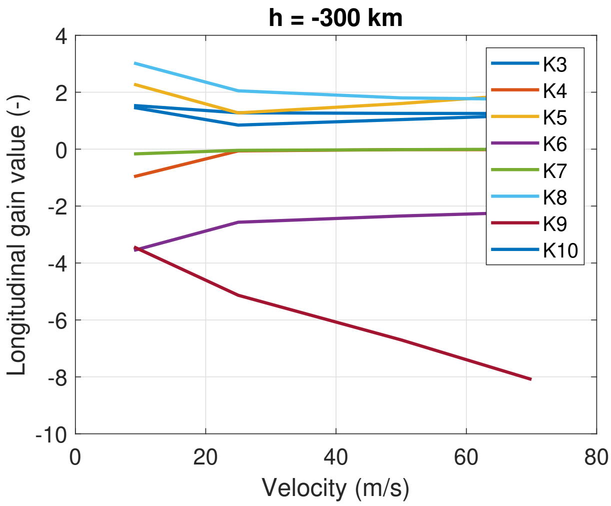


**(d)** Lateral control gains at $h = -300$ km.

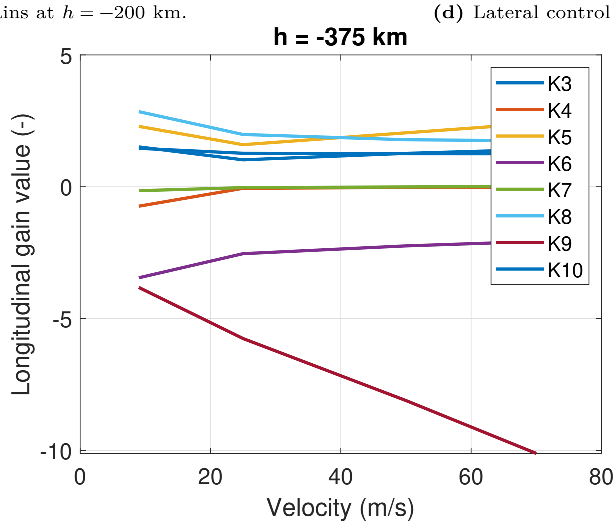


**(e)** Lateral control gains at $h = -375$ km.

**Figure E.4:** Behaviour of lateral control gains $K_3$, $K_4$, $K_5$, $K_6$, $K_7$, $K_8$, $K_9$, and $K_{10}$ at constant altitudes.